The Effect of High Pressure on Crystal Structure Topology

Peter Andrew Wood

Supervisor: Prof. Simon Parsons

PhD **University of Edinburgh** **2008**

Declaration

This thesis has been written entirely by me and has not been submitted in any previous application for a degree. Except where stated, all the work detailed in this thesis has been carried out by me.

Peter Wood

Abstract

This thesis describes the effects of the application of high pressure to single crystals of small organic compounds. A range of different structural analysis techniques have been used with the emphasis on whole molecule interactions rather than atom-atom contacts.

A study of the effect of pressure on the crystal structure of salicylaldoxime showed that the size of a pseudo-macrocyclic cavity within the structure is tuneable by compression. This cavity determines the reactivity of salicylaldoxime as a ligand, when deprotonated it is known to preferentially bind Cu^{2+} ions over other cations in a bis(salicylaldoximato) complex due to the compatibility between the cavity size and the ionic radius of Cu^{2+}. Further compression studies on a range of substituted salicylaldoximes with different ambient cavity sizes showed that the application of pressure consistently decreases the cavity size across the whole series. Variation of substituent and the pressure yields cavities which span the covalent radii of many of the 1^{st} transition series metal dications. This should allow the selectivity of metal extraction to be tuned using pressure.

Computational studies of lattice energies and conformational energies in the compression studies of L-serine and 3-aza-bicyclo(3.3.1)nonane-2,4-dione have shown that significant molecular distortions can occur during compression of a crystal structure below 10 GPa. L-serine shows different conformations between phases with an energy difference of 40 kJ mol^{-1}, whereas the conformation of 3-aza-bicyclo(3.3.1)nonane-2,4-dione is seen to distort within the same phase.

Analysis of a database of compression studies using Hirshfeld surfaces has highlighted the fact that all different types of intermolecular interaction have a lower limit for compression, at least in the pressure regime below 10 GPa. These studies, along with theoretical calculations, have suggested a lower distance limit for H…H contacts of 1.7 Å. This is potentially very useful for prediction of the effects of compression as H…H contacts are almost universal across small organic crystal structures.

Acknowledgements

Firstly I would like to thank my supervisor, Prof. Simon Parsons, without whom this thesis would never have happened, for taking me on as a research student in the first place and always pushing me to achieve more. You have taught me a huge amount about crystallography, chemistry, grammar, doing research and disturbing limericks. I know it probably wasn't obvious at the time, but your efforts have been thoroughly appreciated!

I would also like to thank Stephen Moggach for enduring my endless questions throughout my PhD (almost) without becoming irritated and for being the best office mate I could have asked for. The classic Mojash grin across the desk always made me crack a smile, even when I felt like the thesis would never be finished.

Thanks to Fraser for helping me to keep things in perspective at the low points, for keeping a solid foundation of sarcastic humour within the group and for generally being a great friend. I am also indebted to the rest of the crystallographers at Edinburgh past and present who helped and amused me in equal measure – Patty, Francesca, Iain, Laura, Alessandro, Russell and Anna.

I am also very grateful to the CCDC for firstly sponsoring my PhD project and then, after hiring me as a Research and Applications Scientist, being extremely understanding about the writing-up of my thesis. Thanks especially to Elna Pidcock, my CCDC supervisor, for all the helpful proof-reading and comments.

A big thank-you to all of my family and colleagues (both at Edinburgh and at the CCDC) for not asking constantly about how the thesis is going! Less is most definitely more in this situation…

Finally I would like to say a big thank-you to Rachel, my wonderful girlfriend, for putting up with me throughout the years and for always being happy to read my work even as a non-crystallographer!

Lecture Courses and Meetings Attended

Courses

Aug. 2004	Effective Tutoring course	Edinburgh
Oct. 2004	Radiation Safety lecture course	Edinburgh
Nov. 2004	Science Communication in Action workshop	Edinburgh
Apr. 2005	BCA/CCG Intensive Crystallography course	Durham
Aug. 2005	IUCr Crystallographic Computing school	Siena
Nov. 2005	EaStChem Supramolecular Chemistry course	Edinburgh
May 2006	EaStChem Academic Paper Writing course	St. Andrews
Sep. 2006	EPSRC Advanced Refinement Techniques course	Southampton
Feb. 2007	EaStChem Thesis Writing workshop	Edinburgh

Meetings Attended

Nov. 2004	BCA Autumn Meeting	Aston University	
Apr. 2005	BCA Spring Meeting	Loughborough	*Poster*
May 2005	CCDC Student Day	Cambridge	*Talk*
Aug. 2005	XX IUCr Congress	Florence	*Poster*
Nov. 2005	BCA Autumn Meeting	Daresbury	
Apr. 2006	BCA Spring Meeting	Lancaster	*Poster*
May 2006	CCDC Student Day	Cambridge	*Talk*
Apr. 2007	BCA Spring Meeting	Canterbury	*Poster*
Apr. 2007	Motherwell Symposium	Canterbury	*Talk*
May 2007	CCDC Student Day	Cambridge	*Talk*

Publications

"Mercury CSD 2.0 – New features for the visualization and investigation of crystal structures", C. F. Macrae, I. J. Bruno, J. A. Chisholm, P. R. Edgington, P. McCabe, E. Pidcock, L. Rodriguez-Monge, R. Taylor, J. van de Streek, P. A. Wood, *J. Appl. Cryst.* **41**, 466-470, 2008.

"The anisotropic compression of the crystal structure of 3-aza-bicyclo(3.3.1)nonane-1,2-dione to 7.1 GPa", P. A. Wood, D. A. Haynes, A. R. Lennie, W. D. S. Motherwell, S. Parsons, E. Pidcock, J. E. Warren, *Cryst. Growth Des.* **8**, 549-558, 2008.

"The effect of pressure and substituents on the size of pseudo-macrocyclic cavities in salicylaldoxime ligands", P. A. Wood, R. S. Forgan, A. R. Lennie, S. Parsons, E. Pidcock, P. A. Tasker, J. E. Warren, *CrystEngComm* **10**, 239-251, 2008.

"The use of methylsalicyloxime in manganese chemistry: A [Mn_3^{III}] triangle and its oxidation to a [($Mn_4^{IV}Ce_2^{III}$)] rod", C. J. Milios, P. A. Wood, S. Parsons, D. Foguet-Albiol, C. Lampropoulos, G. Christou, S. P. Perlepes, E. K. Brechin, *Inorg. Chim. Acta.* **360**, 3932-3940, 2007.

"1,4,5,8,9,12-Hexamethyltriphenylene. A molecule with a flipping twist", Y. Wang, A. D. Stretton, M. C. McConnell, P. A. Wood, S. Parsons, J. B. Henry, A. R. Mount, T. H. Galow, *J. Am. Chem. Soc.* **129**, 13193-13200, 2007.

"Supramolecular chemistry in metal recovery; H-bond buttressing to tune extractant strength", R. S. Forgan, P. A. Wood, J. Campbell, D. K. Henderson, F. E. McAllister, S. Parsons, E. Pidcock, R. M. Swart, P. A. Tasker, *Chem. Commun.* 4940-4942, 2007.

"Tagging (arene)ruthenium(II) anticancer complexes with fluorescent labels", F. Zobi, B. Balali Mood, P. A. Wood, F. P. A. Fabbiani, S. Parsons, P. J. Sadler, *Chem. Eur. J.* **18**, 2783-2796, 2007.

"3-Fluorosalicylaldoxime", P. A. Wood, R. S. Forgan, S. Parsons, E. Pidcock, P. A. Tasker, *Acta Cryst.* E**63**, o3132, 2007.

"3-Hydroxysalicylaldoxime", P. A. Wood, R. S. Forgan, S. Parsons, E. Pidcock, P. A. Tasker, *Acta Cryst.* E**63**, o3131, 2007.

"Spin switching via targeted structural distortion", C. J. Milios, A. Vinslava, W. Wernsdorfer, A. Prescimone, P. A. Wood, S. Parsons, S. P. Perlepes, G. Christou, E. K. Brechin, *J. Am. Chem. Soc.* **129**, 6547-6561, 2007.

"Tripodal borate ligands from tris(dimethylamino)borane: the first synthesis of a chiral tris(methimazolyl)borate ligand, and the crystal structure of a single diastereomer pseudo-C3-symmetric Ru(II) complex", P. J. Bailey, C. McCormack, S. Parsons, F. Rudolphi, A. Sanchez-Perucha, P. Wood, *Dalton Trans.* 476-480, 2007.

"A single-molecule magnet with a 'twist'", C. J. Milios, A. Vinslava, P. A. Wood, S. Parsons, W. Wernsdorfer, G. Christou, S. P. Perlepes, E. K. Brechin, *J. Am. Chem. Soc.* **129**, 8-9, 2007.

"The effect of pressure on the crystal structure of salicylaldoxime-I and the structure of salicylaldoxime-II at 5.93 GPa", P. A. Wood, R. S. Forgan, D. Henderson, S. Parsons, E. Pidcock, P. A. Tasker, J. E. Warren, *Acta Cryst.* B**62**, 1099-1111, 2006.

"Tunable dipolar magnetism in high-spin molecular clusters", M. Evangelisti, A. Candini, A. Ghirri, M. Affronte, G.W. Powell, I. A. Gass, P. A. Wood, S. Parsons, E. K. Brechin, D. Collison, S. L. Heath, *Phys. Rev. Lett.* **97**, 167202, 2006.

"Salicylaldoxime-III at 150K", P. A. Wood, R. S. Forgan, S. Parsons, E. Pidcock, P. A. Tasker, *Acta Cryst.* E**62**, o3944-o3946, 2006.

"MOLE: A data management application based on a protein production data model", C. Morris, P. Wood, S. L. Griffiths, K. S. Wilson, A. W. Ashton, *Proteins: Struct., Funct. & Bioinf.* **58**, 285-289, 2005.

"Design of a data model for developing laboratory information management and analysis systems for protein production", A. Pajon, J. Ionides, J. Diprose, J. Fillon, R. Fogh, A. W. Ashton, H. Berman, W. Boucher, M. Cygler, E. Deleury, R. Esnouf, J. Janin, R. Kim, I. Krimm, C. L. Lawson, E. Oeuillet, A. Poupon, S. Raymond, T. Stevens, H. van Tilbeurgh, J. Westbrook, P. Wood, E. Ulrich, W. Vranken, L. Xueli, E. Laue, D. I. Stuart, *Proteins: Struct., Funct. & Bioinf.* **58**, 278-284, 2005.

Contents

Chapter 1

Introduction

1.1 Introduction

The word ‘topology’ derives from the Greek words *topos* and *logos*, literally meaning ‘science of place’. A crystal structure is an infinite three-dimensional lattice of periodically repeating structural units. In reference to a molecular crystal structure, therefore, the term ‘topology’ can be used to describe the study of the spatial relationship between a molecule within the crystal and its neighbouring molecules – i.e. the intermolecular packing pattern.

The experimental technique of x-ray crystallography is still seen by many chemists to be simply an accurate tool for determining the intramolecular structure of a sample. A crystal structure is much more than this; it is the end product of the complex process of crystal nucleation and growth (Davey *et al.*, 2002, Davey, 2003) which produces the most advantageous three-dimensional arrangement of intra- and inter-molecular interactions. The observed structure, and its packing pattern, therefore contains a wealth of information about the delicate balance between the various interactions in the structure.

The solid state is unique in that it exhibits polymorphism – the ability to exist in multiple different forms. This means that a particular molecule may have a large number of different possible ways to pack in a crystal thus forming a range of different intermolecular interactions. It is known that the properties of a compound in the solid state are not determined entirely by the molecular structure and that the intermolecular structure is also important. One example of polymorphism is elemental carbon for which there are a number of structural variants. Most chemists will be familiar with the structures of graphite, diamond and buckminsterfullerene (Figure 1.1), each made up of carbon, but having very different physical properties.

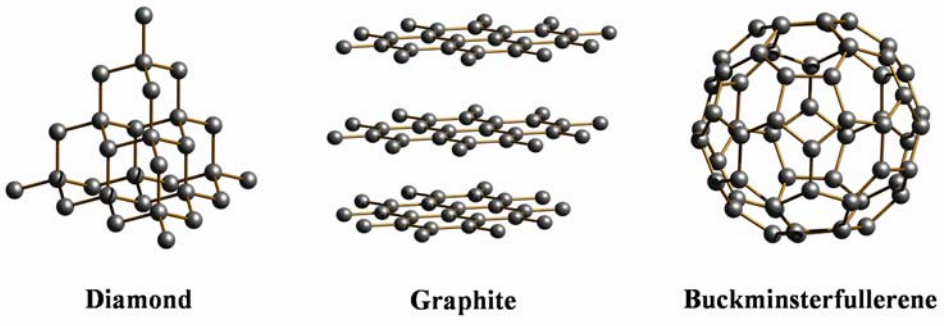

Figure 1.1: Three of the structural variants of carbon in the solid state.

Organic molecular compounds can also display very different properties between polymorphs (Bernstein, 2002). Changes in intermolecular packing can affect a variety of different physical and chemical properties including crystal habit, melting point, solubility, dissolution rate, density, bioavailability, thermal stability. Understandably this phenomenon is of great interest to materials scientists and pharmaceutical companies in particular due to their desire to have some control over the properties of a compound. In the case of a pharmaceutically-relevant compound, not only can a new polymorph give rise to different properties, but it can also be patented separately as seen in the Zantac Patent case (Bernstein, 2002). This desire to control the noncovalent interactions and packing patterns of a compound has given rise to a large area of research called Crystal Engineering.

Crystal Engineering is the design and production of molecular solid-state materials with the desired properties through the use of selected intermolecular interactions. It is known that certain patterns of interactions (or motifs) occur frequently within crystal structures compared to other less common patterns. The existence of common motifs has led to the use of the term 'supramolecular synthon' to describe a particular spatial arrangement of intermolecular interactions. These synthons are used in Crystal Engineering as the connectors between molecules in the rational design of a crystal structure. In the terminology of Crystal Engineering, the building block (or tecton) is the molecule; this building block is then connected to others using supramolecular synthons (for example see Figure 1.2).

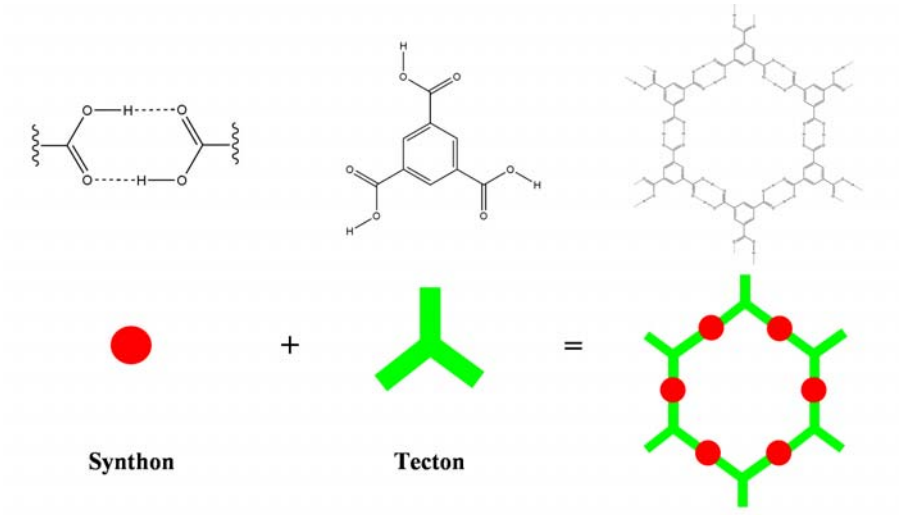

Figure 1.2: Schematic of the use of synthons and tectons in Crystal Engineering.

The majority of synthons used in the field of crystal engineering are based on hydrogen bonding contacts or other atom-atom based noncovalent interactions. The description of hydrogen bonding patterns has been considerably aided by the application of graph-set descriptors to hydrogen bonding (Etter, 1990, Bernstein *et al.*, 1995).

The concept of graph-set analysis is to classify hydrogen bonding patterns based on descriptors which specify the type of pattern along with the number of hydrogen bond donors and acceptors. A graph-set descriptor is therefore written as $\boldsymbol{G}^{\mathbf{a}}_{\mathbf{d}}(\mathbf{n})$, in which ***G*** represents the type of pattern, **a** is the number of hydrogen bond acceptors, **d** the number of donors and **n** the number of atoms in the pattern. The pattern type, ***G***, can be one of four different options; ***C*** for an infinite chain, ***S*** for an intramolecular hydrogen bonding pattern, ***R*** for an intermolecular ring and ***D*** for an interaction between two or more discrete moieties. If the number of donors and acceptors are both one, then these are not written in the symbol. An example of each type of hydrogen bonding pattern is shown in Figure 1.3 along with the graph-set assignments.

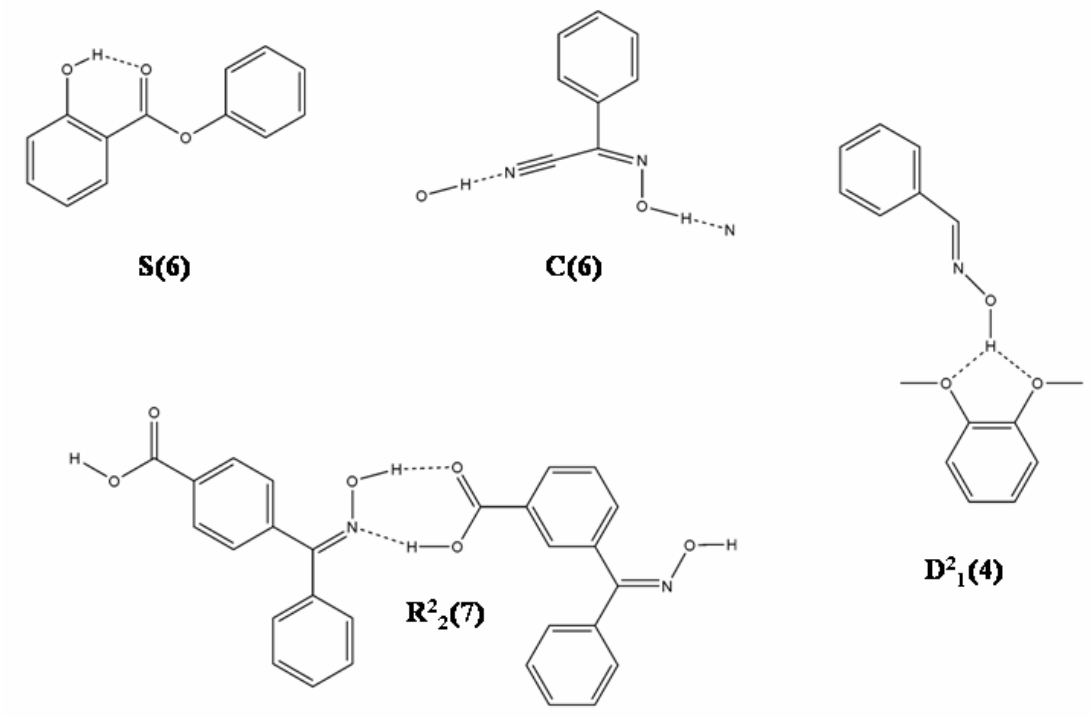

Figure 1.3: The four types of graph-set descriptor for hydrogen bonding patterns.

A great deal of research has also been done on analysing the energies and preferred geometries of hydrogen bonds. A number of substantial reviews have been written about hydrogen bonding and its importance in crystal engineering (Desiraju, 1995, Aackeroy, 1997, Steiner, 2002). Observed crystal structures may not exhibit the expected synthons however, especially if there are multiple potential interaction motifs that are competing. The ideal situation would be to choose a particular molecule and be able to predict accurately the crystal structure of that molecule before performing a crystallisation experiment. This is exactly the problem that is currently being addressed in the field of Crystal Structure Prediction (CSP) by a number of research groups around the world (Day, Motherwell, Ammon *et al.*, 2005).

The programs currently being developed for CSP have improved significantly in the last few years, but there are still a number of significant problems. Not least amongst the issues is the fact that the correct structure is likely to be only of the order of a few $kJmol^{-1}$ more stable than other candidate structures. This means that the calculation of the lattice energies needs to be more accurate than this difference in order to obtain the correct ranking of possible structures. Other obstacles to a correct prediction are that the experimentally observed structure may not necessarily be the thermodynamically most stable structure, there may be other polymorphs of the compound that have not yet been observed; the molecule may also be conformationally flexible.

There have recently been a number of very successful examples of crystal structure prediction (Day, Motherwell & Jones, 2005, Hulme *et al.*, 2005, Oswald, Allan, Day *et al.*, 2005, Nowell *et al.*, 2006). By contrast, the success rate in the international blind tests for CSP which are run by the Cambridge Crystallographic Data Centre (CCDC) (Lommerse *et al.*, 2000, Motherwell *et al.*, 2002, Day, Motherwell, Ammon *et al.*, 2005), has been more limited. The compounds that appear to be particularly problematic in these tests are ones which have significant intramolecular flexibility and those which only form relatively weak hydrogen bonds. It is unsurprising that the intricacies of crystal packing are still not well understood due to the inherent complexity of the problem. An empirical means to

learn more about the nature of intermolecular interactions, however, is to perturb the structure and analyse the changes; this can be achieved by applying pressure to a crystal structure.

1.2 High Pressure Crystallography

1.2.1 Background

Pressure is a useful thermodynamic probe of molecular structure as it forces molecules in the solid state closer to each other. This facilitates the study of intermolecular interactions as the distances are varied, as well as the potential to access new phases of the compound at non-ambient conditions. Recent studies have shown that pressure can be used to form new polymorphs of compounds by recrystallisation at pressure from the melt (Lozano-Casal *et al.*, 2005, Oswald, Allan, Motherwell *et al.*, 2005) and from a solution (Fabbiani *et al.*, 2005, 2006).

Although much of modern high pressure research into organic solids has focussed on producing new polymorphs, the compression of a single phase produces information on the crystal packing forces. Biological organisms have been found to exist at pressures as high as 1000 times atmospheric pressure in deep-sea locations such as at the bottom of the Marianas Trench. These organisms are called piezophiles as they have evolved to survive in high pressure conditions. Studying simple organic molecular structures under pressure will help to develop our understanding of the response of noncovalent bonds to compression and is the first step towards analysis of biologically-relevant structures under pressure.

It is possible that, with enough information from these kinds of studies, the anisotropic compression of a structure could be predicted before performing an experiment. The fundamental understanding of these interactions may also potentially allow predictions of pressure-induced phase transitions in the future, or even the existence of likely high-pressure polymorphs.

1.2.2 Experiments and analysis

The most common tool for the application of hydrostatic pressure to a single crystal is the Merrill-Bassett diamond anvil cell (Merrill & Bassett, 1974). The cell is

made up of a steel body incorporating a pair of Be backing discs. Diamonds are then glued onto the backing discs and a tungsten gasket is placed between the diamonds (see Figure 1.4). A hole is drilled (by spark-erosion) into the tungsten gasket which, when placed between the two diamond anvils, forms a cylindrical sample chamber. Pressure is applied by the tightening of three Allen screws. The cells used in this work had a 40° half-opening angle for admitting x-rays into and out of the sample chamber, as well as allowing visual inspection of the sample through the diamond anvils and holes drilled in the Be backing discs.

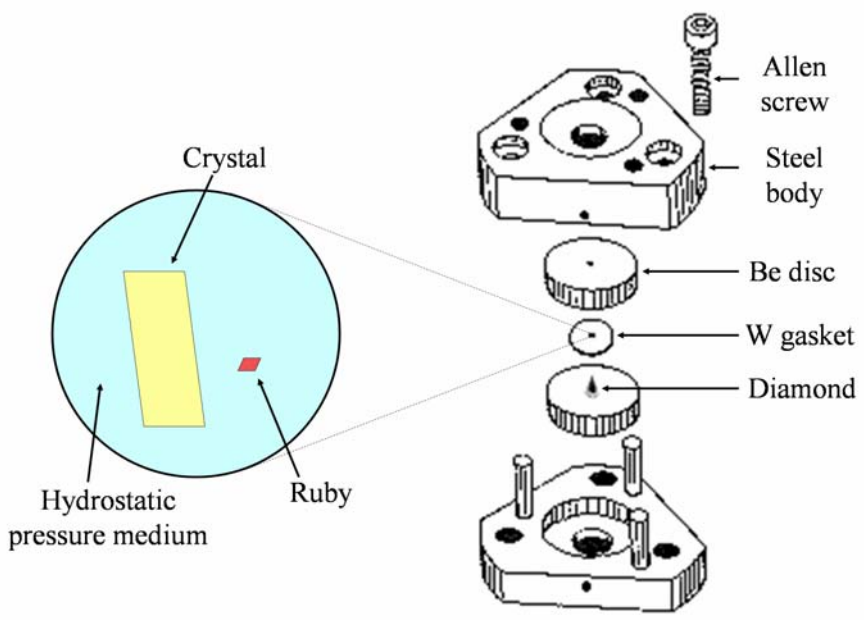

Figure 1.4: Schematic of a Merrill-Bassett diamond anvil cell with contents of the high pressure chamber (High Pressure Diamond Optics, 2003).

In a typical experiment, a single crystal is placed in the sample chamber along with a chip of ruby, for measuring the pressure via the ruby fluorescence method (Piermarini *et al.*, 1975), and a hydrostatic pressure medium that ensures pressure is applied evenly around the crystal. High pressure x-ray diffraction experiments can then be performed using a standard single crystal diffractometer with the high pressure cell attached to a normal goniometer head.

Analysis of high pressure crystal structures, as in the case of ambient pressure structures, has been highly influenced by the study of atom-atom interactions, such as hydrogen bonds and S…S contacts. It has been found in a range of different single

crystal compression studies that intermolecular contacts are not compressed beyond the limits of similar interactions found at ambient conditions in the CSD (Dawson *et al.*, 2005, Moggach, Allan, Parsons *et al.*, 2005, Moggach, Allan, Parsons *et al.*, 2006). Structures that have reached the ambient limits for a particular contact have been seen to undergo phase transitions which relieve these short contacts, e.g. in L-serine and L-cysteine (Moggach, Allan, Morrison *et al.*, 2005, Moggach, Allan, Clark *et al.*, 2006).

The study of molecular structures under compression has also consistently suggested that the size and distribution of voids between molecules found in the crystal structure at ambient conditions is important in determining the effects of pressure. Recent work has shown that the principal effect of compression in a number of cases is reduction of the sizes of these intermolecular voids (Dawson *et al.*, 2005, Moggach, Allan, Parsons *et al.*, 2005). This is exemplified in the pressure study of α-glycine (Dawson *et al.*, 2005) in which structural voids within the hydrogen bonded layers of the *ac* plane decrease visibly between ambient pressure and 6.2 GPa (Figure 1.5).

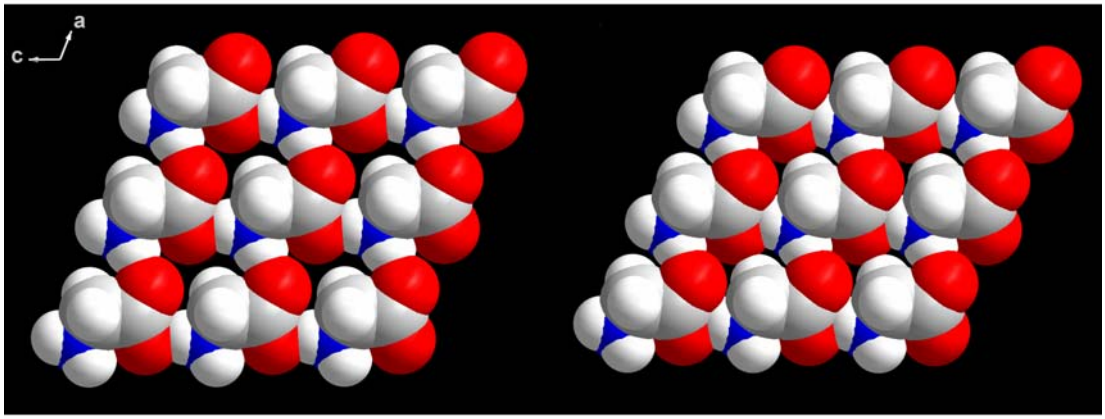

Figure 1.5: Space-filling plots showing the hydrogen bonded layers within the *ac* plane of the α-glycine crystal structure at ambient pressure (left) and 6.2 GPa (right). The intermolecular voids in the layers can clearly be seen to decrease upon the application of pressure.

The number of high pressure studies being performed is still increasing and this provides the opportunity to explore new ways of analysing the structural compression. Some of the questions still to ask include: how necessary is it to take into account the other molecular contacts within the crystal structures even when a

hydrogen bond is present? Are the less directional interactions, such as π…π, CH…π, CH…O and van der Waals contacts significant in terms of structure compression and phase transitions? One way of approaching these questions is to develop a set of analysis techniques more focussed on whole molecule contacts rather than specific atom-atom interactions.

1.3 Structural Analysis Techniques

1.3.1 The PIXEL method

Three methods for analysing crystal structures in particular have been developed which embrace the idea of whole molecule interactions rather than atom-atom contacts. The first of these techniques is based on calculation of intermolecular interaction energies and is called the semi-classical density sums (PIXEL) method (Gavezzotti, 2005). This approach, developed by Gavezzotti, allows the computation of both full lattice and specific dimer energies along with a breakdown of the energies into four components; coulombic, polarisation, dispersion and repulsion (Dunitz & Gavezzotti, 2005).

The PIXEL method starts with taking the geometry of the molecule from the observed crystal structure and extending the X-H distances to standard neutron lengths. Without optimising the geometry, an electron density map for the molecule is then calculated using a standard quantum chemical package such as *GAUSSIAN98* (Frisch *et al.*, 1998). This calculation is done as standard at the MP2/6-31G** level of theory and produces a density map on a three-dimensional grid of step size 0.08 Å. The molecular electron density is then modified in three stages to speed up the subsequent calculations. Firstly the pixels are condensed into super-pixels made from a cube of the original pixels of size n x n x n, where n is the condensation level. This condensation level, as a standard, is set to 4 for a lattice energy calculation and 3 for a dimer calculation. Next the pixels are screened by charge, such that any pixels with a charge below a specified threshold, q_{min} which is set as default to 10^{-6} electrons, are removed. This reduces the number of pixels and the computational cost of the calculation considerably without significantly affecting the electron density. Finally,

the remaining pixels are renormalized such that the sum of the pixel charges is equal to the sum of the nuclear charges in order to achieve electrical neutrality.

The next stage in the calculation is to generate the required cluster of molecules; in the case of a lattice calculation, this relates to a sphere of molecules produced *via* crystal symmetry operations and in the case of a dimer calculation, this refers to the reference molecule plus one other molecule. For the lattice calculation, the radius of the cluster is called the crystal cut-off radius and is set to 18 Å as standard for uncharged molecules. Once the required cluster has been generated, it is possible to begin the intermolecular energy calculation.

Coulombic energies between the molecules in the cluster are calculated as sums of pixel-pixel, pixel-nucleus and nucleus-nucleus terms. Each pixel has its own partial charge, as does each atomic nucleus, so these terms can be calculated with no parameterisation. The formula used for each calculation is the standard electrostatic potential energy equation for two charges (q_1 and q_2) separated by a distance, r:

$$E_{COUL} = \frac{q_1 q_2}{4\pi\varepsilon^o r}$$

Polarisabilities are then allocated to each pixel and this is done on the basis of assigning each pixel to the nearest atom (with number of valence electrons, Z_{atom}) within the molecule, thus the pixel polarisability, α_i, is given by:

$$\alpha_i = \left(q_i / Z_{atom}\right)\alpha_{atom}$$

In order to calculate the intermolecular polarisation energy, the electric field produced at each pixel, ε_i, as a result of the surrounding molecules is determined. The total polarisation energy for the molecule, E_{POL}, is thus calculated as the summation of all of the pixel contributions, $E_{POL,i}$, which are calculated using the following damped formula, where the damping parameter (ε_{max}) is an adjustable empirical parameter:

$$E_{POL,i} = -\tfrac{1}{2}\alpha_i[\varepsilon_i d_i]^2$$

$$d_i = \exp[-(\varepsilon_i/(\varepsilon_{\max} - \varepsilon_i)]$$

$$E_{POL,i} = 0 \;\; for \; \varepsilon > \varepsilon_{\max}$$

The dispersion energies (E_{DISP}) are determined using a London-type formula as sums of pixel-pixel dispersion components, E_{ij}. In order to avoid singularities arising due to very short pixel-pixel distances, the terms are damped *via* the use of a standard quantum mechanical damping term, $f(R)$. The molecular ionization energy (E_{ION}) used is the highest occupied molecular orbital energy from the *GAUSSIAN* calculation. The damping threshold distance parameter, D, is another adjustable empirical parameter in this calculation.

$$E_{DISP,AB} = E_{ION}\left(-\tfrac{3}{4}\right)\sum_i\sum_j f(R)\alpha_i\alpha_j /[(4\pi\varepsilon^o)^2(R_{ij})^6]$$

$$f(r) = \exp[-(D/R_{ij}-1)^2] \ \textit{for}\ R_{ij} < D$$

$$f(r) = 1 \ \textit{for}\ R_{ij} > D$$

The repulsion energy (E_{REP}) between molecules A and B is approximated using the overlap of the electron densities of two molecules, S_{AB}, as shown below

$$E_{REP,AB} = K(S_{AB})^{\gamma}$$

$$S_{AB} = \sum_i\sum_j[\rho_i(A)\rho_j(B)]V$$

where the variables K and γ are also adjustable empirical parameters. This overlap integral is calculated by numerical integration. The repulsion is thus non-zero only for the areas of space where the two molecular electron densities overlap.

The total intermolecular energy is therefore given by:

$$E_{TOT} = E_{COUL} + E_{POL} + E_{DISP} + E_{REP}$$

This breakdown into physically meaningful component terms is invaluable when attempting to understand the changes in intermolecular interaction energies. The speed of the calculations also means that the lattice and dimer calculations for a full compression study are not prohibitive on a standard desktop computer.

Drawbacks to the PIXEL method include the fact that it uses a rigid gas-phase molecular electron density and its use of four empirical parameters. The empirical parameters used in the calculations have, however, been optimised to reproduce experimental sublimation enthalpies for a range of organic molecular crystal structures. This fitting has been tested by comparing the calculated lattice

energies with experimental enthalpies for organic structures which were not used for this fitting process. The PIXEL lattice energy of the most stable anhydrous caffeine polymorph, for example, has been calculated as -105.1 kJ mol^{-1} (Carlucci & Gavezzotti, 2005) compared with the experimental heat of sublimation of 110-115 kJ mol^{-1} (Griesser *et al.*, 1999). Tests have also shown that PIXEL results compare well with the results of intermolecular perturbation theory calculations (Gavezzotti, 2003).

1.3.2 Voronoi-Dirichlet Analysis

The use of a technique called Voronoi-Dirichlet analysis has also been applied to the study of crystal structure space (Blatov *et al.*, 1995). This method is based on the partitioning of space into polygons or polyhedra and can be exemplified using a two-dimensional set of points. Figure 1.5 shows a random distribution of points in two dimensions (left) with one point highlighted, point P. In order to determine the Voronoi-Dirichlet polygon for point P, a line is drawn from P to every other point in the pattern. The perpendicular bisectors of these lines are then drawn and the edges of the polygon are defined by the closest approach of these bisectors to P, thus bounding the space closest to P than any other point. This analysis is then applied to all the remaining points to build up the partitioning map of polygons (Figure 1.5, right).

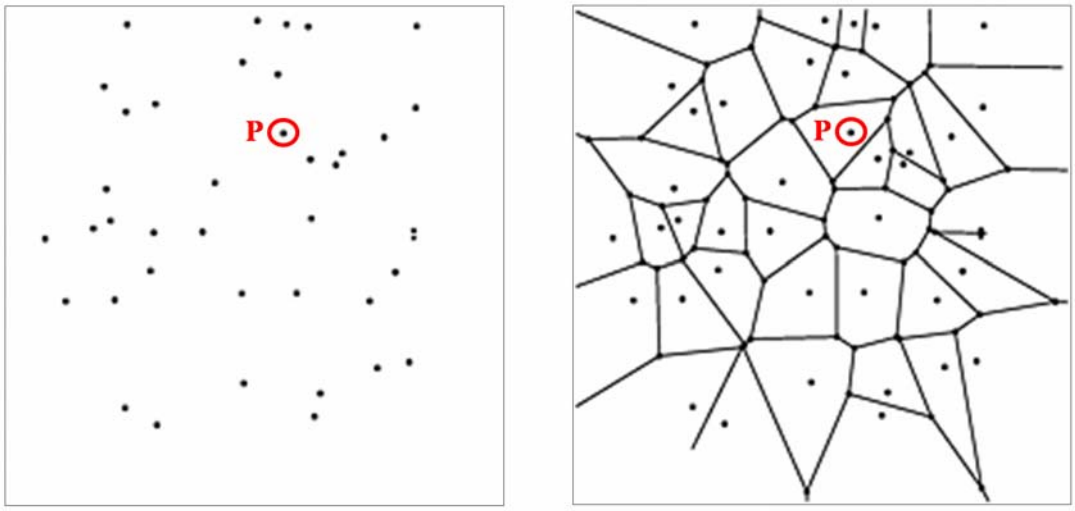

Figure 1.5: Example of Voronoi-Dirichlet analysis for a two-dimensional pattern of points. The set of points is shown before analysis (left) along with the result of partitioning the space into Voronoi-Dirichlet polygons (right).

It is possible to analyse a molecular crystal structure in a similar way by using the centroids of the molecules as the points and partitioning the space into polyhedra. In this case vectors between molecular centroids are drawn, the perpendicular bisectors are planes and the polyhedron is built from the planes closest to the molecular centroid. The faces of the polyhedra are representative of the intermolecular packing pattern (Peresypkina & Blatov, 2000). This construction is therefore called the molecular Voronoi-Dirichlet polyhedron (VDP). An example of a molecular VDP is shown in Figure 1.6 (far left) for the crystal structure of L-alanine.

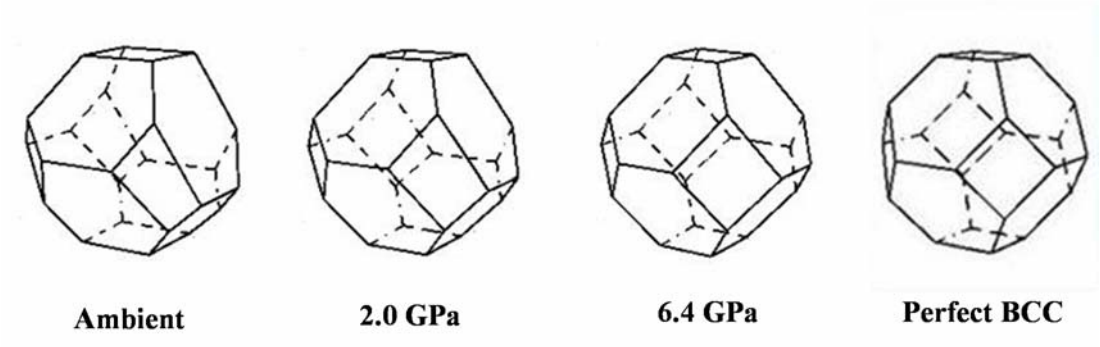

Figure 1.6: Molecular VDP for L-alanine at ambient pressure (far left), 2.0 GPa (centre left) and 6.4 GPa (centre right) along with the VDP for a perfect BCC structure as observed in tungsten (far right). Figures drawn using *TOPOS-Pro* (Blatov *et al.*, 2000).

Figure 1.6 also shows the molecular VDPs of the structure of L-alanine at 2.0 GPa and 6.4 GPa from a single crystal compression study (Dawson, 2003) and the VDP for a perfect body-centred cubic (BCC) lattice as seen, for example, in the crystal structure of tungsten. It is plain to see that the topology of the molecular packing in the L-alanine structure becomes more symmetric as pressure increases and at 6.4 GPa the VDP looks remarkably similar to that of the perfect BCC VDP.

The VDP analysis of crystal structures can also be used to investigate the sizes and locations of intermolecular voids (Blatov & Shevchenko, 2003). Void identification is based on searching for void centres, where the vertices of the VDPs meet, and analysing these void centres with reference to the atoms surrounding the voids. The voids can run into each other, so it is useful to apply a clustering algorithm to reduce the quantity of voids to a reasonable number.

The ability to identify and measure voids is particularly useful in compression studies as a means to rationalise the anisotropic effects of pressure on crystal structures. A high pressure study on L-cystine showed the correlation between the positions of the intermolecular voids determined using VDP analysis and the directions of compression of the structure (Moggach, Allan, Parsons *et al.*, 2005).

1.3.3 The Hirshfeld surface technique

Another recently developed method for studying crystal structures involves calculation of molecular surfaces based on Hirshfeld's stockholder partitioning (Hirshfeld, 1977). The Hirshfeld surface (Spackman & Byrom, 1997) encloses the volume in which the electron density contribution from a sum of spherical atoms for the molecule (the promolecule) dominates the corresponding sum for the whole crystal (the procrystal). Numerically the partitioning is described using a weight function, $w(r)$, which is calculated as follows:

$$w(r) = \sum_{A \in molecule} \rho_A(r) / \sum_{A \in crystal} \rho_A(r)$$

$$= \rho_{promolecule}(r) / \rho_{procrystal}(r)$$

The volume inside the Hirshfeld surface satisfies the condition that the weight function ≥ 0.5 and the surface itself is defined by $w(r) = 0.5$. This choice of definition for the surface means that the molecular surfaces will at most touch but never overlap and in general they tend to fill at least 95 % of the volume for organic molecular crystal structures (McKinnon *et al.*, 2004). The surfaces therefore pack very tightly, only leaving small gaps between molecular surfaces where no molecule dominates the electron density. For calculation of the surface, a cluster of molecules with a radius of *ca* 10 Å is used to approximate the sum over the crystal and hydrogen atom positions are set to standard neutron X-H bond lengths.

The Hirshfeld surface itself (for a structure with $Z' \leq 1$) contains information about all the intermolecular packing contacts in the crystal structure at once. This information is not readily displayed in the form of a monochromatic, three-dimensional object, so it is useful to encode properties onto the surface with a colour scale in order to allow visualisation of important features. One of the structural

properties that can be mapped onto the Hirshfeld surface is the distance from the surface to the nearest external atom, d_e. This property, when displayed using a colour scale, shows close contacts and distinct interaction patterns very effectively. Figure 1.7 shows an example of a Hirshfeld surface for 3-hydroxybenzaldehyde (CSD refcode XAYCIJ) for which four different properties have been mapped onto the surface. The d_e surface, displayed here using a scale running from blue (2.3 Å) through green to red (0.7 Å), shows an intense red circle, which indicates a hydrogen-bonding interaction to the carboxyl acceptor group (O…O = 2.72 Å). Also visible on the d_e surface for this structure is a wheel-like pattern in the upper left corner of the surface with six pale blue spokes, this is indicative of a π-π stacking contact (stacking distance in XAYCIJ = 3.50 Å). The position of the centre of the six-fold wheel pattern away from the centre of the phenyl ring shows in this case that the stacking contact is offset.

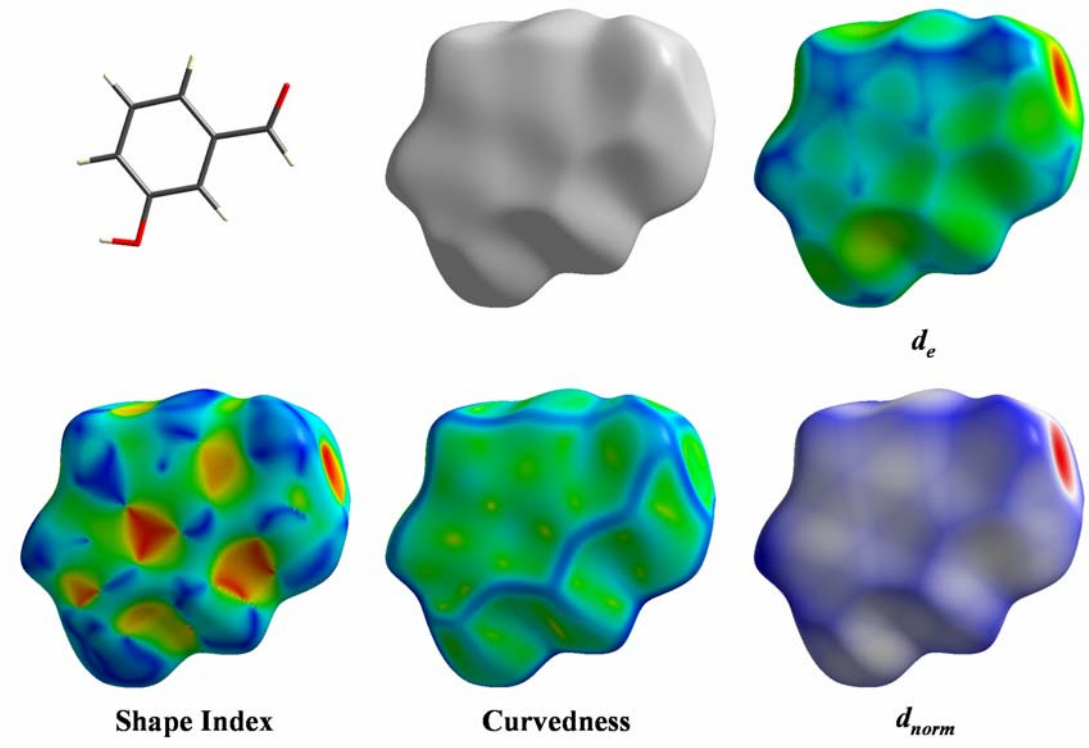

Figure 1.7: The molecular structure of 3-hydroxybenzaldehyde (top left) along with its Hirshfeld surface, plain (top centre) and with four different properties mapped onto it. The properties shown are as follows; the distance to the nearest external atom (d_e, top right), the shape index (bottom left), the curvedness (bottom centre) and the normalised distance to the nearest external atom (d_{norm}, bottom right). The molecule and all of the surfaces are shown at the same scale and in the same orientation.

The shape index (*S*) is another property which can be displayed on the surface and is determined using the principal curvatures of the surface. This property describes the shape of the surface in a dimensionless fashion whereby concave regions are negative (displayed in red) and convex regions are positive (blue). Using this measure, bumps and hollows which fit into one another appear similar in shape but with opposite signs. An example of this effect in Figure 1.7 is the two triangles on the shape index surface that are blue and red – these shapes fit into each other and are another characteristic sign of π-π stacking.

The curvedness (*C*) of the Hirshfeld surface can also be calculated at all points and this property visualises how quickly the shape of the surface is changing. Figure 1.7 (bottom centre) shows the curvedness encoded on the Hirshfeld surface of 3-hydroxybenzaldehyde. From the Figure it can be seen that the curvedness property is mostly green across the faces of the surface with very distinct blue delineations where one face joins to another face. This property effectively shows the contact faces between surfaces and imparts some information about the coordination of the molecule in the crystal structure.

The d_{norm} property is a recently developed addition to the functions that can be displayed on the Hirshfeld surface (McKinnon *et al.*, 2007). This variable is a normalised measure of the distance between atoms which uses the van der Waals radii (r^{vdW}) of the nearest atom inside the surface and the nearest atom outside. Although the d_e property is very useful for visualising packing motifs, it has the drawback that it does not take into account the size of atoms. This means that close contacts between smaller atoms, e.g. H, C, N and O are highlighted better using the d_e function than those between larger atoms, e.g. P, S, Cl. The d_{norm} property avoids this problem by plotting a measure of whether the contact between atoms is greater, the same, or less than the sum of the van der Waals radii. This is calculated also using the distance to the nearest internal atom, d_i, in the function:

$$d_{norm} = \frac{d_i - r_i^{vdW}}{r_i^{vdW}} + \frac{d_e - r_e^{vdW}}{r_e^{vdW}}$$

The values are then encoded onto the Hirshfeld surface using a colour scale from blue (contacts longer than vdW separation), through white (around the vdW separation) to red (shorter than vdW separation). In this way the close contacts are displayed vividly as red patches independent of atom type, for example the hydrogen bonding interaction shows up very clearly in Figure 1.7 (bottom right). Another example of this is illustrated for the crystal structure of 4-chlorophenolpyruvic acid (CSD refcode PENPOO) in Figure 1.8. In the d_e surface we can see the OH…O hydrogen bond acceptor region as a bright red region (labelled 1, O…O = 2.76 Å), a π-π stacking contact (2, stacking distance = 3.45 Å) and a light yellow region corresponding to a close CH…HC contact (3, H…H = 2.36 Å). The d_{norm} surface, however, also very clearly shows the hydrogen bond donor region (4) along with a short Cl…Cl contact (5, Cl…Cl = 3.20 Å) which is not highlighted in the d_e surface due to the relative size of the Cl atoms compared to the other, lighter atoms.

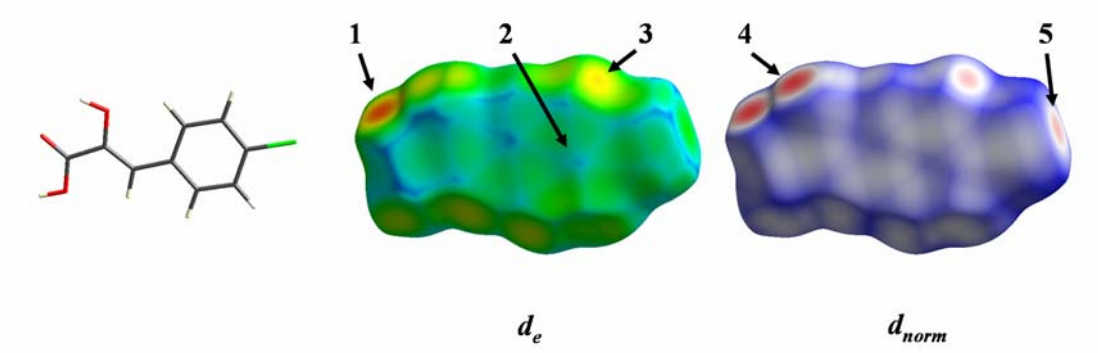

Figure 1.8: The molecular structure of 4-chlorophenolpyruvic acid (left) along with its Hirshfeld surface displayed using the d_e property (centre) and with d_{norm} (right). The molecule and both surfaces are shown at the same scale and in the same orientation. The numbered labels are referred to in the text.

One problematic aspect of the three-dimensional nature of the Hirshfeld surface is that it is quite difficult to compare surfaces between two different crystal structures. Another tool has been developed to allow easy comparison of structures by condensing the distance information calculated into a two-dimensional plot of d_e against d_i. This plot is a histogram of intermolecular contact distances and provides a 'fingerprint' of the crystal packing pattern. These fingerprint plots are formulated using bins of width 0.1 Å and a colour scale is used to show the frequency of contacts in a given bin such that blue bins relate to a small fraction of the overall

contacts, green is a greater fraction and red relates to a large number of contacts. The fingerprint plots themselves have also been shown to have the potential for facilitating simple quantitative comparison of packing patterns (Parkin *et al.*, 2007).

Figure 1.9 shows fingerprint plots for three organic molecular crystal structures; 1,4-butanediol (CSD refcode QATTIO), hexane (HEXANE01) and pyrene (PYRENE02). A range of intermolecular interaction motifs occur in these structures and the fingerprint plots reflect these differences. Distinctive features appear in the plots for standard packing contacts – hydrogen bonds, for example, are seen as two sharp symmetrical 'prongs' at short d_e/d_i (labelled 1 in Figure 1.9). The molecular structure of hexane only contains contacts between hydrogen atoms which are characterised by a 'nose' feature on the d_e/d_i diagonal line (2), a similar feature is also seen in the plot for 1,4-butanediol. In the structure of pyrene, along with contacts between hydrogens, there are π-π stacking contacts which appear as a distinct triangle at around $d_e = d_i = 1.8$ Å (3) and CH…π interactions that appear as two symmetrical 'wings' in the plot (4).

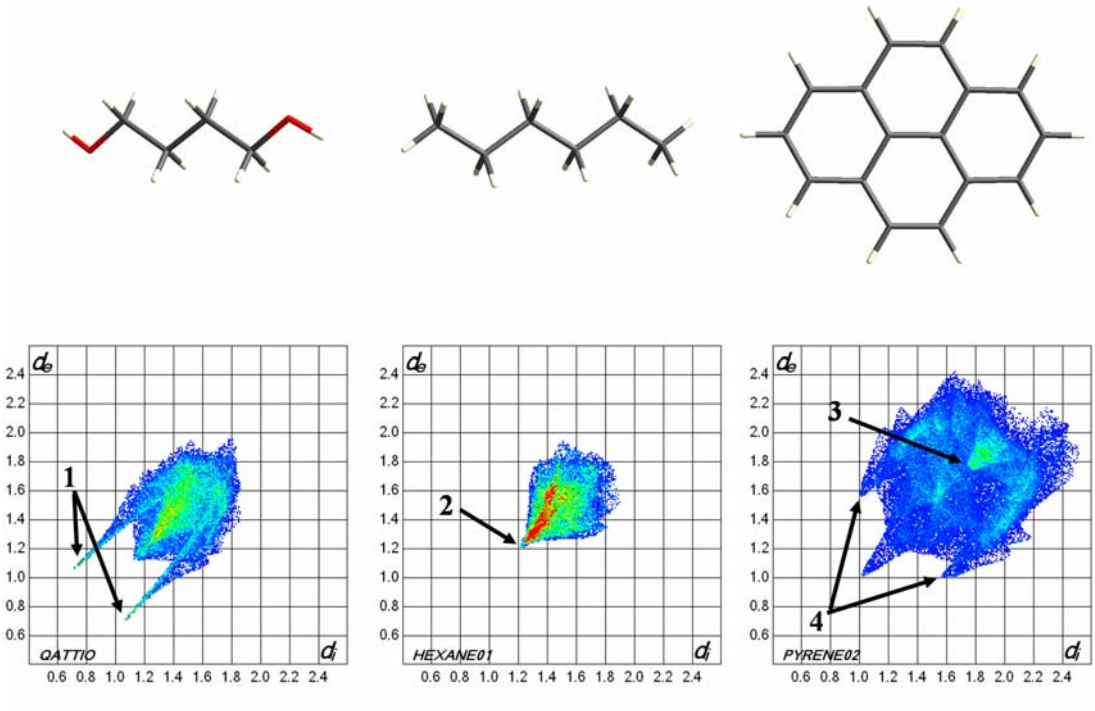

Figure 1.9: The molecular structures and fingerprint plots for 1,4-butanediol (left), hexane (centre) and pyrene (right). The numbered labels are referred to in the text.

These three methods thus represent significantly different approaches, but each encourages the study of packing patterns with an emphasis on the global picture rather than being based on specific atom-atom interactions. As the amount of research performed on organic molecular systems at high pressure is still quite small, it remains to be seen how best to analyse the compression of packing patterns. The causes of compression-induced phase transitions in particular is of fundamental interest and to understand this it is necessary to first understand how pressure affects the balance of intermolecular interactions in a crystal. The further investigation of packing forces under compression is therefore of primary importance and this forms the subject of this thesis.

1.4 References

Aackeroy, C. B. (1997). *Acta Crystallographica, Section B* **53**, 569-586.

Bernstein, J. (2002). Polymorphism in Molecular Crystals. Oxford, UK: Clarendon Press.

Bernstein, J., Davis, R. E., Shimoni, L. & Chang, N.-L. (1995). *Angewandte Chemie, International Edition* **34**, 1555-1573.

Blatov, V. A. & Shevchenko, A. P. (2003). *Acta Crystallographica, Section A* **59**, 34-44.

Blatov, V. A., Shevchenko, A. P. & Serezhkin, V. N. (1995). *Acta Crystallographica, Section A* **51**, 909-915.

Blatov, V. A., Shevchenko, A. P. & Serezhkin, V. N. (2000). *Journal of Applied Crystallography* **33**, 1193.

Carlucci, L. & Gavezzotti, A. (2005). *Chemistry - A European Journal* **11**, 271-279.

Davey, R. J. (2003). *Chemical Communications* 1463-1467.

Davey, R. J., Allen, K., Blagden, N., Cross, W. I., Lieberman, H. F., Quayle, M. J., Righini, S., Seton, L. & Tiddy, G. J. T. (2002). *CrystEngComm* **4**, 257-264.

Dawson, A. (2003). PhD thesis, University of Edinburgh, Edinburgh, UK.

Dawson, A., Allan, D. R., Belmonte, S. A., Clark, S. J., David, W. I. F., McGregor, P. A., Parsons, S., Pulham, C. R. & Sawyer, L. (2005). *Crystal Growth & Design* **5**, 1415-1427.

Day, G. M., Motherwell, W. D. S., Ammon, H. L., Boerrigter, S. X. M., Della Valle, R. G., Venuti, E., Dzyabchenko, A., Dunitz, J. D., Schweizer, B., Van Eijck, B. P., Erk, P., Facelli, J. C., Bazterra, V. E., Ferraro, M. B., Hofmann, D. W. M., Leusen, F. J. J., Liang, C., Pantelides, C. C., Karamertzanis, P. G., Price, S. L., Lewis, T. C., Nowell, H., Torrisi, A., Scheraga, H. A., Arnautova, Y. A., Schmidt, M. U. & Verwer, P. (2005). *Acta Crystallographica, Section B* **61**, 511-527.

Day, G. M., Motherwell, W. D. S. & Jones, W. (2005). *Crystal Growth & Design* **5**, 1023-1033.

Desiraju, G. R. (1995). *Angewandte Chemie, International Edition* **34**, 2311-2327.

Dunitz, J. D. & Gavezzotti, A. (2005). *Angewandte Chemie, International Edition* **44**, 1766-1787.

Etter, M. C. (1990). *Accounts of Chemical Research* **23**, 120-126.

Fabbiani, F. P. A., Allan, D. R., Parsons, S. & Pulham, C. R. (2005). *CrystEngComm* **7**, 179-186.

Fabbiani, F. P. A., Allan, D. R., Parsons, S. & Pulham, C. R. (2006). *Acta Crystallographica, Section B* **62**, 826-842

Frisch, M. J., Trucks, G. W., Schlegel, H. B., Scuseria, G. E., Robb, M. A., Cheeseman, J. R., Zakrzewski, V. G., Montgomery, J. A. J., Stratmann, R. E., Burant, J. C., Dapprich, S., Millam, J. M., Daniels, A. D., Kudin, K. N., Strain, M. C., Farkas, O., Tomasi, J., Barone, V., Cossi, M., Cammi, R., Mennucci, B., Pomelli, C., Adamo, C., Clifford, S., Ochterski, J., Petersson, G. A., Ayala, P. Y., Cui, Q., Morokuma, K., Malick, D. K., Rabuck, A. D., Raghavachari, K., Foresman, J. B., Cioslowski, J., Ortiz, J. V., Stefanov, B. B., Liu, G., Liashenko, A., Piskorz, P., Komaromi, I., Gomperts, R., Martin, R. L., Fox, D. J., Keith, T., Al-Laham, M. A., Peng, C. Y., Nanayakkara, A., Gonzalez, C., Challacombe, M., Gill, P. M. W., Johnson, B. G., Chen, W., Wong, M. W., Andres, J. L., Head-Gordon, M., Replogle, E. S. & Pople, J. A. (1998). *Gaussian 98 revision A.7*, Gaussian, Inc., Pittsburgh, PA, USA.

Gavezzotti, A. (2003). *CrystEngComm* **5**, 429-438.

Gavezzotti, A. (2005). *Zeitschrift fuer Kristallographie* **220**, 499-510.

Griesser, U. J., Szelagiewicz, M., Hofmeier, U. C., Pitt, C. & Cianferani, S. (1999). *Journal of Thermal Analysis and Calorimetry* **57**, 45-60.

High Pressure Diamond Optics (2003). *High Pressure Diamond Optics, Inc.*, http://www.hpdo.com.

Hirshfeld, F. L. (1977). *Theoretica Chimica Acta* **44**, 129-138.

Hulme, A. T., Price, S. L. & Tocher, D. A. (2005). *Journal of the American Chemical Society* **127**, 1116-1117.

Lommerse, J. P. M., Motherwell, W. D. S., Ammon, H. L., D, D. J., Gavezzotti, A., Hofmann, D. W. M., Leusen, F. J. J., Mooji, W. T. M., Price, S. L., Schweizer, B., Schmidt, M. U., Van Eijck, B. P., Verwer, P. & Williams, D. E. (2000). *Acta Crystallographica, Section B* **56**, 697-714.

Lozano-Casal, P., Allan, D. R. & Parsons, S. (2005). *Acta Crystallographica, Section B* **61**, 717-723.

McKinnon, J. J., Jayatilaka, D. & Spackman, M. A. (2007). *Chemical Communications* 3814-3816.

McKinnon, J. J., Spackman, M. A. & Mitchell, A. S. (2004). *Acta Crystallographica, Section B* **60**, 627-668.

Merrill, L. & Bassett, W. A. (1974). *Review of Scientific Instruments* **45**, 290-294.

Moggach, S. A., Allan, D. R., Clark, S. J., Gutmann, M. J., Parsons, S., Pulham, C. R. & Sawyer, L. (2006). *Acta Crystallographica, Section B* **62**, 296-309.

Moggach, S. A., Allan, D. R., Morrison, C. A., Parsons, S. & Sawyer, L. (2005). *Acta Crystallographica, Section B* **61**, 58-68.

Moggach, S. A., Allan, D. R., Parsons, S. & Sawyer, L. (2006). *Acta Crystallographica, Section B* **62**, 310-320.

Moggach, S. A., Allan, D. R., Parsons, S., Sawyer, L. & Warren, J. E. (2005). *Journal of Synchrotron Radiation* **12**, 598-607.

Motherwell, W. D. S., Ammon, H. L., Dunitz, J. D., Dzyabchenko, A., Erk, P., Gavezzotti, A., Hofmann, D. W. M., Leusen, F. J. J., Lommerse, J. P. M., Mooji, W. T. M., Price, S. L., Scheraga, H., Schweizer, B., Schmidt, M. U., Van Eijck, B. P., Verwer, P. & Williams, D. E. (2002). *Acta Crystallographica, Section B* **58**, 647-661.

Nowell, H., Frampton, C. S., Waite, J. & Price, S. L. (2006). *Acta Crystallographica, Section B* **62**, 642-650.

Oswald, I. D. H., Allan, D. R., Day, G. M., Motherwell, W. D. S. & Parsons, S. (2005). *Crystal Growth & Design* **5**, 1055-1071.

Oswald, I. D. H., Allan, D. R., Motherwell, W. D. S. & Parsons, S. (2005). *Acta Crystallographica, Section B* **61**, 69-79.

Parkin, A., Barr, G., Dong, W., Gilmore, C. J., Jayatilaka, D., McKinnon, J. J., Spackman, M. A. & Wilson, C. C. (2007). *CrystEngComm* **9**, 648-652.

Peresypkina, E. V. & Blatov, V. A. (2000). *Acta Crystallographica, Section B* **56**, 1035-1045.

Piermarini, G. J., Block, S., Barnett, J. D. & Forman, R. A. (1975). *Journal of Applied Physics* **46**, 2774-2780.

Spackman, M. A. & Byrom, P. G. (1997). *Chemical Physics Letters* **267**, 215-220.

Steiner, T. (2002). *Angewandte Chemie, International Edition* **41**, 48-76.

Chapter 2

The Effect of Pressure on the Crystal Structure of Salicylaldoxime-I and the Structure of Salicylaldoxime-II at 5.93 GPa*

* Wood, P. A., Forgan, R. S., Henderson, D., Parsons, S., Pidcock, E., Tasker, P. A., Warren, J. E. (2006). *Acta Crystallographica, Section B***62**, 1099-1111.

2.1 Synopsis

The crystal structure of salicylaldoxime has been determined at room temperature at pressures from 0.75 to 5.28 GPa. Salicylaldoxime forms a pseudo-macrocycle which contains a cavity which decreases in size with pressure. Above 5.28 GPa the structure transforms to a new polymorph, the structure of which has been determined at 5.93 GPa. The changes in intermolecular interactions during the phase transition are interpreted with the aid of PIXEL calculations.

2.2 Introduction

The use of high pressure as a probe for studying molecular crystal structures under non-ambient conditions is still relatively lightly explored compared with low-temperature studies. Recent studies of small organic molecules (Dawson *et al.*, 2005, Moggach, Allan, Morrison *et al.*, 2005, Moggach *et al.*, 2006) have found that the primary effect of the compression in these cases is to reduce the sizes of voids present in the ambient-pressure structure. Analysis of the distributions and sizes of voids in crystal structures at ambient and high pressures is therefore an important area of research in terms of understanding the effects of compression. The subject of the effect of pressure on molecular systems has been addressed in a number of recent reviews (Boldyreva, 2003, 2004a, b, Katrusiak, 2004, Hemley & Dera, 2000).

The presence of voids in a structure may also be of importance in the determination of chemical reactivity. Most of the voids in the crystal structure of a small organic compound will be between molecules, but some compounds also have intramolecular voids (usually referred to as *cavities*). One example of this is 18-crown-6, which has a large cavity inside the ring of the molecule and is known to form complexes with metal ions such as Na^+, K^+ and Rb^+. The type of complexation in these complexes is dependent on the size of the metal ion in relation to the crown ether cavity size. In the case of 18-crown-6 the macrocyclic cavity is best suited to the K^+ cation, but it can also form complexes with smaller or larger cations by distorting the conformation of the molecule or by complexing the cation with two crown ether molecules in a ‘sandwich’ arrangement (Gokel, 1991).

Salicylaldoxime (Scheme 2.1) forms a hydrogen-bonded dimer creating a pseudo-macrocyclic cavity in the middle of the hydrogen-bonded *R*-type ring motif (Scheme 2.2a) (Bernstein *et al.*, 1995). Deprotonation of the phenol group enables salicylaldoxime to bind to a transition metal as a mono-anionic, bidentate ligand. A bis(salicylaldoxime) complex is stabilised by hydrogen bonding between the two bidentate ligands.

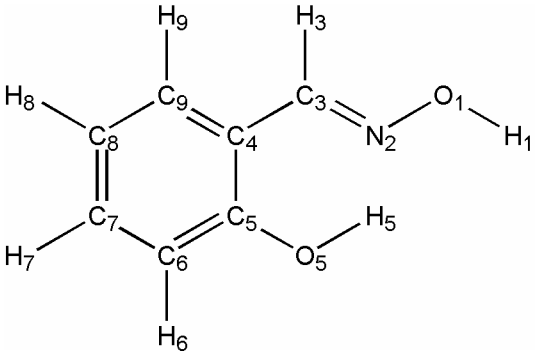

Scheme 2.1: Chemical structure diagram showing atomic numbering scheme.

Salicylaldoxime is known to show a remarkable selectivity for complex formation of copper(II) above other metal ions as a result of the compatibility of the size of the cavity at the centre of the *R* motif and the ionic radius of Cu^{2+} (Smith *et al.*, 2002). Salicylaldoximes bearing branched alkyl chains are used as solvent extractants to effect the 'separation' and 'concentration' operations in the hydrometallurgical recovery of copper, accounting for around 30% of annual production (Kordosky, 2002). The high affinity and selectivity of salicylaldoximes for Cu^{2+} is therefore of great commercial importance (Szymanowski, 1993).

The development of ligands suitable for the selective complexation of metal ions based on synthesizing derivatives to control cavity sizes in polydentate ligands is both time-consuming and costly (Tasker *et al.*, 2004). As salicylaldoximes are predisposed to assemble to provide $N_2O_2^{2-}$ cavities for metal ions, an attractive alternative strategy would be to control the size of the cavity using pressure, and in this chapter we discuss the effect of pressure to 6 GPa on the crystal structure of salicylaldoxime.

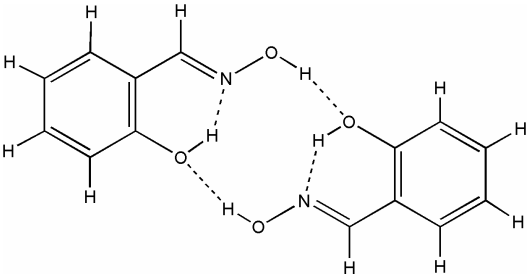

Scheme 2.2a: Chemical structure diagram showing the hydrogen-bonded dimer in the ambient phase structure.

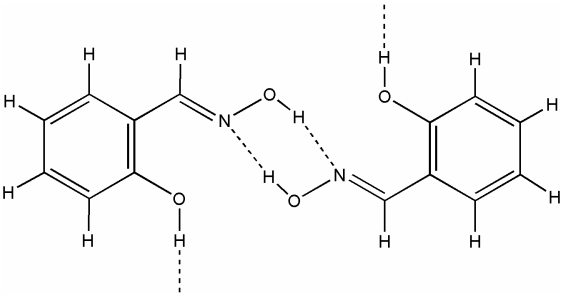

Scheme 2.2b: Chemical structure diagram showing the hydrogen-bonded dimer in the phase II structure.

2.3 Experimental

Note: The crystal growth was performed by Ross Forgan of the University of Edinburgh. The details are included here for the sake of completeness.

2.3.1 Crystal growth

Salicylaldoxime (98%) was purchased from Acros (CAS number 94-67-7); it was then recrystallised by the slow evaporation of a concentrated hexane/chloroform solution. One small, colourless, block-shaped crystal was then taken directly from the recrystallised sample. The unit cell dimensions of the crystal were determined at 150 K and ambient pressure to be monoclinic, a = 10.359 (3), b = 5.007 (1), c = 13.292 (3) Å, β = 112.14 (2) ˚. The structure of salicylaldoxime has previously been reported by Pfluger & Harlow (1973), and we refer to this phase as *salicylaldoxime-I*. The same crystal was then loaded into a diamond anvil cell. For reference, a further polymorph of the compound (salicylaldoxime-III) was also observed from a crystallisation using approximately the same conditions (Wood *et al.*, 2006).

2.3.2 High pressure crystallography

High-pressure experiments were carried out using a Merrill-Bassett diamond-anvil cell (half-opening angle 40°), equipped with brilliant-cut diamonds with 600μm

culets and a tungsten gasket (Merrill & Bassett, 1974). A 1:1 mixture of *n*-pentane and isopentane was used as a hydrostatic medium; this mixture is volatile at room temperature, and the cell was cooled in dry ice prior to loading. A small ruby chip was also loaded into the cell so that the pressure could be monitored using the ruby fluorescence method (Piermarini *et al.*, 1975). Diffraction data were collected on a Bruker-Nonius APEX-II diffractometer with silicon-monochromated synchrotron radiation (λ = 0.6889 Å) on Station 9.8 at the SRS, Daresbury Laboratory.

Data collection and processing procedures for the high-pressure experiments followed the methods of previous studies (Dawson *et al.*, 2004, Moggach, Allan, Parsons *et al.*, 2005). Integrations were carried out using the program *SAINT* (Bruker-Nonius, 2006), and absorption corrections with the programs *SHADE* (Parsons, 2004) and *SADABS* (Sheldrick, 2004). Data collections were taken in approximately 1.0 GPa steps from 0.75 GPa up to a final pressure of 5.93 GPa. Determination of the cell constants at 5.93 GPa showed that a single-crystal to single-crystal phase transition had occurred to a new polymorph, which we have designated *salicylaldoxime-II*. The phase transition degraded the crystal quality somewhat, and no attempt was made to study the effects of subsequent decompression.

In order to facilitate a comparison with the ambient-temperature/high-pressure results, diffraction data were also collected on salicylaldoxime-I at ambient pressure. Data were collected on a Bruker APEX diffractometer with graphite-monochromated Mo-Kα radiation (λ = 0.71073 Å). The crystals were sensitive to radiation damage from the X-ray beam, so this dataset was collected at 273 K. The data were integrated using *SAINT* and corrected for absorption with *SADABS*. The structure was solved using the program *SIR92* (Altomare *et al.*, 1994) and structure refinement yielded a conventional *R* factor of 0.0564, giving structural parameters that are somewhat more precise than those determined in the previous study (Pfluger & Harlow, 1973).

Refinements of the compressed form of salicylaldoxime-I were carried out starting from the coordinates determined at ambient pressure. The structure of the new phase (salicylaldoxime-II) was solved by direct methods using the program

SIR92. Refinements were carried out against $|F|^2$ using all data with the program *CRYSTALS* (Betteridge *et al.*, 2003). Owing to the low completeness of the data-sets, global rigid-bond and body restraints were applied to the anisotropic displacement parameters. The quality of the diffraction pattern deteriorated markedly after the transformation to salicylaldoxime-II, and no attempt was made to study this sample at still higher pressures. Displacement parameters in phase-II were only modelled at the isotropic level; shift-limiting restraints were also applied to all parameters.

Hydrogen atoms attached to carbon atoms were placed geometrically and constrained to ride on their host carbon atoms. The hydroxyl H atoms (H1 and H5) in all cases were found using Fourier difference maps. The positional parameters of H1 and H5 were then refined subject to the restraint r(O-H) = 0.820 (1) Å. Listings of crystal and refinement data are given in Table 2.1.

Crystal structures were visualized using the programs *CAMERON* (Watkin *et al.*, 1993), *Mercury* (Bruno *et al.*, 2002) and *DIAMOND* (Crystal Impact, 2004). Analyses were carried out using *PLATON* (Spek, 2004), as incorporated in the *WinGX* suite (Farrugia, 1999). Searches of the Cambridge Structural Database (CSD; (Allen, 2002, Allen & Motherwell, 2002)) utilized the program *ConQuest* and version 5.27 of the database with updates up to January 2006.

Topological calculations of void distributions (Blatov & Shevchenko, 2003) were carried out with *TOPOS-Pro* (Blatov *et al.*, 1995, 2000). Considerable simplification of the void distributions can be gained by clustering; voids were therefore clustered using what the program refers to as the 'clustering' method with the 'size' parameter specified as 0.5 (Blatov, 2005). Strain tensor calculations were carried out using a locally-written program (*STRAIN*; (Parsons, 2003)), based on the discussion in Hazen and Finger (1982) and employing the *JACOBI* subroutine (Press *et al.*, 1992). Equation-of-state calculations were carried out with *EOSFIT* (Angel, 2002).

The numbering scheme used (see Scheme 2.1) is the same throughout the ambient pressure and high pressure datasets, including the phase II structure. The setting that was used for the salicylaldoxime-II structure was chosen to facilitate the comparison with salicylaldoxime-I.

Pressure/GPa	ambient	0.75	2.37	3.46
Formula	$C_7H_7NO_2$	$C_7H_7NO_2$	$C_7H_7NO_2$	$C_7H_7NO_2$
M_r	137.14	137.14	137.14	137.14
Crystal system	Monoclinic	Monoclinic	Monoclinic	Monoclinic
Space group	$P2_1/n$	$P2_1/n$	$P2_1/n$	$P2_1/n$
a, b, c (Å)	10.346 (4), 5.0294 (17), 13.478 (5)	10.1833 (16), 4.9766 (3), 13.0109 (15)	9.851 (3), 4.9325 (7), 12.286 (3)	9.7148 (16), 4.9322 (3), 12.0145 (16)
β (°)	112.21 (2)	111.938 (10)	111.09 (2)	110.607 (11)
V (Å^3)	649.3 (4)	611.62 (13)	557.0 (3)	538.84 (12)
Z	4	4	4	4
D_x (Mg m^{-3})	1.403	1.489	1.635	1.690
Radiation type	Mo $K\alpha$	Synchrotron	Synchrotron	Synchrotron
No. of reflections for cell	930	363	253	337
θ_{max} (°)	30.7	26.8	26.4	26.4
μ (mm^{-1})	0.10	0.11	0.12	0.13
T_{min}/ T_{max}	0.79, 0.99	0.34, 0.99	0.51, 0.99	0.62, 0.99
Reflections collected	6424	2288	2109	2031
No. Unique [R_{int}]	1982 [0.047]	547 [0.079]	472 [0.075]	412 [0.061]
$R[F^2 > 2\sigma(F^2)]$, $wR(F^2)$, S	0.056, 0.175, 0.92	0.049, 0.136, 0.79	0.040, 0.101, 0.89	0.042, 0.107, 0.88
No. of reflections	1982 reflections	514 reflections	437 reflections	412 reflections
Parameters	97	97	97	97
Restraints	84	84	84	84
$\Delta\rho_{max}$, $\Delta\rho_{min}$ (e Å^{-3})	0.25, –0.23	0.11, –0.11	0.09, –0.16	0.13, –0.14

(a)

Pressure/GPa	4.55	5.28	5.93
Formula	$C_7H_7NO_2$	$C_7H_7NO_2$	$C_7H_7NO_2$
M_r	137.14	137.14	137.14
Crystal system	Monoclinic	Monoclinic	Monoclinic
Space group	$P2_1/n$	$P2_1/n$	$P2_1/n$
a, b, c (Å)	9.5728 (15), 4.9342 (3), 11.7537 (15)	9.513 (2), 4.9319 (4), 11.630 (2)	7.677 (3), 5.7731 (8), 12.159 (3)
β (°)	110.064 (10)	109.859 (14)	110.62 (2)
V (Å^3)	521.48 (11)	513.19 (15)	504.4 (3)
Z	4	4	4
D_x (Mg m^{-3})	1.747	1.775	1.806
Radiation type	Synchrotron	Synchrotron	Synchrotron
No. of reflections for cell	286	302	323
θ_{max} (°)	26.4	26.4	23.3
μ (mm^{-1})	0.13	0.13	0.13
T_{min}/ T_{max}	0.38, 0.99	0.42, 0.99	0.46, 0.99
Reflections collected	1793	1925	1157
No. unique [R_{int}]	417 [0.069]	410 [0.076]	296 [0.126]
$R[F^2 > 2\sigma(F^2)]$, $wR(F^2)$, S	0.044, 0.112, 0.91	0.041, 0.094, 0.94	0.125, 0.275, 0.82
No. of reflections	394 reflections	386 reflections	268 reflections
Parameters	97	97	47
Restraints	84	84	95
$\Delta\rho_{max}$, $\Delta\rho_{min}$ (e Å^{-3})	0.14, –0.12	0.13, –0.11	0.37, –0.40

(b)

Table 2.1: Crystallographic data for salicylaldoxime at increasing pressures (a) ambient to 3.46 GPa and (b) 4.55 to 5.93 GPa.

2.3.3 PIXEL calculations

The final crystal structures obtained were used to calculate the molecular electron density at each pressure by standard quantum chemical methods using the program *GAUSSIAN98* (Frisch *et al.*, 1998) at the MP2/6-31G** level of theory. H-atom distances were set to standard neutron values (CH = 1.083 Å, OH = 0.983 Å). The electron density model of the molecule was then analysed using the program package *OPiX* (Gavezzotti, 2005), which allowed the calculation of dimer and lattice energies. Lattice energy calculations employed a cluster of molecules of radius 18 Å. Calculations were also carried out for pairs of molecules identified in the lattice calculation as being energetically the most significant (*i.e.* with a magnitude > 2.5 kJ mol^{-1}). The output from these calculations yields a total energy and a breakdown into its electrostatic, polarisation, dispersion and repulsion components (Dunitz & Gavezzotti, 2005).

2.4 Results

2.4.1 The structure of salicylaldoxime-I at ambient pressure

Prior to this work two crystalline forms of salicylaldoxime had been characterized. The structure of salicylaldoxime-I was determined by Pfluger & Harlow (1973); salicylaldoxime-III was initially studied by (Merritt & Schroeder, 1956), but its structure was determined only recently (Wood *et al.*, 2006). The crystal structure of salicylaldoxime-I has one molecule in the asymmetric unit in the space group $P2_1/n$. The molecule as a whole is planar; a least-squares mean plane calculated using the C, N and O atoms shows that the average deviation of these atoms from the plane is 0.009 Å.

The molecules form intramolecular O5H5···N2 hydrogen bonds [O5···N2 = 2.621 (2) Å] and intermolecular O1H1···O5 hydrogen bonds [O1···O5 = 2.793 (2) Å]. The latter form a dimer across an inversion centre (Figure 2.1a), yielding a ring motif for which the graph-set descriptor is $R_4^4(10)$ (Bernstein *et al.*, 1995). The two molecules in the dimer are almost coplanar, with a distance of only 0.28 Å between the two least-squares planes.

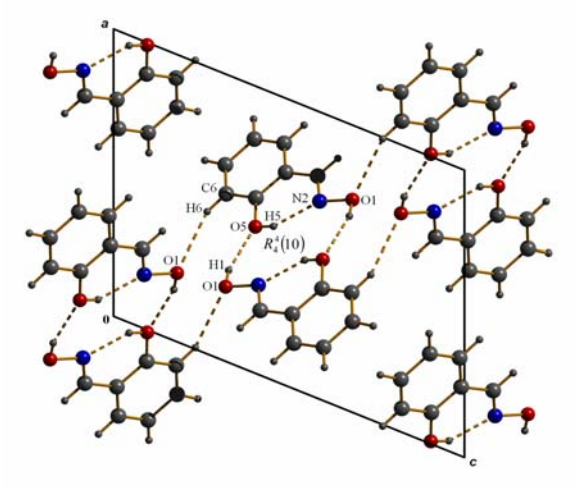

(a)

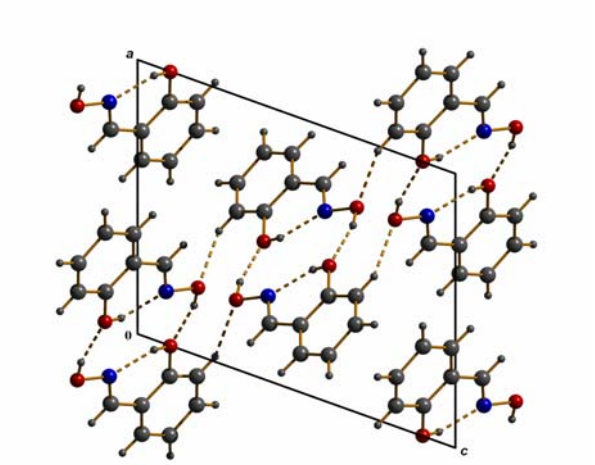

(b)

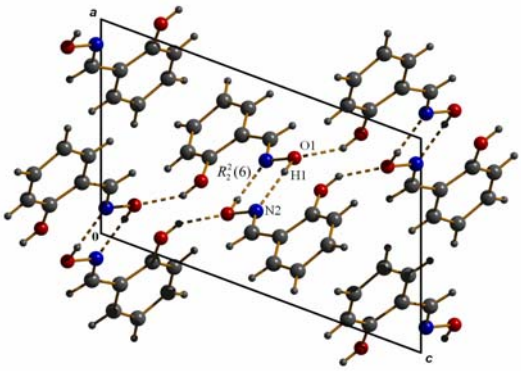

(c)

Figure 2.1: The effect of pressure on the crystal structure of salicylaldoxime as viewed along *b*: (a) salicylaldoxime-I at ambient pressure; (b) salicylaldoxime-I at 5.28 GPa; (c) salicylaldoxime-II at 5.93 GPa. The colour scheme is red: oxygen, blue: nitrogen, light-grey: carbon and dark-grey: hydrogen.

The molecule has three hydrogen bond acceptors (O1, N2 and O5) and only two conventional donors (O1/H1 and O5/H5), and there is therefore an unfulfilled hydrogen-bond acceptor (based on O1). Atom O1 forms a very weak inter-dimer C6H6···O1 interaction with a neighbouring molecule [C6···O1 = 3.404 (2) Å, PIXEL energy = -2.7 kJ mol^{-1}] (Figure 2.2a). Successive C6H6···O1 interactions related by the *n*-glide build primary-level *C*(7) chains, producing 'slabs' which lie in the (1 0 -1) plane (Figure 2.3a). There are no hydrogen bond interactions between the slabs.

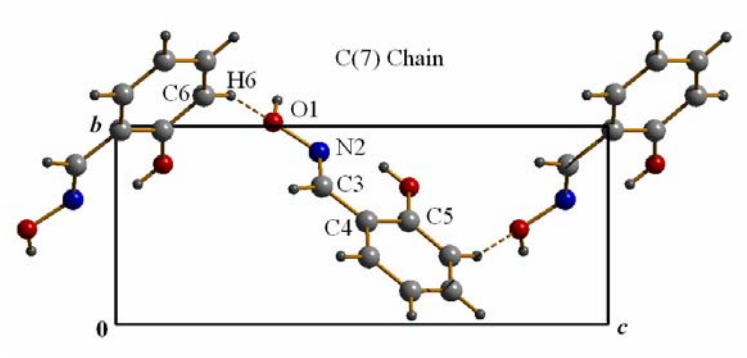

(a)

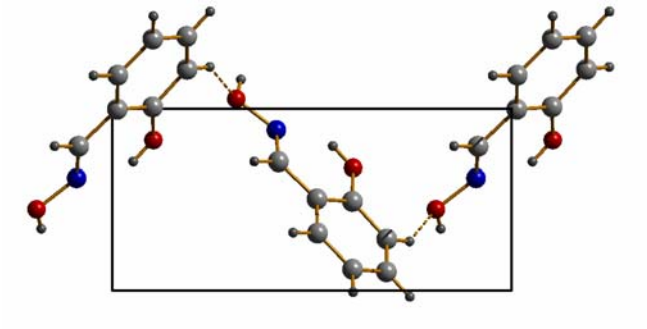

(b)

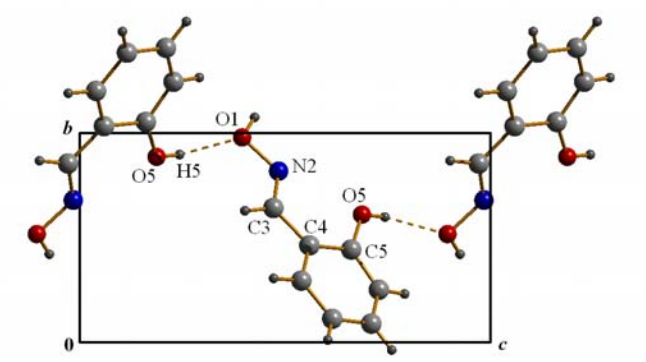

(c)

Figure 2.2: The effect of pressure on the crystal structure of salicylaldoxime as viewed along *a*: (a) salicylaldoxime-I at ambient pressure; (b) salicylaldoxime-I at 5.28 GPa; (c) salicylaldoxime-II at 5.93 GPa. The colour scheme is the same as in Figure 2.1.

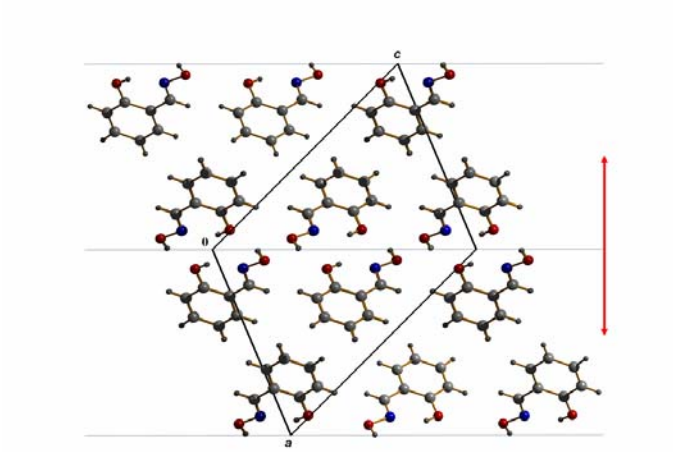

(a)

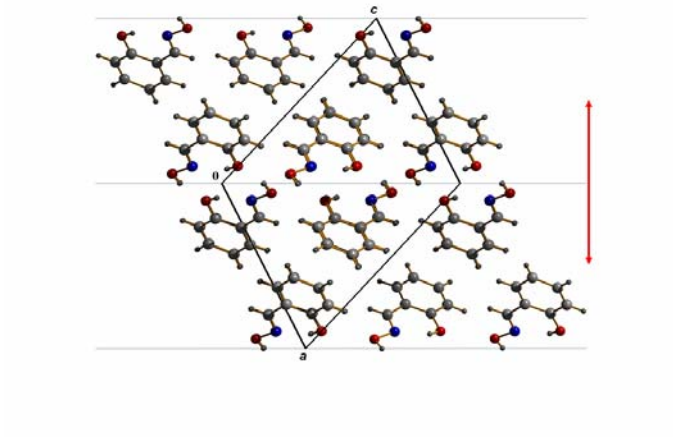

(b)

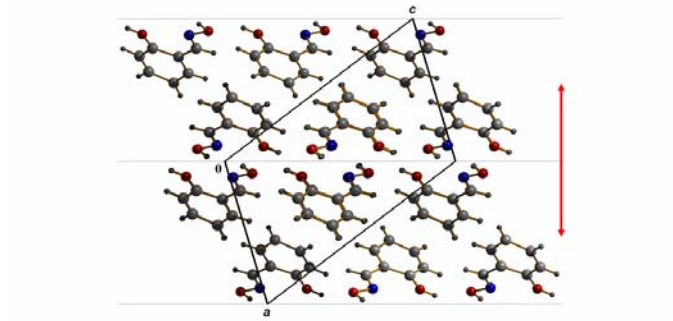

(c)

Figure 2.3: The effect of pressure on the slabs in the salicylaldoxime structure formed from the *C*(7) chains: (a) salicylaldoxime-I at ambient pressure; (b) salicylaldoxime-I at 5.28 GPa; (c) salicylaldoxime-II at 5.93 GPa. The blue lines shown in the diagram are (1 0 -1) planes viewed side-on. The red arrows indicate the extent of one slab in each diagram. The colour scheme is the same as in Figure 2.1.

Within the slabs, dimers interact with other dimers through π-π stacking (Figure 2.4). The inter-plane separations are 3.07 and 3.40 Å between the reference molecule and the molecules labeled 2 and 3, respectively. We show below that these stacking interactions are in fact more energetically significant than the CH…O contacts. The centroids of the phenyl rings are off-set from each other by 3.71 and 5.25 Å for these two interactions along the horizontal direction in Figure 2.4, and the stacking interaction appears to be between $R_4^4(10)$ and phenyl rings.

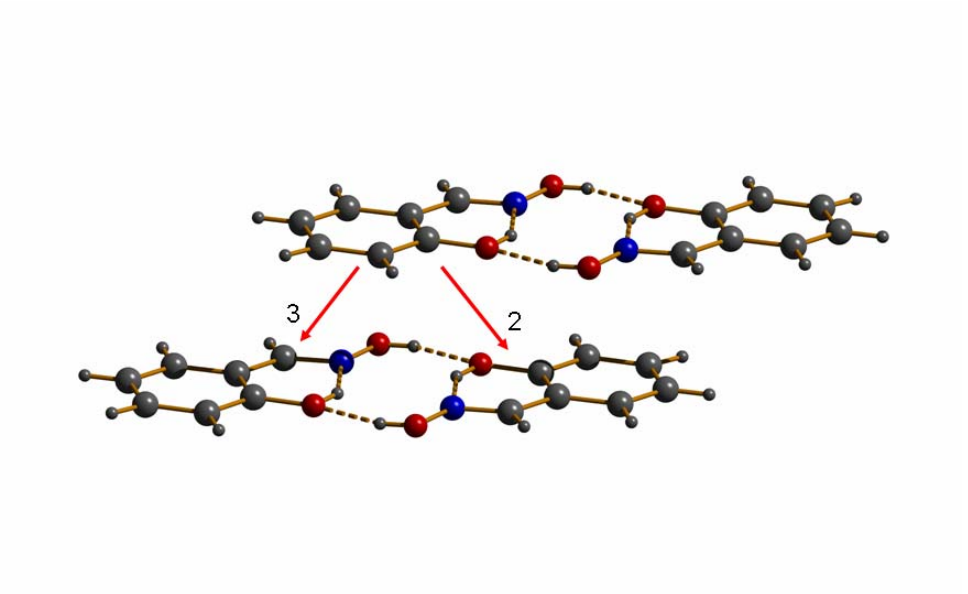

Figure 2.4: The π-π stacking interactions between two dimers. Labels 2 and 3 refer to the specific interactions studied using the PIXEL method, see Figure 2.9. The colour scheme is the same as in Figure 2.1.

2.4.2 The response of salicylaldoxime-I to pressure up to 5.28 GPa

The response of the salicylaldoxime-I structure to hydrostatic pressure is anisotropic (Figure 2.5); the greatest reduction occurs in the *c* axis length (13.7% at 5.28 GPa relative to ambient pressure), while the *a* and *b* axes reduce by 8.1 and 1.9%, respectively. The direction of greatest linear strain lies approximately along the reciprocal axis direction (1 0 -2); the principal axis with the second largest eigenvalue is approximately along (6 0 1). These directions are shown in Figure 2.6. One eigenvector of the strain tensor must correspond to the *b* direction by symmetry, and this is the direction of least compression in the structure.

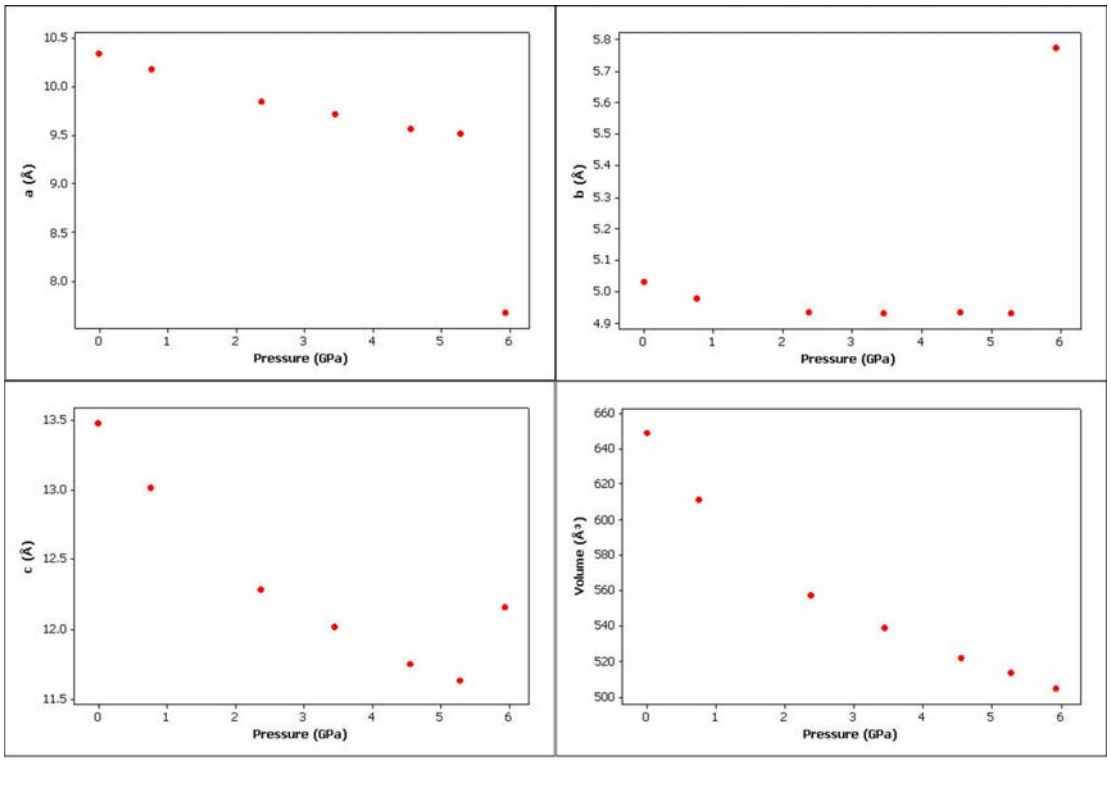

Figure 2.5: The variation of the lattice parameters (*a*, *b* and *c*, Å) and volume (Å³) of salicylaldoxime as a function of pressure (GPa).

The bulk modulus (K_0), refined for a Birch-Murnaghan equation-of-state (Birch, 1947, Angel, 2000) truncated to second order (thus requiring $K' = 4$) is 13.3 (4) GPa (equation reduces to Eq. 1). The data set used to calculate this quantity is admittedly rather limited, and the value of V_0 was fixed at 649.3 Å^3. Molecular solids generally have $K_0 < 30$ GPa (Angel, 2004) and a useful comparison can be made from the following K_0 values: $Ru_3(CO)_{12}$ 6.6 GPa, NaCl 25 GPa, quartz 37 GPa, ceramics 50-300 GPa and diamond 440 GPa (Slebodnick *et al.*, 2004).

$$P = 3K_0 f_E \left(1 + 2f_E\right)^{5/2} \quad (1)$$

$$\text{where } f_E = \left[\left(V_0 / V\right)^{2/3} - 1\right]/2$$

The molecule remains planar at 5.28 GPa, and the distance between the least-squares planes of the molecules in the dimer remains essentially constant (0.27 Å at 5.28GPa).

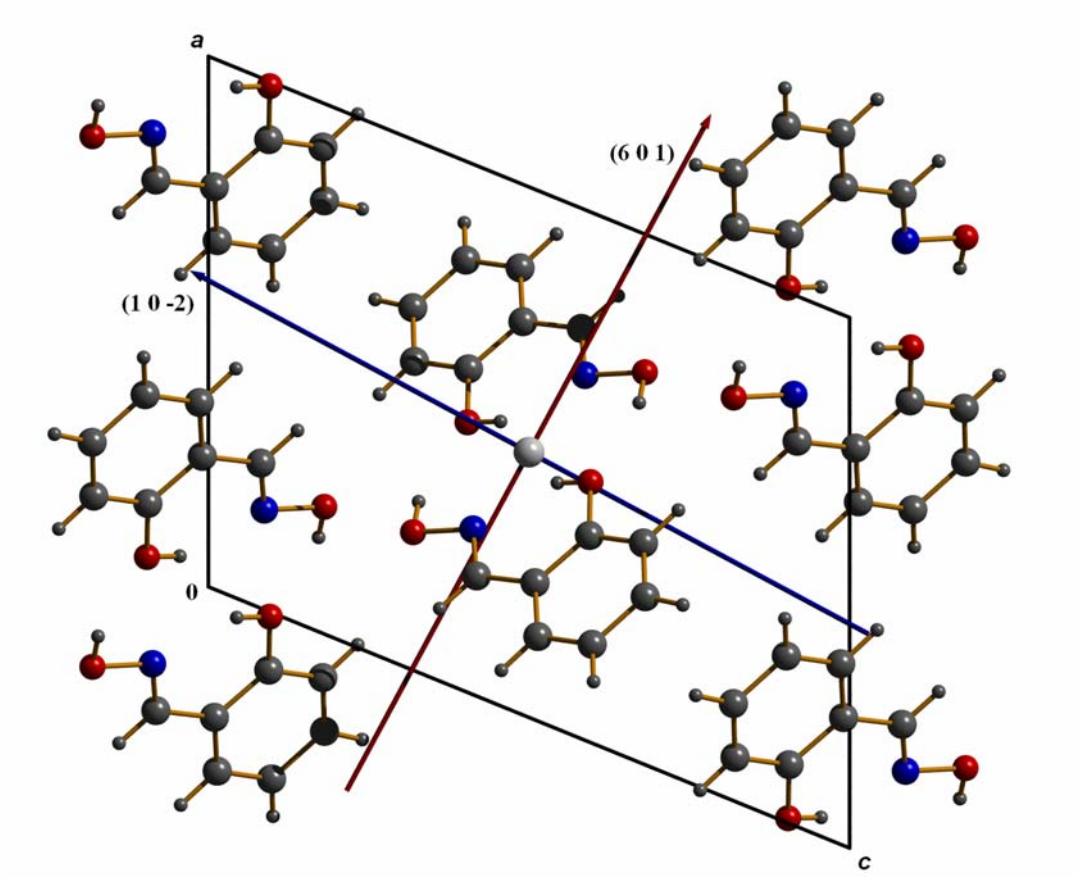

Figure 2.6: The directions of greatest strain in the salicylaldoxime-I crystal structure between ambient pressure and 5.28 GPa as viewed along *b*. The blue arrow shows the largest eigenvector of the strain tensor, the (1 0 -2) reciprocal axis direction, and the red arrow shows the second largest eigenvector, the (6 0 1) reciprocal axis direction. The colour scheme is the same as in Figure 2.1.

The variation of non-covalent interaction parameters in salicylaldoxime-I between ambient pressure and 5.28 GPa is presented in Table 2.2. The least compressible interaction is the intramolecular OH···N hydrogen bond from O5/H5 to N2 (O5···N2 changes by 2.2%). The second conventional hydrogen bond (O1/H1···O5) is significantly more compressible because of the greater spatial flexibility of the molecules; O1···O5 decreases by 6.5% to a distance of 2.612 (6) Å. The OH···O angle remains approximately constant, and so the shape of the hydrogen bonding ring is essentially unchanged (c.f. Figures 2.1a and b).

Pressure/GPa	ambient	0.75	2.37	3.46	4.55	5.28
O5H5..N2[i]						
H5..N2	1.91	1.90	1.87	1.83	1.90	1.86
O5..N2	2.621(2)	2.607(4)	2.588(4)	2.580(4)	2.570(5)	2.564(5)
<O5H5N2	144(2)	143	145	152	138	144
O1H1..O5[ii]						
H1..O5	2.02	1.98	1.92	1.89	1.86	1.83
O1..O5	2.793(2)	2.753(6)	2.683(6)	2.654(6)	2.630(7)	2.612(6)
<O1H1O5	156(2)	157	155	154	156	160
C6H6..O1[iii]						
H6..O1	2.54	2.44	2.35	2.30	2.27	2.27
C6..O1	3.404(2)	3.316(8)	3.169(8)	3.132(7)	3.089(9)	3.077(9)
<C6H6O1	154(1)	150	149	147	147	146
π-π[iv] #2						
plane-plane	3.073(2)	2.984(3)	2.872(3)	2.839(2)	2.798(3)	2.819(3)
offset	5.25(1)	5.24(2)	5.15(2)	5.10(2)	5.03(2)	5.01(2)
π-π[v] #3						
plane-plane	3.402(2)	3.289(3)	3.103(3)	3.024(2)	2.957(3)	2.896(3)
offset	3.71(1)	3.74(2)	3.84(2)	3.90(2)	3.95(2)	3.99(2)

Symmetry Operators

i	*x*,*y*,*z*
ii	-*x*,-*y*,-*z*
iii	1/2+*x*,1/2-*y*,1/2+*z*
iv	1-*x*,1-*y*,1-*z*
v	*x*,-1+*y*,*z*

Table 2.2: Non-covalent interaction parameters in salicylaldoxime-I. Distances are in Å, and angles in °.

The most compressible hydrogen-bonding interaction is C6H6···O1 which decreases by 9.6% to 3.077 (9) Å. The CHO angle decreases steadily with the application of pressure from 154° to 146° at 5.28 GPa as the molecules shift with respect to each other in order to pack more effectively (see Figures 2.1 & 2.2).

The π-π stacking interaction distances, defined as the perpendicular distance between the least-squares mean plane of one phenyl ring and the centroid of another, are also compressed. The distance for interaction 3 in Figure 2.4 decreases by 14.8% from 3.40 Å at ambient pressure to 2.90 Å at 5.28 GPa, and the distance for interaction 2 decreases by 8.3% from 3.07 Å to 2.82 Å at 5.28 GPa. The offset distances for interactions 2 and 3 change from 5.25 Å to 5.01 Å and 3.71 Å to 3.99 Å, respectively, as the molecules slide across each other.

2.4.3 Salicylaldoxime-II at 5.93 GPa

The observation that the transition from phase I to II proceeds from one single crystal to another suggests that the local topologies of the phase I and II structures are similar to each other. The space-group symmetry is retained, and the cell volume also follows a fairly smooth curve from the ambient pressure structure through the transition into phase II at 5.93 GPa (Figure 2.5).

The $R_4^4(10)$ ring motif found in the phase I structure is no longer present in salicylaldoxime-II. At 5.93 GPa atom H1 forms an O1H1···N2 hydrogen bond to N2 instead of O5 [O1···N2 = 2.622 (2) Å]. The new OH···N intra-dimer interaction and its inversion-related equivalent form an $R_2^2(6)$ ring motif in the phase II structure (Scheme 2.2b and Figure 2.1c). This shifting of the molecules in the dimer and formation of a $R_2^2(6)$ ring instead of an $R_4^4(10)$ ring allows the molecules to approach more closely. The molecules themselves remain planar in the phase II structure; moreover the two molecules in the dimer are almost exactly coplanar, with a distance of only 0.02 Å between their respective least-squares planes (calculated for each using the C, N and O positions only).

The intramolecular O5H5···N2 hydrogen bonds found in the phase I structure are also broken and the presence of H1 forming a strong interaction with N2 forces H5 to flip out to the side of the dimer (see Scheme 2.2). This OH group now forms an O5H5···O1 hydrogen bond to O1 [O5···O1 = 2.582 (14) Å] on a neighbouring molecule in a different dimer which is related *via* the *n*-glide. These OH···O interactions form *C*(7) chains which run in the direction of the *n*-glide replacing the CH···O *C*(7) chains in the phase I structure. The chains are then linked to each other by the hydrogen bonds across the dimer forming slabs which lie in the (1 0 -1) plane, just as in the ambient pressure structure. There are no hydrogen-bonded interactions between the slabs (see Figure 2.3c).

The π-π stacking interaction motif found in the salicylaldoxime-I structure is retained in the phase II structure. In the new phase there is still an interaction similar to interaction 3 in Figure 2.4, but now the inter-plane separation has increased from 2.90 Å at 5.28 GPa to 3.06 Å at 5.93 GPa and the offset has increased to 4.90 Å. The reference molecule also forms an interaction similar to 2 in Figure 2.4, but now the inter-plane separation is 2.91 Å and the offset is 4.87 Å at 5.93 GPa. In the phase II structure the reference molecule phenyl ring is approximately equidistant from the centroids of both phenyl rings in the stacking interaction.

2.5 Discussion

2.5.1 Void analysis of the phase I structure

The effect of pressure can be understood in terms of distributions of voids which exist in a structure prior to compression. The voids tend to close up at high pressure, and it is often found that the direction of greatest compressibility in a crystal is directly related to the position and orientation of the largest voids in the structure.

In the salicylaldoxime-I structure it is possible to analyse the distribution and size of structural voids using a Voronoi-Dirichlet analysis as shown in previous studies (Blatov & Shevchenko, 2003, Moggach, Allan, Parsons *et al.*, 2005). The largest void region (volume 16.77 Å^3) consists of three void conglomerates which lie

in between the slabs of the structure. Figures 2.7*a* and 2.7*b* show space-filling plots of the salicylaldoxime-I structure, at ambient pressure and 5.28 GPa, respectively. It is apparent that there is a sizable void between the slabs at ambient pressure which closes up significantly at 5.28 GPa. The direction of movement of the molecules that closes the gap between the slabs is also in the direction of greatest linear strain.

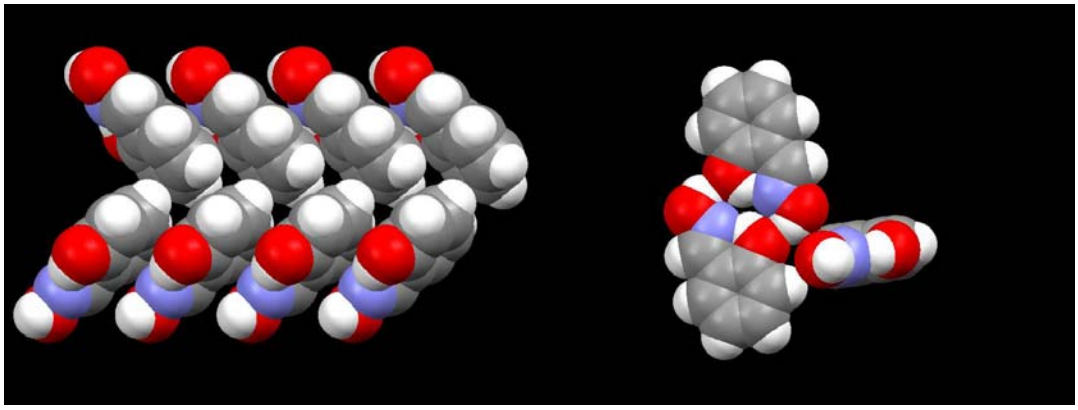

(a) (c)

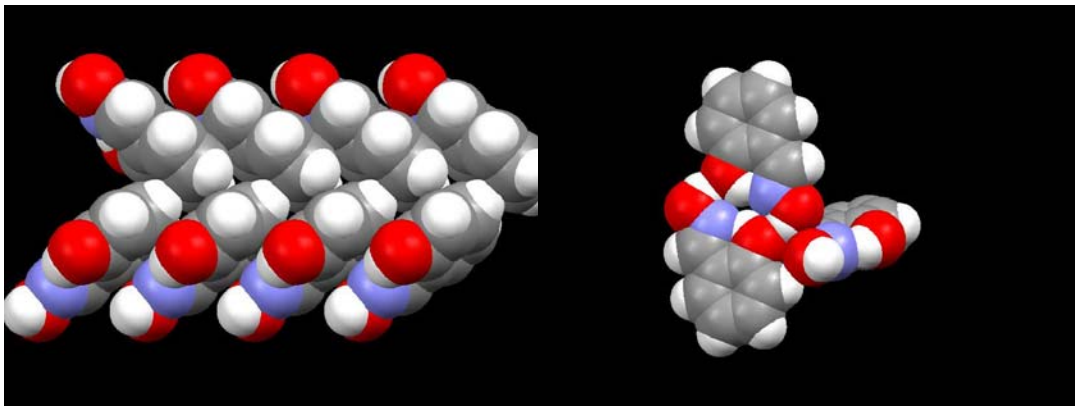

(b) (d)

Figure 2.7: Space-filling plots showing the contraction of voids which occur in salicylaldoxime phase I with the application of pressure. The top and bottom rows correspond to the salicylaldoxime-I structure at ambient pressure and at 5.28 GPa, respectively. On the left of the diagram (a) and (b) show the structure with the *a** direction vertical; there are large voids between the molecules which almost disappear completely with increasing pressure. On the right (c) and (d) show the void between molecules related by the *n*-glide; this gap also closes up considerably with the application of pressure.

The second largest cluster of voids, which has a volume of 9.50 Å^3, lies between molecules related by the *n*-glide, and this void can be seen in the structures at ambient pressure and 5.28 GPa in Figures 2.7*c* and 2.7*d*. The gap relates to the relatively long C6H6···O1 weak hydrogen-bond interaction. The vector between C6 and O1 corresponds approximately to the second direction of greatest strain in the structure (the angle between the vectors is 12°).

The void in the middle of the hydrogen-bonded dimer is formed by relatively strong hydrogen bonds, and it would not be expected to compress as much as voids in the vicinity of more weakly interacting molecules. Nevertheless, the dimer cavity is affected by the application of high pressure. The size of the cavity can be analysed by measuring the mean distance of the donor atoms from the centroid of the dimer. This distance decreases steadily with pressure from 2.0048 (15) to 1.935 (4) Å at 5.28 GPa, as shown in Figure 2.8. The cavity size has been found to be 1.93 (1) Å in the Cu^{2+} salicylaldoxime complex, whereas in the corresponding Ni^{2+} complex it is 1.864 (1) Å, a change of 0.066 Å (Smith *et al.*, 2002). Pressure affects the cavity size by a similar amount. If the size of the cavity can be modified by an amount comparable to the difference in sizes in the different metal complexes, then it is possible that compression may affect the complexation properties of the compound.

Voronoi-Dirichlet analysis shows that the voids present in salicylaldoxime-II are much smaller than those in phase-I. There are still small voids between the slabs in the structure, though the majority are distributed between the molecules related by a unit cell translation in the *b*-direction.

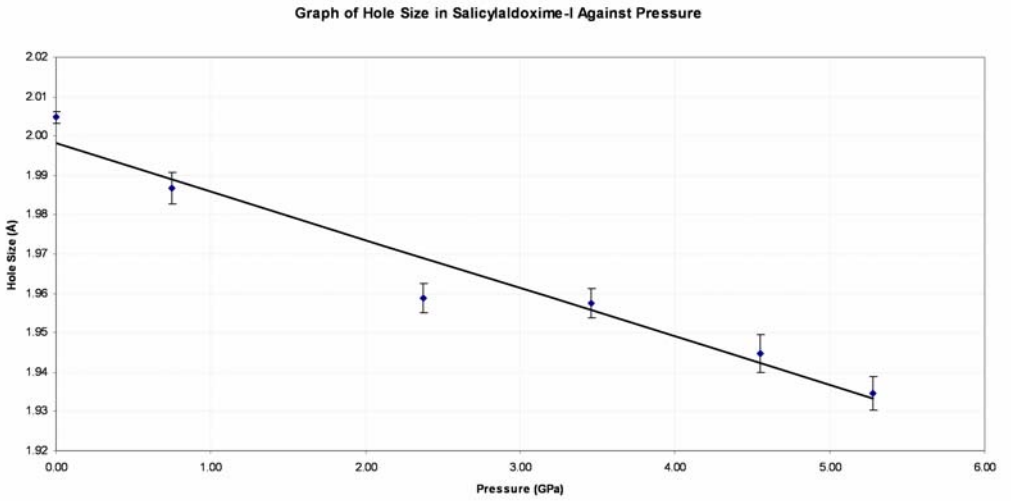

Figure 2.8: A graph of hole size in salicylaldoxime- I as a function of pressure where the hole size is defined as the mean distance of donor atoms from the centroid of the dimer. The error bars are displayed at the 1σ level.

2.5.2 Hydrogen bonding and π-π stacking in salicylaldoxime-I

The three different hydrogen bonds in salicylaldoxime-I do not compress uniformly. The largest compressibility is witnessed for C6H6···O1, which is the longest hydrogen bond in the structure. Our PIXEL calculations (see below) show that this interaction contributes rather little to the lattice energy at ambient or high pressure, and its distance can be varied without incurring a significant energy penalty. The least compressible hydrogen bond is the intramolecular O5H5···N2 interaction, which only decreases by a small amount (2.2%) because of the conformational inflexibility of the molecule.

The compression of the intermolecular O1H1···O5 hydrogen bond is not restricted by the molecular conformation and its compressibility is higher (6.5%) than that of the O5H5···N2 interaction. A search of the CSD revealed the shortest O···O distance in C=NOH···OHC containing systems to be 2.596 Å [for *rac*-2,3:6,7-dibenzobicyclo(3.3.1)-nona-2,6-diene-4,8-dione dioxime methanol solvate, CSD refcode WUHGEL01; (Levkin *et al.*, 2003)]. The O···O distance in salicylaldoxime at 5.28 GPa [2.612 (6) Å] is thus near the lower limit observed for such interactions.

The compression of π-π stacking interactions with hydrostatic pressure has not been extensively studied. Analysis of aromatic stacking interactions in the CSD shows that the minimum stacking distance between the phenyl rings is *ca* 2.9 Å. At 5.28 GPa the stacking distances for interactions 2 and 3 (see Figure 2.4) are 2.82 Å and 2.90 Å, respectively. As in the case of the O1H1···O5 interaction, therefore, the π-π stacking in salicylaldoxime-I at 5.28 GPa is very close to the lower limit of similar interactions found at ambient pressure. The phase transition to salicylaldoxime-II allows the π-π stacking distances to increase (inter-planar distances = 2.91 and 3.05 Å), thus reducing the repulsion terms.

Previous compression studies on small organic molecules which exhibit hydrogen bonding, such as glycine (Dawson *et al.*, 2005), L-serine (Moggach, Allan, Morrison *et al.*, 2005) and L-cysteine (Moggach *et al.*, 2006), have shown that the application of hydrostatic pressure (below about 10 GPa) will not decrease the length of a hydrogen bond or other interaction to lower than can be found for a similar types of contact in ambient-pressure structures. Once a contact reaches its lower limit a phase transition occurs. The salicylaldoxime-I structure at 5.28 GPa has reached a point where one hydrogen bond and the π-π stacking interactions have contracted to near their lower distance limits. Further compression of the structure and the reduction of the void found in the middle of the $R_4^4(10)$ ring can only occur through a phase transition, and so above 5.28 GPa salicylaldoxime-II is formed.

The hydrogen-bonding pattern in salicylaldoxime-II is quite different from the ambient phase (Figures 2.1 and 2.2). The intramolecular O5H5...N2 hydrogen bond is broken in favour of a new intermolecular O5H5···O1 interaction, while the dimer-forming hydrogen bond (O1H1···O5) is also broken in order to create a smaller ring without a cavity through a new O1H1···N2 contact. Overall this yields a more compact structure, though the data in Table 2.3 and CSD searches show that the new hydrogen bonds are still near the lower limit for their contact-types. However, the changes that occur in the distances characterizing the π-π interactions before and after the phase transition suggest that strain is relieved in this region of the structure.

Interaction	
O1H1..N2^{i}	
H1..N2	1.85
O1..N2	2.622(25)
<O1H1N2	156
O5H5..O1^{ii}	
H5..O1	1.83
O5..O1	2.582(14)
<O5H5O1	151
π-π^{iii} #2	
plane-plane	2.925(10)
offset	4.86(4)
π-π^{iv} #3	
plane-plane	3.065(10)
offset	4.89(4)

Symmetry Operators

i	*-x,-y,-z*
ii	1/2+*x*,1/2-*y*,1/2+*z*
iii	1-*x*,1-*y*,1-*z*
iv	*x*,-1+*y*,*z*

Table 2.3: Non-covalent interaction parameters in salicylaldoxime-II at 5.93 GPa. Distances are in Å, and angles in °.

2.5.3 PIXEL analysis

In the foregoing discussion we have presented an analysis of the changes which occur in the crystal structure of salicylaldoxime based on intermolecular distances. The PIXEL procedure, which has been developed recently by Gavezzotti, enables further insight to be gained by calculation of intermolecular interaction energies. The method also enables these energies to be broken down into Coulombic, polarisation, dispersion and repulsion contributions. In a PIXEL calculation the electron density in an isolated molecule is first calculated using a quantum mechanical package such as *GAUSSIAN*. This electron density model is then placed in a crystal structure and divided into pixels of electron density. Each energy term is obtained by summing over energies calculated between pairs of pixels in neighbouring molecules. Further details on the PIXEL method have been published elsewhere (Dunitz & Gavezzotti, 2005, Gavezzotti, 2005).

The lattice energies and a breakdown of the energies into component Coulombic, polarisation, dispersion and repulsion terms for each pressure were calculated and are shown in Table 2.4. The overall lattice energy becomes more positive as pressure is increased due to the steady increase in the repulsion term as the molecules are pushed closer together. The phase transition between 5.28 and 5.93 GPa results in a considerable decrease in the overall lattice energy. The change is caused by significant decreases in the Coulombic and polarisation terms, which outweigh the increase in the repulsion term. By extrapolation of the trend established up to 5.28 GPa we estimate that salicylaldoxime-II has a larger total energy than salicylaldoxime-I by approximately 25 kJ mol^{-1} at 5.93 GPa. This substantial change is likely to be due the loss of an intramolecular hydrogen bond (which only appears in the internal energy) in favour of an intermolecular interaction. The adjusted total energy (U_{adj}) suggests a change of approximately 50 kJ mol^{-1} from phase I to II, though this may be over-estimated due to the relatively poor quality of the phase II structure (Table 2.4).

Pressure/ GPa	Coulombic	Polarisation	Dispersion	Repulsion	Total Energy	U_{adj}*	$H^{\dagger}$
0.00	-56.4	-22.1	-87.5	78.2	-87.9	-87.9	-87.9
0.75	-65.8	-27.5	-101.5	109.4	-85.4	-78.8	-8.8
2.37	-95.9	-44.0	-128.4	190.3	-78.0	-71.6	127.2
3.46	-107.2	-48.9	-137.0	226.5	-66.5	-60.3	219.5
4.55	-121.7	-57.7	-147.9	275.9	-51.4	-39.8	317.4
5.28	-128.3	-65.7	-154.0	304.2	-43.8	-26.4	381.6
5.93	-221.1	-117.2	-163.9	443.0	-59.2	21.4	471.7

***** Adjusted Energy (U_{adj}) = Total Energy – Energy difference due to conformation change relative to 0.0 GPa structure based on *GAUSSIAN98* calculation.

† Enthalpy (H) = $U_{adj} + PV$, where P = pressure (in Pa) and V = molar volume (in $m^3\ mol^{-1}$).

Table 2.4: The components of lattice energy and total energy at each pressure for salicylaldoxime (energies in kJ mol^{-1}) along with the adjusted total energy (U_{adj}) and the enthalpy (H).

Seven pairs of molecules have interaction energies of magnitude greater than 2.5 kJ mol^{-1}. These pairs, shown in Figure 2.9, have been labelled 1-7 in descending order of their total energies at ambient pressure. The total energies of the pairs at each pressure up to 5.28 GPa are also given in Table 2.5. The strongest interaction (1) corresponds to the O1H1···O5 hydrogen-bonded dimer across the inversion centre; this interaction is dominated by the coulombic term, as expected for a hydrogen bond. It continues to be the most important interaction with increasing pressure.

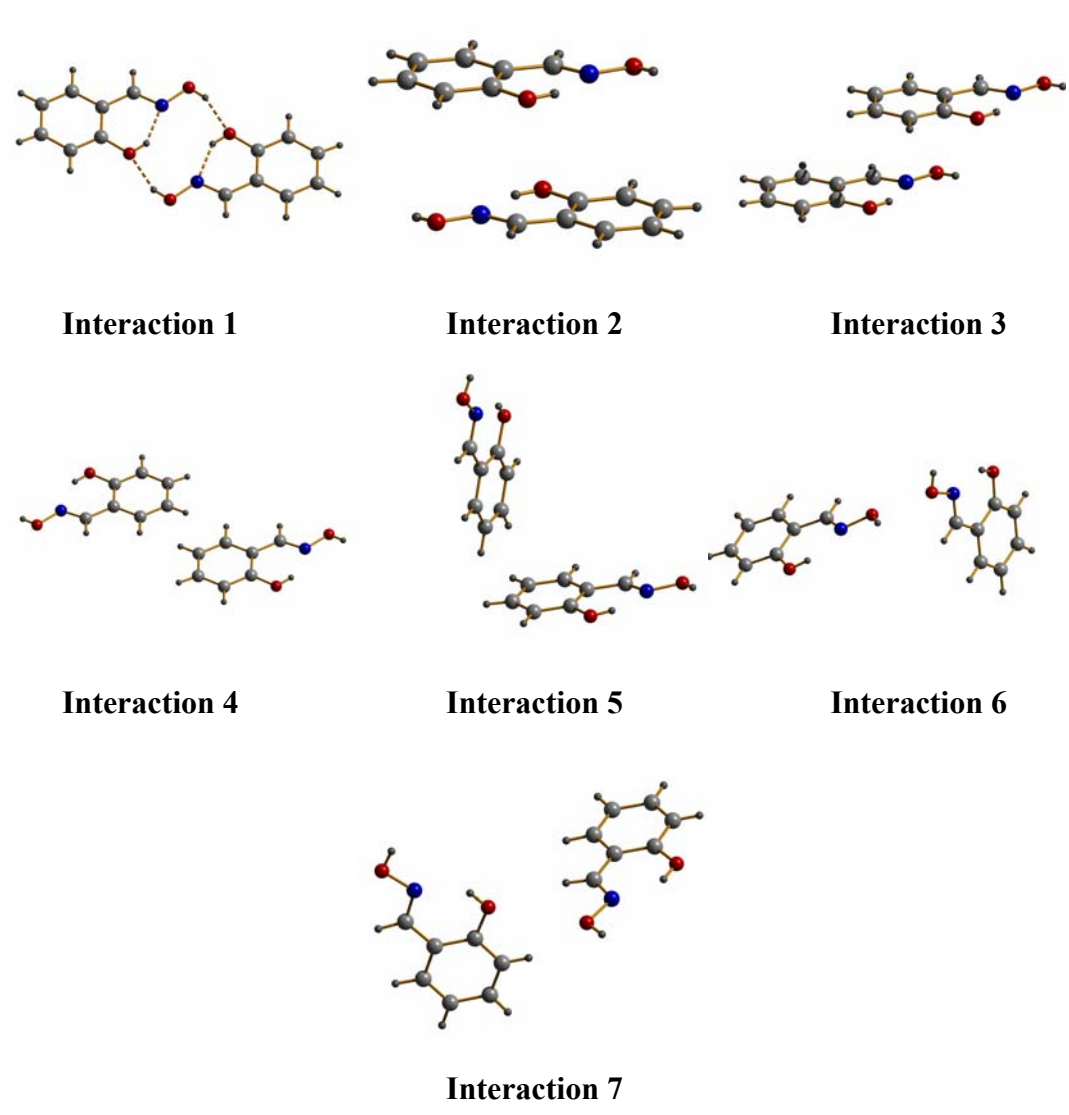

Figure 2.9: Diagrams of the highest energy interactions in the salicylaldoxime-I structure from PIXEL analysis. The colour scheme is the same as in Figure 2.1.

Pressure/ GPa	0.00	0.75	2.37	3.46	4.55	5.28
Interaction 1	-25.0	-24.2	-23.4	-20.6	-17.5	-17.6
Interaction 2	-8.7	-8.8	-7.6	-7.3	-5.9	-5.8
Interaction 3	-8.1	-8.3	-7.5	-5.6	-4.3	-2.8
Interaction 4	-6.2	-6.4	-6.6	-5.8	-6.0	-5.6
Interaction 5	-4.8	-4.6	-3.1	-2.5	-1.6	-1.2
Interaction 6	-4.0	-3.9	-3.9	-3.6	-2.6	-1.4
Interaction 7	-2.7	-2.5	-1.5	-1.0	0.1	0.1

Table 2.5: Total energies of the seven strongest interactions with increasing pressure in salicylaldoxime-I (energies in kJ mol^{-1}).

The next two strongest interactions (2 and 3) are the π-π stacking interactions between the reference molecule and two salicylaldoxime units forming a hydrogen-bonded dimer. Each interaction has an energy in the region of -8-9 kJ mol^{-1}, with a large dispersion component. Interactions 4, 5 & 6 would all be overlooked in a conventional analysis focusing on hydrogen bonding, but each has an overall stabilising interaction, amounting to between -4 and -7 kJ mol^{-1}. These interactions are an H…H contact, an offset CH…π interaction and an O…O contact, respectively. Interaction 7 corresponds to the C6H6···O1 hydrogen bond discussed above. It seems that this 'weak hydrogen-bonding' interaction contributes very little to the overall lattice energy, and has more contribution from the dispersion component than the coulombic component.

The data from structures at increasing pressures shows that each interaction becomes weaker as a result of the increasing repulsion terms. The responses of the interactions to hydrostatic pressure are by no means uniform, and Figure 2.10 shows a graph of the total interaction energies for each of the seven principal interactions against the distance between the molecular centroids of the two molecules involved

in the interaction. The data shown in Figure 2.10 were also calculated using the Gavezzotti force-field [available in the program *RPLUTO* (Motherwell, 2002)] yielding qualitatively similar results.

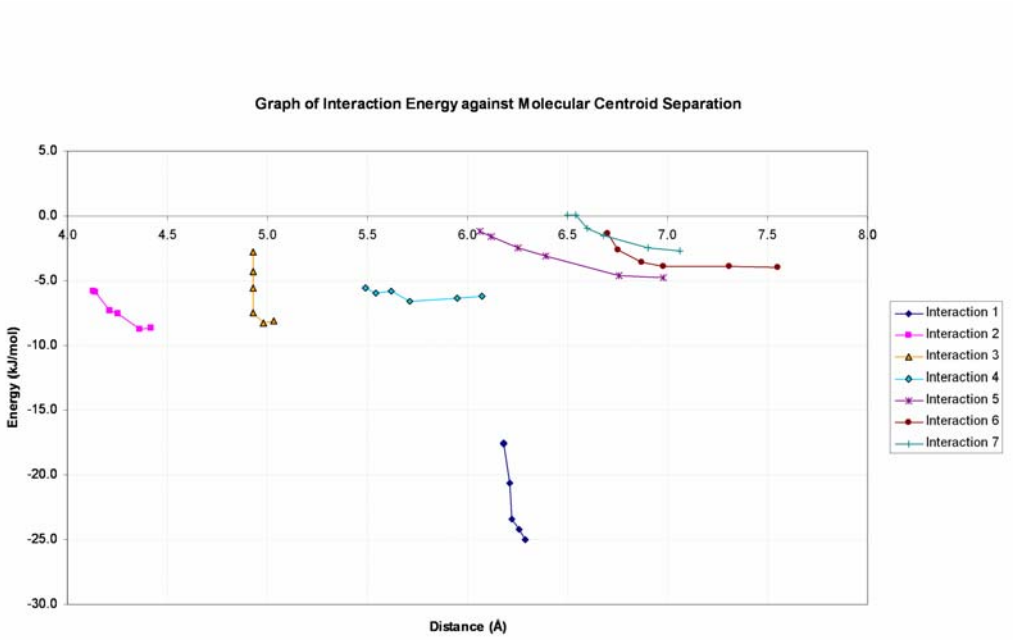

Figure 2.10: A graph of total interaction energy (in kJ mol^{-1}) against the distance between the molecular centroids of the molecules involved in the interaction (in Å).

Interactions 2, 4, 5, 6 & 7 are relatively unaffected by the compression. The interactions between these pairs of molecules would therefore seem to be very soft and not influential in the forcing of the phase transition. In contrast, the curves for interactions 1 and 3 are much steeper (note the distinct difference between the two stacking interactions 2 and 3). These results are consistent with the suggestion made above that the phase transition occurs in order to avoid further shortening of the OH…O hydrogen bond and π-π stacking distances. These results also suggest that the π-π interactions become strongly destabilising upon shortening and would appear to be very important in both the phase I structure and the phase transition to salicylaldoxime-II.

The energy of interactions in the phase II structure were also analysed using the PIXEL method. The most energetically stabilising interaction, as expected, is the $R_2^2(6)$ hydrogen-bonded ring. The pair of molecules involved has a total interaction energy of -16 kJ mol^{-1}, which is comparable to that of the phase I dimer interaction energy at 5.28 GPa. Other significant interactions include π-π interactions similar to those found in the phase I structure, which have total interaction energies of -5.5 and -4.3 kJ mol^{-1}.

The hydrogen bond, O5H5···O1, which was formed by conversion of an intramolecular hydrogen bond into an intermolecular hydrogen bond, is found to have a large stabilising coulombic term (-35.6 kJ mol^{-1}), but is actually not an stabilising interaction overall (E_{tot} = +1 kJ mol^{-1}) owing to the high value for the repulsion term (57.6 kJ mol^{-1}). It seems that the intra- to intermolecular hydrogen bond conversion has allowed a pair of molecules to approach one another in order to pack more efficiently.

2.6 Conclusions

We have described here the effects of the application of hydrostatic pressure on the structure of salicylaldoxime. The principal effects of pressure, up to 5.28 GPa, on the phase I structure are to close up the voids present in the ambient pressure structure by shortening the intermolecular interactions and moving the non-hydrogen-bonding slabs closer together. The only void in the ambient-pressure structure that is still visible in a space-filling plot at 5.28 GPa is in the middle of the $R_4^4(10)$ hydrogen-bonding ring which binds the salicylaldoxime molecules into dimers.

The pseudo-macrocyclic cavity in the salicylaldoxime dimer has been shown to decrease in size steadily with the application of hydrostatic pressure. This contraction of the cavity size is comparable to the difference in the hole sizes in the copper and nickel salicylaldoxime complex structures. The results suggest that it may be possible to tune the metal complex formation selectivity of the salicylaldoximes using high pressure.

The intermolecular hydrogen bonds and π-π interactions in the structure are compressed at 5.28 GPa to the lower limits of similar contacts at ambient pressure found in a search of the CSD. PIXEL calculations show a concomitant sharp increase in the repulsion energy of these interactions. Phase I is stable up to 5.28 GPa, but beyond this pressure the structure transforms to a new polymorph – salicylaldoxime-II. The phase II structure breaks the $R_4^4(10)$ hydrogen-bonded ring in favour of a $R_2^2(6)$ ring, which only has two hydrogen bonds, in order to improve the packing of the molecules. A CH···O interaction is also replaced by an OH···O hydrogen bond; overall this interaction is actually very slightly destabilising, but the intra- to intermolecular hydrogen-bond conversion enables a pair of molecules to approach one another in order to promote more efficient packing.

2.7 References

Allen, F. H. (2002). *Acta Crystallographica, Section B* **58**, 380-388.

Allen, F. H. & Motherwell, W. D. S. (2002). *Acta Crystallographica, Section B* **58**, 407-422.

Altomare, A., Cascarano, G., Giacovazzo, C., Guagliardi, A., Burla, M. C., Polidori, G. & Camalli, M. (1994). *Journal of Applied Crystallography* **27**, 435-435.

Angel, R. J. (2000). *Reviews in Mineralogy and Geochemistry* **41**, 35-59.

Angel, R. J. (2002). *EOSFIT version 5.2*, *Program for fitting equations of state*. Virginia Tech, Blackburg, VA, USA.

Angel, R. J. (2004). High Pressure Crystallography. NATO Science Series II, edited by A. Katrusiak & P. F. McMillan, pp. 21-36.

Bernstein, J., Davis, R. E., Shimoni, L. & Chang, N.-L. (1995). *Angewandte Chemie, International Edition* **34**, 1555-1573.

Betteridge, P. W., Carruthers, J. R., Cooper, R. I., Prout, K. & Watkin, D. J. (2003). *Journal of Applied Crystallography* **36**, 1487.

Birch, F. (1947). *Physical Review* **71**, 809-824.

Blatov, V. A. (2005). TOPOS Manual. Samara, Russia: Samara State University.

Blatov, V. A. & Shevchenko, A. P. (2003). *Acta Crystallographica, Section A* **59**, 34-44.

Blatov, V. A., Shevchenko, A. P. & Serezhkin, V. N. (1995). *Acta Crystallographica, Section A* **51**, 909-915.

Blatov, V. A., Shevchenko, A. P. & Serezhkin, V. N. (2000). *Journal of Applied Crystallography* **33**, 1193.

Boldyreva, E. V. (2003). *Journal of Molecular Structure* **647**, 159-179.

Boldyreva, E. V. (2004a). NATO Science Series, II: Mathematics, Physics & Chemistry, Vol. 140, edited by A. K. P. F. McMillan, pp. 495-512. Dordrecht, The Netherlands: Kluwer Academic Publishers.

Boldyreva, E. V. (2004b). *Journal of Molecular Structure* **700**, 151-155.

Bruker-Nonius (2006). *SAINT version 7*, *Program for integration of area detector data*. Bruker-AXS, Madison, Wisconsin, USA.

Bruno, I. J., Cole, J. C., Edgington, P. R., Kessler, M., Macrae, C. F., McCabe, P., Pearson, J. & Taylor, R. (2002). *Acta Crystallographica, Section B* **58**, 389-397.

Crystal Impact (2004). *DIAMOND version 3.0*, *Visual crystal structure information system*. Crystal Impact GbR, Postfach 1251, 53002, Bonn, Germany.

Dawson, A., Allan, D. R., Belmonte, S. A., Clark, S. J., David, W. I. F., McGregor, P. A., Parsons, S., Pulham, C. R. & Sawyer, L. (2005). *Crystal Growth & Design* **5**, 1415-1427.

Dawson, A., Allan, D. R., Parsons, S. & Ruf, M. (2004). *Journal of Applied Crystallography* **37**, 410-416.

Dunitz, J. D. & Gavezzotti, A. (2005). *Angewandte Chemie, International Edition* **44**, 1766-1787.

Farrugia, L. J. (1999). *Journal of Applied Crystallography* **32**, 837-838.

Frisch, M. J., Trucks, G. W., Schlegel, H. B., Scuseria, G. E., Robb, M. A., Cheeseman, J. R., Zakrzewski, V. G., Montgomery, J. A. J., Stratmann, R. E., Burant, J. C., Dapprich, S., Millam, J. M., Daniels, A. D., Kudin, K. N., Strain, M. C., Farkas, O., Tomasi, J., Barone, V., Cossi, M., Cammi, R., Mennucci, B., Pomelli, C., Adamo, C., Clifford, S., Ochterski, J., Petersson, G. A., Ayala, P. Y., Cui, Q., Morokuma, K., Malick, D. K., Rabuck, A. D., Raghavachari, K., Foresman, J. B., Cioslowski, J., Ortiz, J. V., Stefanov, B. B., Liu, G., Liashenko, A., Piskorz, P., Komaromi, I., Gomperts, R., Martin, R. L., Fox, D. J., Keith, T., Al-Laham, M. A., Peng, C. Y., Nanayakkara, A., Gonzalez, C., Challacombe, M., Gill, P. M. W., Johnson, B. G., Chen, W., Wong, M. W., Andres, J. L., Head-Gordon, M., Replogle, E. S. & Pople, J. A. (1998). *Gaussian 98 revision A.7*, Gaussian, Inc., Pittsburgh, PA, USA.

Gavezzotti, A. (2005). *Zeitschrift fuer Kristallographie* **220**, 499-510.

Gokel, G. W. (1991). Crown Ethers and Cryptands. Cambridge, UK: The Royal Society of Chemistry.

Hazen, R. M. & Finger, L. W. (1982). Comparative Crystal Chemistry: Temperature, Pressure, Composition and the Variation of Crystal Structure, p. 81. Chichester, New York, USA: John Wiley and Sons.

Hemley, R. J. & Dera, P. (2000). *Reviews in Mineralogy and Geochemistry* **41**, 335-419.

Katrusiak, A. (2004). NATO Science Series, II: Mathematics, Physics and Chemistry, Vol. 140, edited by A. Katrusiak & P. F. McMillan, pp. 513-520. Dordrecht, The netherlands: Kluwer Academic Publishers.

Kordosky, G. A. (2002). *South African Institute of Mining and Metallurgy*, pp. 853-862. Cape Town

Levkin, P. A., Lyssenko, K. A., Schurig, V. & Kostyanovsky, R. G. (2003). *Mendeleev Communications* **3**, 106-108.

Merrill, L. & Bassett, W. A. (1974). *Review of Scientific Instruments* **45**, 290-294.

Merritt, L. L. & Schroeder, E. D. (1956). *Acta Crystallographica* **9**, 194.

Moggach, S. A., Allan, D. R., Clark, S. J., Gutmann, M. J., Parsons, S., Pulham, C. R. & Sawyer, L. (2006). *Acta Crystallographica, Section B* **62**, 296-309.

Moggach, S. A., Allan, D. R., Morrison, C. A., Parsons, S. & Sawyer, L. (2005). *Acta Crystallographica, Section B* **61**, 58-68.

Moggach, S. A., Allan, D. R., Parsons, S., Sawyer, L. & Warren, J. E. (2005). *Journal of Synchrotron Radiation* **12**, 598-607.

Motherwell, W. D. S. (2002). *RPLUTO*, *Program for crystal structure visualisation*. Cambridge Crystallographic Data Centre, Cambridge, UK.

Parsons, S. (2003). *STRAIN*, *Program for calculation of linear strain tensors*. The University of Edinburgh, Edinburgh, UK.

Parsons, S. (2004). *SHADE*, *Program for empirical absorption corrections to high pressure data*. The University of Edinburgh, Edinburgh, United Kingdom.

Pfluger, C. E. & Harlow, R. L. (1973). *Acta Crystallographica, Section B* **29**, 2608-2609.

Piermarini, G. J., Block, S., Barnett, J. D. & Forman, R. A. (1975). *Journal of Applied Physics* **46**, 2774-2780.

Press, W. H., Teukolsky, S. A., Vetterling, W. T. & Flannery, B. P. (1992). Numerical Recipes in Fortran, 2nd ed. Cambridge, UK: Cambridge University Press.

Sheldrick, G. M. (2004). *SADABS Version 2004-1*, *Program for absorption corrections to area detector data*. Bruker-AXS, Madison, Wisconsin, USA.

Slebodnick, C., Zhao, J., Angel, R., Hanson, B. E., Song, Y., Liu, Z. & Hemley, R. J. (2004). *Inorganic Chemistry* **43**, 5245-5252.

Smith, A. G., Tasker, P. A. & White, D. J. (2002). *Coordination Chemistry Reviews* **241**, 61-85.

Spek, A. L. (2004). *PLATON*, *A multipurpose crystallographic tool*. Utrecht University, Utrecht, The Netherlands.

Szymanowski, J. (1993). Hydroxyoximes and Copper Hydrometallurgy. London, UK: CRC Press.

Tasker, P. A., Plieger, P. G. & West, L. C. (2004). Comprehensive Coordination Chemistry II, pp. 759-808.

Watkin, D. J., Pearce, L. & Prout, K. (1993). *CAMERON*, *A molecular graphics package*. Chemical Crystallography Laboratory, University of Oxford, Oxford, England.

Wood, P. A., Forgan, R. S., Parsons, S., Pidcock, E. & Tasker, P. A. (2006). *Acta Crystallographica, Section E* **62**, o3944-o3946.

Chapter 3

The Effect of Pressure and Substituents on the Size of Pseudo-Macrocyclic Cavities in Salicylaldoxime Ligands*

* Wood, P. A., Forgan, R. S., Lennie, A. R., Parsons, S., Pidcock, E., Tasker, P. A., Warren, J. E. (2008). *CrystEngComm*, **10**, 239-251, 2008.

3.1 Synopsis

The crystal structures of four substituted salicylaldoximes have been determined at a range of pressures between ambient pressure and 6.2 GPa. Salicylaldoxime forms a pseudo-macrocyclic cavity, and derivatives of the compound are used as selective ligands in the process of copper solvent extraction. The substituted compounds exhibit a range of cavity sizes both larger and smaller than salicylaldoxime, but each compound shows a decrease in the size of the cavity with pressure and thus an even wider range of cavity sizes can be obtained. This implies that, by application of a substituent along with hydrostatic pressure, one of the ligands may favour nickel over copper at elevated pressure.

3.2 Introduction

The use of hydrostatic pressure as a technique for modifying the local geometry of small molecular crystal structures is a rapidly expanding field. Much recent work has shown that pressure can be used to induce polymorphism (Oswald *et al.*, 2005), adjust intermolecular interactions (Boldyreva, 2004) and tune the size of intermolecular voids (Moggach *et al.*, 2006). The voids found within a crystal structure at ambient conditions have been found to have a significant influence on the effects of pressure, with the primary consequences of compression tending to be reduction of these voids.

The voids, or cavities, in a structure can also be of considerable importance in terms of the properties and reactivity of the compound. Examples of this include nanoporous dipeptide structures that can host organic solvents (Gorbitz, 2002), clathrate compounds which can encapsulate larger molecules (Small, 2003) and crown ethers, such as 18-crown-6 which forms different types of complex with Na^+, K^+ and Rb^+ due to the relative sizes of the ions compared to the intramolecular cavity within the crown ether (Gokel, 1991).

Salicylaldoxime (Scheme 3.1a) forms hydrogen bonded dimers, both in solution and in the solid state, which create a pseudo-macrocyclic cavity within the hydrogen bonded ring motif (Scheme 3.2). The compound can form bis-

salicylaldoximato complexes with transition metal ions by deprotonation of the phenol groups. The bis complex is further stabilised by hydrogen bonding between the two bidentate ligands. Salicylaldoxime is known to be highly selective for complex formation of copper(II) over other transition metal ions due to the compatibility of the ionic radius of Cu^{2+} with the size of the intermolecular cavity within the hydrogen bonded ring (Smith *et al.*, 2003). As a result of this, derivatives of salicylaldoxime are used as solvent extractants in the hydrometallurgical recovery of copper, a process which accounts for around a third of annual production (Kordosky, 2002).

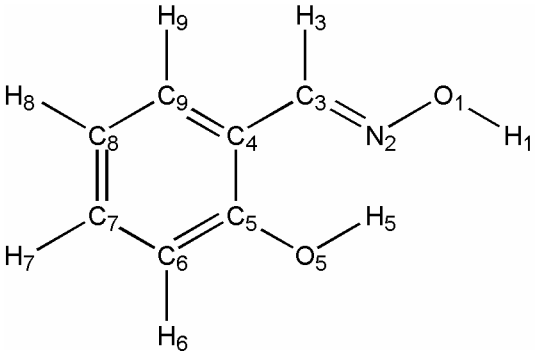

Scheme 3.1a: Chemical structure diagram showing atomic numbering scheme for salicylaldoxime.

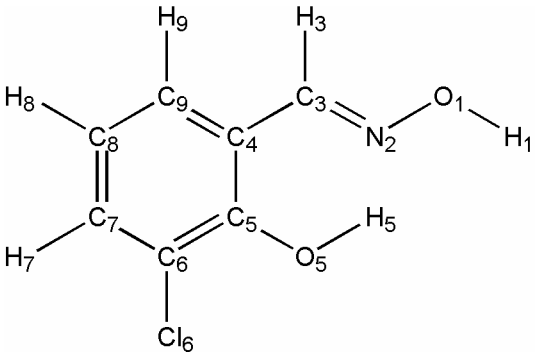

Scheme 3.1b: Chemical structure diagram showing atomic numbering scheme for 3-chlorosalicylaldoxime.

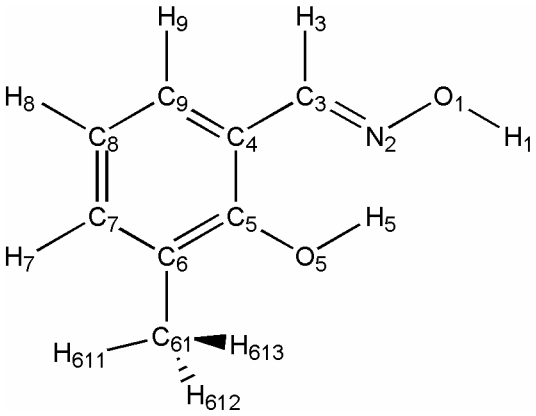

Scheme 3.1c: Chemical structure diagram showing atomic numbering scheme for 3-methylsalicylaldoxime.

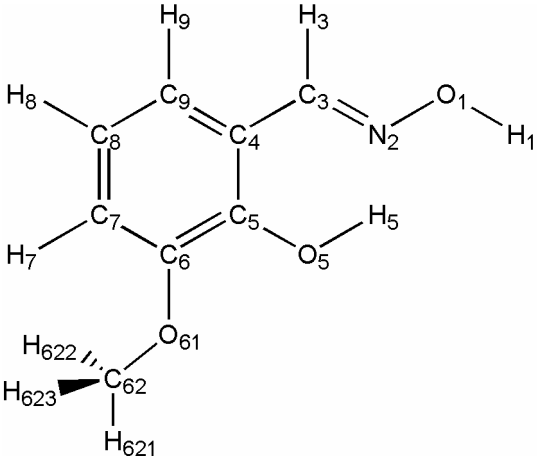

Scheme 3.1d: Chemical structure diagram showing atomic numbering scheme for 3-methoxysalicylaldoxime.

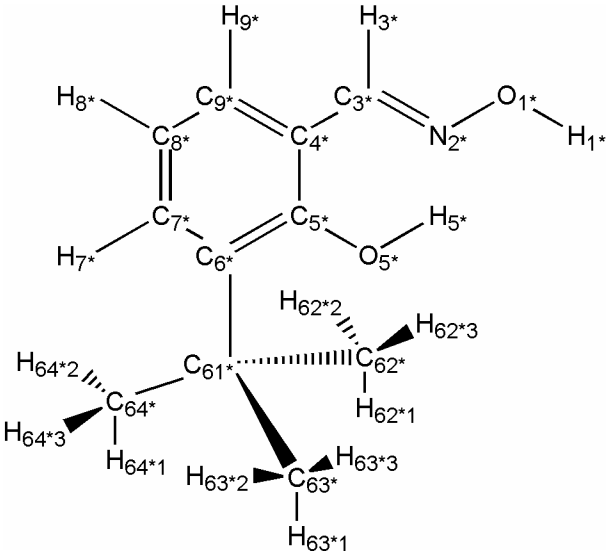

Scheme 3.1e: Chemical structure diagram showing atomic numbering scheme for 3-*tert*-butylsalicylaldoxime (*=1 or 2 for phase I and is not present for phase II).

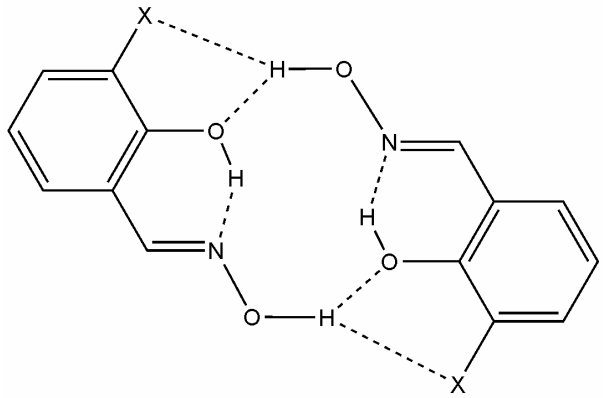

Scheme 3.2: Hydrogen bonding within the pseudo-macrocyclic dimer showing potential interactions with the 3-substituent (X).

In the study of phase I of salicylaldoxime we showed that the size of the pseudo-macrocyclic cavity formed in the centre of the hydrogen bonded dimer can be reduced by the application of pressure (Chapter 2, Figure 2.8). The ligands used industrially for copper solvent extraction are salicylaldoxime derivatives incorporating substituents at different points of the molecule, principally to impart kerosene solubility. Such substituents can also influence extractant strength and selectivity (Szymanowski, 1993). In this chapter we consider how the effects of the application of pressure and of changing the nature of substituents close to the metal binding site influence the structure in the solid state and the size of the pseudo-macrocyclic cavity available to a metal ion. The compounds studied were 3-chlorosalicylaldoxime, 3-methylsalicylaldoxime, 3-methoxysalicylaldoxime and 3-*tert*-butylsalicylaldoxime and results are compared with those for unsubstituted salicylaldoxime (Chapter 2).

3.3 Experimental

Note: All of the syntheses and crystallisations, except for the high pressure in-situ crystallisation of 3-chlorosalicylaldoxime, were performed by Ross Forgan of the University of Edinburgh. The details are included here for the sake of completeness.

3.3.1 General comments

All solvents and reagents were used as received from Aldrich and Fisher. ^{1}H and ^{13}C NMR were obtained using a Bruker AC250 spectrometer at ambient temperature. Chemical shifts (δ) are reported in parts per million (ppm) relative to internal standards. Hydrogen numbering in ^{1}H NMR data refers to Scheme 3.1a-e. Fast atom bombardment mass spectrometry (FABMS) was carried out using a Kratos MS50TC spectrometer with a thioglycerol matrix. Analytical data were obtained using a Carlo Erba CHNS analyser at the EaStCHEM Microanalytical Service.

3.3.2 Synthesis

3-Methyl-, 3-methoxy-, 3-chloro- and 3-*tert*-butylsalicylaldoxime (Scheme 3.1) were synthesised according to the known method (Stepniak-Biniakiewicz, 1980).

Oximation General Procedure. Equivalents of KOH and $NH_2OH.HCl$ were dissolved separately in EtOH, mixed thoroughly and a white KCl precipitate removed by filtration. The filtrate was added to the precursor aldehyde, refluxed for 3 hr and the solvent removed *in vacuo*. The residue was redissolved in $CHCl_3$, washed with water 3 times, dried over $MgSO_4$ and the solvent removed *in vacuo* to yield the crude product.

3-Chlorosalicylaldoxime. Using the general procedure, 3-chlorosalicylaldehyde (Hofslokken & Skattebol, 1999) (0.431 g, 2.75 mmol) was reacted with KOH (0.169 g, 3.0 mmol) and $NH_2OH.HCl$ (0.209 g, 3.0 mmol) to yield a white powder (0.376 g, 80 %). (Anal. Calc. for $C_7H_6ClNO_2$: C, 49.0; H, 3.5; N, 8.2. Found: C, 49.4; H, 3.1; N, 8.0 %); ^{1}H NMR (250 MHz, $CDCl_3$): δ_H (ppm) 6.78 (t, 1H, Ar-H8), 7.05 (dd, 1H, Ar-H9), 7.30 (dd, 1H, Ar-H7), 8.15 (s, 1H, ArCHN); ^{13}C NMR (63 MHz, $CDCl_3$) δ_C (ppm) 117.0 (1C, aromatic **C**-CHN), 121.0 (1C, aromatic **C**H), 122.0 (1C, aromatic **C**-Cl), 129.5 (1C, aromatic **CH**), 132.0 (1C, aromatic **C**H), 153.0 (1C, Ar**C**HN), 154.0 (1C, aromatic **C**-OH; FABMS m/z 172 $(MH)^+$, 100 %.

3-Methylsalicylaldoxime. Using the general procedure, 3-methylsalicylaldehyde (Aldrich, 1.000 g, 7.35 mmol) was reacted with KOH (0.425 g, 7.6 mmol) and $NH_2OH.HCl$ (0.530 g, 7.6 mmol) to yield a white powder, which was recrystallised from hexane to give colourless needles (0.889 g, 80 %). (Anal. Calc. for $C_8H_9NO_2$: C, 63.6; H, 6.0; N, 9.3. Found: C, 63.2; H, 6.0; N, 9.4%); ^{1}H NMR (250 MHz, $CDCl_3$): δ_H (ppm) 2.20 (s, 3H, $ArCH_3$), 6.75 (t, 1H, Ar-H8), 6.95 (dd, 1H, Ar-H7), 7.08 (dd, 1H, Ar-H9); ^{13}C NMR (63 MHz, $CDCl_3$) δ_C (ppm) 14.5 (1C, Ar**C**H_3), 115.0 (1C, aromatic **C**-CHN), 118.5 (1C, aromatic **C**H), 125.0 (1C, aromatic **C**-CH_3), 127.5 (1C, aromatic **C**H), 132.0 (1C, aromatic **C**H), 152.5 (1C, Ar**C**HN), 154.5 (1C, aromatic **C**-OH); FABMS m/z 152 $(MH)^+$, 83 %.

3-Methoxysalicylaldoxime (O-vanillin oxime). Using the general procedure, 3-methoxysalicylaldehyde (Aldrich, 3.00 g, 19.7 mmol) was reacted with KOH (1.35 g, 24.0 mmol) and $NH_2OH.HCl$ (1.42 g, 20.4 mmol) to yield an off-white powder, which was recrystallised from H_2O to give white needles (2.61 g, 79 %). (Anal. Calc. for $C_8H_9NO_3$: C, 57.5; H, 5.4; N, 8.4. Found: C, 57.4; H, 5.6; N, 8.6 %); ^{1}H NMR (250 MHz, $CDCl_3$): δ_H (ppm) 4.12 (s, 3H, OCH_3), 7.08 (m, 3H, 3 x ArH), 8.42 (s, 1H, ArCHN); ^{13}C NMR (63 MHz, $CDCl_3$) δ_C (ppm) 56.5 (1C, O**C**H3), 113.0 (1C, aromatic **C**H), 117.0 (1C, aromatic C-**C**HN), 120.0 (1C, aromatic **C**H), 125.0 (1C, aromatic **C**H), 146.5 (1C, aromatic **C**-OH), 147.5 (1C, aromatic **C**-OCH_3), 153.0 (1C, Ar**C**HN); FABMS m/z 168 $(MH)^+$, 91 %.

3-*tert*-Butylsalicylaldoxime. Using the general procedure, 3-*tert*-butylsalicylaldehyde (Aldrich, 2.50 g, 14.0 mmol) was reacted with KOH (1.35 g, 24.0 mmol) and $NH_2OH.HCl$ (1.42 g, 20.4 mmol) to yield a white powder, which was recrystallised from hexane to give white fluffy needles (2.34 g, 86 %). (Anal. Calc. for $C_{11}H_{15}NO_2$: C, 68.4; H, 7.8; N, 7.3. Found: C, 68.4; H, 8.3; N, 7.4 %); ^{1}H NMR (250 MHz, $CDCl_3$): δ_H (ppm) 1.34 (s, 9H, $C(CH_3)_3$), 6.78 (t, 1H, Ar-H8*), 6.95 (dd, 1H, Ar-H7*), 7.22 (dd, 1H, Ar-H9*); ^{13}C NMR (63 MHz, $CDCl_3$) δ_C (ppm) 29.5 (3C, C(**C**$H_3)_3$), 35.5 (1C, **C**$(CH_3)_3$), 117.0 (1C, aromatic **C**-CHN), 119.5 (1C, aromatic **C**H), 129.5 (1C, aromatic **C**H), 130.0 (1C, aromatic **C**H), 138.0 (1C, aromatic **C**-$C(CH_3)_3$), 154.5 (1C, Ar**C**HN), 157.0 (1C, aromatic **C**-OH); FABMS m/z 194 $(MH)^+$, 100 %.

3.3.3 Crystal growth

The samples were recrystallised by slow evaporation of a concentrated solution of hexane/chloroform (for 3-Me- and 3-^{t}Bu-salicylaldoxime), chloroform (for 3-OMe-salicylaldoxime) or dichloromethane (for 3-Cl-salicylaldoxime). A colourless block of each compound was cut to the required dimensions for high pressure crystallography.

Initial pressure experiments on 3-chlorosalicylaldoxime showed that the crystals were made up of layers, and upon application of pressure the crystals were prone to shearing in the direction of these layers. This meant that it was very difficult to obtain high-quality compression data when using a single crystal cut from a larger sample. A crystal was therefore grown *in-situ* from solution by the application of hydrostatic pressure. A saturated solution in 4:1 methanol/ethanol was loaded into a diamond-anvil cell (see below). Pressure was increased to 0.2 GPa (at room temperature), leading to formation of several crystallites within the cell. The temperature was then increased until the polycrystalline sample began to redissolve. The temperature of the cell was then cycled around this elevated temperature in order to reduce the number of crystallites. Allowing the cell to cool to room temperature yielded a single crystal. Diffraction data were collected on the sample which could be indexed on essentially the same unit cell as the ambient pressure structure [monoclinic, a = 13.076 (5), b = 3.8514 (6), c = 14.234 (3) Å, β = 91.75 (2) ˚ and V = 716.5 (3) Å^3].

3.3.4 High pressure crystallography

Crystal structures at ambient temperature and pressure have been reported separately (Forgan *et al.*, 2007).

High-pressure experiments were carried out using a Merrill-Bassett diamond anvil cell (half-opening angle 40°), equipped with brilliant-cut diamonds with 600μm culets and a tungsten gasket (Merrill & Bassett, 1974). A 1:1 mixture of *n*-pentane and isopentane was used as a hydrostatic medium for 3-methyl-, 3-methoxy- and 3-*tert*-butylsalicylaldoxime; the 4:1 methanol/ethanol mother liquor from crystal growth (see above) was used for 3-chlorosalicylaldoxime. Due to the high volatility of the *n*-pentane/isopentane solution, the cells loaded with this medium were cooled in dry ice prior to loading. A small ruby chip was also loaded into each cell as the pressure calibrant, with the ruby fluorescence method being used to measure the pressure (Piermarini *et al.*, 1975). In the case of 3-chlorosalicylaldoxime, the crystal scattered relatively strongly and so data were collected on a Bruker-Nonius APEX-II diffractometer with graphite-monochromated, sealed-tube Mo-Kα radiation (λ =

0.71073 Å). For the remaining crystals diffraction data were collected on a Bruker-Nonius APEX-II diffractometer with silicon-monochromated synchrotron radiation (λ = 0.4577 Å for the 3-Me- and λ = 0.4869 Å for the 3-MeO- and 3-*t*-Bu-compounds) on Station 9.8 at the SRS, Daresbury Laboratory.

Data collection and processing procedures for the high-pressure experiments followed previous studies (Dawson *et al.*, 2004, Moggach *et al.*, 2005). Integrations were carried out using the program *SAINT* (Bruker-Nonius, 2006), and absorption corrections with the programs *SHADE* (Parsons, 2004) and *SADABS* (Sheldrick, 2004). Data collections were taken in approximately 1.0 GPa steps from between 0.2 – 0.5 GPa up to the highest pressure at which usable data could be collected - between 5.0 and 6.2 GPa. Determination of the cell constants of 3-*tert*-butylsalicylaldoxime at 1.0 GPa showed that a single-crystal to single-crystal phase transition had occurred to a new polymorph, which we have designated 3-*tert*-butylsalicylaldoxime-II. The phase transition did not appear to cause significant degradation of the crystal quality, so the compression study was continued up to the limits of the hydrostatic medium. No phase transitions were found in the single crystal compression studies of the 3-chloro, 3-methyl or 3-methoxy-salicylaldoximes in the pressure ranges studied.

Refinements of the compressed forms of each compound were carried out starting from the co-ordinates determined at ambient pressure. The structure of the new phase of the *t*-butyl derivative (3-*tert*-butylsalicylaldoxime-II) was solved by direct methods using the program *SIR-92* and refinements of the subsequent high-pressure datasets were carried out starting from these coordinates. Refinements were carried out against $|F|^2$ using all data (*CRYSTALS*) (Betteridge *et al.*, 2003). Extreme outlier reflections (e.g. those partially cut-off by the pressure cell, or overlapping with diamond reflections or Be powder lines) were omitted from the refinement. Listings of crystal and refinement data are given in Tables 3.1a-d.

Crystal structures were visualized using the programs *Mercury* (Bruno *et al.*, 2002) and *DIAMOND* (Crystal Impact, 2004). Analyses were carried out using *PLATON* (Spek, 2003), as incorporated in the *WinGX* suite (Farrugia, 1999). Searches of the Cambridge Structural Database (Allen, 2002, Allen & Motherwell,

2002) utilized the program *ConQuest* and version 5.27 of the database with updates up to August 2006. Equation-of-state calculations were carried out with *EOSFIT* (Angel, 2000).

	Ambient	1.6 GPa	2.4 GPa	3.4 GPa	5.0 GPa
Formula	$C_7H_6ClNO_2$	$C_7H_6ClNO_2$	$C_7H_6ClNO_2$	$C_7H_6ClNO_2$	$C_7H_6ClNO_2$
M_r	171.58	171.58	171.58	171.58	171.58
Cell setting, space group	Monoclinic, $P2_1/c$	Monoclinic, $P2_1/c$	Monoclinic, $P2_1/c$	Monoclinic, $P2_1/c$	Monoclinic, $P2_1/c$
a, b, c (Å)	13.1506 (18), 3.8859 (6), 14.3115 (19)	12.843 (3), 3.6613 (3), 13.7921 (16)	12.748 (2), 3.5954 (3), 13.6496 (15)	12.652 (4), 3.5295 (4), 13.509 (2)	12.544 (6), 3.4424 (8), 13.365 (5)
β (°)	91.548 (10)	92.603 (13)	93.115 (13)	93.64 (2)	94.44 (4)
V (Å^3)	731.08 (18)	647.88 (16)	624.71 (15)	602.0 (2)	575.4 (4)
Z	4	4	4	4	4
D_x (Mg m^{-3})	1.559	1.759	1.824	1.893	1.981
Measured, independent and observed reflections	10310, 1955, 1127	3158, 440, 348	3218, 415, 341	2720, 416, 319	3081, 351, 231
R_{int}	0.018	0.064	0.060	0.076	0.098
$R[F^2 > 2\sigma(F^2)]$, $wR(F^2)$, S	0.033, 0.083, 0.80	0.058, 0.158, 1.02	0.046, 0.121, 1.03	0.078, 0.227, 1.02	0.045, 0.123, 1.00
No. of reflections	1955 reflections	440 reflections	415 reflections	409 reflections	344 reflections
Parameters	106	106	106	106	106
$\Delta\rho_{max}$, $\Delta\rho_{min}$ (e Å^{-3})	0.21, –0.12	0.26, –0.22	0.25, –0.22	0.36, –0.40	0.33, –0.33

(a)

	Ambient	1.3 GPa	2.2 GPa	3.5 GPa	4.2 GPa	4.9 GPa	5.6 GPa
Formula	$C_8H_9NO_2$	$C_8H_9NO_2$	$C_8H_9NO_2$	$C_8H_9NO_2$	$C_8H_9NO_2$	$C_8H_9NO_2$	$C_8H_9NO_2$
M_r	151.16	151.16	151.16	151.16	151.16	151.16	151.16
Cell setting, space group	Monoclinic, $P2_1/c$	Monoclinic, $P2_1/c$	Monoclinic, $P2_1/c$	Monoclinic, $P2_1/c$	Monoclinic, $P2_1/c$	Monoclinic, $P2_1/c$	Monoclinic, $P2_1/c$
a, b, c (Å)	13.249 (4), 3.9513 (11), 14.402 (4)	12.998 (3), 3.6988 (5), 13.9167 (16)	12.941 (4), 3.6146 (5), 13.7188 (17)	12.878 (4), 3.5363 (5), 13.5218 (16)	12.831 (3), 3.5096 (4), 13.4462 (13)	12.766 (7), 3.4872 (9), 13.382 (3)	12.750 (4), 3.4482 (6), 13.2910 (18)
β (°)	90.324 (4)	90.99 (2)	91.47 (2)	91.88 (2)	92.10 (2)	92.27 (4)	92.45 (2)
V (Å^3)	754.0 (4)	669.0 (2)	641.5 (2)	615.5 (2)	605.11 (16)	595.2 (4)	583.8 (2)
Z	4	4	4	4	4	4	4
D_x (Mg m^{-3})	1.332	1.501	1.565	1.631	1.659	1.687	1.720
Measured, independent & observed reflections	6640, 1786, 627	6638, 878, 502	6282, 822, 517	8856, 1402, 654	8863, 1415, 618	8106, 1373, 673	7902, 1281, 623
R_{int}	0.041	0.233	0.157	0.199	0.271	0.222	0.242
$R[F^2 > 2\sigma(F^2)]$, $wR(F^2)$, S	0.049, 0.131, 0.69	0.076, 0.212, 1.02	0.068, 0.196, 1.02	0.062, 0.195, 1.00	0.076, 0.240, 0.96	0.099, 0.318, 0.93	0.059, 0.174, 1.02
Reflections	1786 refs	876 refs	818 refs	1395 refs	1404 refs	1371 refs	1267 refs
Parameters	106	106	106	107	106	107	106
$\Delta\rho_{max}$, $\Delta\rho_{min}$ (e Å^{-3})	0.14, –0.17	0.22, –0.23	0.32, –0.19	0.20, –0.20	0.23, –0.32	0.44, –0.38	0.18, –0.22

(b)

	Ambient	1.4 GPa	2.7 GPa	4.4 GPa	5.3 GPa	6.0 GPa
Formula	$C_8H_9NO_3$	$C_8H_9NO_3$	$C_8H_9NO_3$	$C_8H_9NO_3$	$C_8H_9NO_3$	$C_8H_9NO_3$
M_r	167.16	167.16	167.16	167.16	167.16	167.16
Cell setting, space group	Orthorhombic, *Pbca*	Orthorhombic, *Pbca*	Orthorhombic, *Pbca*	Orthorhombic, *Pbca*	Orthorhombic, *Pbca*	Orthorhombic, *Pbca*
a, *b*, *c* (Å)	13.9108 (5), 7.1936 (3), 15.6965 (6)	13.0765 (5), 7.0982 (4), 15.2455 (5)	12.5814 (4), 7.0265 (4), 15.0188 (4)	12.3113 (5), 6.9800 (4), 14.8947 (5)	12.1340 (13), 6.9421 (11), 14.8065 (13)	12.0702 (5), 6.9200 (5), 14.7703 (5)
V (Å^3)	1570.73 (11)	1415.08 (11)	1327.71 (9)	1279.94 (10)	1247.2 (3)	1233.70 (11)
Z	8	8	8	8	8	8
D_x (Mg m^{-3})	1.414	1.569	1.672	1.735	1.780	1.800
Measured, independent & observed reflections	17158, 1615, 793	12848, 1160, 733	12227, 1090, 743	12201, 1425, 890	11069, 1033, 737	11243, 1022, 693
R_{int}	0.027	0.117	0.106	0.110	0.111	0.097
$R[F^2 > 2\sigma(F^2)]$, $wR(F^2)$, S	0.030, 0.126, 1.13	0.046, 0.153, 0.94	0.041, 0.119, 0.90	0.049, 0.162, 0.87	0.048, 0.144, 0.85	0.042, 0.111, 0.90
Reflections	1615 reflections	1155 reflections	1087 reflections	1424 reflections	1029 reflections	1022 reflections
Parameters	115	116	115	115	116	115
$\Delta\rho_{max}$, $\Delta\rho_{min}$ (e Å^{-3})	0.16, –0.12	0.15, –0.17	0.15, –0.18	0.25, –0.19	0.24, –0.24	0.20, –0.17

(c)

	Ambient	0.2 GPa	1.0 GPa	2.3 GPa	3.4 GPa	4.6 GPa	6.2 GPa
Formula	$C_{11}H_{15}NO_2$	$C_{11}H_{15}NO_2$	$C_{11}H_{15}NO_2$	$C_{11}H_{15}NO_2$	$C_{11}H_{15}NO_2$	$C_{11}H_{15}NO_2$	$C_{11}H_{15}NO_2$
M_r	193.25	193.25	193.25	193.25	193.25	193.25	193.25
Cell setting, space group	Triclinic, *P*-1	Triclinic, *P*-1	Monoclinic, *I*2/*a*	Monoclinic, *I*2/*a*	Monoclinic, *I*2/*a*	Monoclinic, *I*2/*a*	Monoclinic, *I*2/*a*
a, *b*, *c* (Å)	6.6132 (3), 13.1087 (6), 13.6382 (6)	6.5597 (7), 12.8532 (9), 13.479 (2)	14.811 (3), 6.4564 (7), 19.759 (4)	14.5745 (13), 6.3779 (4), 19.0922 (18)	14.3941 (14), 6.3329 (4), 18.7250 (19)	14.271 (4), 6.3030 (9), 18.459 (5)	14.101 (3), 6.2699 (6), 18.158 (3)
α, β, γ (°)	68.762(3), 76.739(3), 79.733(3)	69.311(10), 76.054(10), 79.035(6)	90, 94.060 (8), 90	90, 94.882 (4), 90	90, 95.325 (5), 90	90, 95.590 (15), 90	90, 95.817 (10), 90
V (Å^3)	1066.71 (9)	1024.9 (2)	1884.7 (5)	1768.3 (3)	1699.5 (3)	1652.5 (7)	1597.1 (4)
Z	4	4	8	8	8	8	8
D_x (Mg m^{-3})	1.203	1.252	1.362	1.452	1.510	1.553	1.607
Measured, indep. & obs. refs	23029, 4351, 2393	8650, 1697, 875	8727, 1163, 630	8098, 1055, 628	7914, 979, 637	7728, 920, 569	7429, 791, 510
R_{int}	0.050	0.097	0.125	0.125	0.106	0.119	0.110
$R[F^2 > 2\sigma(F^2)]$, $wR(F^2)$, S	0.054, 0.134, 0.85	0.062, 0.200, 0.92	0.062, 0.206, 0.96	0.064, 0.225, 0.98	0.056, 0.184, 0.96	0.067, 0.239, 0.98	0.053, 0.163, 0.95
Reflections	4351 refs	1688 refs	1163 refs	1055 refs	979 refs	918 refs	790 refs
Parameters	265	265	134	134	134	134	134
$\Delta\rho_{max}$, $\Delta\rho_{min}$ (e Å^{-3})	0.17, –0.15	0.12, –0.13	0.16, –0.16	0.23, –0.26	0.18, –0.20	0.24, –0.27	0.16, –0.17

(d)

Table 3.1: Crystallographic data at increasing pressures for (a) 3-chlorosalicylaldoxime (ambient to 5.0 GPa), (b) 3-methylsalicylaldoxime (ambient to 5.6 GPa), (c) 3-methoxysalicylaldoxime (ambient to 6.0 GPa) and (d) 3-*tert*-butylsalicylaldoxime (ambient to 6.2 GPa).

The numbering schemes used (Scheme 3.1a-e) are the same for each compound. The oxime group is formed by H1-O1-N2-C3, and the hydroxyl group by O5H5; in the case of the two molecules comprising the asymmetric unit of 3-*tert*-butylsalicylaldoxime-I these labels are augmented by '1' or '2' (O51-H51, O52-H52 etc.).

3.3.5 PIXEL calculations

The final crystal structures obtained were used to calculate the molecular electron density at each pressure by standard quantum chemical methods using the program *GAUSSIAN98* (Frisch *et al.*, 1998) with the MP2/6-31G** basis set. H-atom distances were set to standard neutron values (C-H = 1.083 Å, O-H = 0.983 Å). The electron density model of the molecule was then analysed using the program package *OPiX* (Gavezzotti, 2003, 2005b) which allows the calculation of dimer and lattice energies. The output from these calculations yields a total energy and a breakdown into its electrostatic, polarisation, dispersion and repulsion components (Dunitz & Gavezzotti, 2005).

3.4 Results

3.4.1 The structures of the substituted salicylaldoximes at ambient pressure

3-Methyl-, 3-methoxy- and 3-chlorosalicylaldoxime all crystallise with one molecule in the asymmetric unit, while the asymmetric unit of 3-*tert*-butylsalicylaldoxime-I contains two molecules. Prior to this work only one of the four compounds studied, 3-methoxysalicylaldoxime, had been crystallographically characterized (Xu *et al.*, 2004). Each of these structures exhibits intramolecular phenolic O5*-H5*…N2* hydrogen bonds and intermolecular oximic O1*-H1*…O5* hydrogen bonds (where * = 1 or 2 for 3-*tert*-butylsalicylaldoxime). The latter form a dimer motif across an inversion centre (Figure 3.1) in a similar manner to that seen in salicylaldoxime (Chapter 2, Scheme 2.2a) for which the graph-set descriptor is $R_4^4(10)$ (Bernstein *et al.*, 1995).

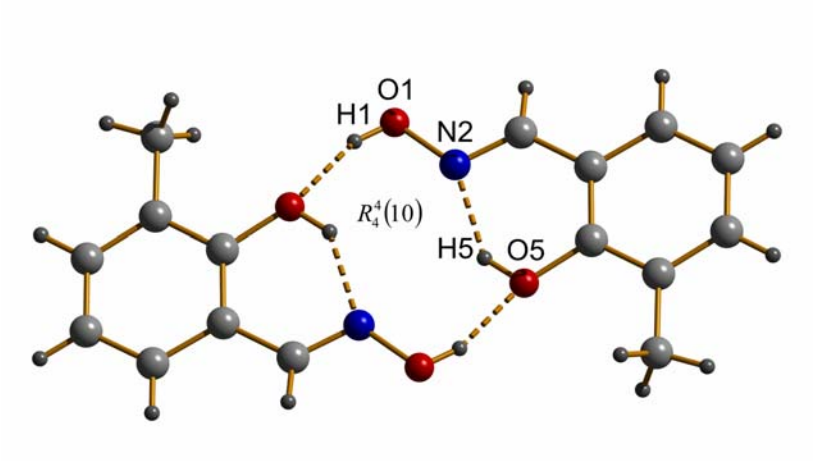

Figure 3.1: The hydrogen-bonded $R_4^4(10)$ ring motif formed across an inversion centre in the structure of 3-methylsalicylaldoxime at ambient pressure. The colour scheme is red: oxygen, blue: nitrogen, light-grey: carbon and dark-grey: hydrogen.

The salicylaldoxime molecule is essentially planar in each structure, though the perpendicular distance between the two molecules of the $R_4^4(10)$ dimer varies. The distances between the least squares planes of the two hydrogen bonded salicylaldoxime molecules are 0.967, 1.122, 0.836, 0.730 and 0.404 Å for 3-chlorosalicylaldoxime, 3-methylsalicylaldoxime, 3-methoxysalicylaldoxime and the two different dimers in 3-*tert*-butylsalicylaldoxime, respectively.

The structures of 3-chlorosalicylaldoxime and 3-methylsalicylaldoxime have similar cell dimensions and are almost isostructural. The $R_4^4(10)$ dimers are stacked *via* cell-translations along [010] to form π-π contacts between phenyl groups [stacking distance = 3.464 (1) Å and 3.533 (2) Å for 3-chloro and 3-methylsalicylaldoxime, respectively], which connect the dimers into ribbons running in the direction of the *b*-axis. The ribbons are then held together by C3H3…O1 interactions [C3…O1 = 3.583 (3) Å and 3.722 (3) Å for 3-chloro and 3-methylsalicylaldoxime respectively] to form slabs in the (100) plane. In the structure of 3-methylsalicylaldoxime the slabs interact only through weak van der Waals contacts and are arranged so that H…H contacts are approximately equidistant (Figure 3.2a). The 3-chlorosalicylaldoxime structure, however, shows a shifting of the slabs with respect to the methyl form in order to optimise the CH…Cl contacts in the structure, two of which are formed between the slabs (Figure 3.2b). The packing

of the 3-chloro form includes three CH…Cl intermolecular interactions of similar length [C…Cl = 3.626 (2), 3.661 (2), 3.699 (2) Å] and two slightly longer CH…Cl contacts [C…Cl = 4.027 (2) and 4.200 (2) Å].

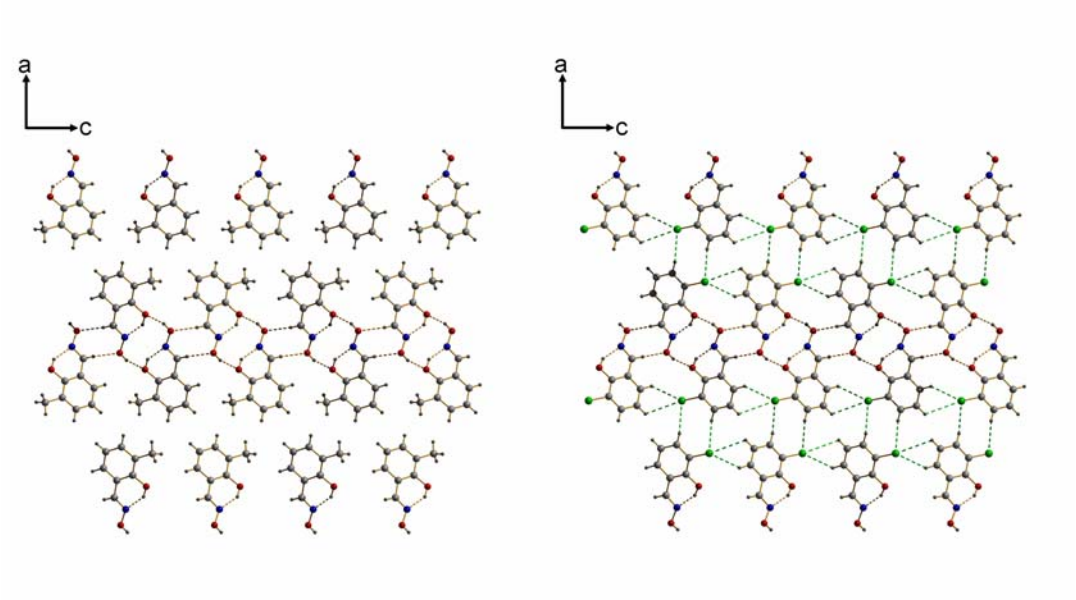

(a) (b)

Figure 3.2: The structure of 3-methylsalicylaldoxime (a) and 3-chlorosalicylaldoxime (b) at ambient pressure as viewed along the *b*-axis. This view illustrates the similarity and differences in the formation of slabs in these crystal structures. Hydrogen bonds are shown as dashed yellow lines and close CH…Cl contacts are shown as dashed green lines. The colour scheme is the same as in Fig. 3.1 with the addition of green: chlorine.

3-Methoxysalicylaldoxime also contains a π-π stacking motif between phenyl rings. In this structure the stacking molecules are related by an inversion centre, and each molecule interacts with only one other in this fashion, rather than in the infinite stack arrangement seen in salicylaldoxime, 3-chlorosalicylaldoxime and 3-methylsalicylaldoxime. The other side of the phenyl ring forms a CH…π interaction with the phenyl hydrogen atoms of an adjacent molecule; repetition of this motif generates a herringbone-like pattern (Figure 3.3). The hydrogen bonded dimer and the stacking motif combine to form ribbons which run along the *b*-axis; the ribbons are then connected *via* the CH…π interactions into slabs in the (001) plane. The slabs then interact with each other through C3H3…O1 interactions [C3…O1 = 3.368 (3) Å].

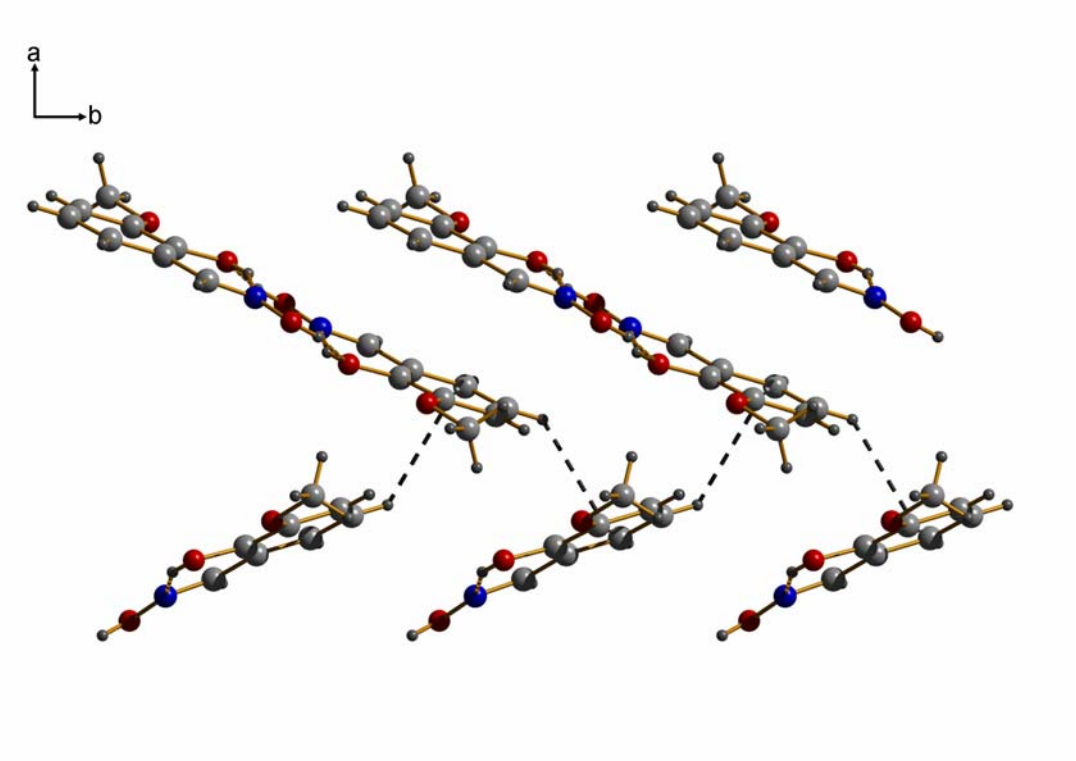

Figure 3.3: The structure of 3-methoxysalicylaldoxime at ambient pressure as viewed along the *c*-axis. This view illustrates the stacking interactions between the dimer units and the CH…π interactions (shown as dashed lines) in the structure which form a herringbone-like pattern. The colour scheme is the same as in Fig. 3.1.

The structure of 3-*tert*-butylsalicylaldoxime contains two molecules in the asymmetric unit and has the space group *P*-1. Each symmetry-independent molecule forms a hydrogen bonded dimer across an inversion centre, and exhibits a π-π stacking interaction with a molecule related by another inversion centre (Figure 3.4). Like the 3-methoxy substituted form, 3-*tert*-butylsalicylaldoxime only forms a stacking interaction on one side of the phenyl ring and is involved in a CH…π interaction on the other side, in this case with the *tert*-butyl group of the other molecule in the asymmetric unit. The hydrogen bonded dimer and stacking interactions again form ribbons, which in this case run along the *a*-axis, and the ribbons are then connected to each other *via* the CH…π interactions to form slabs in the (0-11) plane. These slabs interact with each other through long CH…O interactions [C31…O12 = 3.629 (3) Å and C32…O11 = 3.611 (3) Å].

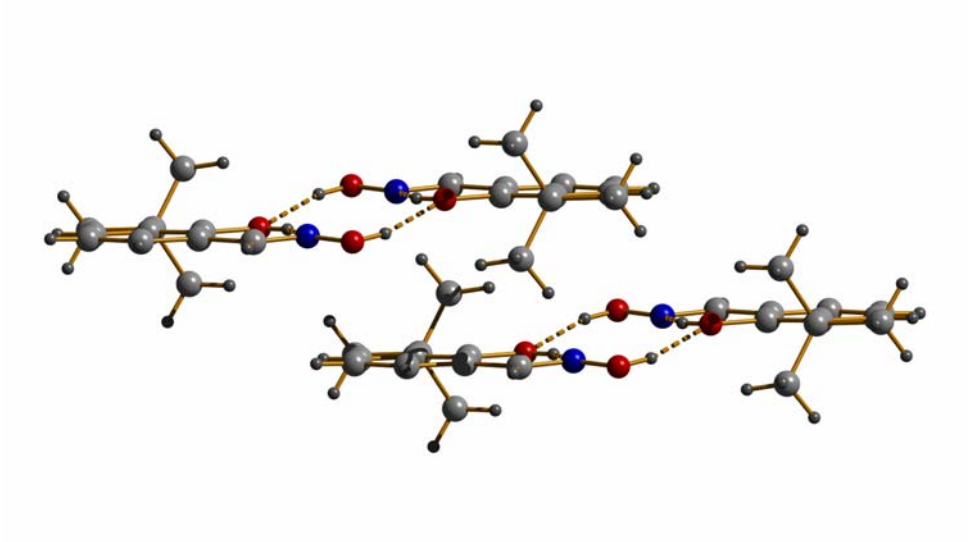

Figure 3.4: The structure of 3-*tert*-butylsalicylaldoxime-I at ambient pressure showing the π-π stacking interaction between two hydrogen-bonded dimers for one of the crystallographically independent molecules. The colour scheme is the same as in Fig. 3.1.

3.4.2 The phase transition in 3-tert-butylsalicylaldoxime

The phase transition from 3-*tert*-butylsalicylaldoxime-I to 3-*tert*-butylsalicylaldoxime-II occurs between 0.2 and 1.0 GPa and proceeds from one single crystal to another single crystal. The space group changes from *P*-1 to *I*2/*a*, the two crystallographically independent molecules of the triclinic phase becoming equivalent after the phase transition. The non-covalent interaction motifs of the structure remain essentially the same through the phase transition with the structure retaining the $R_4^4(10)$ hydrogen bonded dimer motif and the π-π stacking. These two intermolecular interactions form ribbons as in the ambient phase, but these now run along the crystallographic *b*-axis. The independent CH…π interactions of the triclinic phase are averaged with the distances from the closest hydrogen to the plane of the phenyl ring changing from 2.79 and 2.63 Å in the 0.2 GPa phase I structure to 2.69 Å in the 1.0 GPa phase II structure. The ribbons are connected through these CH…π contacts in the high pressure structure to form slabs in the (100) plane. The C3H3…O1 interactions between the slabs persist through the phase transition, though the C…O distances are shorter [C3…O1 = 3.432 (7) Å].

3.4.3 The response to pressure of the substituted salicylaldoximes

The effect of pressure on the substituted oximes is anisotropic, the changes in unit cell dimensions with pressure are given in Tables 3.1a-d. The bulk moduli (K_0) calculated using a Birch-Murnaghan equation-of-state (Birch, 1947, Angel *et al.*, 2000) are 12.1 (4), 12.2 (5), 14.2 (6) and 15.6 (6) GPa respectively for the chloro-, methyl-, methoxy- and *t*-butyl derivatives, compared to the value of 13.3 (4) GPa calculated for salicylaldoxime itself. The variation in unit cell volumes is therefore fairly consistent across this series of compounds. Molecular solids generally have K_0 < 30 GPa and a useful comparison can be made from the following K_0 values (GPa): $Ru_3(CO)_{12}$ 6.6, NaCl 25, quartz 37, ceramics 50–300 and diamond 440 (Slebodnick *et al.*, 2004).

The changes in non-covalent interaction geometries with pressure for the series of compounds are shown in Table 3.2. Consistently across the series of compounds the least compressible interaction is the intramolecular phenolic OH…N hydrogen bonding interaction (O…N distance decreases by between 1.5 and 2.2 %). The other conventional hydrogen bond in the structures, the oximic intermolecular OH…O interaction, is more compressible (the O…O distance decreases by between 4.7 and 6.5 %). These hydrogen bonding interactions retain roughly the same donor-hydrogen-acceptor angles with compression, so the conformation of the hydrogen bonding ring in each structure remains essentially unchanged. The deviation from planarity of the $R_4^4(10)$ rings is also insensitive to pressure throughout the series (e.g. the interplanar distance in 3-methylsalicylaldoxime is 1.122 Å at ambient pressure and 1.149 at 5.6 GPa; corresponding data for the 3-chloro derivative are 0.967 and 1.026 Å at 5 GPa).

The most compressible of the three non-covalent interactions in the structures is the π-π stacking interaction, which can be described by the perpendicular distance between the least-squares mean plane of one phenyl ring to the centroid of another (stacking distances decrease by between 11.2 and 14.9 %).

Pressure/GPa	0.0	1.6	2.4	3.4	5.0
O5H5..N2[i]					
H5..N2	1.85	1.80	1.79	1.77	1.79
O5..N2	2.589(2)	2.562(13)	2.550(11)	2.550(16)	2.538(15)
<O5H5N2	150(2)	149	153	152	146
O1H1..O5[ii]					
H1..O5	2.07	1.97	1.91	1.94	1.88
O1..O5	2.783(2)	2.731(10)	2.709(8)	2.692(12)	2.653(11)
<O1H1O5	156(2)	149	152	147	151
π-π[iii]					
plane-plane	3.464(1)	3.242(3)	3.191(3)	3.122(4)	3.055(4)
offset	1.761(1)	1.701(2)	1.656(3)	1.645(3)	1.586(4)

Symmetry Operators:

i	*x*,*y*,*z*
ii	-*x*,-*y*,-*z*
iii	*x*,-1+*y*,*z*

(a)

Pressure/GPa	0.0	1.3	2.2	3.5	4.2	4.9	5.6
O5H5..N2[i]							
H5..N2	1.85	1.80	1.86	1.79	1.86	1.80	1.82
O5..N2	2.608(2)	2.597(7)	2.585(7)	2.573(6)	2.576(6)	2.572(7)	2.570(6)
<O5H5N2	143(2)	151	138	144	137	147	145
O1H1..O5[ii]							
H1..O5	2.06	2.03	1.94	1.80	1.87	1.88	1.77
O1..O5	2.806(3)	2.750(6)	2.732(5)	2.694(4)	2.684(5)	2.675(6)	2.658(4)
<O1H1O5	153(3)	141	156	168	155	150	156
π-π[iii]							
plane-plane	3.533(2)	3.314(2)	3.238(2)	3.167(2)	3.139(2)	3.117(2)	3.080(2)
offset	1.769(2)	1.643(2)	1.607(2)	1.573(2)	1.571(2)	1.563(2)	1.550(2)

Symmetry Operators:

i	*x*,*y*,*z*
ii	-*x*,-*y*,-*z*
iii	*x*,-1+*y*,*z*

(b)

Pressure/GPa	0.0	1.4	2.7	4.4	5.3	6.0
O5H5..N2[i]						
H5..N2	1.79	1.81	1.77	1.76	1.81	1.85
O5..N2	2.586(3)	2.567(3)	2.552(3)	2.542(2)	2.536(2)	2.534(3)
<O5H5N2	151(3)	144	150	150	150	143
O1H1..O5[ii]						
H1..O5	1.88	1.90	1.79	1.81	1.77	1.77
O1..O5	2.707(2)	2.655(3)	2.617(3)	2.598(3)	2.581(3)	2.578(3)
<O1H1O5	155(3)	152	158	149	156	149
π-π[iii]						
plane-plane	3.429(2)	3.270(2)	3.165(2)	3.102(2)	3.058(2)	3.046(2)
offset	1.820(1)	1.655(1)	1.577(1)	1.548(1)	1.536(1)	1.524(1)

Symmetry Operators:

i	*x*,*y*,*z*
ii	-*x*,-*y*,-*z*
iii	1-*x*,1-*y*,1-*z*

(c)

Pressure/GPa	0.0	0.2
O51H51..N21[i]		
H51..N21	1.81	1.85
O51..N21	2.597(3)	2.620(14)
<O51H51N21	150(2)	145
O11H11..O51[ii]		
H11..O51	2.00	1.96
O11..O51	2.811(3)	2.769(8)
<O11H11O51	156(3)	155
O52H52..N22[i]		
H52..N22	1.84	1.89
O52..N22	2.599(2)	2.614(18)
<O52H52N22	148(2)	143
O12H12..O52[iii]		
H12..O52	1.99	2.00
O12..O52	2.827(3)	2.813(8)
<O12H12O52	164(4)	157
π-π[iv]		
plane-plane	3.371(2)	3.314(5)
offset	3.768(2)	3.745(5)
π-π[v]		
plane-plane	3.696(2)	3.612(6)
offset	3.309(2)	3.249(5)

Symmetry Operators:

i	*x*,*y*,*z*
ii	2-*x*,-*y*,-*z*
iii	1-*x*,1-*y*,1-*z*
iv	1-*x*,-*y*,-*z*
v	-*x*,1-*y*,1-*z*

(d)

Pressure/GPa	1.0	2.3	3.4	4.6	6.2
O5H5..N2^{i}					
H5..N2	1.80	1.84	1.80	1.80	1.76
O5..N2	2.569(6)	2.578(6)	2.586(6)	2.551(7)	2.541(9)
<O5H5N2	148(5)	145	146	145	148
O1H1..O5^{ii}					
H1..O5	1.94	1.96	1.93	1.90	1.90
O1..O5	2.763(5)	2.723(5)	2.694(5)	2.677(6)	2.653(6)
<O1H1O5	157(3)	152	153	148	148
π-π^{iii}					
plane-plane	3.308(3)	3.192(3)	3.114(3)	3.065(4)	3.011(3)
offset	3.382(3)	3.332(3)	3.302(3)	3.274(4)	3.239(3)

Symmetry Operators:

i	*x*,*y*,*z*
ii	0.5-*x*,0.5-*y*,0.5-*z*
iii	0.5-*x*,1.5-*y*,0.5-*z*

(e)

Table 3.2: Non-covalent interaction parameters in the crystal structures of (a) 3-chlorosalicylaldoxime, (b) 3-methylsalicylaldoxime, (c) 3-methoxysalicylaldoxime, (d) 3-*tert*-butylsalicylaldoxime-I and (e) 3-*tert*-butylsalicylaldoxime-II. Distances are in Å, and angles in °.

3.5 Discussion

3.5.1 *The effect of pressure on cavity size in the substituted salicylaldoximes*

The size of the intermolecular cavity, which occurs within the hydrogen bonded ring motif, can be studied by measuring the mean distance from the donor atoms of the ligands (*i.e.* O5, N2) to the centroid of the dimer. This distance was shown (Chapter 2, Figure 2.8) to decrease approximately linearly in the case of salicylaldoxime-I within the pressure range of 0-5.3 GPa. Figure 3.5 shows a graph of the cavity size as a function of pressure as determined in this study. We can see that the cavity sizes decrease for all the compounds and, with the exception of the *tert*-butyl phase I (from 0 – 1 GPa in Figure 3.5), with very similar gradients.

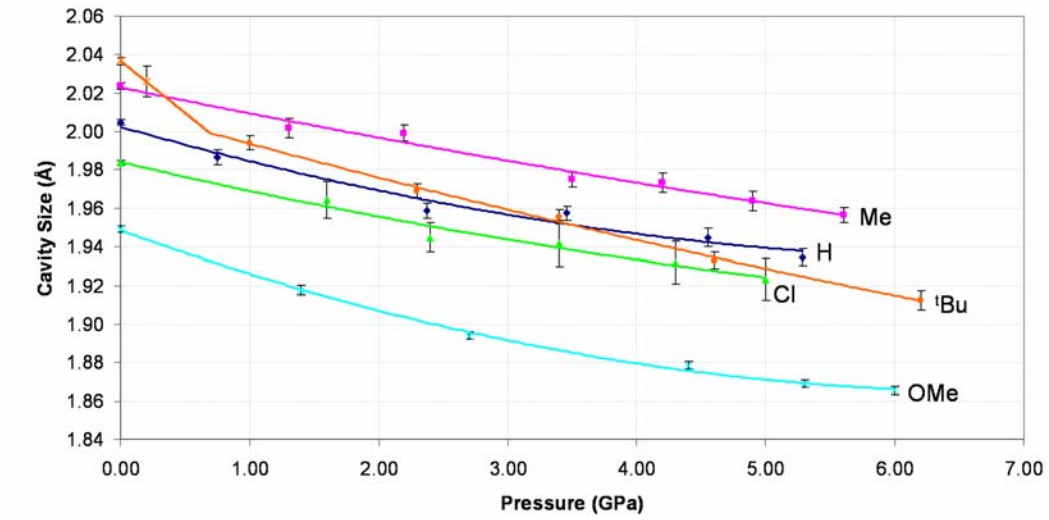

Figure 3.5: Graph of cavity size (in Å) as a function of pressure (in GPa) for salicylaldoxime (dark blue), 3-chlorosalicylaldoxime (green), 3-methylsalicylaldoxime (pink), 3-methoxysalicylaldoxime (light blue) and 3-*tert*-butylsalicylaldoxime (orange). Cavity size is defined as the mean distance of donor atoms from the centroid of the dimer. Each pressure series (except for ^{t}Bu) has been fitted with a line of best fit using a polynomial of order 2; these are guides to the eye rather than equations of state. The two phases of 3-*tert*-butylsalicylaldoxime have been plotted separately with a trend line fitted to each set of points, both are coloured orange. The error bars are shown at the 1σ level.

The cavity size at ambient pressure is found to be markedly dependent on the nature of the 3-substituent which is *ortho* to the phenolic OH group (X in Scheme 3.2). The trend appears to be related to the ability of the substituent to accept a hydrogen bond. If it has a lone pair capable of accepting a hydrogen bond, the oximic hydrogen can in principle form an asymmetric bifurcated hydrogen bond, encouraging the molecules to approach each other more closely (see Scheme 3.2). On this basis the 3MeO- and 3Cl- derivatives are expected and are found to have the smallest cavity radii (Table 3.3) Conversely when the 3-substituent is bulky it will weaken the oximic H to phenolic O hydrogen bonding and a larger cavity will result, as in the 3-^{t}Bu compound (see Table 3.3).

3-Substituent	OMe	Cl	H	Me	^{t}Bu
Cavity size at ambient pressure/Å	1.9492(19)	1.9837(12)	2.0048(15)	2.0237(18)	2.0367(19)
ΔE_{coul} / kJmol^{-1}	-4.8	-0.5	0	+0.2	+2.1
ΔE_{rep} / kJmol^{-1}	-0.4	0.0	0	+0.6	+6.2
ΔE_{pol} / kJmol^{-1}	-1.0	-1.0	0	-0.8	-2.7
ΔE_{disp} / kJmol^{-1}	-0.8	-1.5	0	-1.5	-5.8
ΔE_{TOTAL} / kJmol^{-1}	-7.0	-3.0	0	-1.5	-0.2

Table 3.3: Ambient-pressure cavity sizes and differences in energy for the hydrogen bonded dimers in the substituted oximes structures with and without the substituent. The values are calculated for each dimer and then for the same geometry but with the substituent replaced by an H atom. The energies of the components in the salicylaldoxime-I dimer contact are -37.1, -7.8, 35.0, -15.0 and -25.0 kJ mol^{-1} for the Coulombic, dispersion, repulsion, polarisation and total energies respectively. Energies are in kJ mol^{-1}. The cavity size for the ^{t}Bu derivative is the average for the two molecules comprising the asymmetric unit.

In order to test this theory a set of energy calculations were performed using the geometry of the crystal structures and the PIXEL method (Gavezzotti, 2005a, Dunitz & Gavezzotti, 2005), which models intermolecular interaction energies in terms of Coulombic, polarization and dispersive-repulsion contributions. PIXEL

energies were calculated first for each dimer and then for the same geometry but with the substituent replaced by an H atom. The differences are reported in Table 3.3.

The Coulombic term favours the association of the dimer when the 3MeO- and 3Cl- are present (Table 3.3) which is consistent with their H-bond acceptor properties whilst it disfavours association for the 3Me- and the 3-^{t}Bu substituted compounds. A large repulsion term (E_{rep}) is seen for the ^{t}Bu-substituted ligand, which may explain both its large hole size and poor extractive efficacy (Forgan *et al.*, 2007). However, the method also suggests there is a slightly stronger net stabilising energy between the two halves of the Me and ^{t}Bu substituted dimers than in the unsubstituted system. Both have large, favourable dispersion terms, E_{disp}, due to the number of electrons in the substituents, though it is possible that this term may be over-estimated as it is the most parameterised in the PIXEL formalism (Gavezzotti, 2007).

Figure 3.5 shows that the relative compressibilities of the hole sizes in the five different compounds are quite similar, no doubt reflecting the similarity of the interactions involved. The relative changes in cavity size (= cavity size at ambient pressure / cavity size at 5 GPa) are 1.031(4) (Me) and 1.031(6) (Cl) 1.036(3) (H), 1.043(2) (OMe) and 1.054(3) (*t*Bu). Though these data refer to compression of an entire crystal structure, not an isolated dimer, it is noteworthy that the compressibility of the 3-*tert*-butylsalicylaldoxime cavity is greater than the other salicylaldoximes, and the hole size becomes smaller than that of the 3-methyl and unsubstituted compounds at elevated pressure. This is counter-intuitive as the *tert*-butyl group is expected to be sterically repulsive: indeed steric effects have been used to explain the weakness of this ligand in binding Cu^{2+} at ambient pressure (Forgan *et al.*, 2007).

An important practical consequence of the data presented in Figure 3.5 is that the combination of varying the nature of the 3-substituent and of changing the pressure can change the N_2O_2 cavity radius between 1.87 and 2.04 Å. This range spans the covalent radii of many of the 1st transition series metal dications and should allow the selectivity of metal extraction to be tuned using pressure.

3.5.2 Analysis of non-covalent interactions under compression

The effect of pressure on the intermolecular interactions within the substituted salicylaldoximes is non-uniform. There are three main non-covalent interactions which are found in each of the different compounds; the phenolic OH…N intramolecular hydrogen bond, the oximic OH…O intermolecular hydrogen bond and the π-π stacking interaction. The OH…N intramolecular hydrogen bond is the least compressible non-covalent interaction in the structures and is relatively consistent across the series of compounds due to the rigidity of the salicylaldoxime molecular geometry. The oximic OH…O hydrogen bond geometry is not restricted by the covalent bonds of the molecule and thus is considerably more compressible than the intramolecular hydrogen bond. Figure 3.6 shows a graph of the variation in the donor to acceptor distances for the OH…O hydrogen bond as a function of pressure for each of the compounds.

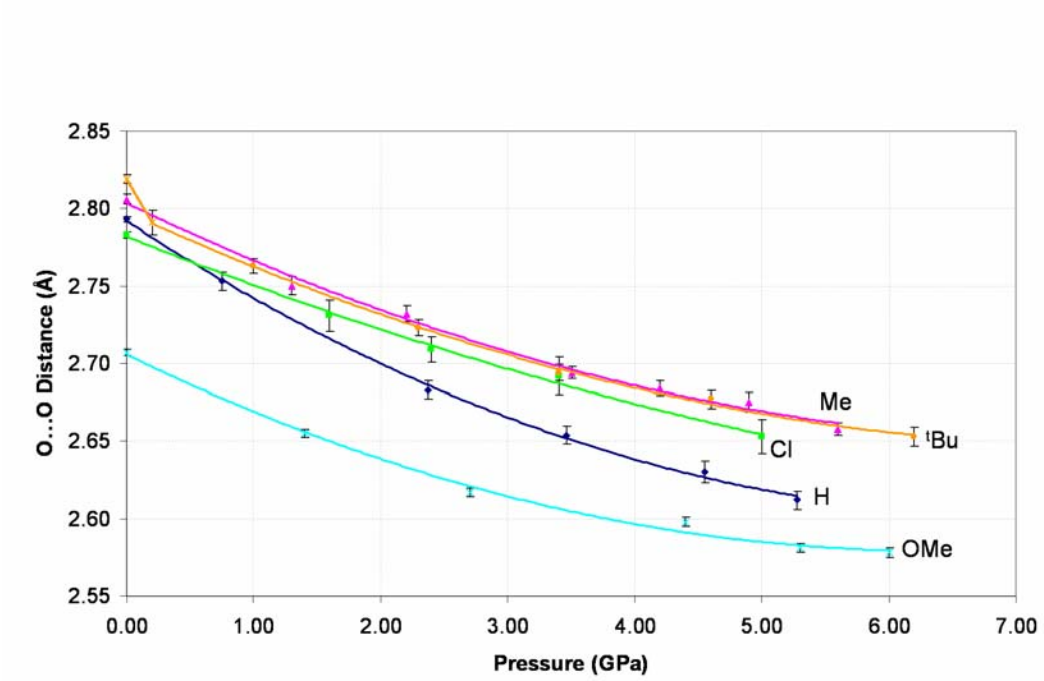

Figure 3.6: Graph of donor to acceptor distance (in Å) of the oximic OH…O intermolecular interaction as a function of pressure (in GPa) for salicylaldoxime (dark blue), 3-chlorosalicylaldoxime (green), 3-methylsalicylaldoxime (pink), 3-methoxysalicylaldoxime (light blue) and 3-*tert*-butylsalicylaldoxime (orange).

The oximic hydrogen bond in the 3-methoxysalicylaldoxime structure is considerably shorter than the corresponding interaction in the other compounds both at ambient pressure and when compressed. As described above, this is ascribable to the availability of the methoxy oxygen atom as a secondary hydrogen bond acceptor (Figure 3.7). The shapes of the H, Me, and Cl curves are very similar though, so it would appear that changing the substituent can modify the length of the OH…O interaction and thus the size of the pseudo-macrocyclic cavity at ambient conditions, but doesn't significantly affect the compressibility of the interaction.

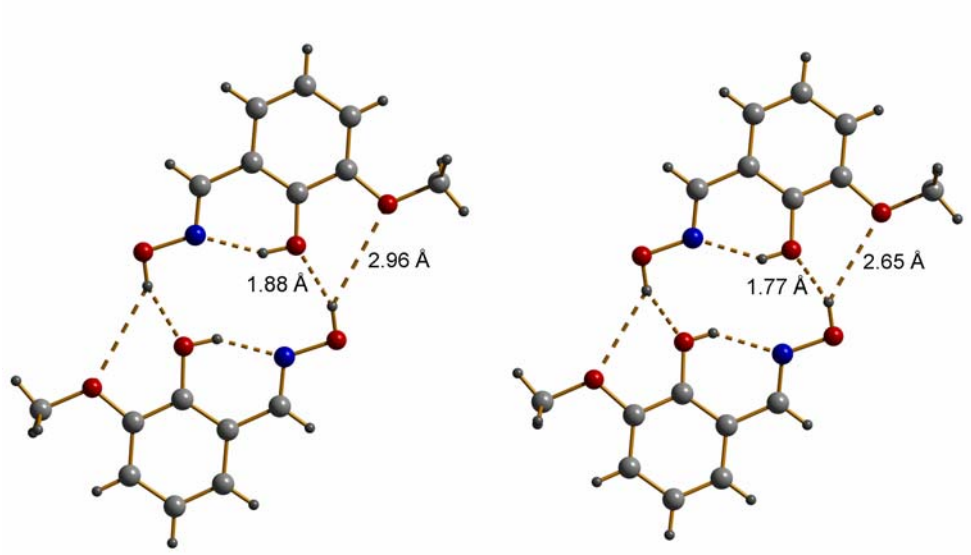

(a) (b)

Figure 3.7: The hydrogen bonded dimer with bifurcated character in 3-methoxysalicylaldoxime at ambient pressure (a) and at 6.0 GPa (b). The distances displayed are H to O distances for O1H1…O5 and O1H1…O61. The colour scheme is the same as in Fig. 3.1.

The stacking interaction in these structures is seen to be more compressible than the hydrogen bonds but, as PIXEL calculations on the salicylaldoxime compression study showed (Chapter 2, Figure 2.10), the interactions can become very destabilising at shorter distances. This sharp increase in repulsion as the stacking distance reaches its minimum means that the interaction can become important in terms of both anisotropic compression and phase transitions. To analyse the compression of these stacking interactions it is useful to compare them to similar interactions found at ambient conditions. The stacking interaction between phenyl

groups can be described using the angle between phenyl ring planes, the perpendicular distance between the groups (stacking distance) and the parallel distance between groups (stacking offset). A search of the CSD was performed for phenyl groups interacting in a stacking configuration with planar angle < 10˚, stacking distance < 4.5 Å, stacking offset < 4.0 Å, 3D coordinates and R-factor < 0.05 in organic-only structures without errors or disorder.

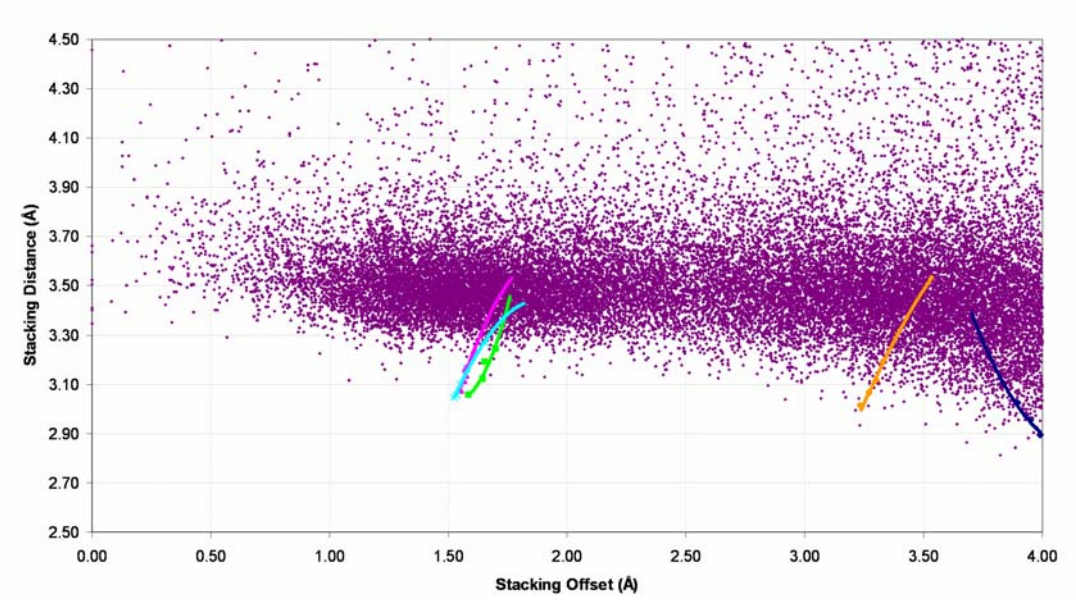

Figure 3.8: Graph of stacking distance (in Å) against stacking offset (in Å) for phenyl group stacking interactions in the CSD. The five oxime compression studies have also been plotted; salicylaldoxime (dark blue), 3-chlorosalicylaldoxime (green), 3-methylsalicylaldoxime (pink), 3-methoxysalicylaldoxime (light blue) and 3-*tert*-butylsalicylaldoxime (orange).

Figure 3.8 shows a graph of stacking distance against stacking offset for all the interactions found in the CSD. Also shown are the stacking contacts in the five salicylaldoxime compression studies performed to date. This graph shows that the stacking interaction for each compound is at a normal distance at ambient conditions, but as pressure is increased the interactions are compressed to the limits of similar interactions seen at ambient pressures. The salicylaldoxime crystal structure was seen to undergo a phase transition between 5.3 and 5.9 GPa (Chapter 2, Table 2.1). This was believed to be caused in part by the stacking interaction reaching the limits of similar interactions found at ambient conditions. The data in Figure 3.8 suggests that

each of the substituted salicylaldoximes studied here may also be close to a phase transition at the highest pressures obtainable in this study.

The range of pressures that were obtained in the experiments described in this chapter was limited by the hydrostatic pressure medium, the tungsten gasket and the single crystals themselves. It would be interesting to investigate the phase behaviour of salicylaldoximes at elevated pressures using powder methods.

3.6 Conclusions

The crystal structures of salicylaldoxime and the four 3-substituted derivatives (OMe, Cl, Me and ^{t}Bu) examined in this study comprise pseudo-macrocyclic dimers based on an $R_4^4(10)$ hydrogen bonding ring motif which pre-organises an N_2O_2 donor-set towards binding of planar transition metal ions, and stabilises the complexes after they have formed. The size of the cavity at the centre of the pseudo-macrocycle is known to influence the binding-selectivity of metal ions, and the aim of this study was to investigate the extent to which the size of this cavity (and presumably metal-ion selectivity) can be varied with pressure.

The crystal structures at ambient pressure show that the size of the cavity varies according to the substituent occupying the 3-position of the salicylaldoxime ring. The smallest cavity was observed for the OMe derivative, and H-bonding analysis combined with PIXEL calculations were used to show that inter-ligand H-bonding involving the OMe group (see Figure 3.7) supports the H-bonds of the $R_4^4(10)$ ring, so reducing the cavity size. The largest cavity was observed for the ^{t}Bu derivative, and could be ascribed to steric effects.

Crystal structures for each derivative were determined between 0 and 5-6 GPa. In each case the pseudo-macrocyclic cavity decreases smoothly with the application of pressure. The combination of varying the nature of the 3-substituent and of changing the pressure can change the N_2O_2 cavity radius between 1.87 and 2.04 Å. This range spans the covalent radii of many of the 1st transition series metal dications and may allow the selectivity of metal extraction to be tuned using a combination of chemical derivatisation and high pressure.

3.7 References

Allen, F. H. (2002). *Acta Crystallographica, Section B* **58**, 380-388.

Allen, F. H. & Motherwell, W. D. S. (2002). *Acta Crystallographica, Section B* **58**, 407-422.

Angel, R. J. (2000). *Reviews in Mineralogy and Geochemistry* **41**, 35-59.

Angel, R. J., Downs, R. T. & Finger, L. W. (2000). *Reviews in Mineralogy and Geochemistry* **41**, 559-596.

Bernstein, J., Davis, R. E., Shimoni, L. & Chang, N.-L. (1995). *Angewandte Chemie, International Edition* **34**, 1555-1573.

Betteridge, P. W., Carruthers, J. R., Cooper, R. I., Prout, K. & Watkin, D. J. (2003). *Journal of Applied Crystallography* **36**, 1487.

Birch, F. (1947). *Physical Review* **71**, 809-824.

Boldyreva, E. V. (2004). *Journal of Molecular Structure* **700**, 151-155.

Bruker-Nonius (2006). *SAINT version 7*, *Program for integration of area detector data*. Bruker-AXS, Madison, Wisconsin, USA.

Bruno, I. J., Cole, J. C., Edgington, P. R., Kessler, M., Macrae, C. F., McCabe, P., Pearson, J. & Taylor, R. (2002). *Acta Crystallographica, Section B* **58**, 389-397.

Crystal Impact (2004). *DIAMOND version 3.0*, *Visual crystal structure information system*. Crystal Impact GbR, Postfach 1251, 53002, Bonn, Germany.

Dawson, A., Allan, D. R., Parsons, S. & Ruf, M. (2004). *Journal of Applied Crystallography* **37**, 410-416.

Dunitz, J. D. & Gavezzotti, A. (2005). *Angewandte Chemie, International Edition* **44**, 1766-1787.

Farrugia, L. J. (1999). *Journal of Applied Crystallography* **32**, 837-838.

Forgan, R. S., Wood, P. A., Campbell, J., Henderson, D. K., McAllister, F. E., Parsons, S., Pidcock, E., Swart, R. & Tasker, P. A. (2007). *Chemical Communications* 4940-4942.

Frisch, M. J., Trucks, G. W., Schlegel, H. B., Scuseria, G. E., Robb, M. A., Cheeseman, J. R., Zakrzewski, V. G., Montgomery, J. A. J., Stratmann, R. E., Burant, J. C., Dapprich, S., Millam, J. M., Daniels, A. D., Kudin, K. N., Strain, M. C., Farkas, O., Tomasi, J., Barone, V., Cossi, M., Cammi, R., Mennucci, B., Pomelli, C., Adamo, C., Clifford, S., Ochterski, J., Petersson, G. A., Ayala, P. Y., Cui, Q.,

Morokuma, K., Malick, D. K., Rabuck, A. D., Raghavachari, K., Foresman, J. B., Cioslowski, J., Ortiz, J. V., Stefanov, B. B., Liu, G., Liashenko, A., Piskorz, P., Komaromi, I., Gomperts, R., Martin, R. L., Fox, D. J., Keith, T., Al-Laham, M. A., Peng, C. Y., Nanayakkara, A., Gonzalez, C., Challacombe, M., Gill, P. M. W., Johnson, B. G., Chen, W., Wong, M. W., Andres, J. L., Head-Gordon, M., Replogle, E. S. & Pople, J. A. (1998). *Gaussian 98 revision A.7*, Gaussian, Inc., Pittsburgh, PA, USA.

Gavezzotti, A. (2003). *OPiX*, *A computer program package for the calculation of intermolecular interactions and crystal energies*. University of Milano, Milan, Italy.

Gavezzotti, A. (2005a). *Structural Chemistry* **16**, 177-185.

Gavezzotti, A. (2005b). *Zeitschrift fuer Kristallographie* **220**, 499-510.

Gavezzotti, A. (2007). Private communication.

Gokel, G. W. (1991). Crown Ethers and Cryptands. Cambridge, UK: The Royal Society of Chemistry.

Gorbitz, C. H. (2002). *Acta Crystallographica, Section B* **58**, 849-854.

Hofslokken, N. U. & Skattebol, L. (1999). *Acta Chemica Scandinavica* **53**, 258-262.

Kordosky, G. A. (2002). *South African Institute of Mining and Metallurgy*, pp. 853-862. Cape Town

Merrill, L. & Bassett, W. A. (1974). *Review of Scientific Instruments* **45**, 290-294.

Moggach, S. A., Allan, D. R., Parsons, S. & Sawyer, L. (2006). *Acta Crystallographica, Section B* **62**, 310-320.

Moggach, S. A., Allan, D. R., Parsons, S., Sawyer, L. & Warren, J. E. (2005). *Journal of Synchrotron Radiation* **12**, 598-607.

Oswald, I. D. H., Allan, D. R., Motherwell, W. D. S. & Parsons, S. (2005). *Acta Crystallographica, Section B* **61**, 69-79.

Parsons, S. (2004). *SHADE*, *Program for empirical absorption corrections to high pressure data*. The University of Edinburgh, Edinburgh, United Kingdom.

Piermarini, G. J., Block, S., Barnett, J. D. & Forman, R. A. (1975). *Journal of Applied Physics* **46**, 2774-2780.

Sheldrick, G. M. (2004). *SADABS Version 2004-1*, *Program for absorption corrections to area detector data*. Bruker-AXS, Madison, Wisconsin, USA.

Slebodnick, C., Zhao, J., Angel, R., Hanson, B. E., Song, Y., Liu, Z. & Hemley, R. J. (2004). *Inorganic Chemistry* **43**, 5245-5252.

Small, R. W. H. (2003). *Acta Crystallographica, Section B* **59**, 141-148

Smith, A. G., Tasker, P. A. & White, D. J. (2003). *Coordination Chemistry Reviews* **241**, 61-85.

Spek, A. L. (2003). *Journal of Applied Crystallography* **36**, 7-13.

Stepniak-Biniakiewicz, D. (1980). *Polish Journal of Chemistry* **54**, 1567-1571.

Szymanowski, J. (1993). Hydroxyoximes and Copper Hydrometallurgy. London, UK: CRC Press.

Xu, T., Li, L.-z. & Ji, H.-w. (2004). *Hecheng Huaxue* **12**, 22-24.

Chapter 4

The Anisotropic Compression of the Crystal Structure of 3-Aza-bicyclo(3.3.1)nonane-2,4-dione to 7.1 GPa*

* Wood, P. A., Haynes, D. A., Lennie, A. R., Motherwell, W. D. S., Parsons, S., Pidcock, E., Warren, J. E. (2008). *Cryst. Growth Des.*, **8**, 549-558, 2008.

4.1 Synopsis

The compound 3-aza-bicyclo(3.3.1)nonane-2,4-dione has been crystallised at high pressure from a solution of ethanol/methanol and the structure has been determined at room temperature at pressures from 0.9 to 7.1 GPa. Within this pressure regime the structure is seen to compress anisotropically with no phase transitions occurring. The changes in intermolecular interactions and molecular packing during the compression are interpreted with the aid of PIXEL calculations and Hirshfeld surfaces.

4.2 Introduction

The effectiveness of high pressure as a means for exploring polymorphism in the organic solid state has been demonstrated in a number of recent studies (Fabbiani *et al.*, 2005, Oswald *et al.*, 2005, Lozano-Casal *et al.*, 2005). The ability to search for new polymorphs in this way is of interest to a number of fields, including the pharmaceutical industry and the crystal structure prediction community. The technique of crystal structure prediction (CSP) involves generating a large number of potential crystal structures and then determining which structure is the most energetically stable, this is then assumed to be the correct structure. In general are a number of different possible structures within a few kJ mol^{-1} of each other and these other structures might correspond to polymorphs of the compound. The application of pressure is one possible method for searching for these potential polymorphs.

3-aza-bicyclo(3.3.1)nonane-2,4-dione, **1**, was one of the test structures used in the second international blind test for crystal structure prediction of small organic molecules, which was organised by the CCDC (Motherwell *et al.*, 2002). During the test, 15 different research groups were each asked to submit a list of three possible crystal structures for the molecule in order of confidence. The correct structure of **1** was only adjudged to have been predicted in two cases out of the 15 submissions and these predictions had energy rankings of 2 and 3. The experimentally-determined structure of **1** consists of H-bonded chains, but several groups predicted incorrect structures based on a hydrogen-bonded dimer with a $R_2^2(8)$ ring motif.

One possible reason for the lack of success of the crystal structure prediction trials for **1** is that the observed structure may not be the most thermodynamically stable, or that other structures may have lower energies under different conditions. This study was initially intended as a search for new polymorphs of the compound to see if they matched to one of the other structural models predicted by CSP. In the event this was not observed. However, the opportunity to observe the compression of small organic structures to high pressures is also of fundamental interest as the compression of intermolecular interactions in the solid state is still only relatively lightly studied. In this chapter we describe the crystal structure of the title compound on crystallisation from solution by the application of hydrostatic pressure and the effect of pressure on the structure up to 7.1 GPa.

4.3 Experimental

High-pressure experiments were carried out using a Merrill-Bassett diamond anvil cell (half-opening angle 40°), equipped with 600μm culets and a tungsten gasket (Merrill & Bassett, 1974). A small ruby chip was also loaded into the cell as a pressure calibrant, with the ruby-fluorescence method being used to measure the pressure (Piermarini *et al.*, 1975).

4.3.1 Crystal growth

A sample of 3-aza-bicyclo(3.3.1)nonane-2,4-dione (**1**) was prepared essentially as described by Hulme and co-workers (Hulme *et al.*, 2007), except that the starting material used was a mixture of *cis*/*trans* 1,3-cyclohexane dicarboxylic acid, which was used without further purification. The distillation of water was carried out at atmospheric pressure and the final product was purified by sublimation.

Preliminary high pressure experiments were carried-out using a hydrostatic medium consisting of a 1:1 mixture of *n*-pentane and iso-pentane, however the quality of the crystals degraded rapidly on increasing pressure. Another commonly-used hydrostatic medium is a 4:1 mixture of methanol and ethanol, but **1** proved to be soluble in this, and a strategy based on loading a crystal under ambient conditions

and applying pressure was therefore unsuitable. It proved possible, however, to grow a crystal from methanol/ethanol *in situ* and use the remaining mother liquor as the hydrostatic medium.

A saturated solution of **1** in 4:1 methanol/ethanol was loaded into a Merrill-Bassett diamond-anvil cell. The sample was pressurized at room temperature until crystallites began to form. The temperature was then increased using a heat-gun, so that the polycrystalline sample was partially redissolved, and then cycled close to this elevated temperature in order to reduce the number of crystallites. A single crystal was eventually obtained at a pressure of 0.9 GPa, which could be indexed on essentially the same unit cell as the ambient pressure structure (Howie & Skakle, 2001).

4.3.2 High pressure crystallography

Diffraction data were collected on a Bruker-Nonius APEX-II diffractometer with silicon-monochromated synchrotron radiation (λ = 0.8640 Å) on Station 16.2SMX at the SRS, Daresbury Laboratory. Data collection and processing procedures for the high-pressure experiments followed previous studies (Dawson *et al.*, 2004, Moggach, Allan, Parsons *et al.*, 2005). Integrations were carried out using the program *SAINT* (Bruker-Nonius, 2006) and absorption corrections with the programs *SHADE* (Parsons, 2004) and *SADABS* (Sheldrick, 2004). Data collections were taken in approximately 1.0 GPa steps from 0.9 GPa up to a final pressure of 7.1 GPa.

In order to facilitate a comparison with the ambient temperature/high-pressure results, diffraction data were also collected on **1** at ambient pressure. Data were collected on a Bruker APEX diffractometer with graphite-monochromated Mo-Kα radiation (λ = 0.71073 Å). The data were integrated using *SAINT* and corrected for absorption with *SADABS*. The structure was solved using the program *SIR-92* (Altomare *et al.*, 1994) and structure refinement yielded a conventional *R*-factor of 0.0553.

Refinements [against $|F|^2$ using all data (*CRYSTALS* (Betteridge *et al.*, 2003))] of the compressed forms of **1** were started from the co-ordinates determined

at ambient pressure. Because of the low completeness of the data-sets, displacement parameters for the high pressure structures were only modelled at the isotropic level. Global rigid bond restraints were also applied. Hydrogen atoms were placed geometrically and constrained to ride on their host atoms. Listings of crystal and refinement data are given in Table 4.1.

Crystal structures were visualized using the programs *Mercury* (Bruno *et al.*, 2002) and *DIAMOND* (Crystal Impact, 2004). Analyses were carried out using *PLATON* (Spek, 2003), as incorporated in the *WinGX* suite (Farrugia, 1999). Searches of the Cambridge Structural Database (Allen, 2002, Allen & Motherwell, 2002) utilized the program *ConQuest* and version 5.28 of the database with updates up to January 2007. Strain tensor calculations were carried out using a locally written program (Parsons, 2003), based on the discussion by Hazen & Finger (Hazen & Finger, 1982) and employing the JACOBI subroutine *Numerical Recipes* (Press *et al.*, 1992). Equation-of-state calculations were carried out with *EOSFIT* (Angel, 2000). Hirshfeld surface analysis was performed using the program *CrystalExplorer* (Wolff *et al.*, 2005).

The numbering scheme used (see Scheme 4.1) is the same throughout the ambient pressure and high pressure datasets.

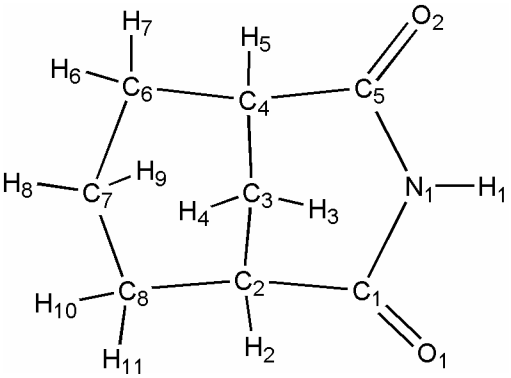

Scheme 4.1: Chemical structure diagram showing atomic numbering scheme.

Pressure/GPa	Ambient	0.9	1.9	3.0
Formula	$C_8H_{11}NO_2$	$C_8H_{11}NO_2$	$C_8H_{11}NO_2$	$C_8H_{11}NO_2$
M_r	153.18	153.18	153.18	153.18
Cell setting, space group	Monoclinic, $P2_1/c$	Monoclinic, $P2_1/c$	Monoclinic, $P2_1/c$	Monoclinic, $P2_1/c$
a, b, c (Å)	9.3214 (11), 10.5932 (12), 7.6988 (9)	8.868 (9), 10.2833 (16), 7.7016 (13)	8.564 (7), 10.0876 (18), 7.6419 (12)	8.367 (8), 9.9317 (17), 7.5667 (12)
β (°)	95.059 (8)	95.88 (3)	96.38 (3)	96.49 (3)
V (Å^3)	757.24 (15)	698.6 (7)	656.1 (6)	624.8 (6)
Z	4	4	4	4
D_x (Mg m^{-3})	1.344	1.456	1.551	1.628
Radiation type	Mo $K\alpha$	Synchrotron	Synchrotron	Synchrotron
μ (mm^{-1})	0.10	0.11	0.11	0.12
T_{min}/ T_{max}	0.75, 0.99	0.67, 0.99	0.76, 0.99	0.71, 0.99
No. of measured, independent and observed reflections	9428, 2086, 1045	1363, 275, 230	1143, 261, 203	1220, 249, 201
R_{int}	0.064	0.067	0.067	0.072
θ_{max} (°)	29.6	26.4	26.4	26.5
$R[F^2 > 2\sigma(F^2)]$, $wR(F^2)$, S	0.055, 0.137, 0.92	0.055, 0.138, 0.95	0.053, 0.140, 0.94	0.050, 0.123, 0.90
No. of relections	1982 reflections	255 reflections	239 reflections	229 reflections
Parameters	104	45	45	45
$\Delta\rho_{max}$, $\Delta\rho_{min}$ (e Å^{-3})	0.22, –0.24	0.15, –0.14	0.15, –0.14	0.13, –0.12

(a)

Pressure/GPa	4.4	5.9	7.1
Formula	$C_8H_{11}NO_2$	$C_8H_{11}NO_2$	$C_8H_{11}NO_2$
M_r	153.18	153.18	153.18
Cell setting, space group	Monoclinic, $P2_1/c$	Monoclinic, $P2_1/c$	Monoclinic, $P2_1/c$
a, b, c (Å)	8.254 (4), 9.8542 (15), 7.5245 (11)	8.054 (7), 9.782 (3), 7.5043 (19)	7.938 (7), 9.754 (3), 7.481 (2)
β (°)	96.63 (3)	96.80 (5)	97.03 (6)
V (Å^3)	607.9 (3)	587.1 (5)	574.9 (6)
Z	4	4	4
D_x (Mg m^{-3})	1.674	1.733	1.770
Radiation type	Synchrotron	Synchrotron	Synchrotron
μ (mm^{-1})	0.12	0.13	0.13
T_{min}/ T_{max}	0.69, 0.99	0.48, 0.99	0.27, 0.99
T_{max}	0.99	0.99	0.99
No. of measured, independent and observed reflections	1147, 229, 189	1063, 222, 169	916, 209, 160
R_{int}	0.061	0.076	0.107
θ_{max} (°)	22.2	22.1	21.8
$R[F^2 > 2\sigma(F^2)]$, $wR(F^2)$, S	0.044, 0.109, 0.90	0.059, 0.162, 0.93	0.076, 0.206, 0.85
No. of relections	210 reflections	201 reflections	191 reflections
Parameters	45	45	45
$\Delta\rho_{max}$, $\Delta\rho_{min}$ (e Å^{-3})	0.12, –0.11	0.17, –0.15	0.22, –0.25

(b)

Table 4.1: Crystallographic data for 3-aza-bicyclo(3.3.1)nonane-2,4-dione at increasing pressures (a) ambient to 3.0 GPa and (b) 4.4 to 7.1 GPa.

4.3.3 PIXEL calculations

The molecular structures obtained at each pressure were used to calculate the molecular electron density by standard quantum chemical methods using the program *GAUSSIAN98* (Frisch *et al.*, 1998) at the MP2/6-31G** level of theory. H-atom distances were set to standard neutron values (CH = 1.083 Å, NH = 1.009 Å). The electron density model of the molecule was then analysed using the program package *OPiX* (Gavezzotti, 2005) which allows the calculation of dimer and lattice energies. Lattice energy calculations employed a cluster of molecules of radius 18 Å. Calculations were also carried out for pairs of molecules identified in the lattice calculation as being energetically the most significant (*i.e.* with an energy < -2.5 kJ mol^{-1}). The output from these calculations yields a total energy and a breakdown into its electrostatic, polarisation, dispersion and repulsion components (Dunitz & Gavezzotti, 2005a).

4.4 Results

4.4.1 The structure of 3-aza-bicyclo(3.3.1)nonane-2,4-dione at ambient conditions

The crystal structure of 3-aza-bicyclo(3.3.1)nonane-2,4-dione (**1**) form I, was initially determined by Howie & Skakle (Howie & Skakle, 2001). A new polymorph, form II, has been described recently; this is meta-stable at ambient conditions, but can be trapped by rapid cooling to 250K (Hulme *et al.*, 2006). In this study the effects of pressure on form I were analysed.

The crystal structure of form I has one molecule in the asymmetric unit in space group $P2_1/c$. The molecule has approximate mirror symmetry in the plane running through the atoms N1, C3 and C7. The dicarboximide fragment of the molecule (N1, C1, O1, C5 and O2 along with the bonded carbon atoms C2 and C4) is nearly planar, with the greatest deviation from a least-squares mean plane of these atoms being 0.043 (3) Å for atom O2 (all data referred to in this section were derived from our own ambient pressure study, Table 4.1).

The molecules form intermolecular N1-H1…O2 hydrogen bonds [N1...O2 = 2.979 (2) Å] with a neighbouring molecule related by the *c*-glide. Successive

N1H1…O2 interactions form a primary-level *C*(4) chain (Bernstein *et al.*, 1995) running in the direction of the *c*-axis. These chains then interact with adjacent chains through C8H10…O1 interactions [C8…O1 = 3.429 (4) Å] to form sheets which lie in the *bc* plane (Figure 4.1*a*).

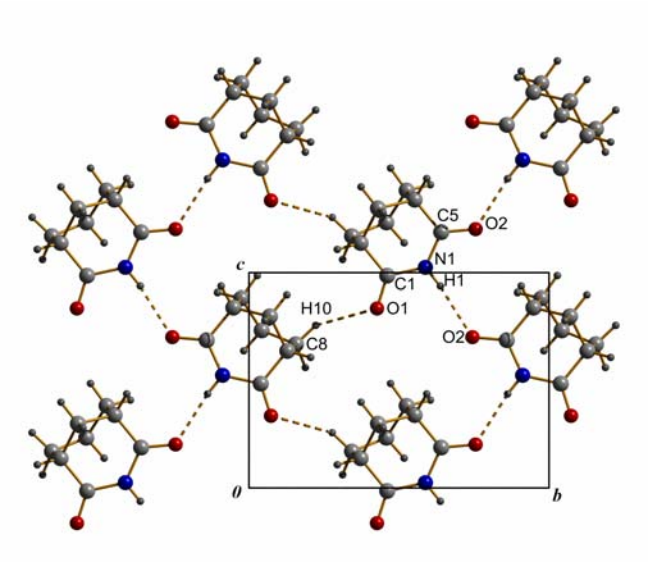

(a)

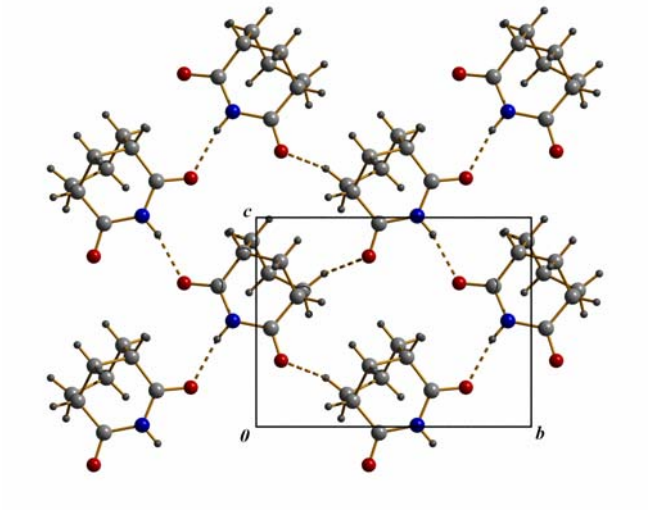

(b)

Figure 4.1: The effect of pressure on the crystal structure of 3-aza-bicyclo(3.3.1)nonane-2,4-dione as viewed along the *a*-axis: (*a*) 3-aza-bicyclo(3.3.1)nonane-2,4-dione at ambient pressure; (*b*) 3-aza-bicyclo(3.3.1)nonane-2,4-dione at 7.1 GPa. The colour scheme is red: oxygen, blue: nitrogen, light-grey: carbon and dark-grey: hydrogen.

A second set of weak hydrogen bonds form symmetry-equivalent pairs of C3-H3…O1 contacts [C3…O1 = 3.503 (4) Å] across an inversion centre, producing a centrosymmetric $R_2^2(10)$ dimer (Figure 4.2*a*). These ring motifs link together pairs of sheets formed in the *bc* plane to produce slabs, such that the dicarboximide sides of the molecules are close together on the inside of the slabs and the alkyl sides of the molecules face each other between the slabs. There are no hydrogen-bonding interactions between the slabs, which only interact with each other through van der Waals contacts (Figure 4.3*a*). The contacts between the molecules include a number of close H…H contacts of which C9-H9…H9-C9 is the shortest [H9…H9 = 2.286 (1) Å].

4.4.2 The response of 3-aza-bicyclo(3.3.1)nonane-2,4-dione to pressure up to 7.1 GPa

The compression of the crystal structure of **1** is anisotropic (Figure 4.4); the greatest reduction occurs in the *a*-axis (14.8% at 7.1 GPa relative to ambient pressure, *cf*. Figs 2 *a* and *b*), while the *b* and *c* axes reduce by 7.9 and 2.8% respectively. The direction of greatest linear strain is found to lie approximately along the *a*-axis; one of the eigenvectors of the strain tensor must correspond to the *b*-axis by symmetry, and this is the direction of the second largest eigenvalue. Finally the direction of least compression in the structure lies approximately along the reciprocal lattice direction (-1 0 5).

The bulk modulus (K_0), refined for a Birch-Murnaghan equation-of-state (Birch, 1947, Angel *et al.*, 2000) to second order, is 13.3 (7) GPa. The data set used to calculate this quantity is rather limited, and the values of V_0 and K' were fixed at 757.24 Å^3 and 4, respectively. Molecular solids generally have K_0 < 30 GPa and a useful comparison can be made from the following K_0 values: $Ru_3(CO)_{12}$ 6.6 GPa, NaCl 25 GPa, quartz 37 GPa, ceramics 50–300 GPa and diamond 440 GPa (Slebodnick *et al.*, 2004).

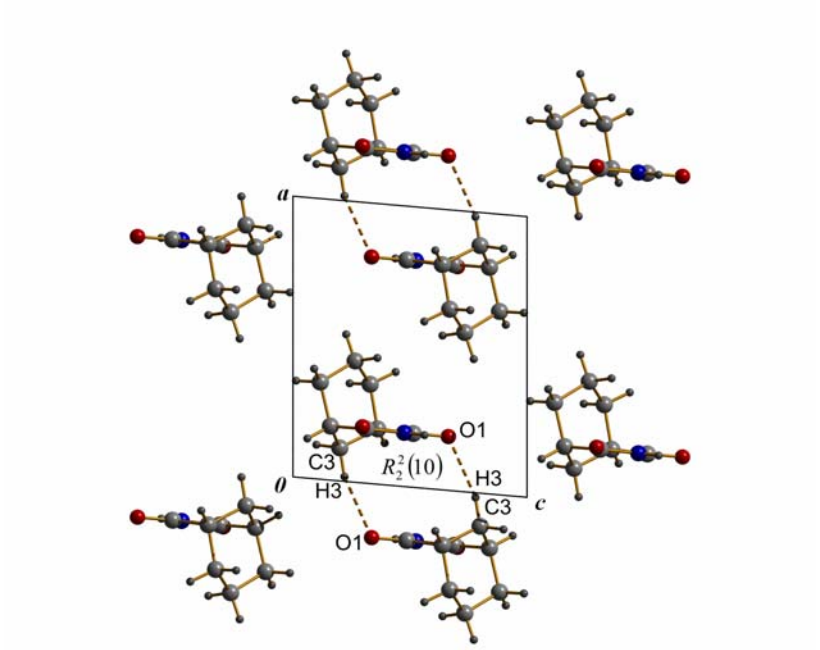

(a)

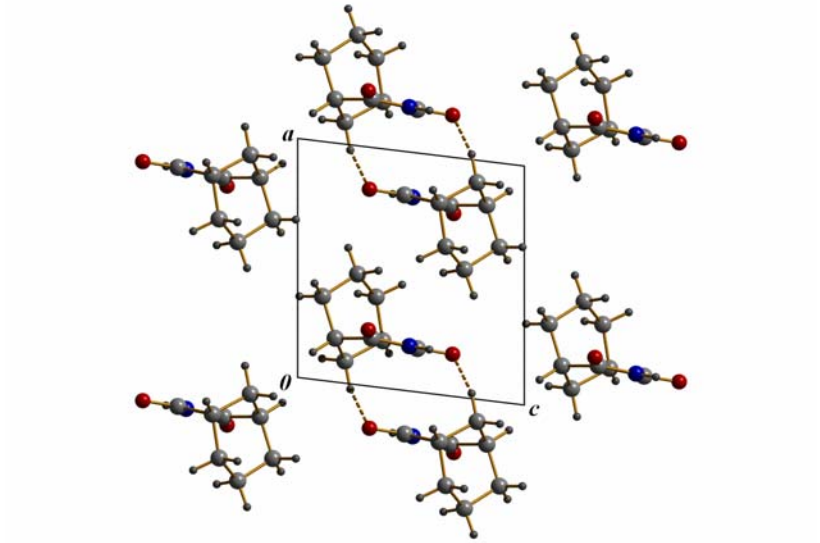

(b)

Figure 4.2: The effect of pressure on the crystal structure of 3-aza-bicyclo(3.3.1)nonane-2,4-dione as viewed along the *b*-axis: (*a*) 3-aza-bicyclo(3.3.1)nonane-2,4-dione at ambient pressure; (*b*) 3-aza-bicyclo(3.3.1)nonane-2,4-dione at 7.1 GPa. The colour scheme is the same as in Fig. 4.1.

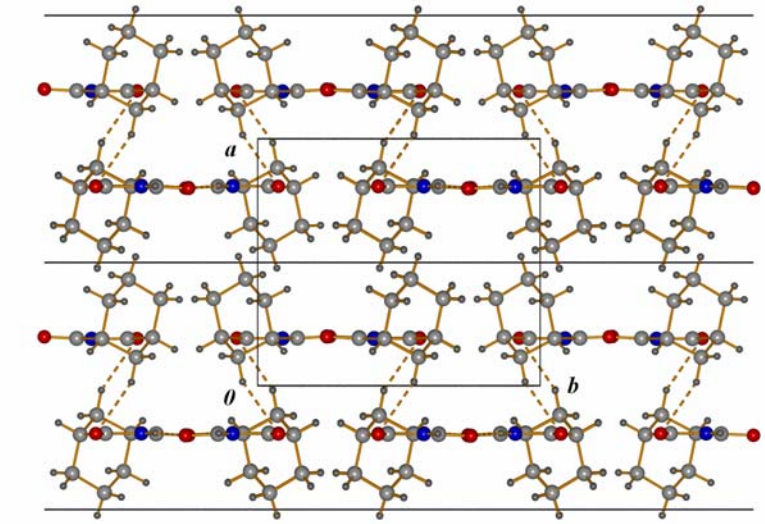

(a)

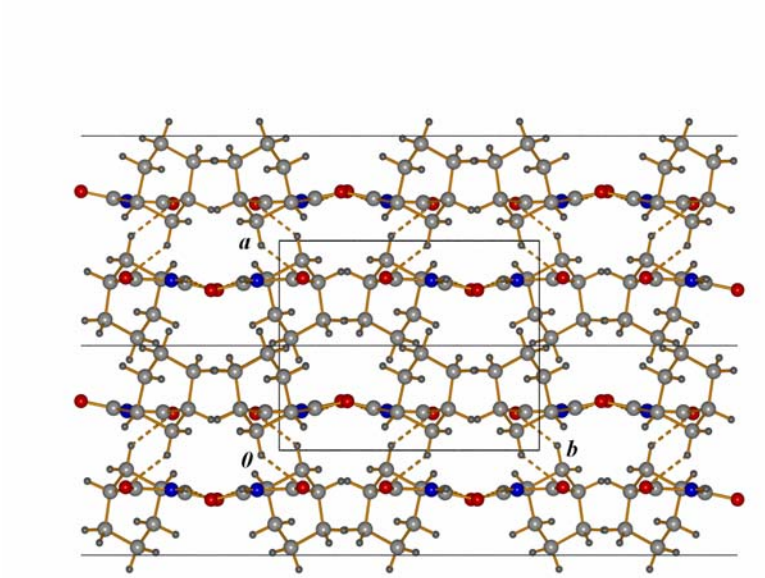

(b)

Figure 4.3: The effect of pressure on the crystal structure of 3-aza-bicyclo(3.3.1)nonane-2,4-dione as viewed along the *c*-axis: (*a*) 3-aza-bicyclo(3.3.1)nonane-2,4-dione at ambient pressure; (*b*) 3-aza-bicyclo(3.3.1)nonane-2,4-dione at 7.1 GPa. The colour scheme is the same as in Fig. 4.1. The horizontal lines indicate the slabs in the structure.

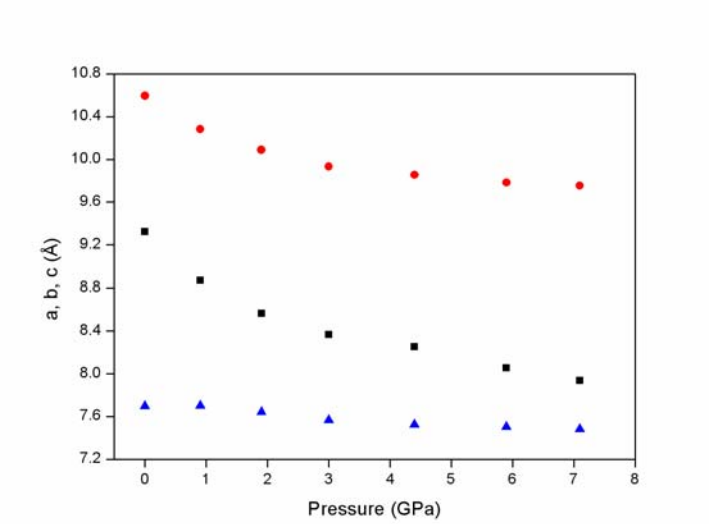

(a)

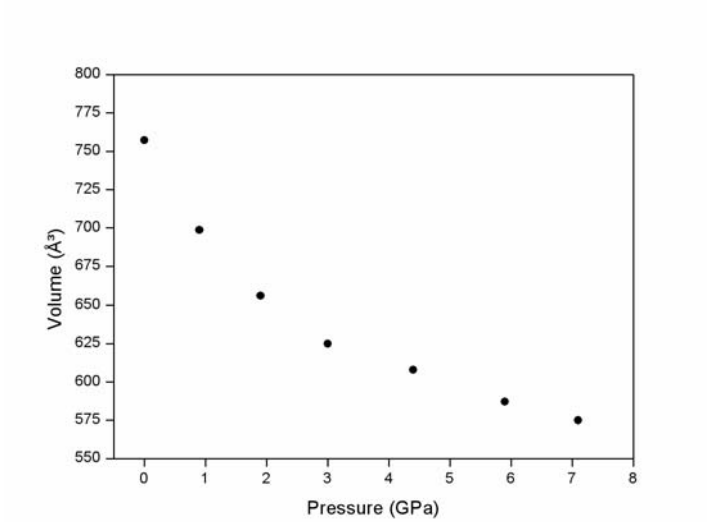

(b)

Figure 4.4: The variation of the lattice parameters *a*, *b*, *c* (Å) and volume (Å³) of 3-aza-bicyclo(3.3.1)nonane-2,4-dione as a function of pressure (GPa). The variation of *a*, *b* and *c* are shown on the same graph, with squares, circles and triangles respectively.

The dicarboximide fragment of the molecule distorts from planarity between ambient pressure and 7.1 GPa. The distances of the two carboxyl oxygen atoms (O1 and O2) from the plane through the atoms N1, C2 and C4 increases from 0.035 (2) (O1) and 0.119 (3) Å (O2) at ambient pressure to 0.19 (2) and 0.47 (2) Å at 7.1 GPa. Refinements in which the dicarboximide fragment was restrained to planarity (with a

restraint s.u. of 0.01 Å) led to an increase in R_1 from 7.6 to 9.2% and distortion of the rest of the structure, with C-C distances ranging from 1.38 to 1.68 Å. The deviation from planarity is therefore genuine, and not a consequence of low completeness or some other crystallographic or refinement artefact.

Pressure/GPa	0.0	0.9	1.9	3.0	4.4	5.9	7.1
N1H1..O2[i]							
H1..O2	2.13	2.10	2.05	2.02	1.97	1.94	1.96
N1..O2	2.979(2)	2.941(5)	2.897(6)	2.849(5)	2.808(5)	2.791(6)	2.799(11)
<N1H1O2	173(2)	170	167	167	168	168	162
C8H10..O1[ii]							
H10..O1	2.66	2.54	2.41	2.38	2.34	2.31	2.30
C8..O1	3.429(4)	3.288(10)	3.164(11)	3.103(11)	3.057(10)	3.017(14)	3.00(3)
<C8H10O1	136(2)	133	132	130	129	129	129
C3H3..O1[iii]							
H3..O1	2.59	2.45	2.41	2.33	2.29	2.19	2.13
C3..O1	3.503(4)	3.332(16)	3.267(17)	3.159(16)	3.111(14)	3.011(16)	2.95(3)
<C3H3O1	155(2)	151	146	144	142	141	141

Symmetry Operators:

i	*x*,-1/2-*y*,-1/2+*z*
ii	*x*,1/2-*y*,-1/2+*z*
iii	2-*x*,-*y*,1-*z*

Table 4.2: Non-covalent interaction parameters in 3-aza-bicyclo(3.3.1)nonane-2,4-dione. Distances are in Å, and angles in °.

The variation of non-covalent interaction parameters in the crystal structure of **1** during compression from ambient pressure to 7.1 GPa is shown in Table 4.2. The least compressible intermolecular interaction in the crystal structure is the N1H1…O2 hydrogen bond for which the N1…O2 distance decreases by 6.0% to a distance of 2.799 (11) Å at 7.1 GPa. Comparison of Figures 4.1*a* and *b* also shows that as the *C*(4) hydrogen bonded chains are pushed closer together, the NH…O geometry becomes less ideal and the N1H1…O2 angle decreases from 173 (1) to 162˚. The C…O distance in the C8H10…O1 contact, also formed in the *bc* plane,

decreases by 12.5%. Finally the C3H3…O1 weak hydrogen bond is the most compressible hydrogen-bonding interaction and the C3…O1 distance is reduced by 15.8%. The two CH…O interactions become less linear with pressure [136 (2) to 129˚ for C8H10…O1 and 155 (2) to 141˚ for C3H3…O1].

It is also notable that there is a considerable number of very short H…H contacts in the crystal structure at 7.1 GPa. In particular, there are five different contacts with a H…H distance shorter than 2.20 Å [H2…H4 = 1.974 (1), H4…H5 = 2.036 (1), H3…H1 = 2.133 (1), H9…H11 = 2.144 (1), H9…H9 = 2.186 (1) Å].

4.5 Discussion

4.5.1 Analysis of Non-covalent Interactions in the Structure

A search of the Cambridge Structural Database (CSD) for R_2N-H…O=CRN hydrogen bonds showed that the mean N…O distance is 2.89 (7) Å, with a minimum of 2.637 (5) Å [CSD refcode JUJSAI (Adhikary *et al.*, 1992)]. At 2.979 (2) Å, therefore, the N1H1…O2 interaction is actually quite long, and is not unusually short [2.799 (11) Å] even at 7.1 GPa. Hulme and co-workers have ascribed the weakness of the H-bonding in **1** to the reduction of the electrostatic potential in the region of the NH group by the neighbouring carbonyl groups (Hulme *et al.*, 2007). The minimum C…O distance in the CSD for CH…O interactions is 2.80 Å with less than 0.4% of 5784 interactions having a distance below this and only 4.4% of the sample having a distance less than 3.00 Å. C8H10…O1 and C3H3…O1, have relatively normal donor to acceptor distances at ambient conditions (Desiraju, 1996); these reduce to 3.00 (3) and 2.95 (3) Å at 7.1 GPa, but, as with the H-bond, these can not be described as unusually short.

We and others have investigated the effect of pressure on a number of organic systems and most either form a polycrystalline mass or undergo a phase transition at pressures considerably lower than 7.1 GPa. It appears that up to about 10 GPa non-covalent interactions tend to only be compressed to the limits of similar interactions seen at ambient conditions in the CSD (Dawson *et al.*, 2005, Moggach, Allan, Morrison *et al.*, 2005); if these limits are reached, further increase of pressure leads to a phase transition (or break-up of the sample). The non-covalent interactions in the

crystal structure of **1** have not attained ambient pressure minimum distances by 7.1 GPa, and so within a framework based purely on analysis of distances this is consistent with the absence of a phase transition in the present compression study.

4.5.2 Hirshfeld Surface Analysis

A particularly useful technique for studying the packing environment in a crystal structure is to analyse the molecular Hirshfeld surface. This surface is constructed by applying the Hirshfeld stockholder partitioning method to divide the crystal structure into regions in which the electron density of the crystal is dominated by the electron density of a specific molecule. A number of different properties can be plotted on the surface, including distances to nearest internal (d_i) and external atoms (d_e). The distance information contained within the Hirshfeld surface can also be condensed into a 2D graph of d_e against d_i, called a *fingerprint plot*, which has been shown to be very useful for identifying changes and similarities in packing (Fabbiani *et al.*, 2006, Moggach, Allan, Parsons *et al.*, 2006). The crystal structure at each pressure was used to calculate the molecular Hirshfeld surface and fingerprint plots using *CrystalExplorer*.

Figure 4.5 shows the Hirshfeld surfaces for **1** with the d_e property plotted on the surfaces using colours for the distance range 0.65 – 2.2 Å. Each surface is shown in two orientations for the ambient pressure and 7.1 GPa crystal structures. The numbering of the labelled regions refers to the dimers studied using the PIXEL method (see below). The blue regions on the surfaces indicate voids in the crystal structure and the red areas show short contacts. It can be seen that the blue areas present in the ambient surface are almost entirely absent at 7.1 GPa, which shows that the void regions in the structure have been reduced considerably. The largest blue regions, labelled V1 and V2 in Figure 4.5, each correspond to a significant void region, the first between the slabs of the structure and the second between the two planes within a slab. These voids are in the direction perpendicular to the slabs of the structure, which also corresponds to the direction of greatest compression in the structure as described earlier. The surfaces also show an increase in yellow and red

regions along with a reduction in surface volume of 24.5 % (from 185.2 to 139.8 Å^3) that is consistent with the overall shortening of packing interactions.

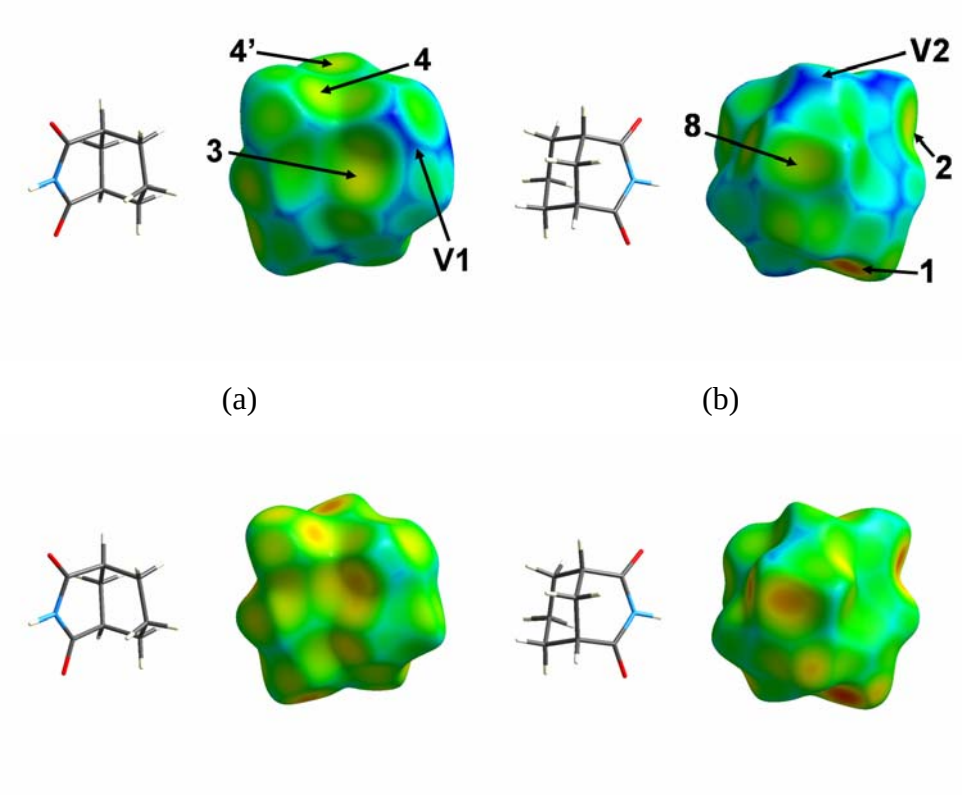

Figure 4.5: The Hirshfeld surface of 3-aza-bicyclo(3.3.1)nonane-2,4-dione at (*a*-*b*) ambient pressure and (*c*-*d*) 7.1 GPa with the d_e property mapped on the surface. Surfaces have been mapped over the range 0.65 – 2.2 Å. All hydrogen distances have been automatically reset to standard neutron X-H lengths (C-H = 1.083 Å and N-H = 1.009 Å. The orientations of the molecules have been included next to each surface for comparison. The colour scheme is red: oxygen, blue: nitrogen, grey: carbon and white: hydrogen. The numbered labels refer to the text.

Figures 4.5*a* and *c* show the appearance of two red regions at 7.1 GPa, labelled 4' & 3, which indicate very short contacts. These two areas correspond to the contacts H2…H4 and H9…H9/H11 respectively. The weak hydrogen bond C8H10…O1 is also seen to compress considerably as the region corresponding to this contact, labelled 4 in Figure 4.5*a*, changes from yellow to red. Other contacts that become visibly shorter in the Hirshfeld surface are C3H3…O1 and H4…H5, labelled 2 & 8 respectively in Figure 4.5*b*, for which the interaction regions again

change from yellow to red. The shortening of the N1H1…O2 hydrogen bond can also be seen in Figure 4.5*d* by the increase in size and darkening of the red region, labelled 1.

The fingerprint plots for the crystal structure of **1** at ambient pressure and 7.1 GPa are shown in Figure 4.6. The shape of the plot itself is seen to become smaller, due to the general shortening of intermolecular interactions, and more symmetrical about the d_e/d_i axis. Asymmetry in fingerprint plots is caused by gaps in the structure where surfaces do not touch (McKinnon *et al.*, 2004), and the increase in symmetry of the plots shown in Figure 4.6 is due to the reduction of intermolecular voids with pressure. The two long spikes in Figure 4.6*a* represent the N1H1…O2 hydrogen bonding interaction and the region highlighted with a red circle in between these spikes represents close H…H contacts in the structure. It can be seen from the two plots that the hydrogen bonds only decrease a small amount on compression to 7.1 GPa and that at this pressure the hydrogen bond spikes are much less pronounced with the H…H region becoming more prominent.

4.5.3 PIXEL Analysis

The preceding discussion has analysed intermolecular interactions in a mostly qualitative manner. The PIXEL method, a technique developed recently by Gavezzotti (Gavezzotti, 2003, 2005, Dunitz & Gavezzotti, 2005a), allows quantitative determination of crystal lattice energies and dimer energies along with a breakdown of these energies into Coulombic, polarisation, dispersion and repulsion terms. This method involves calculating the electron density of an isolated molecule from the crystal structure molecular geometry using a standard quantum mechanical package such as *GAUSSIAN98*. The model of electron density is then condensed into larger pixels and the energies are determined by performing pixel by pixel interaction calculations between molecules and then summing over all the pixels. An example of the use of the PIXEL method in analysing the relative energies of intermolecular interactions within a structure is given by Dunitz & Gavezzotti (Dunitz & Gavezzotti, 2005a, b).

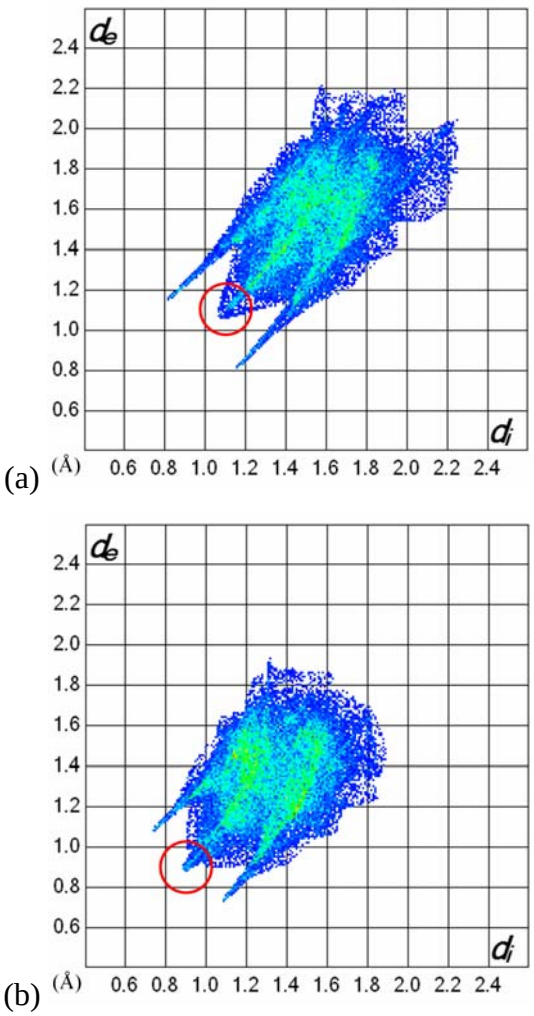

Figure 4.6: Two-dimensional fingerprint plots for 3-aza-bicyclo(3.3.1)nonane-2,4-dione at (*a*) ambient pressure and (*b*) 7.1 GPa. The regions corresponding to close H…H contacts are highlighted using red circles.

The intermolecular lattice energies and a breakdown into the component terms for **1** for each structure from ambient pressure to 7.1 GPa were calculated and are shown in Table 4.3. The dicarboximide fragment of the molecule distorts from planarity during compression, and this affects the internal energy of the molecule. An adjusted total energy (U_{adj}) is shown in the table which is the total lattice energy minus the difference in internal energy of the molecule (as calculated by *GAUSSIAN98*) with respect to the ambient pressure conformation. Also calculated are the values of the enthalpy, $H = U_{adj} + PV$, where P = pressure and V = molar volume = unit cell volume/Z.

Pressure/ GPa	Coulombic	Polarisation	Dispersion	Repulsion	*U*	U_{adj}*	*H*†	*Test*‡
0.0	-55.2	-20.5	-85.2	72.6	-88.4	-88.4	-88.4	253.6
0.9	-69.7	-28.2	-107.7	113.7	-92.0	-71.3	23.4	244.2
1.9	-89.1	-38.5	-128.3	164.5	-91.4	-70.5	117.2	225.8
3.0	-109.3	-49.4	-147.9	226.8	-79.7	-62.0	220.2	220.2
4.4	-124.3	-56.2	-158.5	270.4	-68.6	-48.0	354.7	226.6
5.9	-144.8	-67.2	-174.3	330.8	-55.5	-29.0	492.5	236.2
7.1	-158.8	-76.8	-184.7	378.5	-41.8	-0.3	614.2	259.4

***** Adjusted Energy (U_{adj}) = *U* – Energy difference due to conformation change relative to 0.0 GPa structure evaluated using *GAUSSIAN98* calculations at the MP2/6-31G** level.

† Enthalpy (*H*) = U_{adj} + *PV*, where *P* = pressure (in Pascals) and *V* = molar volume (in $m^3\ mol^{-1}$).

‡ The enthalpy data has been tested for consistency by selecting a pressure (in this test 3.0 GPa was chosen) and evaluating the enthalpy for each structure based on the values of U_{adj} and *V* determined for that structure along with the selected *P* of 3.0 GPa. For example, in the 1.9 GPa structure, U_{adj} = -70.5 kJ mol^{-1}, *V* = 9.878×10^{-5} m^3 mol^{-1}, therefore the enthalpy = $-70.5 \times 10^3 + (3.0 \times 10^9 \times 9.878 \times 10^{-5})$ = 225840 J mol^{-1} = 225.8 kJ mol^{-1}.

Table 4.3: Components of lattice energy, the total intermolecular energy (*U*) and the total energy adjusted for changes in the internal structure of the 3-aza-bicyclo(3.3.1)nonane-2,4-dione molecules during compression (U_{adj}). The enthalpy (*H*) at each pressure is also given along with an example test for the consistency of the enthalpy data (see text). All energies are in kJ mol^{-1}.

The dominant energy terms are Coulombic and dispersion interactions, with polarisation playing a lesser role. It is notable that the value of U_{adj} becomes more positive with increasing pressure, as a result of increased repulsion between molecules. The lattice energy approaches zero at the highest pressure reached in this study (7.1 GPa), and would presumably become positive at still higher pressures: there is a lot of energy stored-up in the compressed intermolecular interactions. Of

course, more stable polymorphs may exist, but the corresponding phase transition may be kinetically hindered.

The values of the enthalpy also become more positive as pressure is increased, reaching an enormous +612 kJ mol^{-1} at 7.1 GPa. To a chemist the numbers in Table 4.3, which are a consequence of the *PV* terms, seem large and unfamiliar, but they reflect the large amount of work done in compressing the sample. Moreover, it is relative enthalpies that are important, and any putative gaseous state would have an even higher *PV* term than the crystal on account of its having a larger volume. A test of the consistency of the data presented in Table 4.3 is to calculate the quantity $U_{adj} + PV$ where *P* is held constant and the U_{adj} and *V* terms are those determined at each pressure (an example is given in Table 4.3); when plotted against *P* this quantity should have a minimum at the value of *P* used in the calculations. This procedure, when carried out for each pressure used in this study, reproduces minima at or near the expected values of *P*, confirming that each structure is at an enthalpy minimum.

PIXEL calculations can be calculated between pairs of molecules in order to find their dimer interaction energies. Initial analysis showed that there are nine dimers in the ambient crystal structure which have a significant stabilising interaction (energy < -2.5 kJ mol^{-1}) and these dimers, shown in Figure 4.7, are labelled 1-9 in descending order of ambient-pressure interaction energy. The hydrogen bond N1H1…O2 is found to be the strongest interaction (1) and the two CH…O interactions, C3H3…O1 and C8H10…O1, correspond to dimers 2 and 4 respectively. Dimer 2 also corresponds to a stacking arrangement of the carboximide fragments in adjacent molecules. The third most stabilising interaction energetically, dimer 3, is a van der Waals interaction between molecules in separate slabs of the structure, for which the closest contact is H9…H9/H11. Interactions 5, 6 and 7 correspond to very long CH…O contacts, C6H6…O1, C3H3…O2 and C7H8…O2 respectively. The last two dimers, interactions 8 and 9, are both van der Waals contacts between the alkyl sides of the molecules where the closest contacts are H5…H3/H4 and H8…H6/H7 for dimers 8 and 9 respectively.

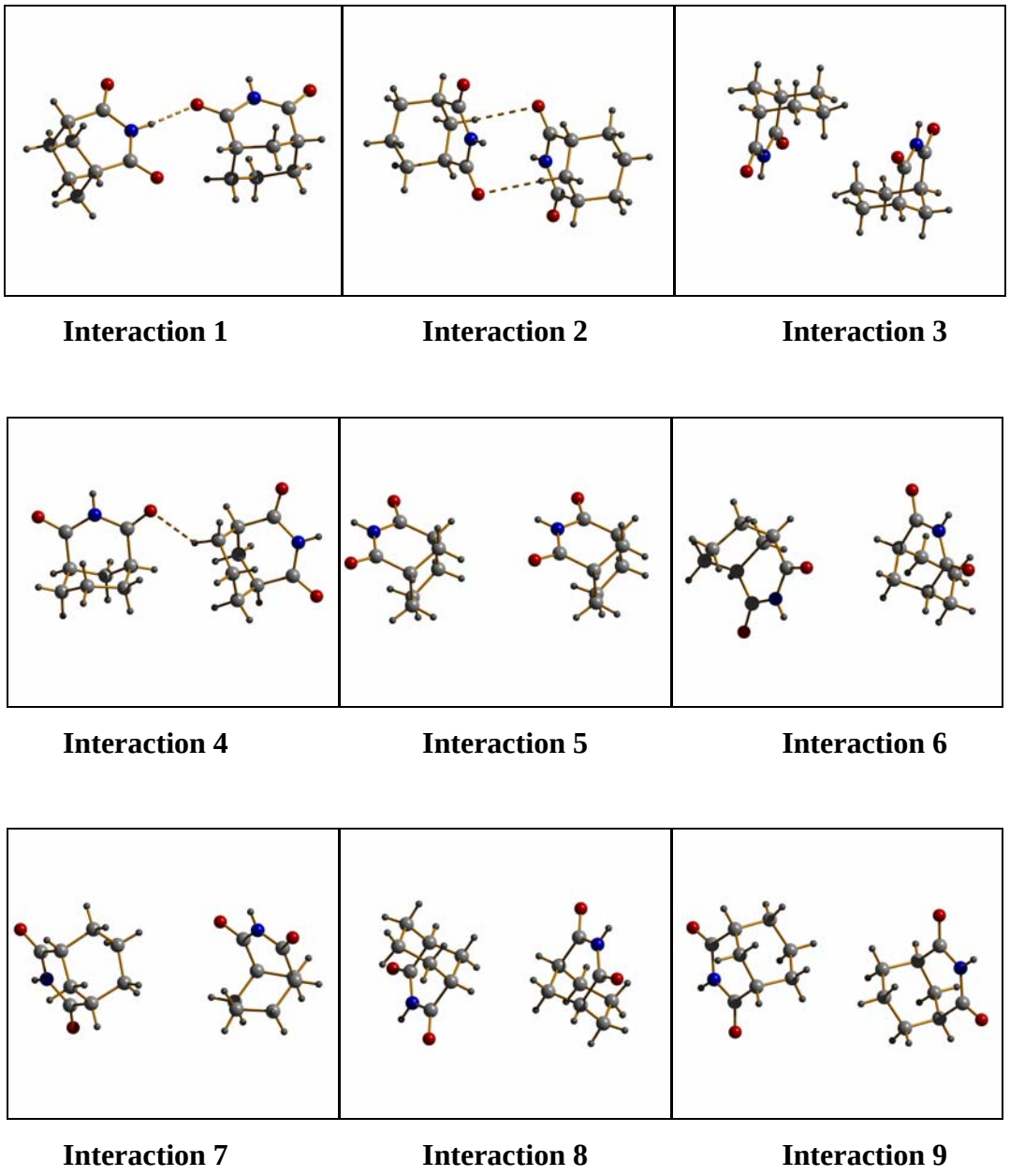

Figure 4.7: Diagrams of the most energetically important dimers in the 3-aza-bicyclo(3.3.1)nonane-2,4-dione crystal structure from PIXEL analysis. The colour scheme is the same as in Fig. 4.1.

Figure 4.8 shows a graph of the total interaction energies of the nine dimers as a function of the distance between the centroids of the two molecules involved in the dimer. These curves show the effect of compression on the energy of each interaction, identifying quantitatively which interactions are becoming short and

destabilising. The graph shows that interactions 5, 6 and 7, the three very long CH…O contacts, are relatively unaffected by the increase in pressure. The curve for interaction 1, the NH…O hydrogen bond, is also very shallow. This result contrasts with PIXEL calculations on salicylaldoxime (Chapter 2, Figure 2.10), in which H-bond energies have been shown to be very sensitive to pressure, but is consistent with the results from CSD searches described above, which indicated that this interaction is not particularly short.

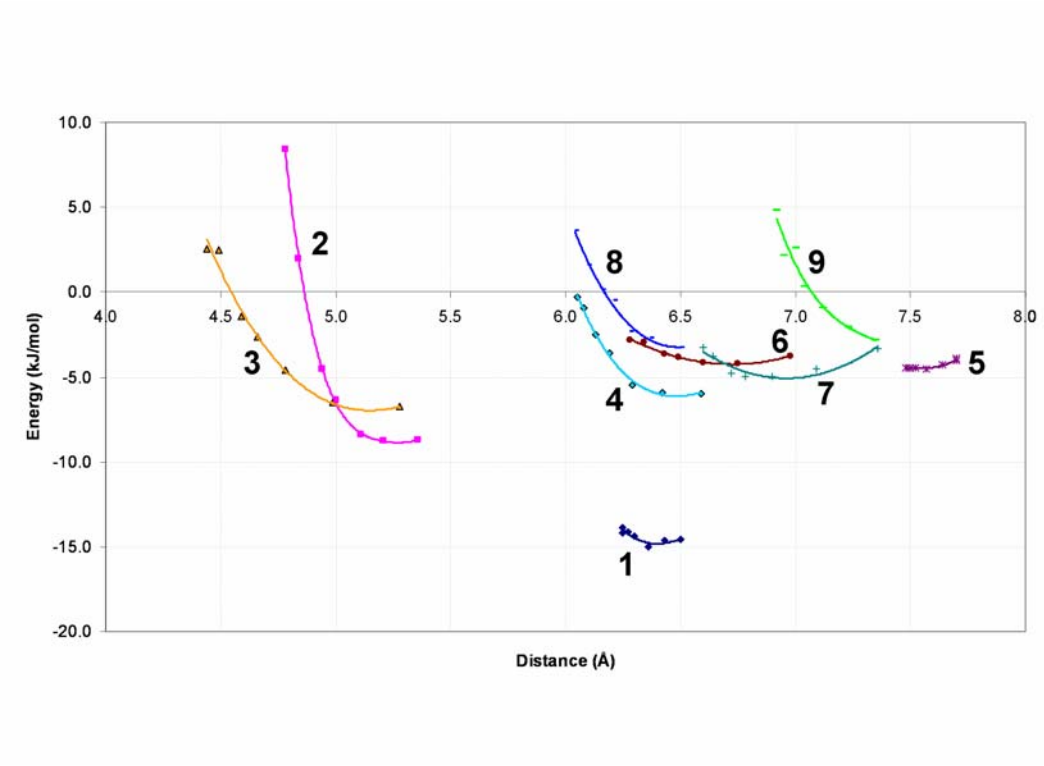

Figure 4.8: Graph of total interaction energy for the nine most energetically important dimers (in kJ mol^{-1}) against the distance between the molecular centroids of the molecules involved in the interaction (in Å).

The curves for interactions 2 and 3 become very steep; in other systems this behaviour has been seen to be a prelude to a phase transition. The fact that interaction 3, an alkyl H9…H9/H11 contact, becomes very destabilising may explain why the NH…O interaction does not become shorter: the alkyl group actually acts as a spacer, keeping apart the two molecules of dimer 1. Dimers 4, 8 and 9, which relate to contacts C8H10…O1, H5…H3/H4 and H8…H6/H7 respectively, also steepen showing that these interactions also become quite destabilising. Dimer 4, which

corresponds to the C8H10…O1 contact, also involves a short H2…H4 contact (1.97 Å), which may explain why this interaction becomes destabilising even though the CH…O distance does not seem to become unusually short. With the exception of interaction 9, these interactions found to be becoming destabilising at high pressures also correspond directly to the contact regions indicated as becoming very short through analysis of the Hirshfeld surfaces (Figure 4.5).

The results of these dimer calculations suggest that dispersion dominated interactions such as CH…O and H…H contacts are just as important in terms of the response of the crystal structure of **1** to compressions as the hydrogen bonds. The compression curves also show that as pressure is increased the CH…O and H…H contacts dominate the changes in lattice energy and that the NH…O interaction is not strongly affected by pressure.

4.6 Conclusions

We have described the crystallisation of **1** at high pressure and the subsequent effects of compression on the crystal structure to 7.1 GPa. The structure consists of *C*(4) chains running in the direction of the *c*-axis formed by N1H1…O2 hydrogen bonds. These chains are connected to neighbouring chains to form sheets in the *bc* plane by C8H10…O1 interactions. Each sheet also interacts with another sheet through C3H3…O1 interactions across an inversion centre, forming slabs. There are no hydrogen bonds between the slabs with the only interaction being van der Waals contacts between the alkyl moieties of the molecules. This phase is found to be stable under compression to 7.1 GPa - this is unusually high: most organic materials studied in our laboratory to date either became polycrystalline or underwent a phase transition at pressures lower than this.

The crystal structure of **1** has been regarded as a ‘problem structure’ because it fails to conform to preconceived ideas of likely preferences for packing based on dimers. A similar case is alloxan, which also contains the carboximide fragment, and which has recently been discussed by Dunitz & Schweizer (Dunitz & Schweizer, 2007). The structure of alloxan is a result of a collection of individually non-optimal interactions which together form a strong lattice which is competitive with more

extensively H-bonded alternatives. Much the same can be said of **1**. PIXEL analysis shows that the NH…O H-bond in the crystal structure of **1** is relatively weak (-14.6 kJ mol^{-1}), and that a pair of CH…O contacts and a van der Waals interaction are of comparable energy (between -8.7 and -6.0 kJ mol^{-1}). These relative energies have very little bearing on the relative preference of **1** for forming chains over dimers as one NH…O hydrogen bond is formed per molecule in either pattern, however they do show that the hydrogen bonding is not as dominant in terms of packing as might otherwise be expected.

The NH…O hydrogen bond is still the least compressible interaction in the structure, but this contact is prevented from shortening further by close contacts between alkyl groups. Analysis of the Hirshfeld surfaces and fingerprint plots of the crystal structure at ambient pressure and 7.1 GPa identified the largest structural voids at ambient conditions and showed how these were reduced by compression. The surfaces also facilitated identification of the short contacts which appeared at pressure including two close CH…O interactions and three contacts between alkyl groups. PIXEL dimer calculations then showed that the CH…O interactions and various H…H contacts in the structure are more affected by pressure than the hydrogen bond, becoming destabilising at the highest pressures studied. It appears that the response to pressure is dominated by dispersion interactions rather than hydrogen bonds. A similar situation to this was seen in a compression study of L-cysteine-I (Moggach, Allan, Clark *et al.*, 2006) where a short S…S contact appeared to drive a transition to a new phase, L-cysteine-III. No phase transition was observed for **1** to a dimer-based or any other structure, though from the curves in Figure 4.8 some sort of structural modification might be expected at pressures higher than 7 GPa.

Analysis of the output of the *GAUSSIAN98* electron density calculations showed that the distortion of the dicarboximide fragment of **1** from planarity had a considerable effect on the internal energy of the molecule. The difference in internal energy became as high as 40 kJ mol^{-1} at a pressure of 7.1 GPa. This significant change in molecular geometry has shown that it is necessary to observe carefully the

effects of pressure on the intramolecular interactions even for molecules that are relatively rigid.

This study has also shown that the use of Hirshfeld surfaces and the PIXEL method together is a particularly effective combination for analysing changes in crystal structures. The Hirshfeld surfaces and fingerprint plots allow qualitative analysis of the crystal packing all at once in a completely unique manner, thus reducing the chance of missing important contacts. Allied to this is the PIXEL method with which it is possible to determine quantitatively the contribution to the lattice energy of individual dimer contacts and the effect of pressure on these energies.

4.7 References

Adhikary, B., Nanda, K. K., Das, R., Venkatsubramanian, K., Paul, P. & Nag, K. (1992). *Journal of Chemical Research* **10**, 332-333.

Allen, F. H. (2002). *Acta Crystallographica, Section B* **58**, 380-388.

Allen, F. H. & Motherwell, W. D. S. (2002). *Acta Crystallographica, Section B* **58**, 407-422.

Altomare, A., Cascarano, G., Giacovazzo, C., Guagliardi, A., Burla, M. C., Polidori, G. & Camalli, M. (1994). *Journal of Applied Crystallography* **27**, 435-435.

Angel, R. J. (2000). *Reviews in Mineralogy and Geochemistry* **41**, 35-59.

Angel, R. J., Downs, R. T. & Finger, L. W. (2000). *Reviews in Mineralogy and Geochemistry* **41**, 559-596.

Bernstein, J., Davis, R. E., Shimoni, L. & Chang, N.-L. (1995). *Angewandte Chemie, International Edition* **34**, 1555-1573.

Betteridge, P. W., Carruthers, J. R., Cooper, R. I., Prout, K. & Watkin, D. J. (2003). *Journal of Applied Crystallography* **36**, 1487.

Birch, F. (1947). *Physical Review* **71**, 809-824.

Bruker-Nonius (2006). *SAINT version 7, Program for integration of area detector data*. Bruker-AXS, Madison, Wisconsin, USA.

Bruno, I. J., Cole, J. C., Edgington, P. R., Kessler, M., Macrae, C. F., McCabe, P., Pearson, J. & Taylor, R. (2002). *Acta Crystallographica, Section B* **58**, 389-397.

Crystal Impact (2004). *DIAMOND version 3.0, Visual crystal structure information system*. Crystal Impact GbR, Postfach 1251, 53002, Bonn, Germany.

Dawson, A., Allan, D. R., Belmonte, S. A., Clark, S. J., David, W. I. F., McGregor, P. A., Parsons, S., Pulham, C. R. & Sawyer, L. (2005). *Crystal Growth & Design* **5**, 1415-1427.

Dawson, A., Allan, D. R., Parsons, S. & Ruf, M. (2004). *Journal of Applied Crystallography* **37**, 410-416.

Desiraju, G. R. (1996). *Accounts of Chemical Research* **29**, 441-449.

Dunitz, J. D. & Gavezzotti, A. (2005a). *Angewandte Chemie, International Edition* **44**, 1766-1787.

Dunitz, J. D. & Gavezzotti, A. (2005b). *Crystal Growth & Design* **5**, 2180-2189.

Dunitz, J. D. & Schweizer, B. W. (2007). *CrystEngComm* **9**, 266–269.

Fabbiani, F. P. A., Allan, D. R., Marshall, W. G., Parsons, S., Pulham, C. R. & Smith, R. I. (2005). *Journal of Crystal Growth* **275**, 185-192.

Fabbiani, F. P. A., Allan, D. R., Parsons, S. & Pulham, C. R. (2006). *Acta Crystallographica, Section B* **62**, 826-842

Farrugia, L. J. (1999). *Journal of Applied Crystallography* **32**, 837-838.

Frisch, M. J., Trucks, G. W., Schlegel, H. B., Scuseria, G. E., Robb, M. A., Cheeseman, J. R., Zakrzewski, V. G., Montgomery, J. A. J., Stratmann, R. E., Burant, J. C., Dapprich, S., Millam, J. M., Daniels, A. D., Kudin, K. N., Strain, M. C., Farkas, O., Tomasi, J., Barone, V., Cossi, M., Cammi, R., Mennucci, B., Pomelli, C., Adamo, C., Clifford, S., Ochterski, J., Petersson, G. A., Ayala, P. Y., Cui, Q., Morokuma, K., Malick, D. K., Rabuck, A. D., Raghavachari, K., Foresman, J. B., Cioslowski, J., Ortiz, J. V., Stefanov, B. B., Liu, G., Liashenko, A., Piskorz, P., Komaromi, I., Gomperts, R., Martin, R. L., Fox, D. J., Keith, T., Al-Laham, M. A., Peng, C. Y., Nanayakkara, A., Gonzalez, C., Challacombe, M., Gill, P. M. W., Johnson, B. G., Chen, W., Wong, M. W., Andres, J. L., Head-Gordon, M., Replogle, E. S. & Pople, J. A. (1998). *Gaussian 98 revision A.7*, Gaussian, Inc., Pittsburgh, PA, USA.

Gavezzotti, A. (2003). *OPiX, A computer program package for the calculation of intermolecular interactions and crystal energies*. University of Milano, Milan, Italy.

Gavezzotti, A. (2005). *Zeitschrift fuer Kristallographie* **220**, 499-510.

Hazen, R. M. & Finger, L. W. (1982). Comparative Crystal Chemistry: Temperature, Pressure, Composition and the Variation of Crystal Structure, p. 81. Chichester, New York, USA: John Wiley and Sons.

Howie, A. R. & Skakle, J. M. S. (2001). *Acta Crystallographica, Section E* **57**, o822-o824.

Hulme, A. T., Fernandes, P., Florence, A., Johnston, A. & Shankland, K. (2006). *Acta Crystallographica, Section E* **62**, o3046-o3048.

Hulme, A. T., Johnston, A., Florence, A. J., Fernandes, P., Shankland, K., Bedford, C. T., Welch, G. W. A., Sadiq, G., Haynes, D. A., Motherwell, W. D. S., Tocher, D. A. & Price, S. L. (2007). *Journal of the American Chemical Society* **129**, 3649-3657.

Lozano-Casal, P., Allan, D. R. & Parsons, S. (2005). *Acta Crystallographica, Section B* **61**, 717-723.

McKinnon, J. J., Spackman, M. A. & Mitchell, A. S. (2004). *Acta Crystallographica, Section B* **60**, 627-668.

Merrill, L. & Bassett, W. A. (1974). *Review of Scientific Instruments* **45**, 290-294.

Moggach, S. A., Allan, D. R., Clark, S. J., Gutmann, M. J., Parsons, S., Pulham, C. R. & Sawyer, L. (2006). *Acta Crystallographica, Section B* **62**, 296-309.

Moggach, S. A., Allan, D. R., Morrison, C. A., Parsons, S. & Sawyer, L. (2005). *Acta Crystallographica, Section B* **61**, 58-68.

Moggach, S. A., Allan, D. R., Parsons, S. & Sawyer, L. (2006). *Acta Crystallographica, Section B* **62**, 310-320.

Moggach, S. A., Allan, D. R., Parsons, S., Sawyer, L. & Warren, J. E. (2005). *Journal of Synchrotron Radiation* **12**, 598-607.

Motherwell, W. D. S., Ammon, H. L., Dunitz, J. D., Dzyabchenko, A., Erk, P., Gavezzotti, A., Hofmann, D. W. M., Leusen, F. J. J., Lommerse, J. P. M., Mooji, W. T. M., Price, S. L., Scheraga, H., Schweizer, B., Schmidt, M. U., Van Eijck, B. P., Verwer, P. & Williams, D. E. (2002). *Acta Crystallographica, Section B* **58**, 647-661.

Oswald, I. D. H., Allan, D. R., Motherwell, W. D. S. & Parsons, S. (2005). *Acta Crystallographica, Section B* **61**, 69-79.

Parsons, S. (2003). *STRAIN, Program for calculation of linear strain tensors*. The University of Edinburgh, Edinburgh, UK.

Parsons, S. (2004). *SHADE, Program for empirical absorption corrections to high pressure data*. The University of Edinburgh, Edinburgh, United Kingdom.

Piermarini, G. J., Block, S., Barnett, J. D. & Forman, R. A. (1975). *Journal of Applied Physics* **46**, 2774-2780.

Press, W. H., Teukolsky, S. A., Vetterling, W. T. & Flannery, B. P. (1992). Numerical Recipes in Fortran, 2nd ed. Cambridge, UK: Cambridge University Press.

Sheldrick, G. M. (2004). *SADABS Version 2004-1, Program for absorption corrections to area detector data*. Bruker-AXS, Madison, Wisconsin, USA.

Slebodnick, C., Zhao, J., Angel, R., Hanson, B. E., Song, Y., Liu, Z. & Hemley, R. J. (2004). *Inorganic Chemistry* **43**, 5245-5252.

Spek, A. L. (2003). *Journal of Applied Crystallography* **36**, 7-13.

Wolff, S. K., Grimwood, D. J., McKinnon, J. J., Jayatilaka, D. & Spackman, M. A. (2005). *CrystalExplorer 1.5*, University of Western Australia, Perth, Australia.

Chapter 5

A Study of Phase Transitions in the Compression of L-serine using *Ab Initio* Structures and PIXEL Calculations*

* Wood, P. A., Marshall, W. G., Moggach, S. A., Parsons, S., Pidcock, E., Rohl, A. L. (2008). *CrystEngComm*, submitted, 2008.

5.1 Synopsis

The crystal structures of L-serine phases I, II and III have been optimised at pressures from ambient to 8.1 GPa using *ab initio* density functional theory. The phase-I to II transition is driven by a change in conformation of the serine molecules and a reduction in volume, while an intermolecular OH…carboxylate hydrogen bond strengthens in the II-to-III transition.

5.2 Introduction

The experimental equipment and techniques involved in small molecule high pressure crystallography are fast becoming accessible to more research groups. The software to deal with high pressure data from CCD detectors has also improved the quality of data and ease of structural determination considerably (Dawson *et al.*, 2004). This means that the number of structure determinations at pressure has risen very quickly in recent years and will continue to rise. The number of organic structures (with 3D coordinates) added per year to the Cambridge Structural Database (CSD) with the required field of pressure included has risen from less than ten in all previous years to over 60 in both 2005 and 2006.

As the number of compression studies performed on small organic crystal structures has increased, a greater number of pressure-induced phase transitions have been found. These phase transitions have been rationalised by analysing the effects of pressure on intermolecular contact distances. Intermolecular interactions have so far been found not to become shorter than those seen for chemically similar contacts at ambient conditions in the Cambridge Database; phase transitions are observed once a lower limit has been reached. This idea has been used to 'explain' transitions due to short hydrogen bonds in L-serine-I (Moggach *et al.*, 2005) and close S…S contacts in L-cysteine-I (Moggach, Allan *et al.*, 2006). In order to advance our understanding of the effects of pressure on a crystal structure and to learn more about why phase transitions occur, it is desirable to quantify the effect of compression on interaction *energies* rather than to rely only on distance information.

Periodic density functional theory (DFT) can provide quantification of interaction energies in the solid state (Morrison & Siddick, 2003, Boese *et al.*, 2003).

These calculations are, however, very computationally expensive and therefore not ideal for systematically studying the effects of pressure on the geometries, and thus the energies, of multiple intermolecular interactions in a crystal structure.

A relatively new technique, called the PIXEL method (Gavezzotti, 2005), has been developed which allows calculation of lattice and intermolecular dimer energies along with a breakdown of the energies into their Coulombic, dispersion, polarisation and repulsion components. This method has already been shown to be particularly useful in determining the causes of the pressure-induced phase transition in the structure of salicylaldoxime-I (Chapter 2).

L-serine is an ideal test case for studying phase transitions caused by compression because there is already structural compression data at pressures from ambient to 8.1 GPa (Moggach, Marshall *et al.*, 2006) and two phase transitions are seen to occur within this pressure regime. The effect of pressure on the crystal structure of L-serine has been studied using X-ray single-crystal diffraction (Moggach *et al.*, 2005) and neutron powder diffraction (Moggach, Marshall *et al.*, 2006). The ambient pressure phase (L-serine-I) crystallises in space group $P2_12_12_1$ and is made up of *C*(5) chains formed along the *c*-axis by N1H5…O2 hydrogen bonds. Pairs of these *C*(5) chains are linked into ribbons by N1H6…O1 hydrogen bonds between molecules related by a 2_1 operation, which form repeated $R_3^3(11)$ ring motifs. The ribbons interact on both sides with adjacent ribbons *via* the hydroxyl side-chains to form an infinite O3H7…O3 hydrogen-bonded chain, thus forming layers in the *bc* plane (Figure 5.1a) which are referred to as the *A* layers by Moggach and co-workers (Moggach *et al.*, 2005). These layers are then linked together by N1H4…O2 hydrogen bonds in the *a*-direction thus forming another set of *C*(5) chains and, when taken with the N1H5…O2 chains, they form another set of layers in the *ac* plane referred to as the *B* layers (Figure 5.2a).

The phase transition from phase I to phase II is isosymmetric and occurs with a substantial decrease in unit cell volume. In phase II the ribbons and $R_3^3(11)$ rings of phase I remain essentially the same except with further compression in the *c*-direction, but now the hydroxyl groups have rotated to form O3H7…O2 hydrogen bonds with the carboxyl group of a neighbouring chain (Figure 5.1b). This transition

is therefore accompanied by a change in the conformation of the L-serine molecule (Figure 5.3). The layers are again linked together by the N1H4…O2 hydrogen bonds (Figure 5.2b).

(a)

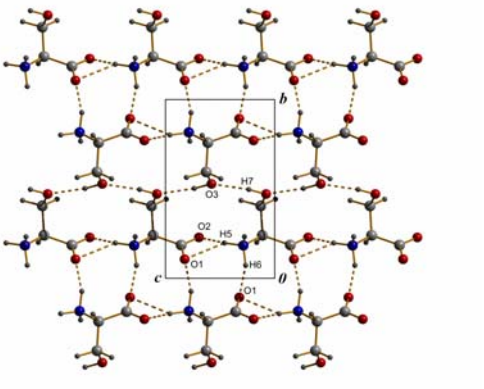

(b)

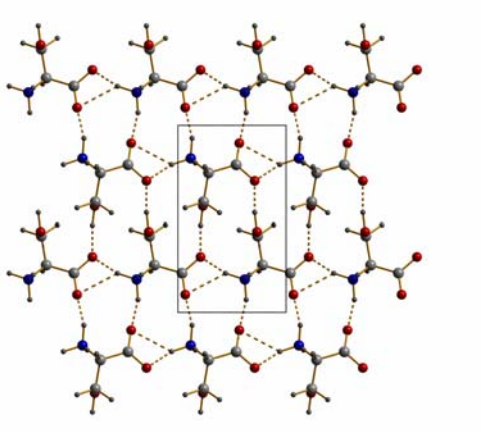

(c)

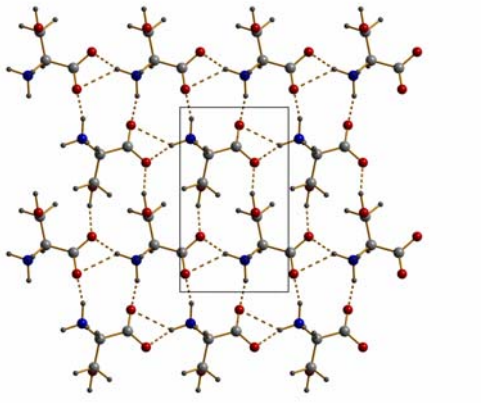

Figure 5.1: The effect of pressure on the theoretical crystal structure of L-serine as viewed along the *a*-axis: (*a*) L-serine-I at ambient pressure; (*b*) L-serine-II at 5.2 GPa; (*c*) L-serine-III at 8.1 GPa. This layer is referred to as the *A* layer in the text. The colour scheme is red: oxygen, blue: nitrogen, light-grey: carbon and dark-grey: hydrogen.

The second phase transition, from phase II to phase III, is also isosymmetric but does not involve a significant decrease in unit cell volume. The hydrogen bonding motifs remain largely the same during this phase transition except there is a substantial shift of the *B* layers (Figure 5.1c) in the structure with respect to each other which causes the O3H7 hydrogen bond donor to form a bifurcated interaction, with O2 and O1 of separate molecules as acceptors.

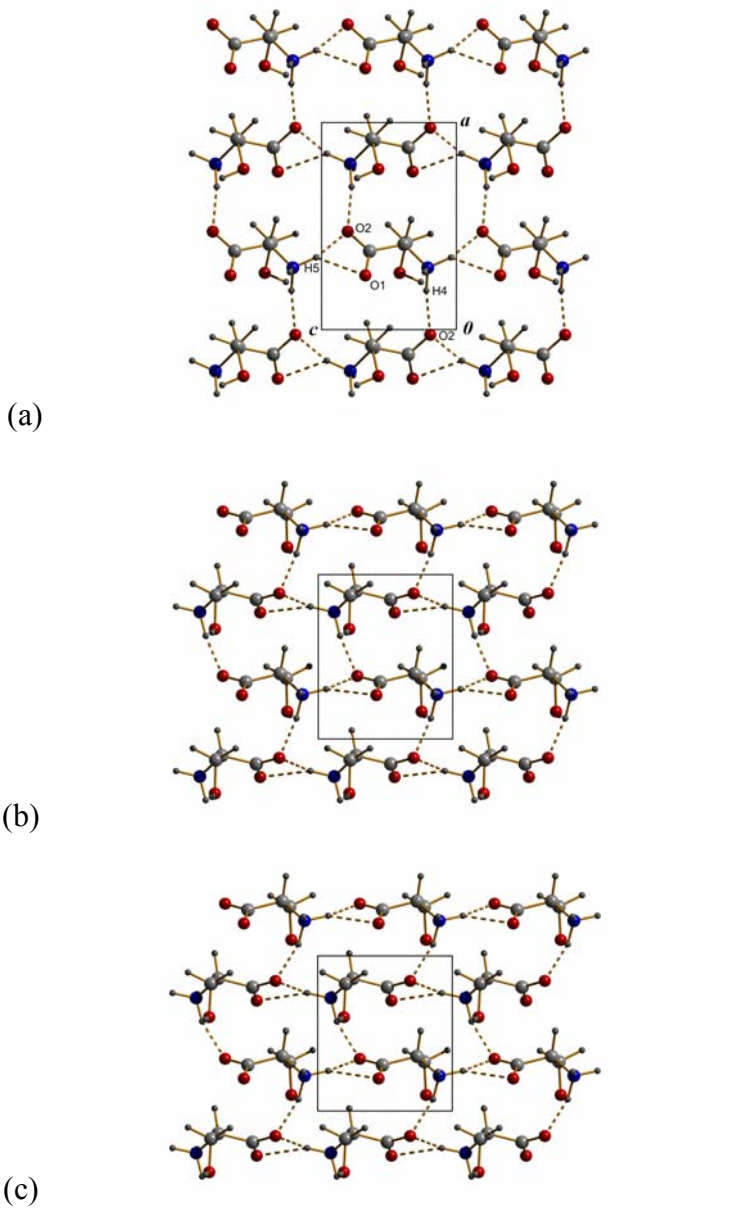

(a)

(b)

(c)

Figure 5.2: The effect of pressure on the theoretical crystal structure of L-serine as viewed along the *b*-axis: (*a*) L-serine-I at ambient pressure; (*b*) L-serine-II at 5.2 GPa; (*c*) L-serine-III at 8.1 GPa. This layer is referred to as the *B* layer in the text. The colour scheme is the same as in Fig. 5.1.

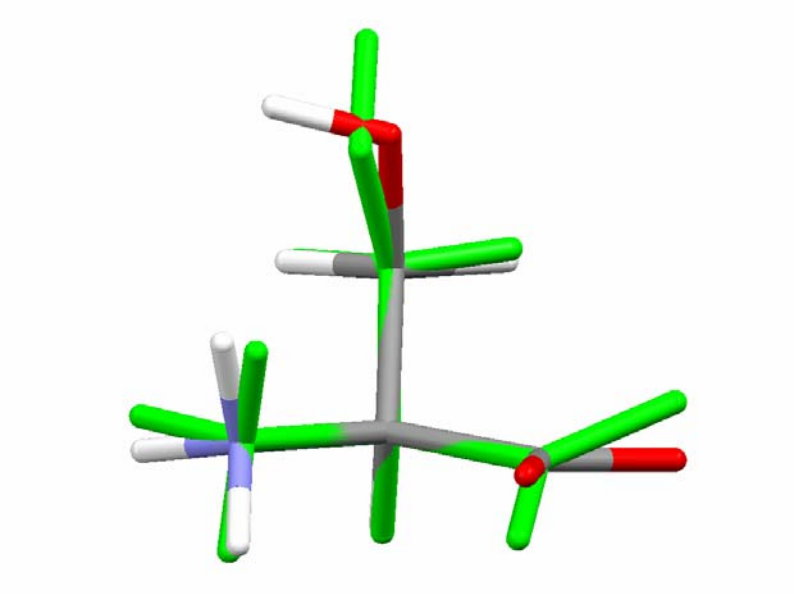

Figure 5.3: Structure overlay using a capped sticks model showing the change in conformation of the L-serine molecule between phase I at 4.5 GPa (coloured by element) and phase-II at 5.2 GPa (green). The overlay shows the rotation of the hydroxyl group, a twisting of the carboxyl group and a slight rotation of the amino group. The colour scheme for the elements is red: oxygen, blue: nitrogen, light-grey: carbon and white: hydrogen.

Here we describe the *ab initio* DFT calculation of the structure of L-serine at pressures from ambient to 8.1 GPa starting from the coordinates determined by neutron powder diffraction. The theoretical structures have also been used to perform PIXEL lattice and dimer calculations in order to analyse the causes of the two phase transitions more fully.

5.3 Experimental

Note: The neutron powder diffraction data were collected by Dr. William Marshall of ISIS and the refinements were carried out by Professor Simon Parsons of the University of Edinburgh. The details are included here for the sake of completeness.

5.3.1 Neutron crystal structures

Ambient temperature, high-pressure neutron powder diffraction data were collected by the time-of-flight technique at the PEARL beamline high-pressure facility (HiPr) at ISIS. Data sets between 0 and 4.3 GPa were collected using a 1:1

mixture of deuterated pentane and isopropanol as a hydrostatic medium; higher pressures were obtained using a reloaded sample with a hydrostatic medium consisting of a 4:1 mixture of deuterated methanol and ethanol. Lead was included with the sample as a pressure marker. Full details of the experiment have been published in an earlier paper (Moggach, Marshall *et al.*, 2006). The coordinates for the structures at 4.5, 5.2, 7.3 and 8.1 GPa have already been published in the CSD [refcodes LSERIN22 to LSERIN25], but full refinements of the structure of L-serine at all pressures for which data were collected between 0 and 8.1 GPa are reported here for the first time.

5.3.2 Crystal structure refinements

All calculations were carried out using *TOPAS-Academic* version 4.1 (Coelho, 2007).

The crystal structures of L-serine-I between 0.1 and 4.5 GPa were initially refined individually starting from the coordinates of previous study at ambient conditions (Kistenmacher *et al.*, 1974). Using the Z-matrix formalism for rigid-body modelling available in *TOPAS*, the primary bond distances and angles were held at ambient pressure values, but the torsional angles, position and orientation of the molecules were allowed to refine. A common isotropic displacement parameter was refined for the C, N and O atoms; the H-atom displacement parameters were made equal to 1.2 or 1.5 times this value. Acceptable fits were obtained in all cases, and 'unconstrained R_{wp}' values are listed for this procedure in Table 5.1.

Though the trends in intermolecular distances obtained followed the expected downward trend, the variation was not smooth. Therefore, following a recent paper (Stinton & Evans, 2007), we tested a second modelling procedure where all data sets were refined together, but with the displacement, position, orientation and torsion parameters all constrained to be a constant, linear or quadratic function of pressure. For example the displacement parameter could be modelled as either constant over all data sets, $B_{iso}(P) = a_0 + a_1P$ or $B_{iso}(P) = a_0 + a_1P + a_2P^2$ where P = pressure in GPa and the coefficients a_0, a_1 and a_2 were allowed to refine. Also included in the refinements were a complete ambient pressure X-ray data set, the high pressure X-

ray data sets reported by Moggach and co-workers (Moggach *et al.*, 2005) and a further data set for phase-III (Drebushchak *et al.*, 2006). In short, all available high pressure X-ray single crystal and neutron powder data sets were refined together for phases I, II and III.

It was found that, for phase-I, the position, orientation and the D7-O3-C3-C2 torsion could be modelled as varying linearly with pressure; incorporation of a quadratic term did not improve the data-fitting, while at the same time introducing correlations between the linear and quadratic coefficients which tended to increase the standard deviations of derived parameters. Allowing other torsional parameters to vary did not significantly improve data-fitting. In the refinements for phases II and III common values of position, orientation and all torsions were refined.

No constraints or restraints were applied to intermolecular distances. The primary bond distances and angles of the serine molecule were assumed to be invariant with pressure, and these were also refined freely. A parameter representing the difference between X-ray and neutron distances to hydrogen was also refined. For the neutron data sets the pressure was calculated during refinement from the lead cell constant using a Birch-Murnaghan equation of state (Birch, 1947) with V_o = 30.3128 Å^3, B_o = 41.92 GPa, B' = 5.72. These parameters were derived by Fortes (Fortes, 2004) as averages of the values determined in three earlier studies (Kuznetsov *et al.*, 2002, Miller & Schuele, 1969, Waldorf & Alers, 1962). For the X-ray data sets the pressure was derived from the equation of state of serine as derived from the neutron data and ruby fluorescence measurements.

The neutron structures were used for comparison with the *ab initio* theoretical structures discussed herein, and crystal and refinement data and intermolecular contact distances are presented for the neutron refinements in Tables 5.1 and 5.2, respectively.

Phase	Serine-I	Serine-I	Serine-I	Serine-I	Serine-I	Serine-I
Pressure (GPa)	0.076(8)	0.940(8)	1.613(9)	2.625(9)	3.458(10)	4.270(8)
Chemical formula	$C_3D_7NO_3$	$C_3D_7NO_3$	$C_3D_7NO_3$	$C_3D_7NO_3$	$C_3D_7NO_3$	$C_3D_7NO_3$
M_r	112.11	112.11	112.11	112.11	112.11	112.11
Cell setting, space group	Orthorhombic, $P2_12_12_1$	Orthorhombic, $P2_12_12_1$	Orthorhombic, $P2_12_12_1$	Orthorhombic, $P2_12_12_1$	Orthorhombic, $P2_12_12_1$	Orthorhombic, $P2_12_12_1$
Temperature (K)	298	298	298	298	298	298
a, b, c (Å)	8.5720 (7), 9.3012 (5), 5.6043 (5)	8.4877 (7), 9.0943 (5), 5.5754 (5)	8.4435 (7), 8.9641 (6), 5.5546 (5)	8.3918 (7), 8.8060 (5), 5.5219 (5)	8.3547 (7), 8.7062 (5), 5.4968 (5)	8.3216 (6), 8.6243 (4), 5.4739 (4)
V (Å^3)	446.83 (6)	430.36 (6)	420.43 (6)	408.05 (6)	399.82 (6)	392.85 (5)
Z	4	4	4	4	4	4
D_x (Mg m^{-3})	1.666	1.730	1.771	1.825	1.862	1.895
Radiation type	Neutron	Neutron	Neutron	Neutron	Neutron	Neutron
Specimen form, colour	Powder (particle morphology: Block), colourless	Powder (particle morphology: Block), colourless	Powder (particle morphology: Block), colourless	Powder (particle morphology: Block), colourless	Powder (particle morphology: Block), colourless	Powder (particle morphology: Block), colourless
Specimen size (mm^3)	55					
Diffractometer	HiPr/PEARL, ISIS	HiPr/PEARL, ISIS	HiPr/PEARL, ISIS	HiPr/PEARL, ISIS	HiPr/PEARL, ISIS	HiPr/PEARL, ISIS
d-spacing range (Å)	4.3 to 0.6	4.3 to 0.6	4.3 to 0.6	4.3 to 0.6	4.3 to 0.6	4.3 to 0.6
Refinement on	I	I	I	I	I	I
R factors and goodness of fit	R_p = 3.222, R_{wp} = 2.845, R_{exp} = 1.821, S = 1.56	R_p = 3.290, R_{wp} = 2.974, R_{exp} = 1.855, S =1.60	R_p = 3.142, R_{wp} = 2.848, R_{exp} = 1.976, S =1.48	R_p = 3.085, R_{wp} = 2.848, R_{exp} = 1.917, S =1.48	R_p = 3.049, R_{wp} = 2.522, R_{exp} = 1.961, S =1.29	R_p = 2.735, R_{wp} = 2.232, R_{exp} = 1.567, S = 1.42
Parameters	273					
$(\Delta/\sigma)_{max}$	<0.0001	<0.0001	<0.0001	<0.0001	<0.0001	<0.0001

	Serine-I	Serine-II	Serine-II	Serine-II	Serine-II	Serine-III
Pressure (GPa)	4.514(15)	5.199(16)	5.700(17)	6.28(2)	7.243(19)	8.162(18)
Chemical formula	$C_3D_7NO_3$	$C_3D_7NO_3$	$C_3D_7NO_3$	$C_3D_7NO_3$	$C_3D_7NO_3$	$C_3D_7NO_3$
M_r	112.11	112.11	112.11	112.11	112.11	112.11
Cell setting, space group	Orthorhombic, $P2_12_12_1$	Orthorhombic, $P2_12_12_1$	Orthorhombic, $P2_12_12_1$	Orthorhombic, $P2_12_12_1$	Orthorhombic, $P2_12_12_1$	Orthorhombic, $P2_12_12_1$
Temperature (K)	298	298	298	298	298	298
A, b, c (Å)	8.3099 (5), 8.5951 (4), 5.4658 (4)	6.8700 (3), 9.6373 (6), 5.6066 (3)	6.8107 (4), 9.6227 (7), 5.5934 (3)	6.7627 (4), 9.6073 (7), 5.5825 (4)	6.6869 (3), 9.5802 (6), 5.5624 (3)	6.5487 (3), 9.5386 (5), 5.6078 (3)
V (Å^3)	390.39 (4)	371.21 (3)	366.58 (4)	362.70 (4)	356.34 (3)	350.30 (3)
Z	4	4	4	4	4	4
D_x (Mg m^{-3})	1.907	2.006	2.031	2.053	2.089	2.125
Radiation type	Neutron	Neutron	Neutron	Neutron	Neutron	Neutron
Specimen form, colour	Powder (particle morphology: Block), colourless	Powder (particle morphology: Block), colourless	Powder (particle morphology: Block), colourless	Powder (particle morphology: Block), colourless	Powder (particle morphology: Block), colourless	Powder (particle morphology: Block), colourless
Specimen size (mm^3)	55	55	55	55	55	55
Diffractometer	HiPr/PEARL, ISIS	HiPr/PEARL, ISIS	HiPr/PEARL, ISIS	HiPr/PEARL, ISIS	HiPr/PEARL, ISIS	HiPr/PEARL, ISIS
d-spacing range (Å)	4.3 to 0.6	4.3 to 0.6	4.3 to 0.6	4.3 to 0.6	4.3 to 0.6	4.3 to 0.6
Refinement on	I	I	I	I	I	I
R factors and goodness of fit	R_p = 2.720, R_{wp} = 2.223, R_{exp} = 1.659, S = 1.34	R_p = 2.879, R_{wp} = 2.555, R_{exp} = 1.541, S = 1.66	R_p = 2.939, R_{wp} = 2.596, R_{exp} = 1.616, S = 1.61	R_p = 3.202, R_{wp} = 2.552, R_{exp} = 1.877, S = 1.36	R_p = 2.961, R_{wp} = 2.503, R_{exp} = 1.602, S = 1.56	R_p = 3.017, R_{wp} = 2.407, R_{exp} = 1.834, S = 1.31
Parameters	273	141				58
$(\Delta/\sigma)_{max}$	<0.0001	<0.0001	<0.0001	<0.0001	<0.0001	<0.0001

Table 5.1: Crystallographic data for neutron powder diffraction study of L-serine at increasing pressures; L-serine-I (ambient to 4.5 GPa), L-serine-II (5.2 to 7.3 GPa) and L-serine-III (8.1 GPa).

Pressure/ GPa	0.0	0.1	0.9	1.7	2.7	3.5	4.3	4.5	Δ (I)
N1H5..O2[i]									
H5..O2	1.73	1.74	1.72	1.71	1.72	1.71	1.69	1.71	
	1.990(10)	*1.930(6)*	*1.909(6)*	*1.894(6)*	*1.871(6)*	*1.853(6)*	*1.837(6)*	*1.832(6)*	
N1..O2	2.771	2.781	2.753	2.740	2.747	2.729	2.716	2.723	0.048
	2.887(5)	*2.875(5)*	*2.851(5)*	*2.834(5)*	*2.807(5)*	*2.786(5)*	*2.768(5)*	*2.761(5)*	*0.126*
<N1H5O2	165	165	164	163	162	161	161	160	
	154(3)	*153(1)*	*152(1)*	*152(1)*	*151(1)*	*151(1)*	*150(1)*	*150(1)*	
N1H5..O1[i]									
H5..O1	2.34	2.30	2.31	2.28	2.21	2.20	2.19	2.16	
	2.304(11)	*2.246(6)*	*2.220(6)*	*2.201(6)*	*2.171(6)*	*2.148(6)*	*2.127(6)*	*2.120(6)*	
N1..O1	3.119	3.064	3.080	3.056	2.985	2.973	2.954	2.942	0.177
	3.124(5)	*3.109(5)*	*3.081(5)*	*3.061(5)*	*3.029(5)*	*3.004(5)*	*2.982(5)*	*2.974(5)*	*0.150*
<N1H5O1	128	128	128	128	128	128	128	129	
	142(2)	*141(1)*	*141(1)*	*141(1)*	*141(1)*	*140(1)*	*140(1)*	*140(1)*	
N1H4..O2[ii]									
H4..O2	1.88	1.86	1.80	1.78	1.74	1.71	1.70	1.68	
	1.967(8)	*1.902(5)*	*1.856(5)*	*1.831(5)*	*1.803(5)*	*1.783(6)*	*1.767(6)*	*1.761(6)*	
N1..O2	2.911	2.886	2.827	2.804	2.763	2.732	2.713	2.699	0.212
	2.879(4)	*2.866(4)*	*2.813(4)*	*2.784(4)*	*2.748(4)*	*2.723(5)*	*2.700(5)*	*2.693(5)*	*0.186*
<N1H4O2	163	163	163	161	161	160	159	160	
	157(3)	*156(2)*	*155(1)*	*154(1)*	*153(1)*	*152(1)*	*150(1)*	*150(1)*	
N1H6..O1[iii]									
H6..O1	1.75	1.76	1.73	1.72	1.69	1.69	1.67	1.66	
	1.938(9)	*1.865(5)*	*1.808(5)*	*1.776(5)*	*1.743(5)*	*1.727(5)*	*1.718(6)*	*1.713(6)*	
N1..O1	2.775	2.788	2.753	2.741	2.720	2.712	2.695	2.689	0.086
	2.858(4)	*2.837(4)*	*2.781(4)*	*2.750(4)*	*2.718(4)*	*2.703(4)*	*2.695(5)*	*2.690(5)*	*0.168*
<N1H6O1	162	163	162	162	163	163	163	163	
	159(4)	*158(2)*	*158(2)*	*158(2)*	*159(2)*	*159(2)*	*159(2)*	*159(2)*	
O3H7..O3[iv]									
H7..O3	1.95	1.95	1.92	1.90	1.89	1.87	1.86	1.84	
	2.103(14)	*2.038(11)*	*2.002(13)*	*1.981(15)*	*1.96(2)*	*1.94(2)*	*1.93(4)*	*1.93(4)*	
O3..O3	2.891	2.884	2.852	2.837	2.817	2.795	2.783	2.778	0.113
	2.923(3)	*2.906(3)*	*2.863(2)*	*2.839(2)*	*2.812(2)*	*2.796(2)*	*2.786(2)*	*2.782(2)*	*0.141*
<O3H7O3	158	157	158	157	156	155	154	156	
	155(4)	*154(2)*	*152(3)*	*152(3)*	*151(4)*	*151(5)*	*150(7)*	*150(7)*	

Symmetry Operators:

i	*x*,*y*,1+*z*
ii	-1/2+*x*,3/2-*y*,1-*z*
iii	3/2-*x*, 2-*y*,1/2+*z*
iv	3/2-*x*, 1-*y*,1/2+*z*
v	1-*x*, -1/2+*y*,3/2-*z*

Pressure/ GPa	5.2	5.8	6.3	7.3	8.1
N1H5..O2[i]					
H5..O2	1.65	1.65	1.66	1.67	1.67
	1.887(13)	*1.877(13)*	*1.869(13)*	*1.855(13)*	*1.82(3)*
N1..O2	2.686	2.686	2.694	2.692	2.708
	2.836(12)	*2.825(12)*	*2.816(12)*	*2.799(12)*	*2.81(2)*
<N1H5O2	164	163	163	162	164
	152(3)	*152(3)*	*152(3)*	*151(3)*	*160(9)*
N1H5..O1[i]					
H5..O1	2.38	2.37	2.34	2.31	2.37
	2.221(13)	*2.209(13)*	*2.199(13)*	*2.180(13)*	*2.32(3)*
N1..O1	3.185	3.171	3.139	3.120	3.165
	3.099(12)	*3.086(12)*	*3.075(12)*	*3.056(12)*	*3.14(3)*
<N1H5O1	131	131	131	132	131
	142(2)	*142(2)*	*142(2)*	*142(2)*	*135(4)*
N1H4..O2[ii]					
H4..O2	1.81	1.80	1.80	1.79	1.83
	1.861(11)	*1.835(11)*	*1.814(11)*	*1.782(11)*	*1.84(2)*
N1..O2	2.834	2.819	2.822	2.806	2.836
	2.832(9)	*2.805(9)*	*2.783(9)*	*2.749(9)*	*2.828(18)*
<N1H4O2	164	164	164	162	161
	157(3)	*156(3)*	*156(3)*	*155(3)*	*158(6)*
N1H6..O1[iii]					
H6..O1	1.66	1.65	1.63	1.63	1.57
	1.745(11)	*1.734(11)*	*1.723(11)*	*1.705(11)*	*1.675(19)*
N1..O1	2.654	2.643	2.632	2.622	2.608
	2.644(10)	*2.635(10)*	*2.627(10)*	*2.612(10)*	*2.642(17)*
<N1H6O1	157	157	158	157	165
	144(2)	*144(2)*	*144(2)*	*145(2)*	*154(5)*
O3H7..O2[iv]					
H7..O2	1.64	1.63	1.62	1.60	1.68
	1.639(16)	*1.629(16)*	*1.619(16)*	*1.602(16)*	*1.84(3)*
O3..O2	2.635	2.625	2.614	2.599	2.615
	2.630(13)	*2.629(13)*	*2.608(13)*	*2.590(13)*	*2.66(3)*
<O3H7O2	173	173	173	172	155
	169(10)	*168(10)*	*168(10)*	*167(9)*	*136(5)*
O3H7..O1[v]					
H7..O1	-	-	-	-	2.38
	-	-	-	-	*2.13(3)*
O3..O1	-	-	-	-	2.940
					2.89(3)
<O3H7O1					114
					131(4)

Table 5.2: Non-covalent interaction parameters in L-serine theoretical and experimental crystal structures. The theoretical values are shown first and the experimental values given in italics underneath. Distances are in Å and angles in °. The Δ column refers to the D...A distance at the highest pressure obtained for phase I (4.5 GPa) subtracted from the same distance at the lowest pressure obtained (ambient).

5.3.3 DFT calculations

First principles electronic structure calculations were performed with the localised basis set pseudopotential method as employed in the code *SIESTA* (Ordejon *et al.*, 1996, Soler *et al.*, 2002). The generalised gradient Perdew-Burke-Ernzerhof exchange correlation potentials were employed in the calculations (Perdew *et al.*, 1996). Valence double-ζ basis sets augmented with polarisation functions were used. The basis sets are numerical ones, consisting of the exact solutions of the pseudopotential for the atomic state, except that a radial confinement is included to localise the orbital corresponding to an energy shift of 0.0001 Rydberg. A real space mesh equivalent to a plane wave cut-off of 250 Rydberg was used for the evaluation of the Hartree and exchange-correlation energies. Optimisations performed on the solid-state structures over the range of pressures were constrained to the neutron compression study unit cell dimensions, while all other degrees of freedom were free to relax with no symmetry restrictions. The input files were prepared using the program *GDIS* (Fleming & Rohl, 2005).

5.3.4 PIXEL calculations

The final theoretical structures obtained were used to calculate the molecular electron density at each pressure by standard quantum chemical methods using the program *GAUSSIAN98* (Frisch *et al.*, 1998) with the MP2/6-31G** basis set. The electron density model of the molecule was then analysed using the program package *OPiX* (Gavezzotti, 2005) which allows the calculation of dimer and lattice energies. Lattice energy calculations employed a cluster of molecules with maximum distance from the central molecule of 40 Å and a top radius for search of 50 Å. This size of cluster was used in order to minimise the effect of long-range electrostatic contributions from molecules at the outer edges of the cluster due to the charged nature of zwitterionic L-serine. Calculations were also carried out for pairs of molecules identified in the lattice calculation as being energetically the most significant (*i.e.* with a magnitude > 2.5 kJ mol^{-1}). The output from these calculations yields a total energy and a breakdown into its Coulombic, polarisation, dispersion and repulsion components (Dunitz & Gavezzotti, 2005).

5.3.5 Other programs used

Theoretical and experimental crystal structures were visualised using the programs *Mercury* (Macrae et al., 2008) and *DIAMOND* (Crystal Impact, 2004). Analyses were carried out using *PLATON* (Spek, 2003), as incorporated in the *WinGX* suite (Farrugia, 1999). Searches of the CSD (Allen, 2002, Allen & Motherwell, 2002) utilised the program *ConQuest* and version 5.28 of the database with updates up to January 2007. Scatter-plots of intermolecular interaction geometries from the CSD were generated using the *IsoStar* library (Bruno *et al.*, 1997).

The numbering scheme used (Scheme 5.1) is the same throughout the ambient-pressure and high-pressure datasets. This numbering scheme also matches the numbering used for L-serine in the previous two compression studies.

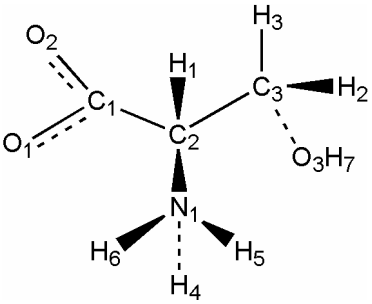

Scheme 5.1: Chemical structure diagram showing atomic numbering scheme.

5.4 Results

5.4.1 A comparison of the experimental & theoretical structures

The experimental primary bond distances and angles in L-serine I, II and III are compared to the average values for each phase of the theoretical structures in Table 5.3. A recently developed option in *CRYSTALS* (Betteridge *et al.*, 2003) was used to perform a geometrical comparison between the experimental and theoretical intramolecular structures in the solid state at each individual pressure (Collins *et al.*, 2006). This comparison of geometries found that the rms deviation of bond lengths in the structures was never greater than 0.08 Å and the rms deviation in positions was never larger than 0.15 Å. The largest variation with pressure in bond length in the theoretical data is 0.015 Å (for C1-O1 between phases I and II); this is within the

precision of experimentally determined structures at high pressure, and validates the commonly used procedure of restraining high pressure structure refinements with bond distances derived at ambient pressure. With the exception of <C1C2N1, the trends in the theoretical and experimental bond angles (Table 5.3) are consistent. The C2-C3-O3 bond angle, for example, changes from approximately 112° to 106° between phases I and II in both sets of structures.

	Neutron Phase I	**Neutron Phase II**	**Neutron Phase III**	**SIESTA Phase I**	**SIESTA Phase II**	**SIESTA Phase III**
C1-C2	1.536 (2)	1.492 (5)	1.504 (10)	1.537	1.534	1.531
C2-C3	1.528 (2)	1.539 (5)	1.511 (8)	1.536	1.529	1.526
C1-O1	1.2303 (19)	1.222 (6)	1.266 (8)	1.268	1.253	1.257
C1-O2	1.2583 (19)	1.279 (5)	1.266 (8)	1.282	1.293	1.286
C3-O3	1.4225 (18)	1.437 (3)	1.402 (11)	1.432	1.422	1.428
C2-N1	1.4899 (18)	1.520 (3)	1.483 (7)	1.479	1.476	1.474
<C1C2C3	109.94 (10)	111.1 (2)	110.7 (3)	111.7	113.0	113.6
<C1C2N1	109.33 (10)	109.2 (2)	110.7 (4)	111.8	107.9	108.2
<C2C1O1	119.21 (13)	117.2 (4)	114.0 (8)	118.5	117.7	117.5
<C2C1O2	114.60 (13)	119.5 (4)	121.4 (6)	116.3	118.1	118.4
<C2C3O3	111.97 (13)	105.6 (3)	105.9 (6)	112.2	106.0	106.7
<C3C2N1	109.31	108.8	108.2	110.3	108.3	108.1

Table 5.3: Average non-hydrogen bond lengths and angles in the experimental and theoretical structures of L-serine. For the neutron structures the non-hydrogen primary bond lengths and angles were assumed to be constant during refinement. The theoretical values shown are the averages of the parameters for the structures within each phase. Bond lengths are in Å and bond angles are in °.

Another technique for comparing structures, which is used by the Crystal Structure Prediction (CSP) community, is to compare the relative coordinates of a cluster of 15 molecules in each structure. This comparison can be performed using the program *COMPACK* (Chisholm & Motherwell, 2005) and the functionality has also been incorporated into the November 2007 release of *Mercury CSD 2.0* (Macrae *et al.*, 2008). A root-mean-squared deviation (RMSD) is calculated over this cluster

of 15 molecules for each comparison and a structural overlay is automatically carried out. For the purposes of this study the hydrogens were ignored for comparison of structures. Comparison across the pressure series for L-serine calculated RMSD values of between 0.06 and 0.12 Å for the experimental and theoretical structures. The largest deviation was seen for the structure of L-serine-III at 8.1 GPa which shows an RMSD of 0.121 Å between the neutron and *ab initio* structures. An example of the overlay between molecular clusters is shown in Figure 5.4 for L-serine-II at 5.2 GPa (RMSD of 0.105 Å) with the experimental structure in green and the theoretical structure in red. Typically, in the field of CSP, a matched (correctly predicted) structure will give an RMSD for this size of cluster of less than 1.0 Å compared to the experimental structure, values less than 0.2 Å are considered to be a very good match (Day *et al.*, 2005). In CSP, however, the structures will not necessarily have the same unit cell dimensions, whereas in our comparision the experimental and theoretical structures have identical cell dimensions.

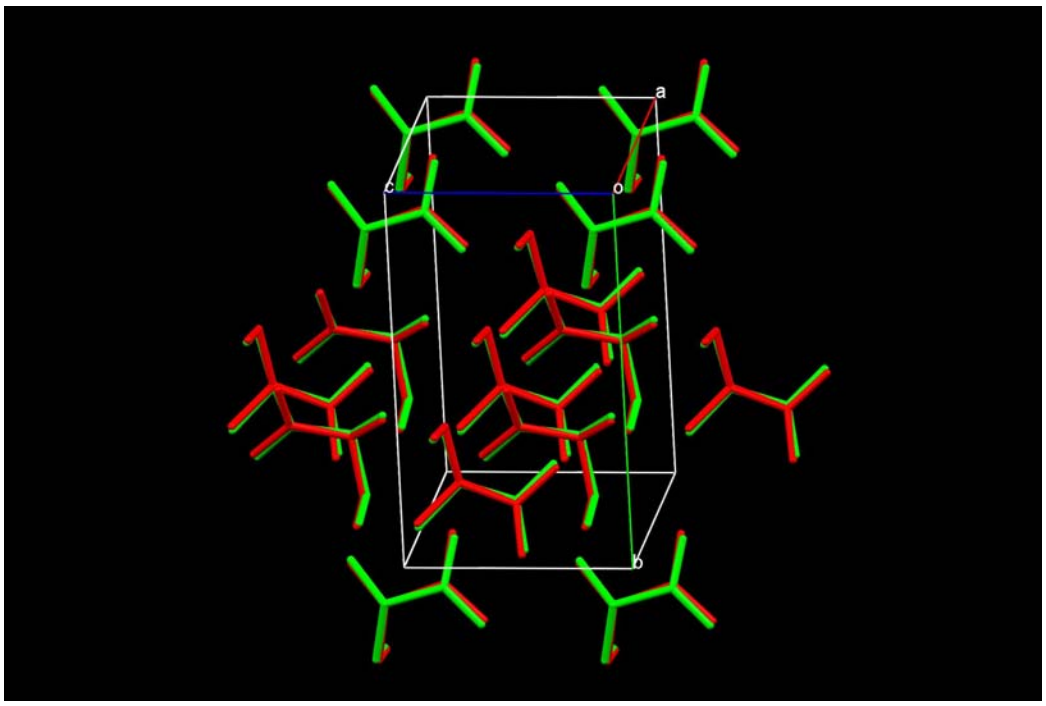

Figure 5.4: Structural overlay of a 15 molecule cluster in the L-serine-II experimental structure at 5.2 GPa (green) with the equivalent theoretical structure (red). Hydrogen atoms have been removed for clarity. The RMSD for this cluster comparison is 0.105 Å over the whole cluster.

5.4.2 The response of the theoretical structure to pressure

Figure 5.5 shows the experimental and *ab initio* donor to acceptor distances for each of the shortest four hydrogen bonds as a function of pressure for the phase I structures of L-serine. Apart from the N1H5…O2 hydrogen bond, each of the theoretical compression curves matches well with that of the experimentally determined distances. The donor to acceptor distance in the N1H5…O2 interaction is seen to be in the region of 0.10 to 0.05 Å shorter in the theoretical structures compared to the experimental structures. This may be related to the fact that the C1-O2 bond length is longer in the *SIESTA* calculations, though only by 0.024 Å.

The data on variation of the non-covalent interaction parameters in the theoretical structures between ambient pressure and 8.1 GPa are presented in Table 5.2. The least compressible hydrogen bond during the compression of phase I is seen to be the major component of the bifurcated hydrogen bond N1H5…O2 (N1…O2 decreases by 1.7 % between ambient pressure and 4.5GPa). The N1H6…O1 hydrogen bond is the next least compressible interaction, for which N1…O1 decreases by 3.1 % to a distance of 2.689 Å at 4.5 GPa. The O3H7…O3 hydrogen bond compresses by 3.9 % from an O3…O3 distance of 2.891 at ambient pressure to 2.778 Å at 4.5 GPa. Finally, the last two hydrogen bonds, N1H5…O1 and N1H4…O2 which are relatively long at ambient conditions, decrease by 5.7 and 7.3 % respectively (N1…O1 decreases to 2.942 Å and N1…O2 is compressed to 2.699 Å at 4.5 GPa). The three main N…O distances all compress to approximately the same value (N1H5…O2 = 2.723 Å, N1H6…O1 = 2.689 Å and N1H4…O2 = 2.699 Å at 4.5 GPa).

The phase transition from L-serine-I to L-serine-II is accompanied by a lengthening of the N1H4…O2 hydrogen bond from 2.699 Å in phase I at 4.5 GPa to 2.834 Å in phase II at 5.2 GPa. The minor component of the bifurcated hydrogen bond, N1H5…O1, also becomes longer as the bifurcated character of the interaction decreases. Both of the remaining two NH…O hydrogen bonds (N1H5…O2 and N1H6…O1) decrease slightly during the phase transition. The new OH…O interaction in the phase II structure (O3H7…O2) is seen to be substantially shorter than the OH…O interaction in phase I (O3…O2 = 2.635 Å at 5.2 GPa).

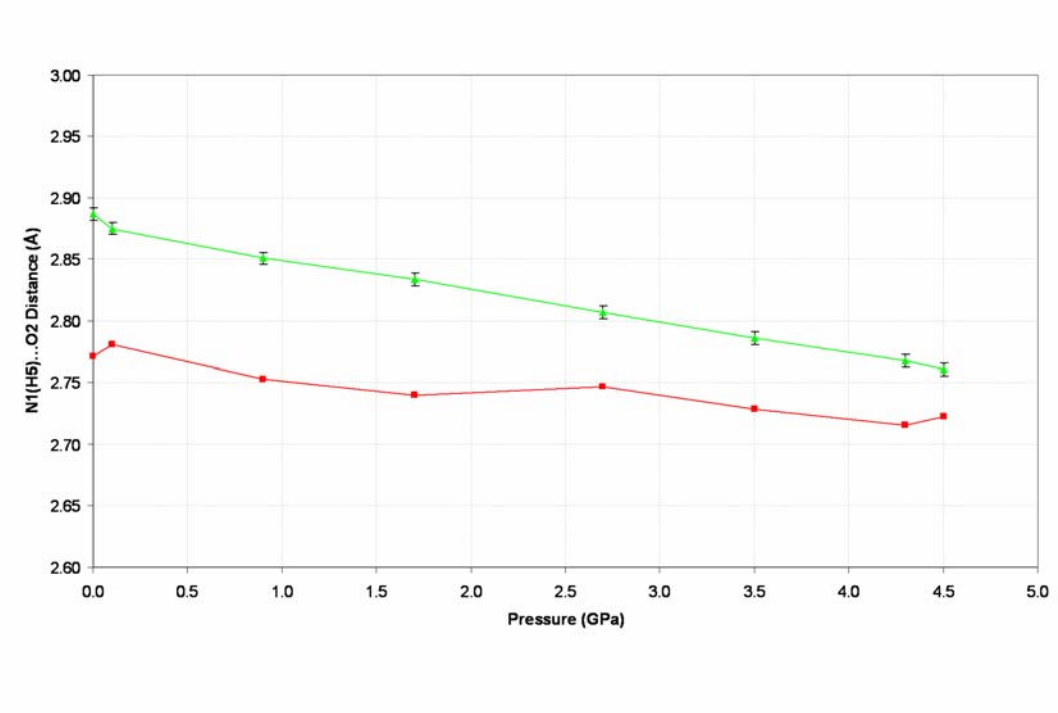
N1(H5)...O2 Distance (Å)
3.00
2.95
2.90
2.85
2.80
2.75
2.70
2.65
2.60
0.0
0.5
1.0
1.5
2.0
2.5
3.0
3.5
4.0
4.5
5.0
Pressure (GPa)

(a)

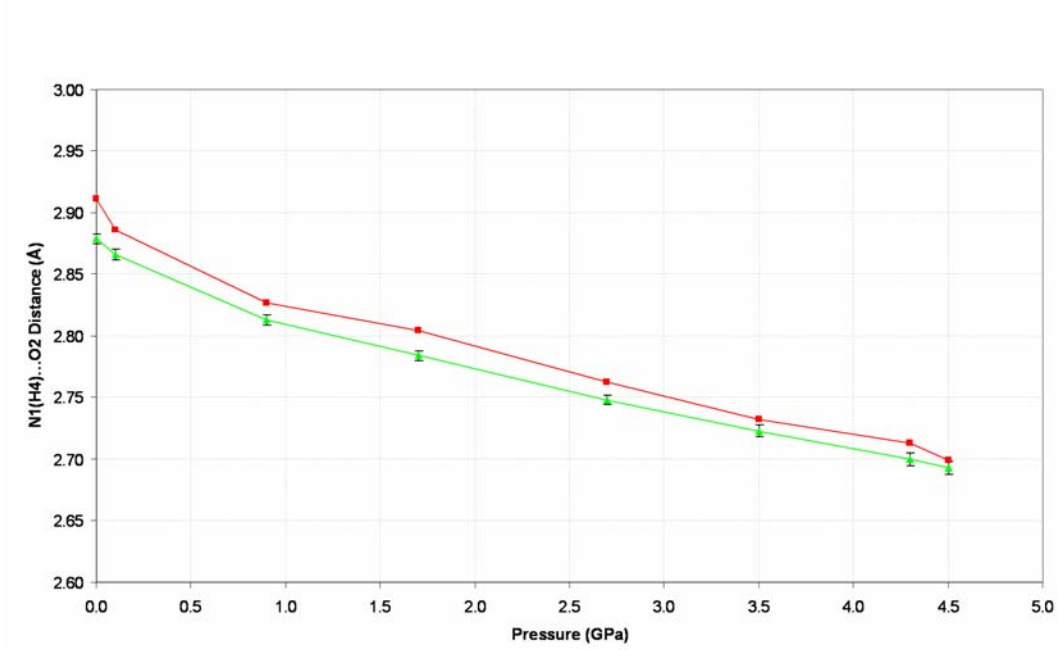
N1(H4)...O2 Distance (Å)
3.00
2.95
2.90
2.85
2.80
2.75
2.70
2.65
2.60
0.0
0.5
1.0
1.5
2.0
2.5
3.0
3.5
4.0
4.5
5.0
Pressure (GPa)

(b)

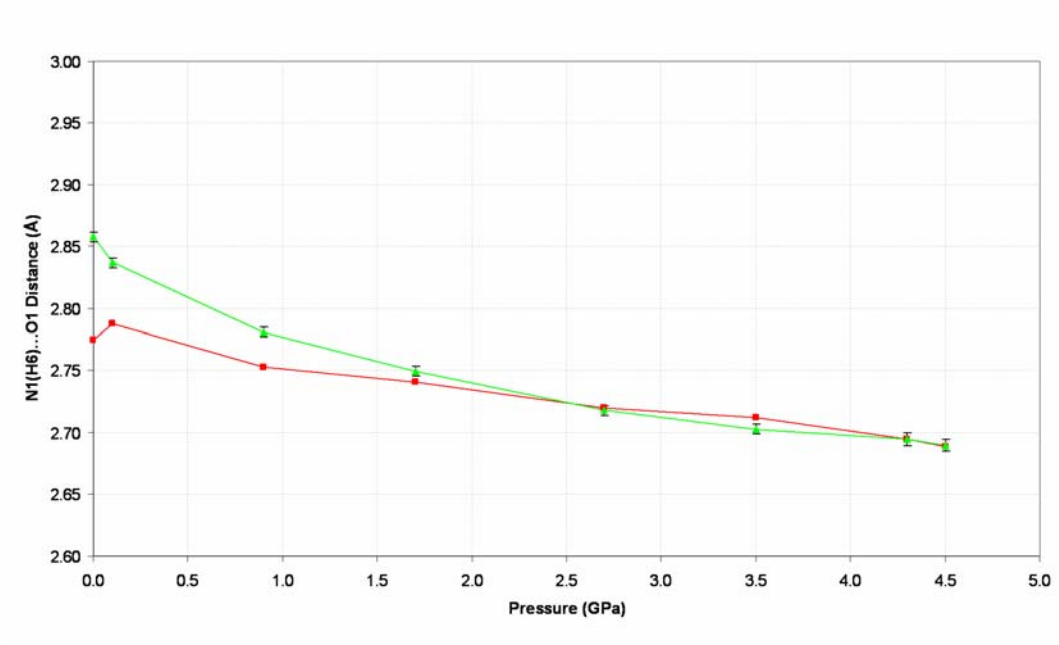

(c)

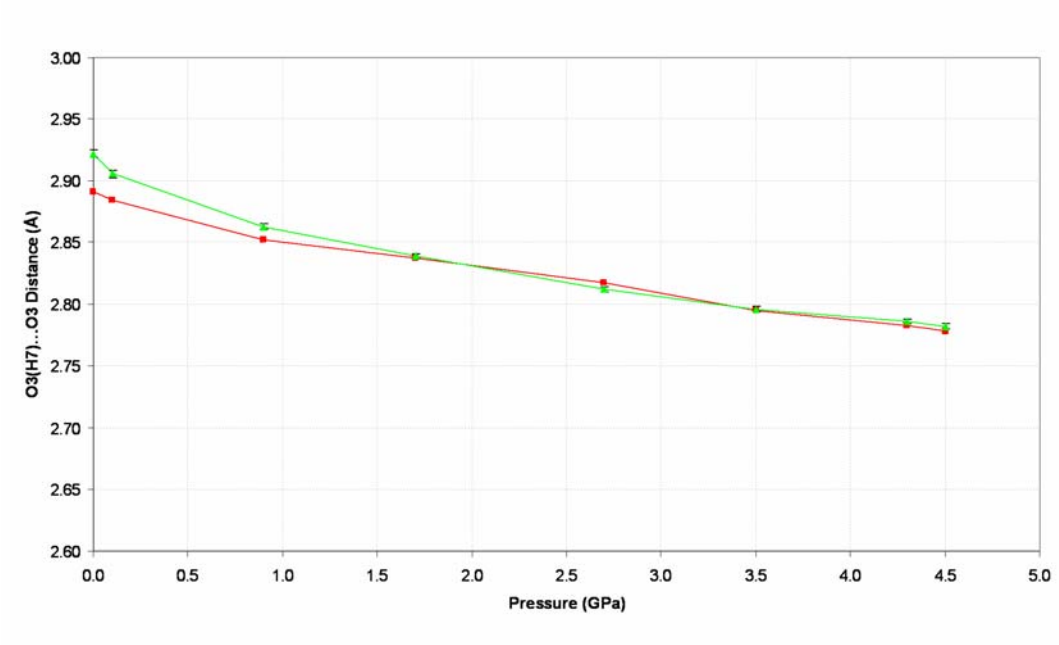

(d)

Figure 5.5: Graphs of hydrogen bond donor to acceptor distances (in Å) as a function of pressure (in GPa) for the interactions N1(H5)…O2 (a), N1(H4)…O2 (b), N1(H6)…O1 (c) and O3(H7)…O3 (d) in L-serine-I. The data are shown in each graph for the neutron powder structures (green) and the *SIESTA* theoretical structures (red). Error bars have been displayed for the interactions in the experimental structures at the 1 σ level. Each plot is shown on the same scale using distances from 2.6 to 3.0 Å and pressures from 0.0 to 5.0 GPa.

In the second phase transition, from phase II to phase III, each of the hydrogen bonds N1H5…O2/O1, N1H4…O2 and O3H7…O2 increases slightly during the shifting of the *B* layers with respect to each other. The hydrogen bond donor O3H7 does now, however, form a bifurcated hydrogen bond with O3H7…O2 the major component (O3…O2 = 2.615 Å) and O3H7…O1 the minor component (O3…O1 = 2.940 Å). The only hydrogen bonding interaction seen to decrease during this phase transition is N1H6…O1 (N1…O1 = 2.608 Å at 8.1 GPa).

5.5 Discussion

5.5.1 The phase I to II transition

The pressure-induced phase transitions in the crystal structure of L-serine were rationalised in the previous two studies by analysis of the hydrogen bonding distances as pressure was increased. As described above, each of the main NH…O interactions in the theoretical structures reaches a N…O distance of approximately 2.70 Å at 4.5 GPa, just before the phase transition to L-serine-II. A search of NH…O contact distances in the CSD for amino acid structures suggested that 2.70 Å approaches the minimum distance for this type of interaction, and we suggested that relief of strain in this contact 'drove' the transition from phase I to II.

A more general search of the Cambridge Structural Database (CSD) for any R_3NH^+ to $RCOO^-$ interactions in organic structures with R-factor <= 0.075 showed that there is still a number of NH…O contacts shorter than this, with the shortest N…O contact being 2.533 (2) Å for QIBSAV (Burchell *et al.*, 2001). This implies that the conclusion reached in our previous study was based on too restrictive search criteria, and it would appear that the hydrogen bonds in the phase I structures calculated are not yet at their ambient limits at 4.5 GPa. If this is the case then the phase transition is driven by some other factor. This was investigated further using PIXEL calculations.

The PIXEL method is a technique that has been developed recently by Gavezzotti which allows substantial insight to be gained into the nature of intermolecular interactions through the calculation of crystal lattice and dimer energies. The technique is applied by determination of a molecular electron density

map (using *GAUSSIAN*), condensation of the map into larger pixels and then calculation of energy terms between pairs of pixels in adjacent molecules. Studies using the program to analyse the compression of organic molecules (Chapters 2 & 4), have shown that the PIXEL technique is particularly useful for investigating the variation of intermolecular interactions within a crystal structure.

The lattice energies of the L-serine theoretical structures and a breakdown into the component Coulombic, dispersion, polarisation and repulsion terms have been calculated and are shown in Table 5.4. A plot of the overall lattice energy as a function of pressure for each of the three phases of L-serine is shown in Figure 5.6. In order to validate the energy calculations it is useful to compare the ambient lattice energy (-290.9 kJ mol^{-1}) with lattice energies determined using other techniques. The enthalpy of sublimation of L-serine has been experimentally determined (de Kruif *et al.*, 1979) to be -173.6 kJ mol^{-1}, though proton transfer occurs between the ammonium and carboxylate groups during sublimation. If the proton transfer energy is taken into account (Kyoung *et al.*, 1994) the lattice energy of zwitterionic serine is -279.9 kJ mol^{-1}, which is close to the value determined by the PIXEL method.

The PIXEL method only calculates energies of interactions *between* molecules and any change in the internal energy of the molecule is not taken into account. There is, however, a change in the conformation of the L-serine molecule between phases I and II which is characterised by a rotation of the hydroxyl group, a rotation of the amino group and a twisting of the carbonyl group about the C1-C2 bond (Figure 5.3). *GAUSSIAN* calculations indicate that energy associated with the conformational change is -40 kJ mol^{-1}, indicating that the conformation of the serine molecules in the ambient pressure structure is therefore not optimal. A recent DFT study reached a similar conclusion for L-alanine, quoting a difference between the solid state and gas-phase conformations of 40 kJ mol^{-1} (Cooper *et al.*, 2007). Table 5.4 includes a column showing an adjusted total energy (U_{adj}) which corresponds to the total lattice energy minus the difference in internal energy of the molecule as calculated by *GAUSSIAN*. Also displayed in the table are values for the enthalpy, $H = U_{adj} + PV$, where P = pressure and V = molar volume = unit cell volume/Z. Lattice enthalpy is plotted against pressure in Figure 5.6.

Pressure/ GPa	Coulombic	Polarisation	Dispersion	Repulsion	Total Energy	U_{adj}*	$H^{\dagger}$
0.0	-319.8	-121.6	-85.1	235.6	-290.9	-290.9	-290.9
0.1	-320.9	-122.6	-86.9	239.6	-290.7	-286.7	-280.0
0.9	-341.3	-134.3	-94.8	279.6	-290.8	-289.6	-231.3
1.7	-350.3	-140.5	-99.9	302.5	-288.2	-287.9	-180.3
2.7	-368.1	-151.1	-107.3	335.8	-290.8	-286.5	-120.6
3.5	-376.4	-157.1	-112.3	364.9	-280.9	-276.8	-66.2
4.3	-389.0	-165.9	-117.1	393.8	-278.1	-273.8	-19.7
4.5	-395.2	-170.9	-118.7	403.9	-280.9	-277.1	-12.7
5.2	-388.7	-162.1	-129.7	452.2	-228.4	-268.1	22.5
5.8	-396.4	-167.4	-133.5	473.3	-223.9	-262.7	57.3
6.3	-404.2	-171.0	-136.8	490.8	-221.2	-259.8	84.0
7.3	-413.5	-178.4	-141.9	517.3	-216.6	-255.2	136.4
8.1	-428.7	-180.0	-149.4	547.6	-210.5	-246.8	180.5

***** Adjusted Energy (U_{adj}) = Total Energy – Energy difference due to conformation change relative to 0.0 GPa structure based on *GAUSSIAN98* calculation.

† Enthalpy (H) = $U_{adj} + PV$, where P = pressure (in Pa) and V = molar volume (in $m^3\ mol^{-1}$).

Table 5.4: The components of lattice energy and the total energy at each pressure (GPa) for L-serine theoretical structures (energies in kJ mol^{-1}) along with the adjusted total energy (U_{adj}) and the enthalpy (H).

The lattice enthalpy becomes more positive as pressure increases throughout each of the three phases due to the increasing repulsion and the pV terms. There is a discontinuity in the graph near 5 GPa, where the phase transition from L-serine-I to L-serine-II takes place, the enthalpy becoming more negative, as expected. Analysis of the data in Table 5.4 shows that this can be ascribed to (i) the stabilisation of the internal energy of the serine molecules, and (ii) a diminution in the pV term as a structure with a smaller molecular volume is formed. Presumably the new phase formed, L-serine-II, has a hydrogen bonding pattern which can accommodate this lower energy conformation, but which only becomes stable at elevated pressures.

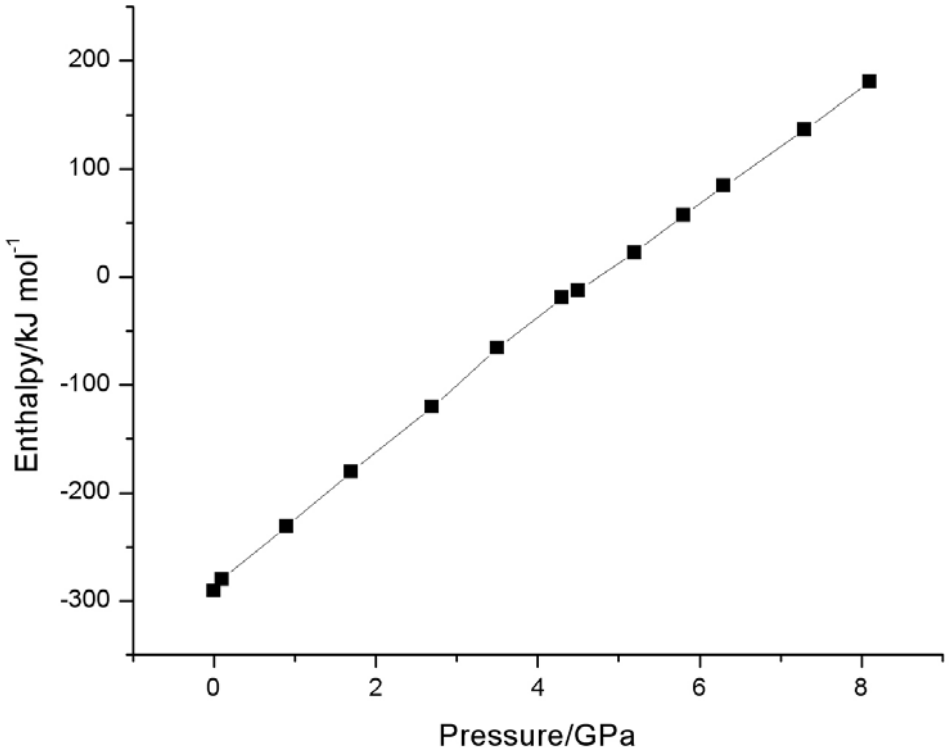

Figure 5.6: Graph of theoretical structure lattice enthalpy (in kJ mol^{-1}) of the three phases of L-serine as a function of pressure (in GPa).

5.5.2 Intermolecular interactions in L-serine-I as a function of pressure

The PIXEL method also allows calculation of the intermolecular interaction energies between two molecules within the crystal structures. Six pairs of molecules in the L-serine-I theoretical crystal structure are found to have a stabilising interaction energy of magnitude greater than 2.5 kJ mol^{-1} at ambient pressure. These dimers, which are shown in Figure 5.7, are designated 1-6 in descending order of their interaction energy at ambient conditions; the energies and a breakdown into their component terms is shown in Table 5.5. The variation in energy as a function of the centroid-centroid distance for these interactions is displayed in Figure 5.8. The data in Figure 5.8 were calculated with the *SIESTA*-optimised structures, but similar results are obtained when experimental data are used.

The dimer with the strongest interaction energy (1) at ambient conditions corresponds to the N1H4…O2 hydrogen bond in the L-serine-I structure. The next

strongest interaction (2) is the bifurcated hydrogen bond N1H5…O1/O2. Interactions 3 and 4 relate to dimers which are not hydrogen bonded, 3 corresponds to a van der Waals contact and 4 corresponds to the interaction C3H3…O1. The final two interactions, 5 and 6, are also relatively weak and correspond to the hydrogen bonds N1H6…O1 and O3H7…O3 respectively.

Dimer	Coulombic	Polarisation	Dispersion	Repulsion	Total Energy
1	-71.6	-19.2	-11.3	26.9	-75.1
2	-70.4	-23.4	-8.5	44.2	-58.1
3	-11.7	-3.8	-5.5	3.8	-17.3
4	-7.7	-2.8	-2.3	0.9	-11.8
5	-15.0	-16.8	-5.3	27.3	-9.8
6	-4.4	-7.4	-6.7	14.8	-3.6

Table 5.5: The total interaction energy and a breakdown into the component terms for the six most stabilising interactions at ambient conditions in the L-serine-I theoretical structure (energies in kJ mol^{-1}).

The energy of interaction 5 (corresponding to the N1H6…O1 contact) seems to be small compared to the other charge-assisted NH…O hydrogen bonds (Table 5.5): even though N1H5…O2 has similar H-bond geometric parameters to N1H6…O1 (Table 5.2), interaction 2 has an energy of -58.1 kJ mol^{-1} compared to -9.8 kJ mol^{-1} for interaction 5. Figure 5.9 shows an *IsoStar* contoured scatter-plot of intermolecular interactions between anionic $RCOO^-$ groups (fixed central fragment) and cationic RNH_3^+ groups (distribution around carboxylate) found within the CSD. The N-H donor group shows a distinct preference for H-bonding to either of the carboxylate lone pairs. The hydrogen bond corresponding to interaction 5 exhibits a contact between the lone pairs and out of the plane of the carboxylate group.

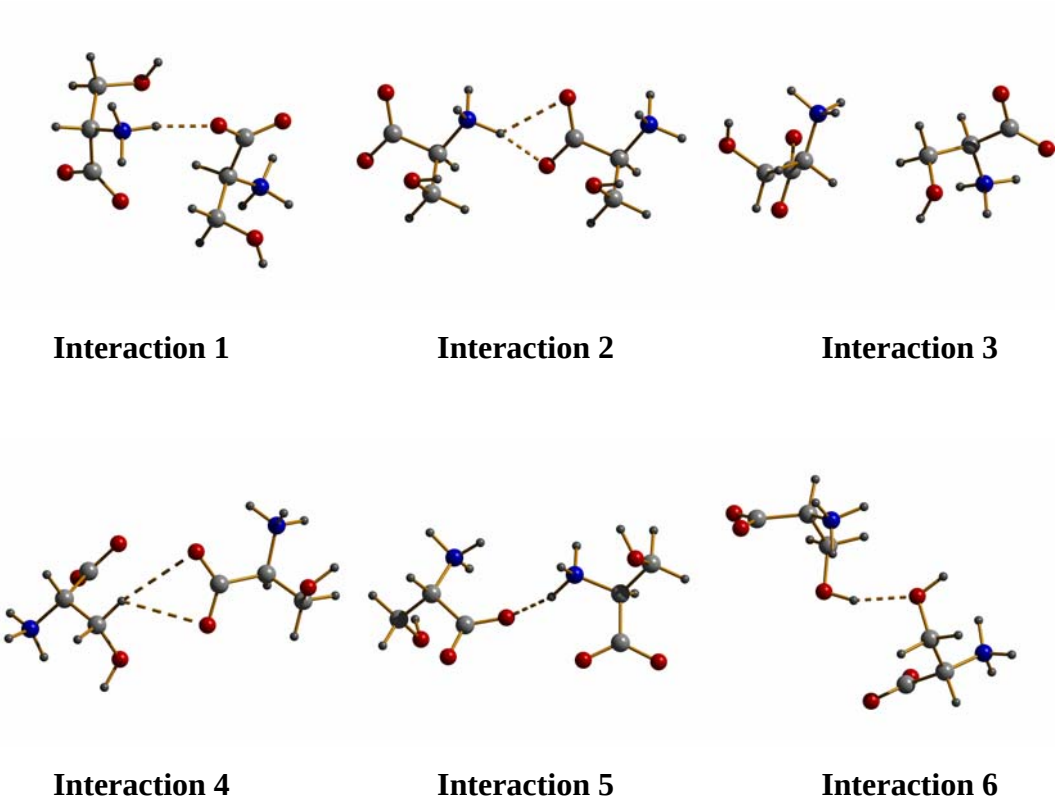

Figure 5.7: Diagrams of the most energetically important dimers in the L-serine-I theoretical crystal structure at ambient pressure from PIXEL analysis. The colour scheme is the same as in Fig. 5.1.

These observations are consistent with a study of intermolecular contact energies in α-glycine (Volkov & Coppens, 2004), which showed that there was also a weak hydrogen bond in that structure with a donor to acceptor geometry that would ordinarily suggest a strong interaction. This H-bond was also formed out of the plane of the carboxylate group. It is noticeable that the geometry of interaction 5 brings the carboxylate groups on neighbouring molecules relatively close to each other; the same is also true, though to a lesser extent, for the ammonium groups. This added repulsion between like charges may have a contributing effect upon the low interaction energy for this intermolecular contact.

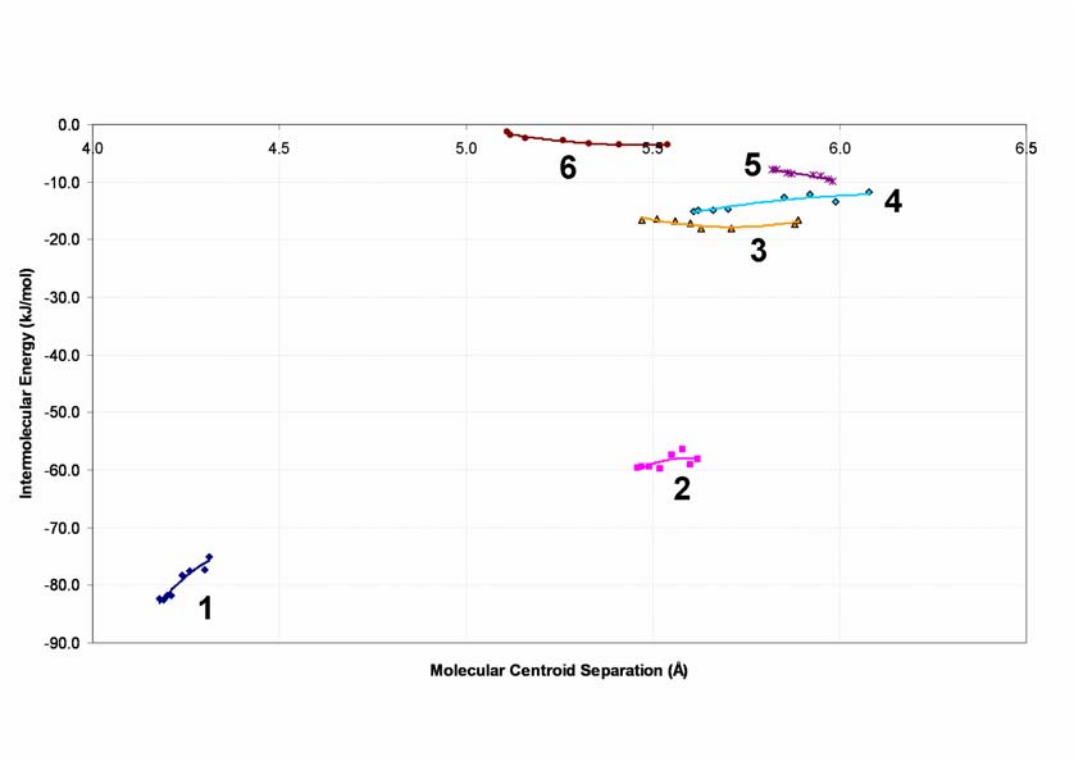

Figure 5.8: Graph of total interaction energy for the six most energetically important dimers in the L-serine-I theoretical structure (in kJ mol^{-1}) against the distance between the molecular centroids of the molecules involved in the interaction (in Å). A line of best fit has been displayed for each interaction.

Although each of the six interactions has an increasing repulsion term with increasing pressure as the dimers are forced closer together, none of the interactions weaken considerably within this pressure regime. Three of the interactions (dimers 1, 2 and 4) are actually seen to strengthen as pressure is increased, whereas the remaining three interactions are only slightly weakened by the compression. Although these results are different to the behaviour of interactions seen in other pressure studies (Chapter 2, Figure 2.10), they do appear to agree with the conclusion (see above) that the I-to-II phase transition is not driven by relief of unfavourable contacts.

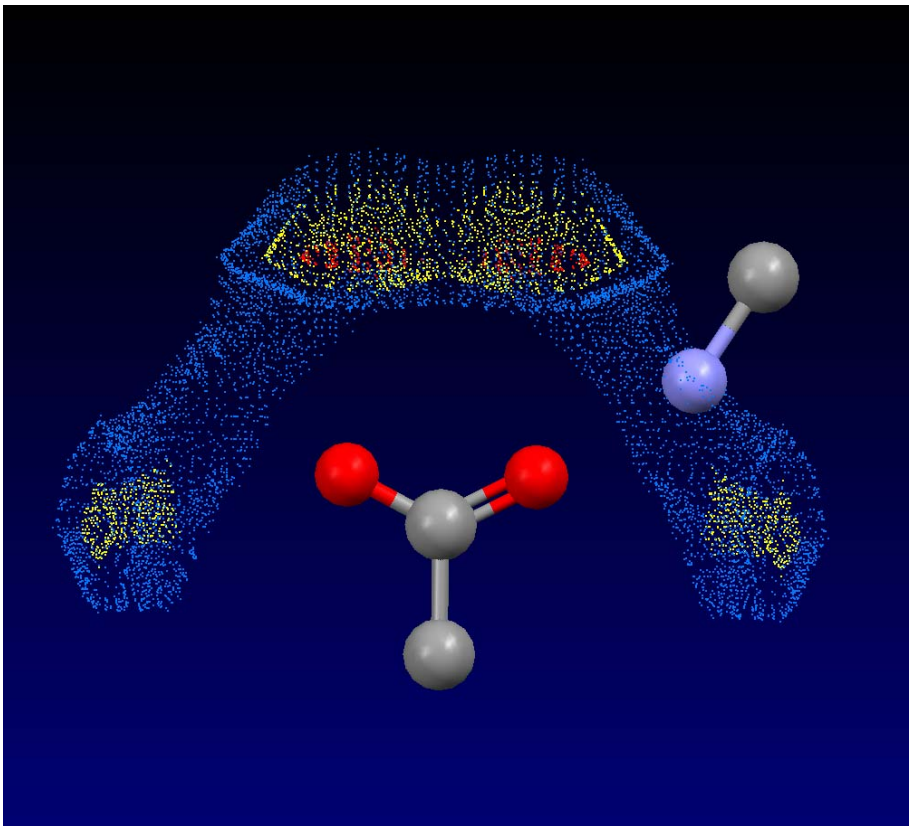

Figure 5.9: *IsoStar* contoured scatter-plot of an RNH_3^+ contact group around a central $RCOO^-$ group, contoured on the amide-N atoms. The colours show three different levels of contact density with red being the greatest density followed by yellow and then blue. The contact displayed corresponds to the weak NH…O interaction in the structure of L-serine-I (labelled interaction 5 in the PIXEL analysis).

5.5.3 The phase II to III transition

During the compression of phase II the N1H5…O2 hydrogen bond actually increases marginally, while the remaining interactions each decrease by 2 % or less up to 7.3 GPa. With the exception of N1H6…O1, the H-bonds in L-serine-III at 8.1 GPa are actually longer than in phase-II prior to the phase transition. The main difference during the phase transition is the bifurcation of the O3H7…O2 interaction to form a hydrogen bond to a carbonyl acceptor (O1). In the theoretical structure the O3…O2 hydrogen bond is seen to be the major component of the bifurcated O3H7…O2/O1 interaction, whereas in the experimental structure O3…O1 is the major component.

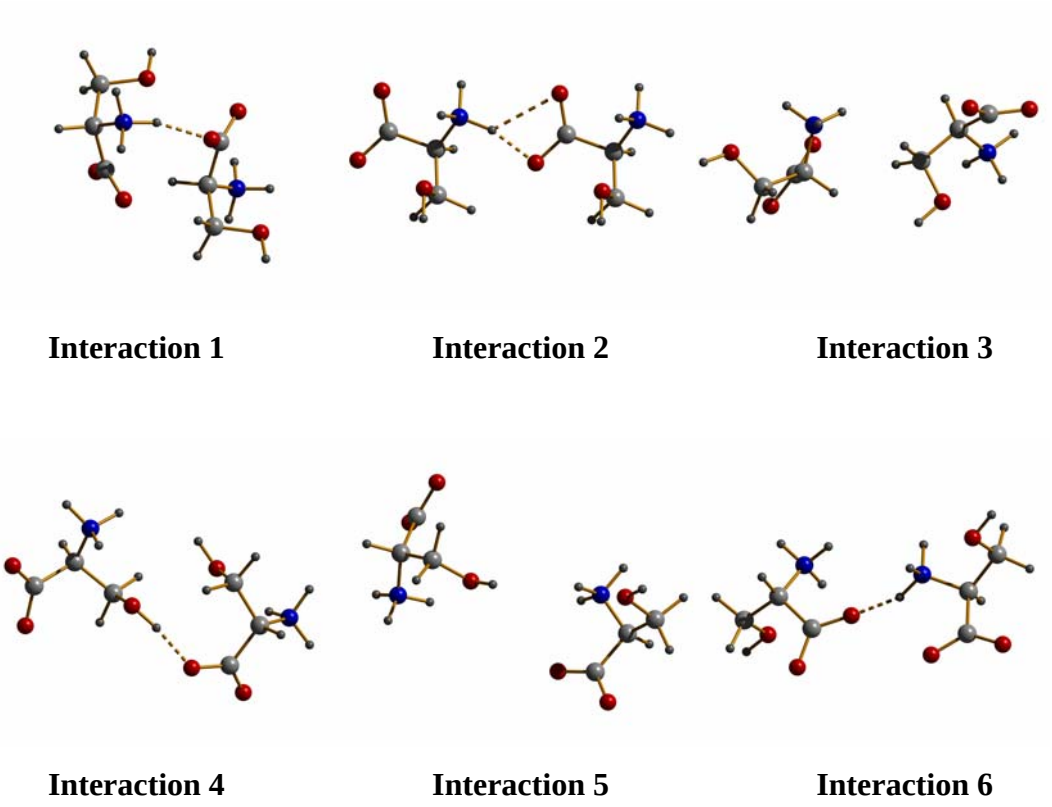

Figure 5.10: Diagrams of the most energetically important dimers in the L-serine-II theoretical crystal structure at 5.2 GPa from PIXEL analysis. The colour scheme is the same as in Fig. 5.1.

The conformation of the serine molecule does not change in moving from phase II to phase III, and the lattice enthalpy of phase III lies approximately along the trend line established for phase II. PIXEL calculations (using the theoretical structural data) show that there are six important interactions in the phase II structure. These are labelled 1-6 in Figure 5.10 in descending order of interaction energy at 5.2 GPa; the variation of interaction energy with distance is plotted in Figure 5.11. Interaction 1 is again the N1H4…O2 hydrogen bond which was also the strongest interaction in phase I. The next strongest interactions, 2 & 3, are also the same as interactions 2 & 3 in the phase I structure, namely the N1H5…O1/O2 bifurcated hydrogen bond and a van der Waals contact respectively. The fourth interaction is now the hydrogen bonded O3H7…O2 contact which replaced the O3H7…O3 contact during the phase transition. Finally interactions 5 & 6 correspond

to another van der Waals contact and the hydrogen bonding interaction N1H6…O1 respectively.

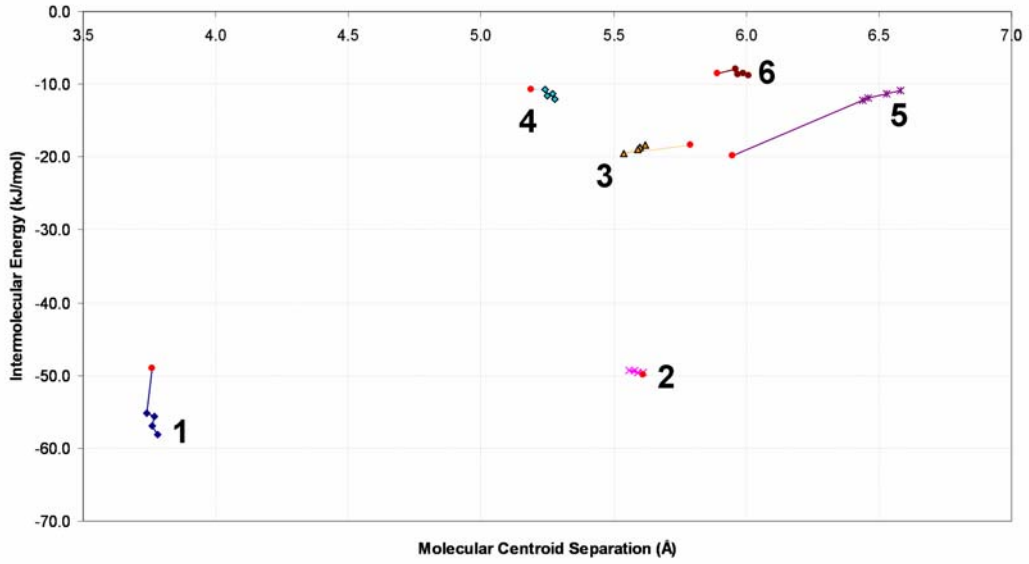

Figure 5.11: Graph of total interaction energy for the six most energetically important dimers in the L-serine-II and L-serine-III theoretical structures (in kJ mol^{-1}) against the distance between the molecular centroids of the molecules involved in the interaction (in Å). The point corresponding to the phase III interaction energy for each dimer has been displayed as a red circle.

The phase transition from phase II to phase III occurs with a marked increase in the stabilising energy of interaction 5 which, in phase III, now corresponds to the newly formed minor component of the bifurcated hydrogen bond O3H7…O2/O1. It appears that the II-to-III transition is driven by a rearrangement into a more optimal intermolecular packing pattern. At 7.3 GPa the O3H7…O2 H-bond (O3…O2 = 2.599 Å) is seen to approach the shortest interaction distance for a primary alcohol donor to carboxyl acceptor OH…O hydrogen bond in the CSD [2.584 (2) Å for GOLWIN] (Tusvik *et al.*, 1999), and the new phase allows the interaction to lengthen slightly as well as forming a hydrogen bonding interaction with another molecule.

5.6 Conclusions

We have described DFT geometry optimisations of the three phases of serine which exist between ambient pressure to 8.1 GPa and compared these structures to those determined using neutron powder diffraction. The theoretical structures are seen to compare very favourably with the experimental ones with only small differences in the primary geometry and molecular packing. These findings suggest that it may be possible to predict high pressure structures by performing a geometry relaxation on an ambient pressure structure using the *SIESTA* code with the addition of a fixed external pressure parameter.

PIXEL calculations show that there is a substantial energy gap between the internal lattice energies of phases I and II. Analysis of individual dimer energies also suggests that none of the intermolecular interactions becomes significantly destabilising as the transition pressure to phase-II is approached. The transition between phases I and II is driven partly by the opportunity for the molecule to change its conformation during the phase transition to a new conformation, which is 40 kJ mol^{-1} more stable than the ambient pressure conformation. The hydrogen bonding pattern in phase II which allows this new conformation of L-serine is presumably only feasible at this higher pressure. The phase transition also involves a substantial decrease in the unit cell volume which means a further stabilisation in enthalpy of phase II with respect to phase I.

Analysis of the intermolecular interaction energies during the compression of the phase II structure showed that the largest gain in energy during the second phase transition from L-serine-II to L-serine-III was in the formation of a bifurcated OH…O/O hydrogen bond.

5.7 References

Allen, F. H. (2002). *Acta Crystallographica, Section B* **58**, 380-388.

Allen, F. H. & Motherwell, W. D. S. (2002). *Acta Crystallographica, Section B* **58**, 407-422.

Betteridge, P. W., Carruthers, J. R., Cooper, R. I., Prout, K. & Watkin, D. J. (2003). *Journal of Applied Crystallography* **36**, 1487.

Birch, F. (1947). *Physical Review* **71**, 809-824.

Boese, R., Downs, A. J., Greene, T. M., Hall, A. W., Morrison, C. A. & Parsons, S. (2003). *Organometallics* **22**, 2450-2457.

Bruno, I. J., Cole, J. C., Lommerse, J. P. M., Rowland, R. S., Taylor, R. & Verdonk, M. L. (1997). *Journal of Computer-Aided Materials Design* **11**, 525-537.

Burchell, C. J., Glidewell, C., Lough, A. J. & Ferguson, G. (2001). *Acta Crystallographica, Section B* **57**, 201-212.

Chisholm, J. A. & Motherwell, S. (2005). *Journal of Applied Crystallography* **38**, 228-231.

Coelho, A. A. (2007). *TOPAS-Academic*, Version 4.1, *General profile and structure analysis software for powder diffraction data*. Bruker-AXS, Madison, Wisconsin, USA.

Collins, A., Cooper, R. I. & Watkin, D. J. (2006). *Journal of Applied Crystallography* **39**, 842-849.

Cooper, T. G., Jones, W., Motherwell, W. D. S. & Day, G. M. (2007). *CrystEngComm* **9**, 595-602.

Crystal Impact (2004). *DIAMOND version 3.0*, *Visual crystal structure information system*. Crystal Impact GbR, Postfach 1251, 53002, Bonn, Germany.

Dawson, A., Allan, D. R., Parsons, S. & Ruf, M. (2004). *Journal of Applied Crystallography* **37**, 410-416.

Day, G. M., Motherwell, W. D. S., Ammon, H. L., Boerrigter, S. X. M., Della Valle, R. G., Venuti, E., Dzyabchenko, A., Dunitz, J. D., Schweizer, B., Van Eijck, B. P., Erk, P., Facelli, J. C., Bazterra, V. E., Ferraro, M. B., Hofmann, D. W. M., Leusen, F. J. J., Liang, C., Pantelides, C. C., Karamertzanis, P. G., Price, S. L., Lewis, T. C., Nowell, H., Torrisi, A., Scheraga, H. A., Arnautova, Y. A., Schmidt, M. U. & Verwer, P. (2005). *Acta Crystallographica, Section B* **61**, 511-527.

de Kruif, C. G., Voogd, J. & Offringa, J. C. A. (1979). *Journal of Chemical Thermodynamics* **11**, 651-656.

Drebushchak, T. N., Sowa, H., Seryotkin, Y. V., Boldyreva, E. V. & Ahsbahs, H. (2006). *Acta Crystallographica, Section E* **62**, o4052-o4054.

Dunitz, J. D. & Gavezzotti, A. (2005). *Angewandte Chemie, International Edition* **44**, 1766-1787.

Farrugia, L. J. (1999). *Journal of Applied Crystallography* **32**, 837-838.

Fleming, S. & Rohl, A. (2005). *Zeitschrift fuer Kristallographie* **220**, 580–584.

Fortes, A. D. (2004). thesis, University of London, London, UK.

Frisch, M. J., Trucks, G. W., Schlegel, H. B., Scuseria, G. E., Robb, M. A., Cheeseman, J. R., Zakrzewski, V. G., Montgomery, J. A. J., Stratmann, R. E., Burant, J. C., Dapprich, S., Millam, J. M., Daniels, A. D., Kudin, K. N., Strain, M. C., Farkas, O., Tomasi, J., Barone, V., Cossi, M., Cammi, R., Mennucci, B., Pomelli, C., Adamo, C., Clifford, S., Ochterski, J., Petersson, G. A., Ayala, P. Y., Cui, Q., Morokuma, K., Malick, D. K., Rabuck, A. D., Raghavachari, K., Foresman, J. B., Cioslowski, J., Ortiz, J. V., Stefanov, B. B., Liu, G., Liashenko, A., Piskorz, P., Komaromi, I., Gomperts, R., Martin, R. L., Fox, D. J., Keith, T., Al-Laham, M. A., Peng, C. Y., Nanayakkara, A., Gonzalez, C., Challacombe, M., Gill, P. M. W., Johnson, B. G., Chen, W., Wong, M. W., Andres, J. L., Head-Gordon, M., Replogle, E. S. & Pople, J. A. (1998). *Gaussian 98 revision A.7*, Gaussian, Inc., Pittsburgh, PA, USA.

Gavezzotti, A. (2005). *Zeitschrift fuer Kristallographie* **220**, 499-510.

Kistenmacher, T. J., Rand, G. A. & Marsh, R. E. (1974). *Acta Crystallographica, Section B* **30**, 1610-1612.

Kuznetsov, A. Z., Dmitriev, V., Dubrovinsky, L., Prakapenka, V. & Weber, H. P. (2002). *Solid State Communications* **122**, 125-127.

Kyoung, T. N., Kwang, H. C., Kwon, O. Y., Jhon, M. S. & Scheraga, H. A. (1994). *Journal of Physical Chemistry* **98**, 10742-10749.

Macrae, C. F., Bruno, I. J., Chisholm, J. A., Edgington, P. R., McCabe, P., Pidcock, E., Rodriguez-Monge, L., Taylor, R., van de Streek, J. & Wood, P. A. (2008). *Journal of Applied Crystallography* **41**, 466-470.

Miller, R. A. & Schuele, D. E. (1969). *Journal of Physics and Chemistry of Solids* **30**, 589-600.

Moggach, S. A., Allan, D. R., Clark, S. J., Gutmann, M. J., Parsons, S., Pulham, C. R. & Sawyer, L. (2006). *Acta Crystallographica, Section B* **62**, 296-309.

Moggach, S. A., Allan, D. R., Morrison, C. A., Parsons, S. & Sawyer, L. (2005). *Acta Crystallographica, Section B* **61**, 58-68.

Moggach, S. A., Marshall, W. G. & Parsons, S. (2006). *Acta Crystallographica, Section B* **62**, 815-825

Morrison, C. A. & Siddick, M. M. (2003). *Chemistry - A European Journal* **9**, 628-634.

Ordejon, P., Artacho, E. & Soler, J. M. (1996). *Physical Review B* **53**, R10441-R10444.

Perdew, J. P., Burke, K. & Ernzerhof, M. (1996). *Physical Review Letters* **77**, 3865-3868.

Soler, J. M., Artacho, E., Gale, J. D., Garcia, A., Junquera, J., Ordejon, P. & Sanchez-Portal, D. (2002). *Journal of Physics: Condensed Matter* **14**, 2745–2779.

Spek, A. L. (2003). *Journal of Applied Crystallography* **36**, 7-13.

Stinton, G. W. & Evans, J. S. O. (2007). *Journal of Applied Crystallography* **40**, 87-95.

Tusvik, P. H., Mostad, A., Dalhus, B. & Rosenqvist, E. (1999). *Acta Crystallographica, Section C* **55**, 1113-1115.

Volkov, A. & Coppens, P. (2004). *Journal of Computational Chemistry* **25**, 921-934.

Waldorf, D. L. & Alers, G. A. (1962). *Journal of Applied Physics* **33**, 3266-3269.

Chapter 6

Analysis of the Compression of Molecular Crystal Structures using Hirshfeld Surfaces*

* Wood, P. A., McKinnon, J. J., Parsons, S., Pidcock, E., Spackman, M. A. *CrystEngComm*, DOI:10.1039/b715494a, 2008.

6.1 Synopsis

A dataset of molecular compression studies has been analysed using Hirshfeld surfaces in order to investigate the effect of pressure on the balance of crystal packing interactions. This study has found a range of consistently recurring features, including the reduction of any voids within the structures and the appearance of a greater number of short contacts. The examination of fingerprint plots has also suggested a likely ambient pressure distance limit for H…H contacts within these organic crystal structures of 1.7 Å. A series of further analyses have been performed in order to assess the validity of this distance limit.

6.2 Introduction

The technique of high pressure crystallography using diamond anvil cells is a valuable probe for studying the fundamental properties of solid state materials. Of the many different areas to which high pressure crystallography has been applied, including metals, minerals and ices, the field of small organic molecules has still been only lightly explored. Much of the recent work looking at small molecules at high pressure has focussed on the opportunity to access new polymorphs of a compound either through pressure-induced freezing (Allan *et al.*, 2002, Lozano-Casal *et al.*, 2005, Oswald *et al.*, 2005, Gajda *et al.*, 2006) or in-situ recrystallisation from a solution at pressure (Fabbiani *et al.*, 2003, Fabbiani *et al.*, 2004, Fabbiani *et al.*, 2005). There is also a great deal to learn from the straightforward compression of single crystals. With good quality single crystal diffraction experiments at a range of pressures it is possible to analyse the compressibilities of different types of interaction and explore the dynamic effects of pressure on crystal packing.

The analysis of small molecule crystal structures has long been dominated by the description, when present, of hydrogen bonding patterns. A crystal structure, at any pressure, is determined by a balance of many forces, so it is important to take into account all of the intermolecular interactions present in a structure. This is especially true for high pressure structural analysis because the contacts in a structure will become considerably distorted from their ambient pressure geometries. For this reason it is necessary to utilize a method which allows the visualization and

exploration of all of the intermolecular contacts in a structure at the same time. This can be achieved in the program *CrystalExplorer* (Wolff *et al.*, 2007), which facilitates the calculation of the molecular Hirshfeld surface – a space partitioning construct that summarises the crystal packing into a single 3D surface (Spackman & Byrom, 1997, McKinnon *et al.*, 1998, Spackman & McKinnon, 2002).

The Hirshfeld surface is defined as the boundary of the region where 'the electron distribution of a sum of spherical atoms for the molecule (the promolecule) dominates the corresponding sum over the crystal (the procrystal)' (McKinnon *et al.*, 2004). For a weight function such that $w(\mathbf{r}) = \rho_{promolecule}(\mathbf{r})/\rho_{procrystal}(\mathbf{r})$, the Hirshfeld surface therefore corresponds to $w(\mathbf{r}) = 0.5$. A range of properties can be mapped onto the Hirshfeld surface in order to display information about the surface including distances of atoms external (d_e) and internal (d_i) to the surface and the shape properties of the surface. It is also possible to condense the distance information summarised in the surface into a 2D histogram of d_e against d_i which is a unique identifier of a crystal structure, called the 'fingerprint plot' (Spackman & McKinnon, 2002). The histogram displays the distance data using discrete data bins of width 0.01 Å and each data point is assigned a colour based on the fraction of the surface area which corresponds to that pair of d_e and d_i. In this way blue points represent a small fraction of the surface area with the colour changing through green to red for increasing fractions. Recent developments in the program now allow the possibility to map a distance normalised using atomic van der Waals radii (d_{norm}) onto the surface and to analyse types of interactions individually, both using the Hirshfeld surface and the corresponding fingerprint plot (McKinnon *et al.*, 2007).

The occurrence of phase transitions in small organic molecules arising due to compression of single crystals has previously been rationalised by studying the changes in intermolecular interactions such as hydrogen bonding (Moggach, Allan, Morrison *et al.*, 2005), π…π interactions (Chapter 2) and S…S contacts (Moggach, Allan, Clark *et al.*, 2006). It has been found that, below 10 GPa, these types of interactions do not compress below the limits of similar contacts found at ambient conditions in the Cambridge Structural Database (CSD) (Allen, 2002, Allen & Motherwell, 2002). The phase transitions in these systems are found to occur when

these interactions reach their ambient limits. It is hoped that the use of a program in which the packing of the whole crystal structure can be studied at once will allow further insight to be gained into the effect of pressure on the delicate balance of intermolecular forces within a crystal. The ultimate goal for this area of research is to be able to predict both the anisotropic compression of organic crystal structures and at what pressures phase transitions will occur.

6.3 Experimental

6.3.1 Development of the data set

The data required for this study were multiple series of organic molecular structures for which the same phase of the compound was stable under compression for a pressure range of at least 2.0 GPa and contains at least three crystal structures including an ambient pressure structure. It was also necessary to check that the placement of hydrogen atoms in the compression studies used were reasonable as this affects the Hirshfeld surface analysis considerably. The data were found through searches of the CSD combined with some of our own, as yet unpublished, data. These searches of the CSD utilised the program *ConQuest* and version 5.28 of the database.

The resulting data set contains compression studies for 13 different compounds, which are listed, along with references, in Table 6.1. These compounds have been studied under compression over a range of different pressures making a total of 75 ambient phase crystal structures, two of which have been shown to undergo a single crystal to single crystal phase transition at higher pressures (L-serine-I and salicylaldoxime-I). The compression data used for L-serine-I are from the neutron powder study on the compound (Moggach, Marshall *et al.*, 2006) due to the higher precision of the structures compared to the single crystal x-ray diffraction structures. The neutron structures follow the same trend as the x-ray structures and the phase transition to form II of the compound occurs at approximately the same pressure in the two studies.

No.	Compound	HP*	PT†	Refcodes	References
I	Acetaminophen-I	4.0	No	HXACAN09-12	(Boldyreva *et al.*, 2000)
II	3-Aza-bicyclo(3.3.1)nonane-2,4-dione-I	7.1	No	-	(Chapter 4)
III	3-Chloro-salicylaldoxime	5.0	No	-	(Chapter 3)
IV	3-Fluoro-salicylaldoxime	6.5	No	-	(Wood *et al.*, 2008)
V	α-Glycine	6.2	No	GLYCIN63-64	(Dawson *et al.*, 2005)
VI	α-Glycylglycine	4.7	No	GLYGLY14-18	(Moggach, Allan, Parsons *et al.*, 2006)
VII	L-alanine	6.4	No	-	(Dawson, 2003)
VIII	L-cystine	3.7	No	LCYSTI15-19	(Moggach, Allan, Parsons *et al.*, 2005)
IX	L-serine-I	4.5	Yes	-	(Moggach, Marshall *et al.*, 2006)
X	3-Methoxy-salicylaldoxime	6.0	No	-	(Chapter 3)
XI	3-Methyl-salicylaldoxime	5.6	No	-	(Chapter 3)
XII	Naphthalene	2.1	No	NAPHTA19-22	(Fabbiani *et al.*, 2006)
XIII	Salicylaldoxime-I	5.3	Yes	SALOXM03-09	(Chapter 2)

* HP = Highest pressure achieved in GPa for compression of the ambient phase structure.
† PT = Single crystal to single crystal phase transition observed.

Table 6.1: List of compounds for which compression data has been analysed in this particular study along with CSD refcodes for the structural data and references.

The further study of H…H contacts in high pressure structures used an expanded set of structures made up of the original data set with the addition of a series of extra structures obtained from the CSD. The extra structures consist of those which satisfied the following search conditions: a high pressure (≥ 0.1 GPa), room temperature structure of an organic compound containing at least one hydrogen atom with no disorder and 3D coordinates. A further restriction was also applied to remove

any structures with an R-factor of greater than 10%. The details of these extra structures along with their CSD refcodes are given in Table 6.2. A total of 48 further crystal structures were obtained, two of which required the addition of hydrogen atoms in calculated positions (FACRIK03 and FACRIK04).

6.3.2 Hirshfeld surface calculations

Each of the crystal structures in the data set was taken without modification from the CSD, or *via* a private communication, for Hirshfeld surface analysis. When the structures are read into the program for analysis *CrystalExplorer* automatically modifies all bond lengths to hydrogen to standard neutron values (C-H = 1.083 Å, N-H = 1.009 Å and O-H = 0.983 Å). For the purpose of this study all the Hirshfeld surfaces were generated using a standard (high) surface resolution. The Hirshfeld surfaces mapped with d_e use a fixed colour scale of 0.65 (red) to 2.2 (blue) for easy comparison between structures. The d_{norm} surfaces are mapped over a fixed colour scale of -0.75 (red) to 1.10 (blue). The fingerprint plots displayed each use the standard 0.4 – 2.6 Å view with the d_e and d_i distance scales displayed on the graph axes.

6.3.3 PIXEL Calculations

An idealised geometry model for methane was created as a test molecule for study of H…H interactions. This model was used to calculate the molecular electron density by standard quantum chemical methods using the program *GAUSSIAN98* (Frisch *et al.*, 1998) with the MP2/6-31G** basis set. The electron density model of the molecule was then analysed using the program package *OPiX* (Gavezzotti, 2005) which allows the calculation of dimer energies. The output from these calculations yields a total energy and a breakdown into its electrostatic, polarisation, dispersion and repulsion components (Dunitz & Gavezzotti, 2005).

CSD Refcodes	No. CIFs	Compound	Pressure(s) (GPa)	Reference
ACETAC09	1	Acetic Acid	0.46	Dawson, 2004
BENZEN04, 11	2	Benzene	2.5, 0.7	Fourme, 1971, Budzianowski, 2006
BISMEV04	1	Piracetam	0.4	Pulham, 2005
DATREV01	1	bis(Ethylenedithio)-tetrathiafulvalene tri-iodide	0.95	Molchanov, 1986
DCLMET11, 12	2	Dichloromethane	0.7	Podsiadlo, 2005
FACRIK03, 04	2	1,3-Cyclohexanedione	1.14,1.9	Katrusiak, 1990
FIGYID01	1	Cyclopropylamine	1.2	Lozano-Casal, 2005
GLYCIN36, 41, 44-47, 50, 61, 65-68	12	Glycine	0.95, 7.1, 5.1, 4.38, 3.63, 3.12, 1.39, 6.47, 0.5, 1.3, 1.9, 4.3	Boldyreva, 2005 & Dawson, 2005
GUHHAS01-03	3	Chlorotrimethylsilane	0.23, 0.3, 0.58	Gajda, 2006
HEGHUX	1	Cyclopentanol	1.5	Moggach, 2005a
KETVEK03	1	Cyclobutanol	1.3	McGregor, 2005
LCYSTN24, 25, 27	3	L-Cysteine	2.6, 4.2, 1.8	Moggach, 2006
LSERIN11-16	6	L-Serine	0.3, 1.4, 2.9, 4.1, 4.8, 5.4	Moggach, 2005b
NAGHOT, 02, 03	3	2,5-bis(4-Nitrophenyl)-(1,3,4)-oxadiazole	2.9, 1.1, 2.0	Orgzall, 1999
NAPHTA12	1	Naphthalene	0.51	Alt, 1982
PHENOL11	1	Phenol	0.16	Allan, 2002
PRONAC02	1	Propionic Acid	1.4	Allan, 2000
QAMTUU01	1	3-Fluorophenol	0.12	Oswald, 2005
QAMVEG01	1	3-Chlorophenol	0.1	Oswald, 2005
THIOUR19	1	Thiourea	0.97	Asahi, 2000
TTFTCG06	1	Tetradeutero-tetrathiafulvene	0.46	Filhol, 1981
WAFNAT	1	Paracetamol dihydrate	1.1	Fabbiani, 2004
WANMUU01	1	2-Chlorophenol	0.12	Oswald, 2005

Table 6.2: Additional high pressure structures mined from the CSD using the search conditions: high pressure (≥ 0.1 GPa), room temperature, only organic compounds with at least one H or D atom, R-factor > 10%, no disorder, must have 3D coordinates. The CSD refcodes are given along with the pressure each crystal structure was collected at, the year of the publication and the first author listed in the publication. The data in the original set of compression studies was also removed to avoid duplication.

6.4 Results & Discussion

6.4.1 Variation of Hirshfeld surfaces with pressure

The data set of crystal structures contains a range of different elements (C, H, N, O, S, Cl, F) and a range of different intermolecular interaction types including conventional hydrogen bonds, S…S, CH…halogen, CH…π and π…π contacts. There are, however, a number of recurring packing features within the set of structures. The Hirshfeld surface mapped with d_e is a particularly useful tool for comparing packing patterns, especially when the colour scale is standardised such that close contacts in different compounds will appear the same colour.

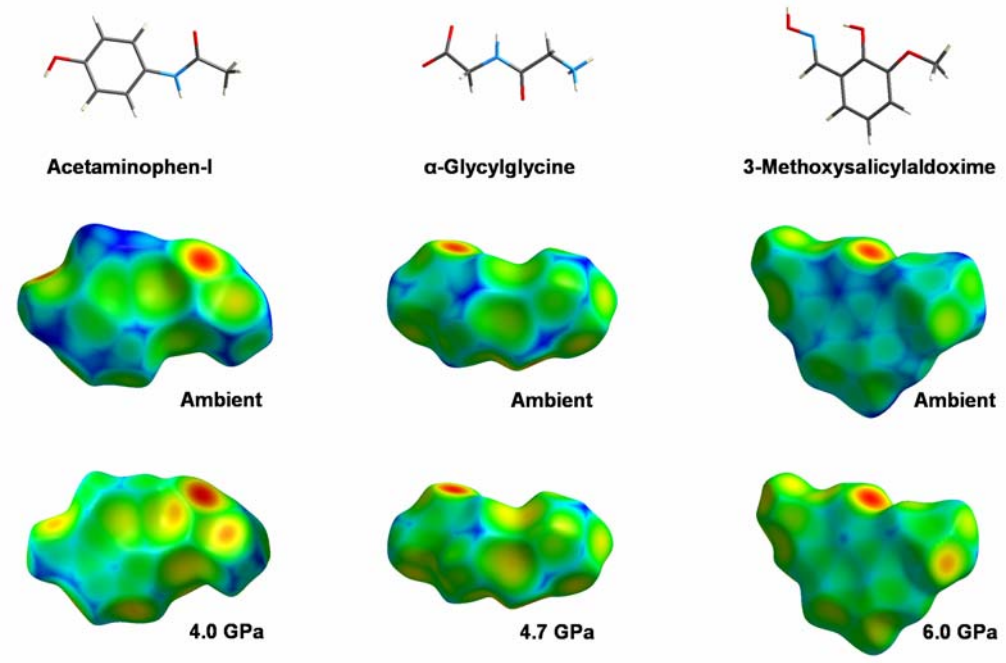

Figure 6.1: Hirshfeld surfaces mapped with d_e for acetaminophen-I (left), α-glycylglycine (middle) and 3-methoxysalicylaldoxime (right). The diagram shows the molecular structure (top), the Hirshfeld surface at ambient pressure (middle) and the Hirshfeld surface at high pressure (bottom).

It is immediately obvious from the systematic study of the variation of the surfaces with pressure that the blue areas on the surfaces decrease considerably. Figure 6.1 shows the Hirshfeld surfaces of acetaminophen-I, α-glycylglycine and 3-methoxysalicylaldoxime both at ambient conditions and at the highest pressure obtained for these structures. The blue regions that are visible at ambient conditions almost completely disappear in the higher pressure structures. These blue areas on

the surface correspond to particularly long contacts and thus tend to indicate voids within molecular crystal structures. The reduction of the blue areas is therefore consistent with the observations from previous studies (Dawson *et al.*, 2005, Moggach, Allan, Morrison *et al.*, 2005, Moggach, Allan, Clark *et al.*, 2006) that the primary effect of compression in molecular crystal structures is to decrease the sizes of voids present in the ambient pressure structures.

The compression of these molecular structures is also seen to produce more red regions in the d_e-mapped Hirshfeld surfaces, which indicates significantly close intermolecular contacts. The d_e property does not, however, take into account the size of the atoms, so close contacts between larger atoms are less obvious in the surfaces than those between smaller atoms. A recent development in *CrystalExplorer* allows the mapping of a new function, d_{norm}, onto the Hirshfeld surface (McKinnon *et al.*, 2007). This property is a contact distance normalised using the van der Waals (vdW) radii of the two atoms internal (r_i^{vdW}) and external (r_e^{vdW}) to the surface using the following equation.

$$d_{norm} = \frac{d_i - r_i^{vdW}}{r_i^{vdW}} + \frac{d_e - r_e^{vdW}}{r_e^{vdW}}$$

This normalisation means that contacts closer than the vdW separation have a negative d_{norm} value and contacts further apart than the vdW separation have a positive value. The d_{norm} values are mapped onto the Hirshfeld surface using a colour scale that displays negative values as red regions and positive values as blue regions with values of zero (where the distance is exactly the vdW separation) being shown as white areas. Very close intermolecular contacts are therefore more easily identified on the Hirshfeld surface using this property rather than the d_e property.

A study of the changes in the d_{norm} surface for the compounds in the dataset shows that the number of red regions (i.e. close contacts) increases significantly at higher pressures. Figure 6.2 shows the effect of compression upon the d_{norm} Hirshfeld surface of three of the compounds in the data set (3-aza-bicyclo(3.3.1)nonane-2,4-dione-I, 3-chlorosalicylaldoxime & naphthalene) from ambient pressure to the highest pressure achieved for each of the structures. In each of these studies it can be seen from Figure 6.2 that the number of contacts closer than the vdW separation has

increased at the highest pressure obtained compared to the ambient structure. This is particularly noticeable in the Hirshfeld surface for naphthalene, where there is only one very faint area of close contacts at ambient conditions which corresponds to a CH…π interaction.

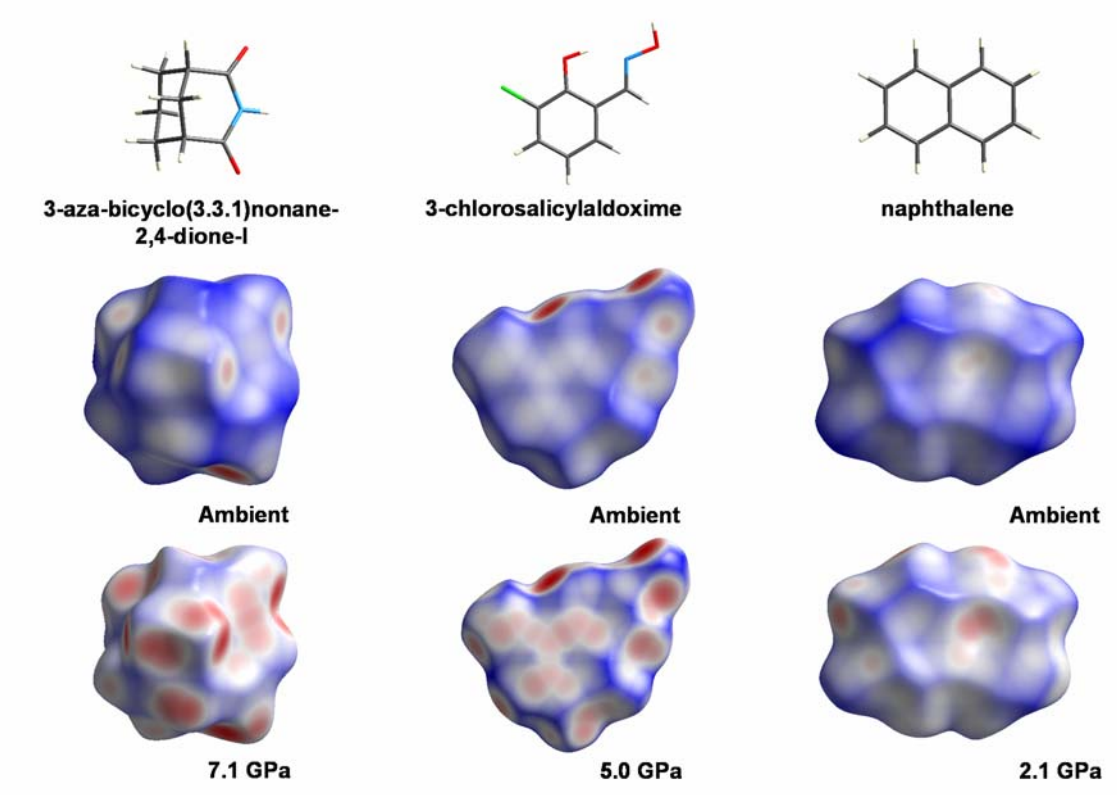

Figure 6.2: Hirshfeld surfaces mapped with d_{norm} for 3-aza-bicyclo(3.3.1)nonane-2,4-dione-I (left), 3-chlorosalicylaldoxime (middle) and naphthalene (right). The diagram shows the molecular structure (top), the Hirshfeld surface at ambient pressure (middle) and the Hirshfeld surface at high pressure (bottom).

The red region in the surface of naphthalene expands considerably at pressures up to just 2.1 GPa and another two contacts closer than the vdW separation appear. We can also see in this case that for each contact region on the d_{norm} surface there must necessarily be an identical region somewhere else on the surface due to the definition of the property. These observations show that as pressure is increased it is not just the conventional intermolecular interactions which become close; all types of contacts can shorten, as exemplified in the high pressure d_{norm} surface for 3-aza-bicyclo(3.3.1)nonane-2,4-dione-I (Figure 6.2).

This analysis illustrates the particular effectiveness of Hirshfeld surfaces in the evaluation of crystal structure compression studies – the surfaces highlight intermolecular contacts that become a lot shorter under pressure. The d_{norm} surface property also allows an impartial indication of which contacts become significantly short at pressure by using the van der Waals radii. Study of these surfaces is a lot faster and easier than looking at long lists of intermolecular atomic distances and changes in distances as the structures vary with pressure.

6.4.2 Variation of fingerprint plots with pressure

The calculation of the Hirshfeld surface of a structure allows all of the intermolecular contacts to be analysed at the same time, but as the surface is a 3-dimensional object detailed comparisons need interactive computer graphics and this is not ideal for illustrations in publications. However, the fingerprint plot, which is a condensed 2D graph of internal and external distances of atoms from the surface, is an ideal tool for directly comparing structures to identify changes in packing. In addition, analysis of the fingerprint plot allows a very quick overview of all of the intermolecular interactions without simply focussing on specific interactions (such as H-bonds) that are perceived to be important. By studying the changes in the fingerprint plots for the range of structures in the data set it is possible to spot features which occur consistently upon compression.

Figure 6.3 shows the fingerprint plots for three of the structures from the present study at ambient pressure and at the highest pressure obtained for that particular phase of the compound. The fingerprint for the structure in each case moves towards the origin of the plot as the overall structure has been compressed and, because the intramolecular geometry is relatively rigid, the intermolecular contacts must decrease on average. It can also be seen for each structure that, although the hydrogen bonding interactions (visible as a pair of spikes either side of the $d_i = d_e$ diagonal) decrease, the longer interactions are compressed more, so the plot becomes squashed as the spread of intermolecular contact distances reduces. The shape of the plot also tends to change somewhat with compression; there is a noticeable increase in symmetry about the *x*/*y* diagonal as pressure increases,

especially at the higher distance end of the fingerprints. For 3-aza-bicyclo(3.3.1)nonane-2,4-dione-I and salicylaldoxime-I the asymmetric regions seen at ambient conditions are indicated in Figure 6.3 by red arrows. Hirshfeld surfaces leave small voids in the crystal and asymmetry in the fingerprint plot occurs due to these voids, where adjacent surfaces do not touch each other. Thus, an increase in symmetry along the diagonal of the fingerprint plot indicates a reduction in the intermolecular voids. This is consistent with the decrease in blue areas seen in the Hirshfeld surfaces and the previous experience of our group of the compression of molecular structures.

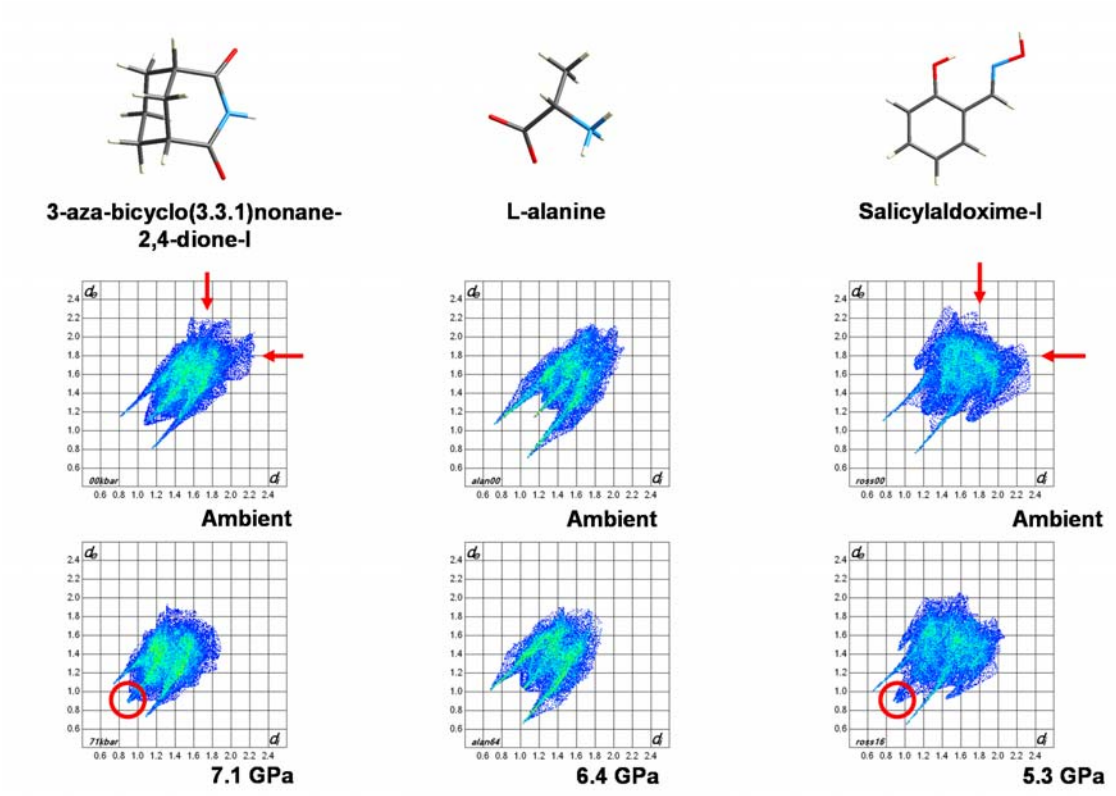

Figure 6.3: Fingerprint plots for 3-aza-bicyclo(3.3.1)nonane-2,4-dione-I (left), L-alanine (middle) and salicylaldoxime-I (right). The diagram shows the molecular structure (top), the fingerprint plot at ambient pressure (middle) and the fingerprint plot at high pressure (bottom). The red arrows and circles are referred to in the main text.

Another recent improvement in the functionality of *CrystalExplorer* is the ability to breakdown the fingerprint plot, and the surface itself, into regions corresponding to contacts between specific atom types, for example just O to H

contacts. This allows the easy identification of the causes of different areas of the fingerprint plot and simple study of the movement of these sections. In the analysis of the neutron powder diffraction study of L-serine, Moggach *et al.* (Moggach, Marshall *et al.*, 2006) noted that close contacts between H atoms are seen in the fingerprint plot at high pressures and that these close H…H contacts are characteristic of the plots obtained for alkanes. The authors stated that the increasing prominence of the H…H region in the L-serine fingerprint plot illustrates the tendency for efficient packing to compete with hydrogen bonding in structure direction at higher pressures.

This H…H region of the fingerprint is seen to become prominent across a range of compression studies as can be seen from the red circled sections for two of the structures in Figure 6.3. For two of these structures, the H…H contact becomes as short as the shortest hydrogen bond. Interestingly the H…H regions both seem to reach approximately the same point, i.e. with d_e and d_i around 0.9 Å. The H…H contact region does not seem to become prominent in the fingerprint plot for L-alanine, and this is due to the extensive 3D hydrogen bonding pattern which restricts the packing such that the hydrogens cannot approach each other freely. This is also the case for the structures of α-glycine, α-glycylglycine, L-cystine and L-serine-I. Figure 6.4 shows a graph of the fractional variation relative to the ambient value for the shortest contact for a particular type (O…H, C…C and H…H are shown) as a function of pressure for the structures within the data set. This graph shows that although the H…H contacts seem to be more compressible and have greater variation in comparison to the other two interaction types, there does appear to be a flattening of the curve at higher pressures suggesting that the contacts may be reaching a distance limit.

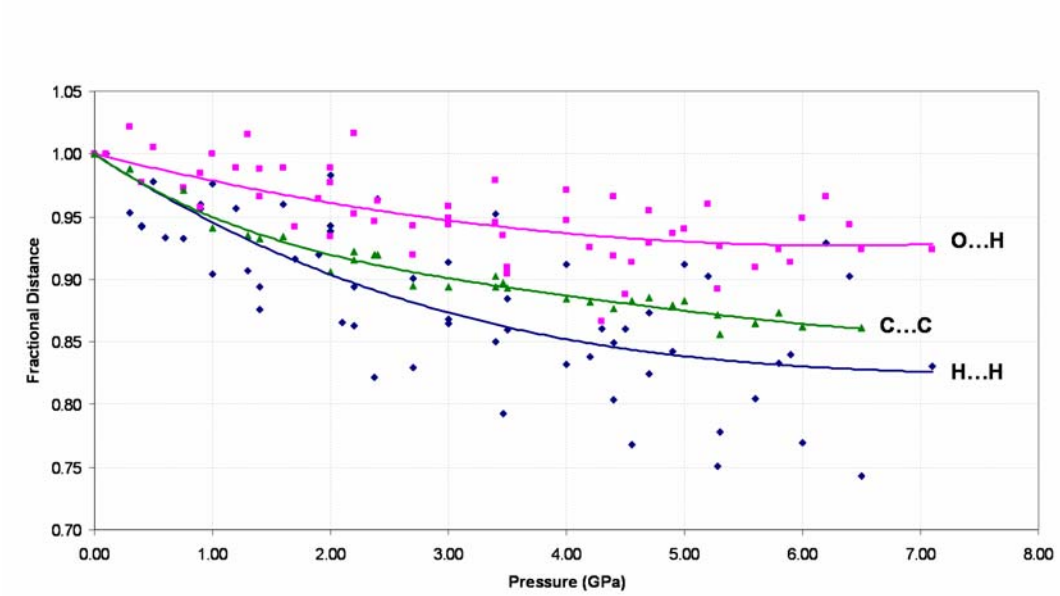

Figure 6.4: Graph of shortest $d_e + d_i$ distance for a particular contact type expressed as a fraction of the ambient pressure value plotted against pressure for the full data set. The data are coloured by contact type as follows; O…H pink squares, C…C dark green triangles and H…H dark blue diamonds. A line of best fit has been added for each contact type.

6.4.3 Analysis of short H…H interactions

The observation of prominent H…H contacts at elevated pressures in a number of structures led to an investigation of the causes of this phenomenon. Visual study of the fingerprint plots suggested that these contacts were compressing to similar distances in a range of different structures. Figure 6.5 shows a graph of the sum of the $d_e + d_i$ distances for the shortest H…H interaction in the structure against pressure for all the compression studies as well as a further set of high pressure structures obtained from the CSD. It can be seen from the graph that these contacts do not compress below a distance of 1.7 Å (highlighted as a red line in Figure 6.5) in any of the structures analysed. The four shortest distances seen at elevated pressures in the compression studies have been circled and these points correspond to the highest pressure achieved for each of acetaminophen-I (labelled I in the diagram), 3-aza-bicyclo(3.3.1)nonane-2,4-dione-I (II), 3-fluorosalicylaldoxime (IV) and salicylaldoxime-I (XIII). The first structure (acetaminophen-I) is believed to undergo a phase transition at higher pressures, although this has not been confirmed. The

single crystal compression study on acetaminophen-I was aborted after 4.0 GPa due to the limits of the pressure cell, but structural analysis suggested that the structure had limited room to compress further (Boldyreva *et al.*, 2000), powder pressure studies (Boldyreva *et al.*, 2002) also showed a partial transformation from form I to form II at pressure. Salicylaldoxime-I is known to undergo a single crystal to single crystal phase transition into form II of the compound between 5.3 and 5.9 GPa (Chapter 2). Interestingly, the crystals of the final two structures circled in Figure 6.5 (3-aza-bicyclo(3.3.1)nonane-2,4-dione-I and 3-fluorosalicylaldoxime) were seen to disintegrate under further compression, which may be indicative of a reconstructive phase transition.

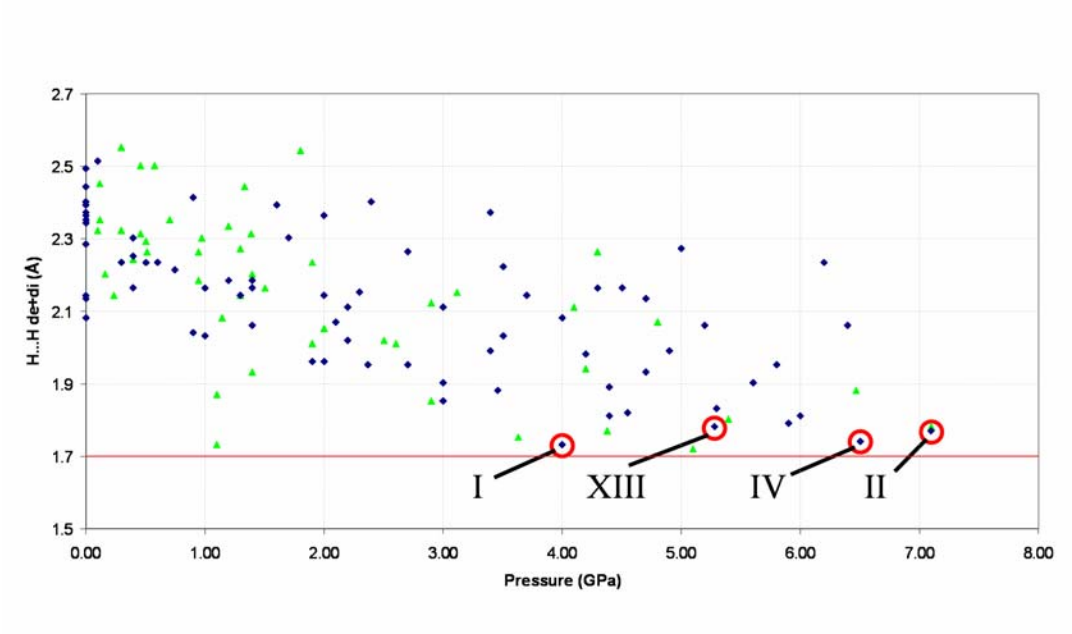

Figure 6.5: Graph of shortest H…H contact $d_e + d_i$ distance against pressure for all the ambient phase compression structures (shown as dark blue diamonds) and for the extra high pressure structures found in the CSD (shown as green triangles). The points circled represent the final structure in a compression series before either a known phase transition or the failure of the crystal. The Roman numbers refer to the main text and Table 1. The red line shown at 1.7 Å indicates the proposed limit for H…H contacts in organic structures within the pressure regime of ambient to 10 GPa.

These results seem to suggest that this distance of 1.7 Å is the limit for contacts between hydrogens in organic structures at pressure to around 10 GPa. Throughout the dataset of pressure studies, none of the structures exhibit H…H

distances below this limit and the ones that approach the limit appear to undergo phase transitions. Although some structures have restricted H…H contacts due to extensive 3D hydrogen bonding patterns, as mentioned earlier, there are a large number that do not (around 73% of organic structures that contain a C-H bond display C-H…H-C contacts between 1.7 and 2.4 Å). If these H…H contacts have such a consistent limit across a wide range of structures as they appear to, then the limit could be very useful for predicting phase transitions due to the application of hydrostatic pressure. In order to investigate this limit, two different studies were initiated; firstly to query the CSD in order to determine the ambient limits of H…H contacts, and secondly to analyse the effect of distance on the interaction energy between C-H groups.

The CSD currently contains more than 400,000 crystal structures, the majority of which contain contacts between hydrogen atoms, and the search needed to be restricted in a number of ways. As the structures within the set of compression studies are all organics, and in order to avoid any unusual intermolecular hydrogen interactions, the search was restricted to molecules only containing the elements C, N, O and H. The search space was also restricted to structures with an R-factor < 0.05, not disordered, no errors, not polymeric, no ions and no powder structures. This produced a more tractable quantity of data, which were then searched for H…H contacts within the sum of the van der Waals radii after normalising the terminal hydrogen positions to the same standard neutron lengths as *CrystalExplorer* uses. Figure 6.6 shows a histogram of the H…H separations for these close contacts found in the subset of the CSD. It can be seen from the histogram that only a small fraction (1.8%) of the 44,421 contacts analysed show H…H separations less than 2.0 Å. The ambient limit for these interactions would appear to be in the region from 1.7 to 1.9 Å, though there are a small proportion of structures with shorter distances than this (146 contacts; 0.3% of the sample). These shorter contacts seem to be mainly due to errors in the structures, for example poorly placed hydrogens (e.g. DEBLAY, DEFTUD), possible incorrect symmetry (e.g. AWOTAH) or the presence of un-flagged disorder (e.g. AFEBOC).

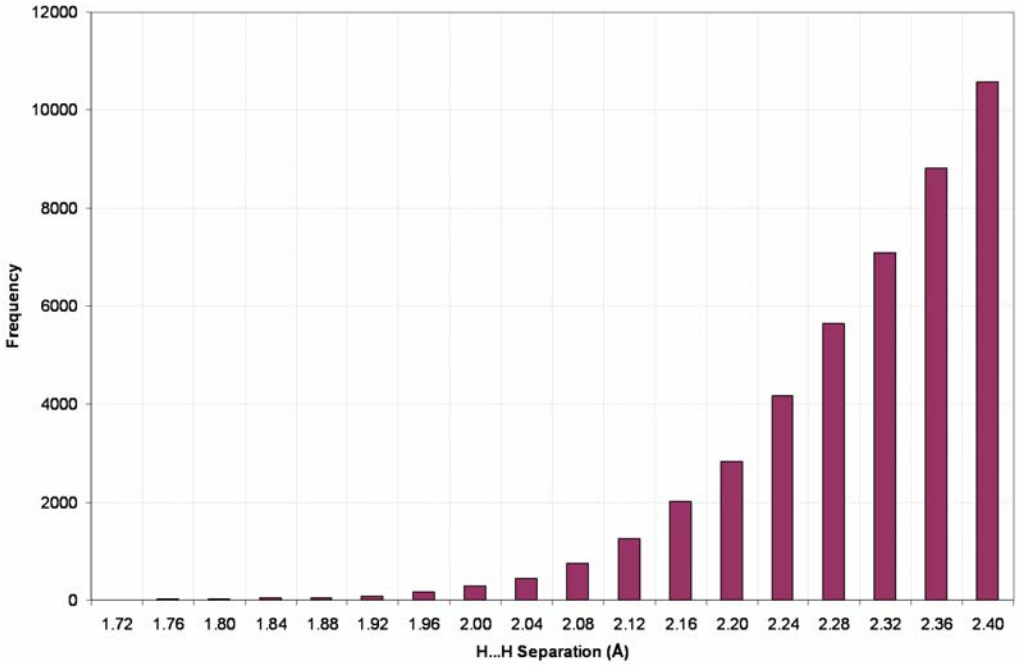

Figure 6.6: A histogram showing the H…H separations for contacts between hydrogens that are closer than the sum of the van der Waals radii within a subset of the CSD only containing molecules made up of the elements C, N, O and H.

In order to quantitatively analyse the destabilising H…H interaction at short distances, methane dimer interaction energies were calculated for varying molecular separations using the PIXEL method. Idealised methane geometries (C-H = 1.083 Å, <HCH = 109.47 °) were used with a linear C-H…H-C approach (Figure 6.7) and the contact distance between the hydrogens varying in 0.2 Å steps from 4.0 to 3.0 Å and then in 0.1 Å steps from 3.0 to 1.6 Å. This produced a simplified model for the effect of decreasing contact distance on the interaction between hydrogens attached to carbon. The results of the dimer calculations are shown in Table 6.3 including the total dimer interaction energy as well as a breakdown of the component Coulombic, dispersion, polarisation and repulsion terms. The energies calculated describe the interaction felt by the reference molecule as a result of its neighbour, multiplying this value by two gives the dimerization energy. Figure 6.8 shows a graph of the total interaction energy of the collinear $(CH_4)_2$ dimer as a function of the H…H separation.

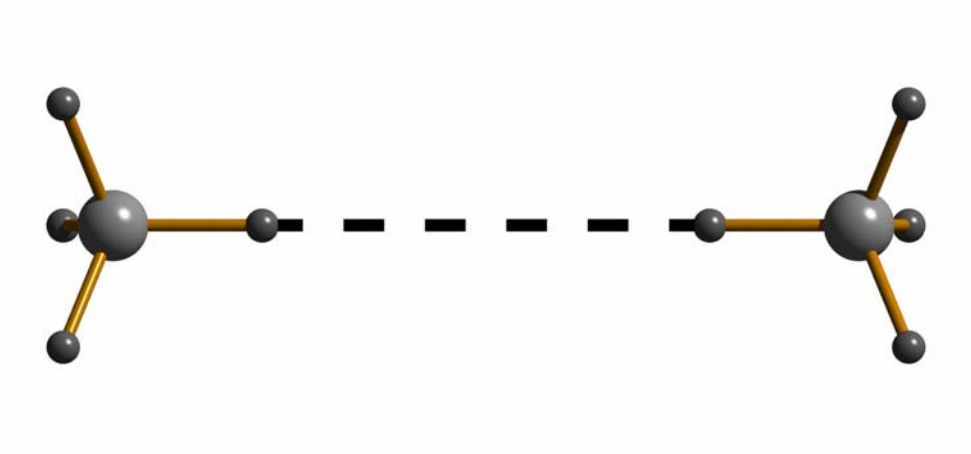

Figure 6.7: The geometry of the collinear C-H…H-C contact between methane molecules in the PIXEL dimer calculations. Dashed black line indicates the contact between hydrogens. The colour scheme is light-grey: carbon and dark-grey: hydrogen.

H…H Distance	Coulombic	Dispersion	Repulsion	Polarisation	Total
4.0	0.00	-0.10	0.00	0.00	-0.05
3.8	0.00	-0.10	0.00	0.00	-0.10
3.6	0.00	-0.15	0.00	0.00	-0.10
3.4	0.00	-0.20	0.00	0.00	-0.15
3.2	0.05	-0.25	0.05	0.00	-0.20
3.0	0.05	-0.35	0.05	0.00	-0.25
2.9	0.05	-0.45	0.10	0.00	-0.30
2.8	0.05	-0.50	0.15	0.00	-0.35
2.7	0.00	-0.60	0.25	-0.05	-0.35
2.6	0.00	-0.70	0.40	-0.05	-0.40
2.5	-0.05	-0.85	0.60	-0.10	-0.40
2.4	-0.10	-1.00	0.85	-0.15	-0.40
2.3	-0.20	-1.20	1.30	-0.25	-0.30
2.2	-0.30	-1.40	1.95	-0.40	-0.15
2.1	-0.50	-1.65	2.80	-0.65	0.00
2.0	-0.75	-1.95	3.95	-0.95	0.30
1.9	-1.10	-2.25	6.05	-1.50	1.20
1.8	-1.65	-2.65	8.60	-2.35	2.05
1.7	-2.20	-3.05	12.20	-3.30	3.65
1.6	-3.40	-3.45	16.90	-5.30	4.75

Table 6.3: PIXEL dimer interaction energies for methane collinear C-H…H-C contact at varying H…H separation. Distances are in Å, energies are in kJ mol^{-1}. The energies for each component and the total are rounded to the nearest 0.05 kJ mol^{-1}.

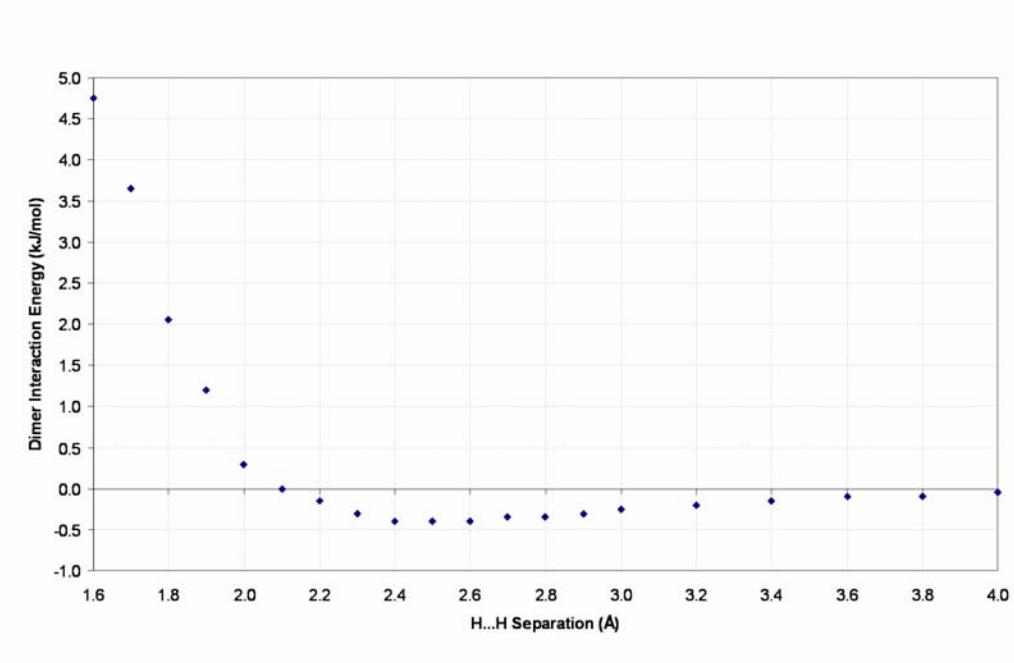

Figure 6.8: Graph of PIXEL dimer interaction energies for the methane collinear C-H…H-C contact at varying H…H separation.

The data in Figure 6.8 show that the interaction displays a smoothly decreasing interaction energy from an infinite separation until its optimum distance of around 2.5 Å. At H…H separations below 2.5 Å the repulsion term starts to outweigh the stabilising terms and the energy starts to become less negative, with the intermolecular interaction energy reaching 0.0 kJ mol^{-1} at a distance of 2.1 Å. The repulsion term is then seen to continue increasing sharply with further reduction of the H…H distance and at the proposed limit of these contacts in organic crystal structures the repulsion component of the energy is 12.2 kJ mol^{-1}. This behaviour of the repulsion energy is consistent with results from the compression studies and the search of the CSD described above. It is particularly noticeable that the drop-off in frequency as a function of H…H distance in the CSD data (Figure 6.6) mirrors the increase in repulsion seen in Figure 6.8.

The overall curve for the dimer interaction energy agrees well with a two previous studies of collinear C-H…H-C methane interactions using *ab initio* MP2/6-311G(2*d*,2*p*) (Novoa *et al.*, 1991) and counterpoise corrected MP2/6-311+G(2*df*,2*pd*) (Rowley & Pakkanen, 1998) calculations. In both these cases the minimum energy was seen to have a H…H separation of approximately 2.5 Å and a

stabilising energy of approximately -0.4 kJ mol^{-1} with the interaction becoming destabilising at distances around 2.1-2.2 Å. There has also been a considerable number of theoretical studies on the intermolecular interaction between methane molecules in the more stable D_{3d} configuration with a face-to-face contact between the methane tetrahedra (Rowley & Pakkanen, 1998, Williams & Malhotra, 2006, Li & Chao, 2006). These studies show a minimum energy point with a C…C distance of approximately 3.7 Å and an intermolecular interaction of around -1.0 kJ mol^{-1}. The energies for these interactions are seen to become destabilising at C…C distances of about 3.3-3.4 Å.

6.5 Conclusions

There are many aspects of variation of the Hirshfeld surfaces due to compression which could have been discussed in this study, but we have chosen to focus on the effect of pressure on the intermolecular H…H contacts. Hirshfeld surfaces display all of the intermolecular interactions within the crystal at once and are therefore ideal for analysing the changes in crystal packing due to compression. This study has shown that systematic analysis of structures using Hirshfeld surfaces can help to identify common features which would be more difficult to recognise using more traditional methods of structure analysis.

Previous work within our laboratory has pointed to interstitial void reduction as an important effect of pressure in molecular solids. It was also very noticeable that at elevated pressures a large number of close contacts tend to occur, but none of the intermolecular interactions, including hydrogen bonds, become exceptionally short. The present analysis based on Hirshfeld surfaces supports these general remarks.

An approximate distance limit for H…H interactions of 1.7 Å has been identified from a combination of Hirshfeld surface fingerprints, a search of the CSD and PIXEL calculations on methane. The particularly interesting aspect of the H…H contacts and understanding their compression is that these interactions are relatively consistent across a huge range of different compounds. Whilst hydrogen bonds are highly affected by the chemical environment of the donor and acceptor atoms as well as the geometry of the interaction, the H…H contact is not as sensitive to these

parameters. This means that, in cases where the hydrogens have the freedom to approach closely, this information about the compressibility of H…H interactions and their ambient limit could be used to predict at what pressure a phase transition is likely to happen.

6.6 References

Allan, D. R., Clark, S. J., McGregor, P. A. & Parsons, S. (2002). *Acta Crystallographica, Section B* **58**, 1018-1024.

Allen, F. H. (2002). *Acta Crystallographica, Section B* **58**, 380-388.

Allen, F. H. & Motherwell, W. D. S. (2002). *Acta Crystallographica, Section B* **58**, 407-422.

Boldyreva, E. V., Shakhtshneider, T. P., Ahsbahs, H., Sowa, H. & Uchtmann, H. (2002). *Journal of Thermal Analysis and Calorimetry* **68**, 437-452.

Boldyreva, E. V., Shakhtshneider, T. P., Vasilchenko, M. A., Ahsbahs, H. & Uchtmann, H. (2000). *Acta Crystallographica, Section B* **56**, 299-309.

Dawson, A. (2003). PhD thesis, University of Edinburgh, Edinburgh, UK.

Dawson, A., Allan, D. R., Belmonte, S. A., Clark, S. J., David, W. I. F., McGregor, P. A., Parsons, S., Pulham, C. R. & Sawyer, L. (2005). *Crystal Growth & Design* **5**, 1415-1427.

Dunitz, J. D. & Gavezzotti, A. (2005). *Angewandte Chemie, International Edition* **44**, 1766-1787.

Fabbiani, F. P. A., Allan, D. R., David, W. I. F., Moggach, S. A., Parsons, S. & Pulham, C. R. (2004). *CrystEngComm* **6**, 504-511.

Fabbiani, F. P. A., Allan, D. R., Dawson, A., David, W. I. F., McGregor, P. A., Oswald, I. D. H., Parsons, S. & Pulham, C. R. (2003). *Chemical Communications* **24**, 3004-3005.

Fabbiani, F. P. A., Allan, D. R., Marshall, W. G., Parsons, S., Pulham, C. R. & Smith, R. I. (2005). *Journal of Crystal Growth* **275**, 185-192.

Fabbiani, F. P. A., Allan, D. R., Parsons, S. & Pulham, C. R. (2006). *Acta Crystallographica, Section B* **62**, 826-842

Frisch, M. J., Trucks, G. W., Schlegel, H. B., Scuseria, G. E., Robb, M. A., Cheeseman, J. R., Zakrzewski, V. G., Montgomery, J. A. J., Stratmann, R. E., Burant, J. C., Dapprich, S., Millam, J. M., Daniels, A. D., Kudin, K. N., Strain, M. C., Farkas, O., Tomasi, J., Barone, V., Cossi, M., Cammi, R., Mennucci, B., Pomelli, C., Adamo, C., Clifford, S., Ochterski, J., Petersson, G. A., Ayala, P. Y., Cui, Q., Morokuma, K., Malick, D. K., Rabuck, A. D., Raghavachari, K., Foresman, J. B., Cioslowski, J., Ortiz, J. V., Stefanov, B. B., Liu, G., Liashenko, A., Piskorz, P., Komaromi, I., Gomperts, R., Martin, R. L., Fox, D. J., Keith, T., Al-Laham, M. A., Peng, C. Y., Nanayakkara, A., Gonzalez, C., Challacombe, M., Gill, P. M. W., Johnson, B. G., Chen, W., Wong, M. W., Andres, J. L., Head-Gordon, M., Replogle,

E. S. & Pople, J. A. (1998). *Gaussian 98 revision A.7*, Gaussian, Inc., Pittsburgh, PA, USA.

Gajda, R., Dziubek, K. & Katrusiak, A. (2006). *Acta Crystallographica, Section B* **62**, 86-93.

Gavezzotti, A. (2005). *Zeitschrift fuer Kristallographie* **220**, 499-510.

Li, A. H.-T. & Chao, S. D. (2006). *Journal of Chemical Physics* **125**, 094312/094311-094312/094318.

Lozano-Casal, P., Allan, D. R. & Parsons, S. (2005). *Acta Crystallographica, Section B* **61**, 717-723.

McKinnon, J. J., Jayatilaka, D. & Spackman, M. A. (2007). *Chemical Communications* 3814-3816.

McKinnon, J. J., Mitchell, A. S. & Spackman, M. A. (1998). *Chemistry - A European Journal* **4**, 2136-2141.

McKinnon, J. J., Spackman, M. A. & Mitchell, A. S. (2004). *Acta Crystallographica, Section B* **60**, 627-668.

Moggach, S. A., Allan, D. R., Clark, S. J., Gutmann, M. J., Parsons, S., Pulham, C. R. & Sawyer, L. (2006). *Acta Crystallographica, Section B* **62**, 296-309.

Moggach, S. A., Allan, D. R., Morrison, C. A., Parsons, S. & Sawyer, L. (2005). *Acta Crystallographica, Section B* **61**, 58-68.

Moggach, S. A., Allan, D. R., Parsons, S. & Sawyer, L. (2006). *Acta Crystallographica, Section B* **62**, 310-320.

Moggach, S. A., Allan, D. R., Parsons, S., Sawyer, L. & Warren, J. E. (2005). *Journal of Synchrotron Radiation* **12**, 598-607.

Moggach, S. A., Marshall, W. G. & Parsons, S. (2006). *Acta Crystallographica, Section B* **62**, 815-825

Novoa, J. J., Whangbo, M.-H. & Williams, J. M. (1991). *Journal of Chemical Physics* **94**, 4835-4841.

Oswald, I. D. H., Allan, D. R., Motherwell, W. D. S. & Parsons, S. (2005). *Acta Crystallographica, Section B* **61**, 69-79.

Rowley, R. L. & Pakkanen, T. (1998). *Journal of Chemical Physics* **110**, 3368-3377.

Spackman, M. A. & Byrom, P. G. (1997). *Chemical Physics Letters* **267**, 215-220.

Spackman, M. A. & McKinnon, J. J. (2002). *CrystEngComm* **4**, 378-392.

Williams, R. W. & Malhotra, D. (2006). *Chemical Physics* **327**, 54-62.

Wolff, S. K., Grimwood, D. J., McKinnon, J. J., Jayatilaka, D. & Spackman, M. A. (2007). *CrystalExplorer*, Version 2.0, University of Western Australia, Perth, Australia.

Wood, P. A., Forgan, R. S., Parsons, S., Pidcock, E. & Tasker, P. A. (2008). Unpublished work.

Chapter 7

Conclusion

7.1 Conclusion

The rationalisation of structural compression and phase transitions that occur due to the application of pressure has in the past been based to a large extent on the lower distance limits observed for similar intermolecular interactions at ambient conditions in the CSD. This method has been used to explain phase transitions due to short hydrogen bonds and also short S…S contacts. Further analysis of high pressure studies in this work has shown that other less directional interactions, such as π-π interactions and even H…H contacts, also have relatively well-defined distance limits. These results imply that there is the potential in the future for prediction of the effects of pressure on organic structures and possibly the pressures at which phase transitions will occur.

Analysis of hydrogen bonding interactions based simply on D(H)…A distances and DHA angles has been found in this study to be inadequate for describing these contacts in some cases. Results of the L-serine dimer interaction calculations showed that two interactions, which have almost identical geometries when described in this simple way, have drastically different interaction energies. In this case the important geometrical parameter appeared to be the angle of approach of the hydrogen bond donor to the acceptor. This illustrates clearly the benefits of evaluating interaction energies quantitatively both when describing a crystal structure and analysing the compression of a structure.

Study of the energies of molecular structures under compression has also helped to highlight the fact that it is important to consider the intramolecular geometry as well as the intermolecular geometries at pressure. The covalent bond lengths in molecules are relatively incompressible at pressures up to 10 GPa. This work has shown, however, that the bond angles and torsions can be seriously distorted, even in the case of rigid molecules as illustrated by the compression of 3-aza-bicyclo(3.3.1)nonane-2,4-dione-I. It is necessary, therefore, to examine the primary geometry carefully with compression and also to take this into account when explaining the effects of pressure.

In conclusion, the use of multiple complementary tools for structural analysis of compression studies is of great importance since reliance on one technique can

lead to failure in the identification of important features. Investigations using the PIXEL method and Hirshfeld surfaces together, for example, have been shown in this work to more easily allow identification of intermolecular contacts, quantification of their relative importance and the study of their changes with pressure. The structural analysis techniques based on whole molecule interactions that have been demonstrated in this thesis have consistently revealed important features that may not otherwise have been identified.